Exploring Performance Scaling Properties of Local Helicity Injection Plasma Startup on Pegasus-III

By

Justin Daniel Weberski

A Dissertation submitted in partial fulfillment of

the requirements for the degree of

Doctor of Philosophy

(Nuclear Engineering and Engineering Physics)

at the

UNIVERSITY OF WISCONSIN—MADISON

2025

Date of final oral examination: 04/18/2025

This dissertation is approved by the following members of the Final Oral Committee:

Stephanie J. Diem, Assistant Professor, Nuclear Engineering and Engineering Physics
Benedikt Geiger, Assistant Professor, Nuclear Engineering and Engineering Physics
Carl R. Sovinec, Professor Emeritus, Nuclear Engineering and Engineering Physics
Amy E. Wendt, Professor, Electrical and Computer Engineering
Paul P. Wilson, Professor, Nuclear Engineering and Engineering Physics

This dissertation is dedicated to my fiancée and family who have sustained me through this long journey with their unconditional love and support

Acknowledgements

Although my name is on the front page of this dissertation, the completion of this thesis work would not have been possible without the help and support of many individuals. I am eternally grateful to all who have contributed to my memorable time as a graduate student at UW-Madison.

First, I would like to thank both of my thesis advisors who helped mold me into the scientist I am today. To Ray Fonck, who initially persuaded me to come to UW-Madison and join the Pegasus team. The wisdom, guidance, and perspective you provided throughout my first five years of graduate school laid the foundation for me to confidently develop and execute the research that comprises this thesis. To Stephanie Diem, who has guided me through this final almost four years. Under your leadership I have developed confidence as an independent scientist capable of defining and executing research. In this way, you have prepared me well for the responsibilities and accountability required of an early career scientist.

I also want to extend my thanks to the rest of my committee members: Benedikt Geiger, Carl Sovinec, Amy Wendt, and Paul Wilson. Your patience, flexibility, and support has been much appreciated throughout this process. I would like to especially thank Carl Sovinec for discussions throughout this work that provided valuable insight and perspective while interpreting this research.

I have been lucky enough to be mentored by an incredible team of scientists throughout my time on Pegasus. My gratitude goes out to Mike Bongard and Josh Reusch who have provided guidance and mentorship since I joined Pegasus. There was never a moment when my questions or curiosities regarding Pegasus, LHI, KFIT, developing APS narratives, and everything in between were not met with great enthusiasm and thorough discussion. My breadth of technical knowledge has greatly benefited from these numerous discussions. The Pegasus team was also lucky enough to expand during the Pegasus-III upgrade with the wonderful additions of John

Goetz, Mark Nornberg, and Aaron Sontag. The diverse set of experiences and knowledge provided by all of you further enriched my development and time at Pegasus. I'd like to especially thank John for his humor and positive attitude, which was always much appreciated, especially after long days wrangling cables, building capacitor banks, and numerous other tasks throughout the Pegasus-III upgrade.

I'd like to thank the entire Pegasus staff consisting of Mike Borchardt, Ben Kujack-Ford, Ben Lewicki, and Greg Winz. Collectively, you have all taught me everything I know about high voltage systems, machining, vacuum maintenance, and everything else needed to maintain a functioning fusion experiment. Your expertise and hard work are what drove the design and construction of the Pegasus-III facility which made this work possible.

Of all the places I considered for graduate school, the graduate students working at Pegasus stood out as being the most welcoming and supportive group. This has proven to be true throughout my entire time at Pegasus. I am grateful to have been given the opportunity to work with and make lifelong friendships with an incredible community of graduate students.

Many thanks to the group of "old" graduate students – Jayson Barr, Galen Burke, Justin Perry, and Dave Schlossberg – who welcomed me into the Pegasus group. Your advice and wisdom were invaluable for adapting as a new graduate student. A special thanks goes out to Justin Perry who taught me basically everything I know about LHI scenario development. He also graciously endured sharing an office with a particularly distracting group of younger students throughout the final stretch of his thesis work. I only now understand how impressive a feat that was, and you did it all while serving as a great mentor for us all.

I am extremely grateful to my primary cohort of graduate students and friends: Grant Bodner, Armand Keyhani, Matt Kriete, Max Major, Jessica Pachicano, Chris Pierren, Alex Rhodes, Nathan Richner, Temo Rodriguez-Sanchez, and Carolyn Schaefer. I found a strong support system amongst you all and a true group of friends who not only helped me survive graduate school but made it possible to truly enjoy it. I will always remember all the Badger games, bar crawls, Terrace sessions, birthday celebrations, and countless laughs inside and outside the office. I consider myself truly lucky to have had the privilege to get to know all of you and look forward to knowing you all for many years to come.

I'd like to especially thank Carolyn, Chris, and Temo for being around for my entire time in graduate school and being a part of the most recent "old" group of students. I know we have all greatly benefited from each other's support on this long journey to each of our own finish lines. An extra special acknowledgement goes to Chris Pierren, who joined Pegasus and began graduate school with me back in Fall 2016. It has always been an absolute pleasure to work with you—so much so that I even followed you to your job. Thank you so much for your support throughout the years and especially in my post-grad job search. I am excited to continue working together as we embark on our careers.

I also want to thank a newer group of graduate students consisting of Molly Aslin, Louise Ferris, Jill Peery, Sophie Redd, Sassella, and Tim Tierney who have known me as one of the "old grad students." The new perspectives, ideas, and excitement that each of you brought into the group helped remind me of the passion that I have for fusion research which can be forgotten amongst the rigors of graduate school.

It is true that a primary reason I came to UW-Madison for graduate school was for the amazing plasma physics program. An equally important reason was it gave me the opportunity to get a great education very close to the best family support system anyone could ask for. I am very appreciative of all my aunts, uncles, and cousins who have always shown great interest in my work and support for my goals. Especially, the entire Piotroski clan who always have reminded me to prioritize family and not forget to enjoy life.

My entire close knit family network all started with the love and support of my selfless grandparents. They have always expressed the utmost interest and pride in even my smallest of accomplishments. I count myself tremendously blessed to have gotten to share many years of these accomplishments with them. It saddens me that I cannot celebrate this one with them, but I know they are aware and proud of me all the same.

During my time in graduate school, I have been fortunate enough to gain another strong and supportive family that I will soon be lucky to officially call my in-laws. My sincere appreciation goes out to Forrest, Amy, Andy, Sarah, Jeremy, Oliver and the entire Brown and Huestis families for welcoming me with open arms over these past few years.

It is no exaggeration to say that graduate school and the pursuit of this dream would have been impossible without the unconditional love and support of my immediate family. My deepest

admiration goes to my Mom, Dad, three younger brothers—Matthew, Tyler, and Adam—and sister-in-law, Makenzie. It has never been easy having to "go back to school" after enjoying a weekend, holiday, or vacation in your company. You all made it effortless for me to put aside any stress and just enjoy life. These wonderful retreats not only have provided so many unforgettable memories but always recharged my desire and motivation to continue working towards my goals. You all have always been there for me without hesitation, and I will never be able to fully articulate the profound impact this had on this entire journey.

Last, but certainly not least, I owe an unending debt of gratitude for the unwavering patience, support, and love from my fiancée, Emily. Little did I know that the most important reason for choosing to go to UW-Madison for graduate school was that I would be lucky enough to meet the most caring, patient, supportive, and loving life partner that I could have ever asked for. I told you from the beginning that I was a poor graduate student that had a long way to go before graduating and you stuck by my side through it all. You have helped keep me sane through COVID, research stresses, presentation anxiety, job searching, and especially through these final months of immense change culminating in this thesis. Whatever the day held, I have always known that I was fortunate enough to come home to your love, support, and humor which would instantly make my day better. It has been a long road that I could not have completed without you. Although I have thoroughly enjoyed our time in Madison, I am excited to finish this chapter of our story and begin the rest of our lives together.

Contents

List of Figures ..... **viii**

List of Tables ..... **xii**

Abstract ..... **xiii**

Chapter 1 Introduction **1**

1.1 Tokamaks 2
1.2 Spherical Tokamaks 5
1.3 Solenoid-Free Tokamak Startup 7
1.4 Outline of Dissertation 8

Chapter 2 Background Theory and Motivation **10**

2.1 Magnetic Helicity and Helicity Injection Current Drive 10
2.2 Local Helicity Injection 12
2.3 Magnetic Relaxation 14
2.4 Local Helicity Injection Global Current Limits 19
2.5 0-D Power Balance Model 21
2.6 Scaling LHI to High Current Tokamak Startup 24
2.7 Electron Temperature and Energy Confinement During Helicity Injection 26
2.7.1 Coaxial Helicity Injection in Spheromaks 27
2.7.2 Coaxial Helicity Injection in Tokamaks 31
2.7.3 Local Helicity Injection on Pegasus 34
2.8 Electron Confinement and Transport 38
2.8.1 Tokamaks 38
2.8.2 Spherical Tokamaks 41
2.8.3 Stochastic Magnetic Fields and Transport 42
2.8.4 T_e Sustained on Open Magnetic Field Lines 44
2.9 Simple Steady-State Confinement Model 45
2.10 I_p Scaling Trends Observed During LHI on Pegasus 48
2.11 Expected Qualitative Scaling Trends 49
2.12 Exploring the Scaling Properties of LHI on Pegasus-III 55

Chapter 3 The Pegasus-III Toroidal Experiment **57**

3.1 The Pegasus-III Machine 57
3.2 LHI System 59
3.3 Diagnostic Capabilities 61
3.3.1 Optical Diagnostics 61
3.3.2 Magnetic Diagnostics 63
3.3.3 KFIT Equilibrium Reconstruction Code 65
3.3.4 Power Spectral Density Analysis 66

Chapter 4 Advancing Analysis Capabilities for LHI Plasmas **69**

4.1 Extended 0-D Power Balance Model 69
4.1.1 Derivation of Extended Model 70
4.1.2 Validation of Extended Model 74
4.2 ShapeFIT Fast Plasma Boundary Reconstruction Code 78
4.2.1 Algorithm description 78
4.2.2 Output uncertainty 81

Chapter 5 Taylor Limit Studies on Pegasus-III 89

5.1 Taylor Limit B_T Scaling in Expanded Operating Space 89
5.2 Taylor Limit I_{inj} Scaling in Expanded Operating Space 95
5.3 Inferred w_{inj} Across Different Injector Geometries 98
5.4 Quantitative Assessment of I_{TL} Calculation 101
5.5 Magnetic Activity in Discharges Over-driven at Taylor Limit 103
5.6 Helicity Dissipation in Discharges Over-driven at Taylor Limit 115

Chapter 6 Helicity Dissipation Scaling Studies in Pegasus-III 121

6.1 Fiducial LFS LHI Flattop Discharge 122
6.2 B_T Scan in LFS LHI Flattop Discharges 126
6.3 n_e Scan in LFS LHI Flattop Discharges 130
6.4 Impact of Increased Plasma-Material Interactions and Radiated Power 136
6.5 Comparison of Experimental Observations to Confinement Scaling Models 144

Chapter 7 Conclusions 158

7.1 Technical Accomplishments 158
7.2 LHI Taylor Limit Scaling Validated in Expanded Pegasus-III Operating Space 159
7.3 Scaling of Helicity Dissipation during LHI Assessed in Pegasus-III 160
7.4 Future Work 161

Appendix A 164

Appendix B 167

Bibliography 170

LIST OF FIGURES

Figure 1.1: Schematic of magnetic field and coil configuration in a tokamak..... 3
Figure 1.2: Comparison of conventional and spherical tokamak geometries..... 6
Figure 2.1: CAD model of LFS and HFS LHI systems implemented in Pegasus. 13
Figure 2.2: High-speed visible images of a typical LFS LHI startup plasma on Pegasus-III 14
Figure 2.3: Evolution of λ during NIMROD simulations of LHI illustrating reconnection of injected current streams releasing an axisymmetric ring of current which diffuses inward. 17
Figure 2.4: Bursts of $n = 1$ activity correlated with discrete increases in plasma current on Pegasus..... 18
Figure 2.5: 0-D Power balance model comparison of LFS and HFS LHI discharges 23
Figure 2.6: 0-D power balance model projections for LFS LHI startup on Pegasus-III with constant $A_{inj}V_{inj}$ and varied B_T..... 25
Figure 2.7: Sensitivity of predicted $I_p(t)$ from 0-D power balance model for different assumed η 26
Figure 2.8: Example SSPX discharge evolution 28
Figure 2.9: Closed flux surfaces predicted by NIMROD simulations of SSPX discharges enabling good energy confinement..... 29
Figure 2.10: Scaling of core χ_e vs T_e in SSPX compared with various transport models..... 30
Figure 2.11: T_e and n_e measurements for several similar sustained CHI discharges on HIT-II.... 31
Figure 2.12: Comparison of OH-only and CHI-assisted OH discharges on HIT-II..... 32
Figure 2.13: Overview of successful transient CHI to ohmic handoff on NSTX for different sized CHI power supplies 33
Figure 2.14: Time evolution of electron temperature profiles for a CHI-ohmic induction handoff discharge on NSTX..... 34
Figure 2.15: Comparison of electron kinetic profiles between similar LHI and ohmic L-mode discharges on Pegasus 36
Figure 2.16: Radial profiles of electron pressure and integrated magnetic power measured during a HFS LHI 37
Figure 2.17: Transition from linear ohmic confinement to saturated ohmic confinement observed in Alcator C-Mod ohmic plasmas 40
Figure 2.18: I_p scaling for collisional stochastic confinement model at different values of α 48
Figure 2.19: Comparison of experimental data with predicted I_p scaling assuming neo-Alcator and globally stochastic confinement 49
Figure 2.20: Pegasus-III steady-state I_p estimates 53
Figure 3.1: Comparison of Pegasus and upgraded Pegasus-III facility. 58
Figure 3.2: Cross-section and circuit schematic of an LHI injector..... 60

Figure 3.3: Schematic of Pegasus-III LHI power supply 61
Figure 3.4: Pegasus-III magnetic diagnostic layout..... 63
Figure 4.1: Comparison of extended 0-D power balance model and simple steady-state confinement model outputs for identical input parameters 74
Figure 4.2: Comparison of extended 0-D power balance model inputs and their experimental values 76
Figure 4.3: Comparison of extended 0-D power balance model outputs and their experimental values 77
Figure 4.4: Standard $N = 4$ VCF kernel parameterization used for ShapeFIT 79
Figure 4.5: Representative ShapeFIT Monte Carlo analysis 82
Figure 4.6: ShapeFIT output relative uncertainty for Pegasus-III discharge #4898..... 83
Figure 4.7: Comparison of ShapeFIT output for different sets of diagnostic constraints 84
Figure 4.8: Representative comparison of high-speed visible imaging and ShapeFIT solutions for different sets of diagnostic constraints 85
Figure 4.9: Representative comparison of plasma boundary predicted by KFIT and ShapeFIT during the decay of Pegasus-III discharge 86
Figure 5.1: Overview of B_T scan on Pegasus up to 0.15 T..... 90
Figure 5.2: Overview of B_T scan on Pegasus-III up to 0.30 T..... 92
Figure 5.3: Overview of baseline and over-driven discharges at $B_T = 0.3$ T 94
Figure 5.4: Overview of Pegasus-III discharges with varying levels of I_{inj} at $B_T = 0.15$ T 96
Figure 5.5: Scatterplot of I_p vs I_{inj} for times when $R_0 \approx 50$ cm in Pegasus and Pegasus-III discharges 97
Figure 5.6: Comparison of Pegasus and Pegasus-III injector arrays 99
Figure 5.7: Scatterplots of I_p vs $\sqrt{\Psi_T I_{inj}/\left(B_{p,inj}/I_p\right)}$ for the Pegasus and Pegasus-III injector arrays with different d_{inj}..... 100
Figure 5.8: Comparisons of I_p and I_{TL} calculated by 0-D model for discharges spanning Pegasus-III operating space..... 102
Figure 5.9: Overview of discharges sustained with varying amounts of helicity input..... 105
Figure 5.10: Magnetic field fluctuation power spectral density in baseline and over-driven discharges 106
Figure 5.11: Comparison of integrated power in low frequency $\tilde{b}_Z$ 107
Figure 5.12: Poloidal distribution of the cross-power and coherence for low frequency $\tilde{b}_Z$ 108
Figure 5.13: Comparison of I_p and representative LFS $\dot{B}_Z$ signal during period of bursty $n = 1$ magnetic activity in baseline and over-driven discharges..... 110
Figure 5.14: Comparison of ΔT_{burst} throughout baseline and over-driven discharges..... 111
Figure 5.15: Comparison of low frequency $\tilde{b}_Z^2$ and ΔT_{burst} for similar discharges with varying levels of V_{inj}..... 112
Figure 5.16: Comparison of magnetic equilibrium of baseline and over-driven discharge 115
Figure 5.17: Comparison of electron kinetic profiles near at end of baseline and over-driven discharges 117

Figure 5.18: Comparison of $\eta_{neo}(R,Z)$ distributions near peak I_p for the baseline and over-driven discharges 118
Figure 5.19: Summary of 0-D model calculations with different amounts of helicity input and dissipation 119
Figure 5.20: Comparison of representative AXUV signal from baseline and over-driven discharges 120
Figure 6.1: Overview of fiducial flattop discharge (#7145) 123
Figure 6.2: Interpretative 0-D power balance analysis of Pegasus-III discharge #7145 124
Figure 6.3: MPTS measurements during various times during flattop of discharge #7145 125
Figure 6.4: Overview of Pegasus-III discharges at different B_T levels 127
Figure 6.5: Overview of plasma shape evolution in discharges developed at different B_T levels 128
Figure 6.6: Comparison of electron kinetic profiles at different times during the flattop in discharges at different B_T levels 129
Figure 6.7: Overview of discharges developed at $B_T = 0.15$ T with different densities 131
Figure 6.8: Overview of plasma shape evolution in Pegasus-III discharges with different densities at $B_T = 0.15$ T 132
Figure 6.9: Comparison of electron kinetic profiles at different times during the flattop in discharges developed at $B_T = 0.15$ T with different densities 133
Figure 6.10: Overview of discharges developed at $B_T = 0.23$ T with different densities 134
Figure 6.11: Comparison of electron kinetic profiles during the flattop in discharges developed at $B_T = 0.23$ T with different densities 135
Figure 6.12: High-speed visible image from Pegasus-III discharges #7292 and #7285 137
Figure 6.13: Overview of bifurcated discharges with identical programming 139
Figure 6.14: Comparison of radiated power and electron kinetic profiles in bifurcated discharges with different PMI characteristics 140
Figure 6.15: Comparison of radiated power in discharges that comprise the Pegasus-III B_T scan described in Section 6.2 142
Figure 6.16: Comparison of radiated power in discharges that comprise the density scan at $B_T = 0.15$ T scan described in Section 6.3 143
Figure 6.17: Estimated volume-averaged radiated power density as a function of the core n_e throughout the density scan performed at $B_T = 0.15$ T 143
Figure 6.18: Interpretative 0-D power balance model analysis of Pegasus-III discharge #7145 with and without P_{aux} assuming neo-Alcator confinement scaling 146
Figure 6.19: Interpretative 0-D power balance model analysis of Pegasus-III discharge #7145 with and without P_{aux} assuming a global Rechester-Rosenbluth collisional stochastic confinement scaling model 147
Figure 6.20: 0-D power balance model calculations to represent Pegasus-III B_T scan assuming global Rechester-Rosenbluth collisional stochastic confinement scaling model 149
Figure 6.21: 0-D power balance model calculations to represent Pegasus-III n_e scan assuming global Rechester-Rosenbluth collisional stochastic confinement scaling model 150
Figure 6.22: 0-D power balance model calculations to represent Pegasus-III B_T scan assuming neo-Alcator τ_E scaling 151

Figure 6.23: 0-D power balance model calculations to represent Pegasus-III n_e scan assuming neo-Alcator τ_E scaling 152
Figure 6.24: 0-D power balance calculations to represent Pegasus-III discharges with different P_{rad} assuming neo-Alcator τ_E scaling 154
Figure 6.25: 0-D power balance calculations to represent a hypothetical Pegasus-III B_T scan with lower P_{rad} assuming neo-Alcator τ_E scaling 155
Figure 6.26: Estimated maximum T_e sustained along open field lines as a function of the field line length 157
Figure A.1: Comparison of Alcator C-MOD experimental data to estimates from the steady-state confinement model 165
Figure B.1: Representative $N = 15$ FCF kernel node distribution 169

LIST OF TABLES

Table 1: Summary of qualitative I_p and T_e scaling trends for various assumed confinement scaling estimates 54
Table 2: Comparison of Pegasus and Pegasus-III operational parameters 59
Table 3: Calculated Ψ_T from ShapeFIT and KFIT for several Pegasus-III LHI discharges 88
Table 4: Comparison of ShapeFIT errors in shaping moments relative to KFIT for ohmic and LHI discharges 88
Table 5: Summary of I_p and T_e scaling trends for various assumed standard tokamak and globally stochastic confinement scalings along with the experimentally observed trends. 144
Table A.1: Comparison of ST data to steady-state confinement model estimates 166

Abstract

Solenoid-free tokamak startup techniques can simplify the design and reduce the cost of tokamak-based fusion energy systems. The newly commissioned Pegasus-III spherical tokamak provides a dedicated platform for developing a scalable solenoid-free startup approach. Local helicity injection (LHI) is one promising technique being developed on Pegasus-III which uses compact edge current sources to drive open field line current I_{inj} which is redistributed via helicity-conserving instabilities and subsequently relaxes to a tokamak-like state with plasma current I_p far greater than I_{inj}. Validated predictive models are needed to accurately project LHI performance on Pegasus-III and beyond. This work advances this goal by characterizing the scaling of a fundamental global I_p limit, referred to as the Taylor limit I_{TL}, and helicity dissipation during LHI discharges in the expanded operating space provided by Pegasus-III. These experiments illustrate that increasing the Taylor limit leads to more effective utilization of the available helicity input and higher I_p plasmas. Further, they verify the expected $I_{TL} \propto \left(I_{inj}B_T\right)^{1/2}$ scaling holds for toroidal field B_T and I_{inj} up to 0.3 T on axis and 12 kA, respectively. Additionally, data from different injector arrays show that the width of the injector aperture directly alters I_{TL} and can be leveraged for future injector design optimization. Discharges over-driven at $I_p = I_{TL}$ experienced more frequent bursts of $n = 1$ magnetic activity consistent with large scale reconnection events. These reconnection events appear to drive magnetic relaxation in these discharges as indicated by a flattening of the $\lambda = \mu_0 J_\parallel / |B|$ profile, where $J_\parallel$ is the parallel current density. When operating with $I_p < I_{TL}$, the I_p is dictated by the balance of magnetic helicity input and dissipation. Parametric B_T and density scans were assessed in the context of global energy confinement models

to characterize the scaling of helicity dissipation during LHI. Relatively high amounts of radiated power attributed to plasma-material interactions appear to be dominating the power balance in these discharges and may mask the behavior of the underlying energy confinement properties. Still, interpretive analysis with an extended 0-D power balance model suggests that the experimental trends may be described by linear ohmic energy confinement scaling estimates.

Chapter 1
Introduction

The worldwide demand for energy is continually increasing and is expected to grow by ~30% by 2050 according to a 2023 report by the US Energy Information Administration [1]. This expected growth in energy demand coincides with an imperative need to reduce global greenhouse emissions to combat climate change. A landmark 2018 report by the Intergovernmental Panel on Climate Change (IPCC) stresses the importance of reaching net-zero carbon dioxide emissions by 2050 to limit the irreversible environmental and societal impacts of climate change [2]. A recent report by the United Nations Environment Programme indicates aggressive action is needed to reverse the present emission trends and achieve the net-zero goals set forth in the Paris Agreement [3]. These two societal challenges motivate the need for an abundant, clean, and reliable energy source that can be deployed over the next couple of decades. Nuclear fusion can provide such an energy source.

Nuclear fusion is a reaction in which two lighter atomic nuclei combine to form a single heavier nucleus. The mass of the newly formed nucleus is less than the combined mass of the initial two nuclei. This mass difference Δm releases a large amount of energy given by $E = \Delta m c^2$. Under appropriate conditions, this process can become self-sustaining and provide an essentially limitless amount of energy. Although difficult to attain on Earth, nuclear fusion is the most prominent source of energy in the universe as it powers all stars, including our Sun.

For fusion to occur, the repulsive Coulomb force between the two positively charged atomic nuclei must be overcome. The immense gravity within stars is able to overcome this force and fuse

hydrogen atoms to create helium and release lots of energy. Since the 1950s, researchers have been trying to replicate these conditions on Earth without the aid of immense gravity. These approaches rely on heating the fusion fuel to extreme temperatures. Typically, a mix of hydrogen isotopes (deuterium and tritium) are used and need to be heated to ~100 million ℃ to generate an appreciable amount of fusion reactions. At these temperatures, the atoms are completely ionized which creates a collection of positively (ion) and negatively (electron) charged particles with a net-neutral charge known as a plasma.

The fundamental challenge for fusion energy is to confine this hot and dense plasma for a long enough time for the reaction to become self-sustaining [4]. As such, the performance of fusion devices is quantified through the triple product of confinement time τ_E, temperature T, and density n. To achieve a self-sustaining fusion reaction, also known as ignition, the following condition must be achieved [5]

$$nT\tau_E > 5 \times 10^{21} \mathrm{m}^{-3}\mathrm{s\ keV} \tag{1.1}$$

Plasmas are comprised of charged particles and thus respond to forces imposed by magnetic fields. Magnetic confinement fusion (MCF) concepts leverage this fact to create a self-sustaining fusion environment that is required for a fusion-based power plant. One of the most promising and widely studied magnetic configurations is the tokamak.

1.1 Tokamaks

The tokamak confines plasma in a toroidal geometry through helical magnetic field lines. The helical magnetic field is generated from various sources, which are depicted in Figure 1.1. The toroidal field ($\vec{B}_T$) is generated by coils outside of the confined plasma. After the plasma is initiated, a toroidal current (I_p) is driven within the plasma. This plasma current creates its own poloidal magnetic field ($\vec{B}_p$) and leads to the formation of helical field lines. External poloidal field coils provide additional poloidal field for force balance and plasma shape control. Additionally, conventional tokamaks rely on an ohmic solenoid which wraps down the center of the torus for plasma initiation and sustainment.

To be in equilibrium, the force on the plasma must be zero everywhere. Ideal magnetohydrodynamics (MHD) is the most basic description of the force balance in magnetically

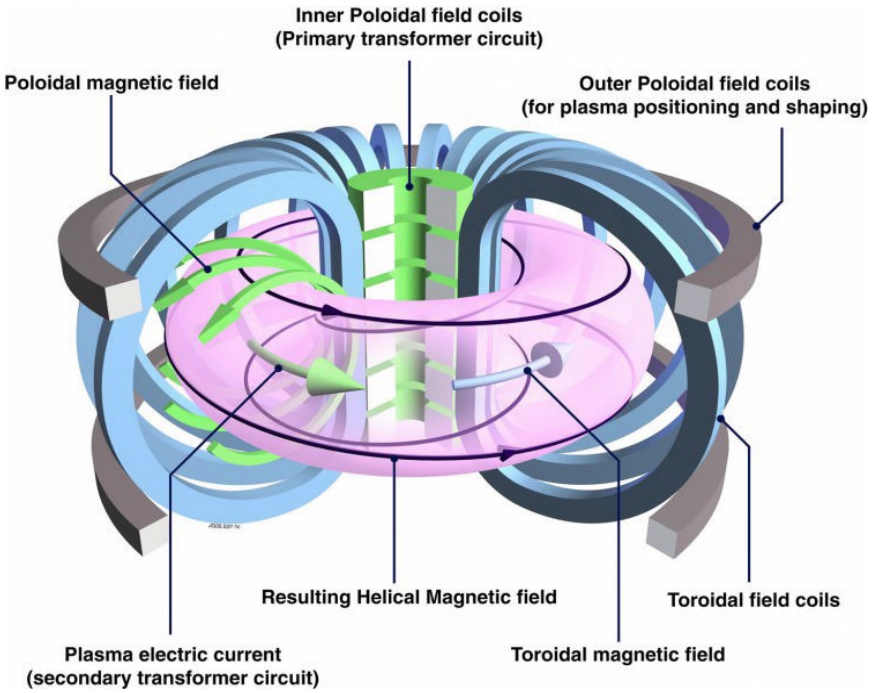

Figure 1.1: Schematic of magnetic field and coil configuration in a tokamak [6].

confined plasmas. In the time-independent limit of ideal MHD, the equations that describe the equilibrium solution are:

$$\vec{J} \times \vec{B} = \vec{\nabla} p \tag{1.2}$$

$$\vec{\nabla} \times \vec{B} = \mu_0 \vec{J} \tag{1.3}$$

$$\vec{\nabla} \cdot \vec{B} = 0 \tag{1.4}$$

where $\vec{J}$ is the current density, $\vec{B}$ is the magnetic field, and p is the plasma pressure. It can be seen from equation 1.2 that $\vec{B} \cdot \vec{\nabla} p = 0$ and $\vec{J} \cdot \vec{\nabla} p = 0$. Maintaining a region of non-zero plasma pressure leads to finite pressure gradients ($\vec{\nabla} p \neq 0$). This implies the existence of constant-pressure surfaces within the plasma and that the magnetic field lines and current must lie along these surfaces. These magnetic surfaces are referred to as flux surfaces. It is convenient to introduce the poloidal magnetic flux function,Ψ, which is the amount of poloidal flux within each magnetic surface:

$$\Psi = \iint_{S_p} \vec{B}_p \cdot \vec{n} dS \tag{1.5}$$

where $\vec{n}$ is the normal unit vector to the surface S_p which is a ring-shaped ribbon stretched between the magnetic axis ($\Psi \equiv 0$) and the flux surface. Ψ satisfies $\vec{B} \cdot \vec{\nabla}\Psi = 0$ thus making it a constant for each surface and a useful coordinate for these surfaces.

The magnetic field in a toroidal geometry (R, ϕ, Z) can be decomposed into its toroidal and poloidal components in the following way:

$$\vec{B} = \vec{B}_T + \vec{B}_p = B_T\hat{\phi} + \frac{1}{2\pi R}\vec{\nabla}\Psi \times \hat{\phi} \tag{1.6}$$

where $\hat{\phi}$ is the unit vector in the toroidal (ϕ) direction. The poloidal field can be further decomposed into vertical and radial components:

$$\vec{B}_p = \vec{B}_Z + \vec{B}_R = \frac{1}{2\pi R}\frac{\partial \Psi}{\partial Z}\hat{Z} - \frac{1}{2\pi R}\frac{\partial \Psi}{\partial R}\hat{R} \tag{1.7}$$

where $\hat{Z}$ and $\hat{R}$ are the unit vectors in the Z and R directions, respectively.

Assuming toroidal symmetry, equations 1.2-1.4 can be reduced to

$$\Delta^*\Psi = R\frac{\partial}{\partial R}\left(\frac{1}{R}\frac{\partial \Psi}{\partial R}\right) + \frac{\partial^2 \Psi}{\partial Z^2} = 2\pi R\mu_0 J_\phi, \tag{1.8}$$

where J_ϕ is the toroidal current density. J_ϕ depends on the plasma pressure and a toroidal field flux function $G \equiv \frac{RB_T}{R_0 B_{T0}}$ with respect to the poloidal flux:

$$J_\phi = -2\pi\left(R\frac{dp}{d\Psi} + \frac{(R_0 B_{T0})^2}{2R\mu_0}\frac{dG^2}{d\Psi}\right), \tag{1.9}$$

where R_0 is the plasma major radius and B_{T0} is the corresponding externally applied toroidal magnetic field at R_0. Finally, the Grad-Shafranov equation is derived by substituting equation 1.9 into equation 1.8 which leads to

$$\Delta^*\Psi = R\frac{\partial}{\partial R}\left(\frac{1}{R}\frac{\partial \Psi}{\partial R}\right) + \frac{\partial^2 \Psi}{\partial Z^2} = -4\pi^2\mu_0 R^2\frac{dp}{d\Psi} - 2(\pi R_0 B_{T0})^2\frac{dG^2}{d\Psi}, \tag{1.10}$$

There are several key parameters for describing tokamak plasmas. The plasma shape is often described by the plasma major radius (R_0), minor radius (a), aspect ratio ($A \equiv R_0/a$), elongation (κ), and triangularity (δ).

Global plasma stability is often represented by the safety factor profile. The safety factor q is defined to be the number of toroidal transits per poloidal transit of a field-line on a flux surface. Mathematically, q is given by [5]

$$\mathrm{q} = \frac{1}{2\pi}\oint \frac{1}{R}\frac{B_T}{B_p} ds \tag{1.11}$$

where the integral is performed over a poloidal path around a given flux surface. In general, the stability of the plasma increases with higher values of q.

The ratio of the plasma kinetic pressure (p) and magnetic pressure, known as plasma beta (β), is an important measure of confinement efficiency. The fusion power scales as $P_{fus} \propto p^2$ and the magnetic field coils are often a cost-driver in tokamak designs [5]. Therefore, maximizing β enables a more cost-effective tokamak design

$$\beta = \frac{p}{B^2/2\mu_0} \tag{1.12}$$

There are many variations on this ratio depending on what pressure and magnetic field values are used. Some commonly used variants are the toroidal beta β_t, poloidal beta β_p, and normalized beta β_N, which are given by

$$\beta_t = \frac{\langle p \rangle}{B_{T0}^2/2\mu_0} \tag{1.13}$$

$$\beta_p = \frac{\langle p \rangle}{\bar{B}_p^2/2\mu_0} \tag{1.14}$$

$$\beta_N = \frac{\beta_t}{I_p/aB_{T0}} = \frac{\beta_t}{I_N} \tag{1.15}$$

where $\langle p \rangle$ is the volume-averaged pressure and $\bar{B}_p^2$is the average poloidal magnetic field. The normalized plasma current is commonly defined to be $I_N[\mathrm{MA}\cdot \mathrm{m}^{-1}\mathrm{T}^{-1}] \equiv I_p/aB_{T0}$, where B_{T0} is in T, a is in m, and I_p is in MA.. However, there are limits to what β can be achieved. Numerical work by Troyon identified a stability limit for tokamaks that limits β_N below a constant value C_β over a large sample of plasma stability calculations [7]. Experiments across many conventional tokamaks have verified this "Troyon limit" with $C_\beta = 3.5 \pm 0.5 \frac{\%\mathrm{m}\cdot\mathrm{T}}{\mathrm{MA}}$ [8].

1.2 Spherical Tokamaks

A special class of tokamaks with $A < 2$ are commonly referred to as spherical tokamaks (STs). The low A of the ST configuration is enabled by drastically reducing the size of the central column compared to conventional tokamaks, as can be seen in Figure 1.2. The compact ST geometry

results in natural elongation, higher edge safety factor, and more efficient toroidal field utilization compared to high A tokamaks [9,10].

The ST provides many potential benefits for a compact, cost-effective fusion energy facility. STs have demonstrated the ability to operate at significantly higher β_t than conventional tokamaks even up to $\beta_t \approx 100\%$ [11–13]. This is an attractive operating space as it demonstrates more efficient utilization of the available B_T. This could aid in reducing the size of the TF magnet in tokamak designs which is thought to be a leading cost-driver of future fusion energy systems [14,15]. The improved stability of the ST also enables access to higher β_N with experiments achieving $\beta_N \leq 6.5$ [11,13]. This is also an attractive feature for a compact fusion facility as the amount of self-driven current, quantified by the bootstrap current fraction f_{BS}, increases with β_N at otherwise fixed parameters [16]. Fusion power plants are typically designed to operate at high-f_{BS} to minimize the need for auxiliary current drive systems which can significantly contribute to the capital cost [15,17,18]. It can be shown that the fusion power generated from high-f_{BS} facilities scales like $P_{fus} \propto A^{-1}(\kappa\beta_N B_T)^4$ [19]. It is important to note that the maximum B_T generally decreases as aspect ratio is reduced due to a variety of engineering factors [19]. Still, the higher κ and β_N in STs can offset the negative impacts of lower A and may allow for a compact and potentially more cost-effective fusion energy system [14,18,20].

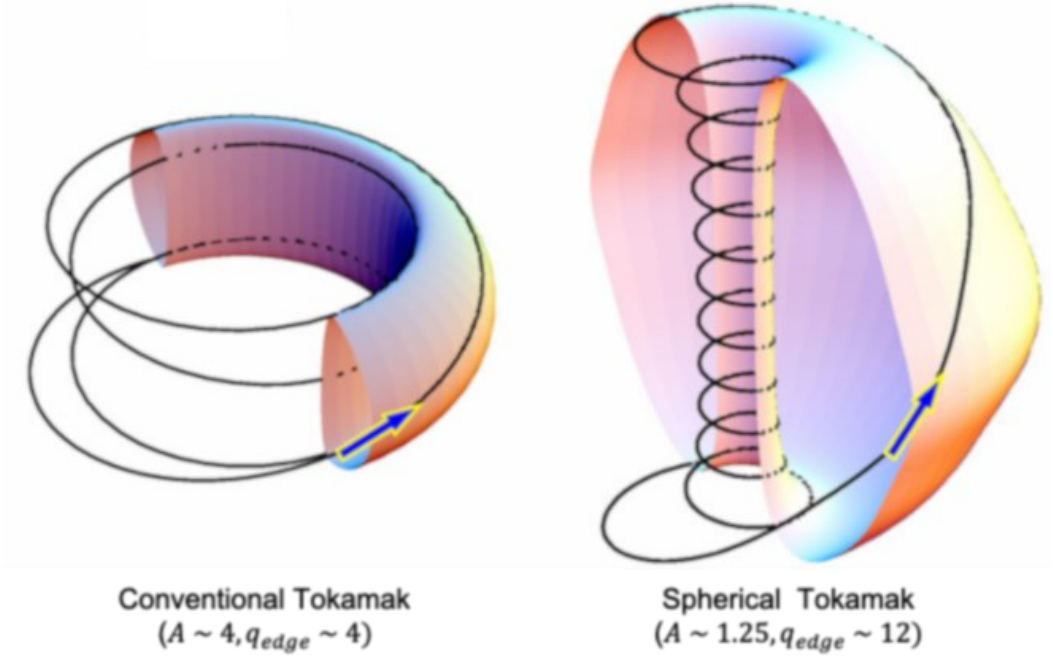

Figure 1.2: Comparison of conventional and spherical tokamak geometries. Adapted from [10].

A major obstacle facing ST-based fusion energy systems is plasma startup. Conventional tokamaks and STs utilize transformer action from a central solenoid for initial plasma breakdown and current drive [21]. The small central column of the ST places significant engineering constraints on the capability of this solenoid. These constraints may preclude the installment of a sufficient solenoid for plasma startup in future nuclear ST devices [19,22]. This necessitates the need for alternative approaches for plasma current startup and sustainment.

1.3 Solenoid-Free Tokamak Startup

The limited space for a central solenoid in STs has motivated the development of solenoid-free tokamak startup techniques. Numerous techniques have been explored on a variety of experiments to address this issue. The most prominent are poloidal field (PF) induction, merging plasma compression, radio-frequency (RF) wave injection, and helicity injection [21–23].

The outer poloidal field coils can be leveraged for tokamak startup. PF induction techniques use the outer PF coils to induce plasma current, similar to conventional central solenoid startup [24,25]. Merging plasma compression also utilizes outer PF coils. In this technique, the outer PF coils create two plasma rings that merge and undergo magnetic reconnection to form a tokamak-like plasma [22,26,27].

RF wave injection has been routinely used for tokamak heating and current drive. The basic principle of all RF injection methods is to launch waves that are resonant within the plasma volume to deposit energy. With appropriate conditions and antenna design, the deposited energy can be used to drive net plasma current. The RF methods most commonly used for plasma startup are electron cyclotron heating and current drive (ECH/ECCD), electron Bernstein wave (EBW) current drive and lower hybrid (LH) current drive [21,22].

Helicity injection relies on the conservation of magnetic helicity and turbulent relaxation processes to drive plasma current [28]. Magnetic helicity represents the topological linkedness of the magnetic field within a volume and is proportional to the amount of I_p driven in tokamaks. Among helicity injection techniques, coaxial helicity injection (CHI) and local helicity injection (LHI) are the most promising for tokamak startup. They utilize biased electrodes to drive current along open magnetic field lines and inject helicity [22].

The thesis work outlined in this dissertation is focused on developing the LHI technique. Specifically, it is concerned with characterizing how LHI may scale toward facilities which operate at higher I_p and B_T. A 0-D power balance model has been previously developed to interpret and project the I_p evolution during LHI discharges [29]. This model has identified a path to higher I_p which has a favorable scaling with B_T. Testing this approach is a central focus of this work. Despite this insight provided by the model, its predictive capability is limited due to the uncertainty in the assumed dissipation. This motivates the second thrust of this work which is to better characterize the scaling of helicity dissipation during LHI. Previous work [30] suggested that the use of global confinement scaling estimates may prove useful for describing LHI discharges, albeit in a rather limited operating space. Those efforts will be continued in this work with model development and parametric B_T and n_e scans to assess the utility, if any, provided by simple global confinement scalings for estimating the dissipation during LHI discharges.

Overall, the scaling of the amount of current that can be driven by LHI is thoroughly explored throughout this thesis work. Further, this work leverages the expanded operating space of the newly commissioned Pegasus-III facility [31] to extend the LHI physics basis.

1.4 Outline of Dissertation

This dissertation is organized as follows:

Chapter 2 provides an overview of the theory behind helicity injection, specifically focusing on LHI and its open questions for scaling to high current tokamak startup. This chapter also introduces a 0-D power balance model used for estimating the plasma current evolution in LHI discharges. Lastly, this chapter motivates and introduces different energy confinement models that may be useful for scaling LHI performance.

Chapter 3 describes the newly commissioned Pegasus-III facility on which the experiments discussed herein were performed. The description is focused on the LHI system used throughout this work as well as relevant diagnostics. A description of analysis techniques used throughout this work, including equilibrium reconstruction and standard power spectral density analysis techniques, is also provided.

Chapter 4 presents code development efforts undertaken as a part of this thesis work. It is focused on extensions and/or refinement of two previously developed codes for analysis of LHI

discharges. First, an extension of the 0-D power balance model is described which incorporates global confinement scaling estimates to provide a self-consistent calculation of the plasma current and electron temperature T_e evolutions. Next, the ShapeFIT fast boundary reconstruction code is described in detail along with a new method of solution that was implemented in this work. Further, a detailed uncertainty analysis for the ShapeFIT output is also described which focuses on quantifying random and systematic errors in the analysis of LHI discharges developed on Pegasus-III.

Chapter 5 describes results from experiments in the expanded Pegasus-III operating space which characterized the scaling of a global I_p constraint that exists during LHI, referred to as the Taylor limit. The accuracy of the Taylor limit estimate used in the 0-D model is also assessed using this dataset. Finally, the properties of discharges that are over-driven at this Taylor limit are discussed.

Chapter 6 describes experimental parametric scans that were performed to characterize the scaling of I_p and T_e with B_T, plasma density, and impurity content. The qualitative trends observed in these scans are discussed in the context of expectations from simple global confinement estimates to assess if any such models are descriptive of LHI discharges.

Finally, Chapter 7 summarizes the key results from this thesis work as well as avenues for future work.

Chapter 2
Background Theory and Motivation

2.1 Magnetic Helicity and Helicity Injection Current Drive

Magnetic helicity K quantifies the linkage or twist of flux tubes in a volume. In a simply connected volume, it can be mathematically defined as

$$K = \int_V \vec{A} \cdot \vec{B} d^3x \tag{2.1}$$

where $\vec{A}$ is the vector potential and the integral is carried out over the closed volume. For multiply-connected volumes, like a torus, the following gauge independent form of helicity is used [32,33]

$$K = \int_V \left(\vec{A} + \vec{A}_{vac}\right) \cdot \left(\vec{B} - \vec{B}_{vac}\right) d^3x \tag{2.2}$$

where the vac subscript refers to vacuum fields generated outside the volume of interest. In a tokamak, magnetic helicity measures the linkage between the toroidal and poloidal magnetic fluxes. For a given toroidal field and plasma current profile, the magnetic helicity content of the tokamak is directly related to the driven plasma current $K \propto I_p$.

To drive current, helicity must be injected at a rate faster than it is dissipated. The helicity balance can be derived by taking the time derivative of equation 2.22.1 and simplifying with Maxwell's equations to arrive at [33,34]

$$\frac{dK}{dt} = -2\Psi_T \frac{\partial \Psi}{\partial t} - 2 \oint_S dS\left(\varphi \vec{B} \cdot \hat{n}\right) - 2 \int_V dV\left(\vec{E} \cdot \vec{B}\right) \tag{2.3}$$

$$\frac{dK}{dt} = \dot{K}_{AC} + \dot{K}_{DC} - \dot{K}_{dis} \tag{2.4}$$

where Ψ_T is the toroidal flux inside the bounding surface, Ψ is the poloidal flux outside the bounding surface, $\vec{E}$ is the electric field, and φ is the electric potential between two points where open field lines puncture the bounding volume. The dS and dV integrals are over the bounding surface and its enclosed volume, respectively. The time rate of change of helicity is balanced by the three terms on the right-hand-side of equation 2.3. Each of these terms has a specific physical interpretation.

The first term represents the AC helicity injection rate which arises from induction. Changes to the poloidal flux, due to plasma shape evolution or ohmic induction, results in a toroidal loop voltage, $V_{IND} = -\frac{\partial \Psi}{\partial t}$. This AC helicity injection rate can then be written as

$$\dot{K}_{AC} = -2\frac{\partial \Psi}{\partial t}\Psi_T = 2V_{IND}\Psi_T \tag{2.5}$$

The second term represents the DC helicity injection rate. This shows that helicity can be injected into the system when an electrostatic potential is applied along magnetic field lines which penetrate the plasma boundary. This is typically accomplished by using biased electrodes that intercept magnetic flux at the plasma edge. Current drive techniques that inject magnetic helicity via this term are typically referred to as "helicity injection."

The final term represents the helicity dissipation in the system. Substituting an Ohm's law expression for the electric field yields

$$\dot{K}_{diss} = 2\int_V dV\left(\eta\vec{J}\cdot\vec{B}\right) \tag{2.6}$$

where η is the plasma resistivity.

With finite resistivity, the magnetic helicity and magnetic energy of a plasma will decay. Finite resistivity also allows magnetic fields lines to break and reconnect. Magnetic reconnection can drive fluctuations which will redistribute current and flux. In the presence of these fluctuations, magnetic energy will dissipate on a faster timescale than the magnetic helicity [35]. In a process known as "Taylor relaxation", the plasma will self-organize towards a minimum energy state while conserving the total magnetic helicity [35]. The minimal energy configuration resulting from this relaxation process, called the "Taylor state", is described by the following equation [36]

$$\nabla \times \vec{B} = \lambda\vec{B} \tag{2.7}$$

where the eigenvalue, λ, is uniform throughout the plasma. By applying Ampere's Law to equation 2.7, λ can be expressed as

$$\lambda = \frac{\mu_0 \vec{J} \cdot \vec{B}}{B^2} = \frac{\mu_0 J_\parallel}{|B|}. \tag{2.8}$$

where $J_\parallel$ is the current density parallel to the magnetic field and $|B|$ is the magnetic field strength.

The combination of helicity injection and the magnetic relaxation process enables plasma current drive techniques [28,37]. There are two main helicity injection techniques used for tokamak startup. The first is coaxial helicity injection (CHI). CHI utilizes electrically isolated axisymmetric electrodes within the vacuum vessel. These electrodes are biased relative to one another to drive current along open magnetic field lines that connect the two electrodes. During startup operation, the injected current is increased until the "bubble-burst" current is exceeded. This occurs at the point when the $\vec{J}_{pol} \times \vec{B}_T$ force exceeds the poloidal field line tension [22]. After this critical threshold, the injected flux can expand to fill the vessel. Plasma startup using CHI can be operated in a sustained or transient manner. In sustained CHI, current is continuously driven on open field lines after the plasma expands to fill the vessel [22,38,39]. In transient CHI, the injected current is rapidly extinguished after the plasma fully expands which forces axisymmetric reconnection leading to the formation of closed flux surfaces [22,40–42]. To date, transient CHI has shown more promise as a tokamak startup technique [22,43].

The focus of this work is an alternative helicity injection technique known as local helicity injection.

2.2 Local Helicity Injection

Local helicity injection (LHI) utilizes small current sources to drive open field line current and inject helicity. The localized sources are negatively biased relative to a designated anode to supply electron current, I_{inj}. The LHI technique was first explored on CDX at PPPL [44] and CCT at UCLA [45]. These initial experiments demonstrated the feasibility of high current multiplication ($I_p \gg I_{inj}$) and the formation of tokamak-like plasmas [45]. However, impurity generation related to the thermionic emitter cathode source design limited performance and was not attractive for scaling to higher current operation.

In recent years, a major focus of the Pegasus Toroidal Experiment has been advancing the LHI technique using washerstack-stabilized plasma arc guns as the helicity injectors [23,46]. The LHI system on Pegasus has demonstrated solenoid-free tokamak startup of $I_p \leq 225$ kA with $I_{inj} \leq 8$ kA as well as the ability to couple to conventional ohmic current drive [23,47,48].

The choice of source location has a significant impact on the physics of LHI discharges [23]. Pegasus experiments have explored two variants of source placement which are shown in Figure 2.1. The low-field side (LFS) approach places the injectors just below the outboard midplane of the device. The high-field side (HFS) implementation uses injectors in the lower divertor region. LFS LHI discharges are characterized by a highly dynamic shape evolution which results in a significant inductive current drive contribution (AC helicity injection). Whereas HFS LHI plasmas have a largely static shape and are predominantly driven by DC helicity injection. Both injector systems have demonstrated high current multiplication [23] and the ability to hand-off to ohmic current drive [47,48]. From an engineering perspective, the LFS LHI geometry is a more attractive system for implementing on larger devices due to the available space on the outboard midplane.

The formation of a tokamak-like plasma from open field line current streams is a multi-step process. High-speed visible imaging from the Pegasus-III facility demonstrates this evolution in

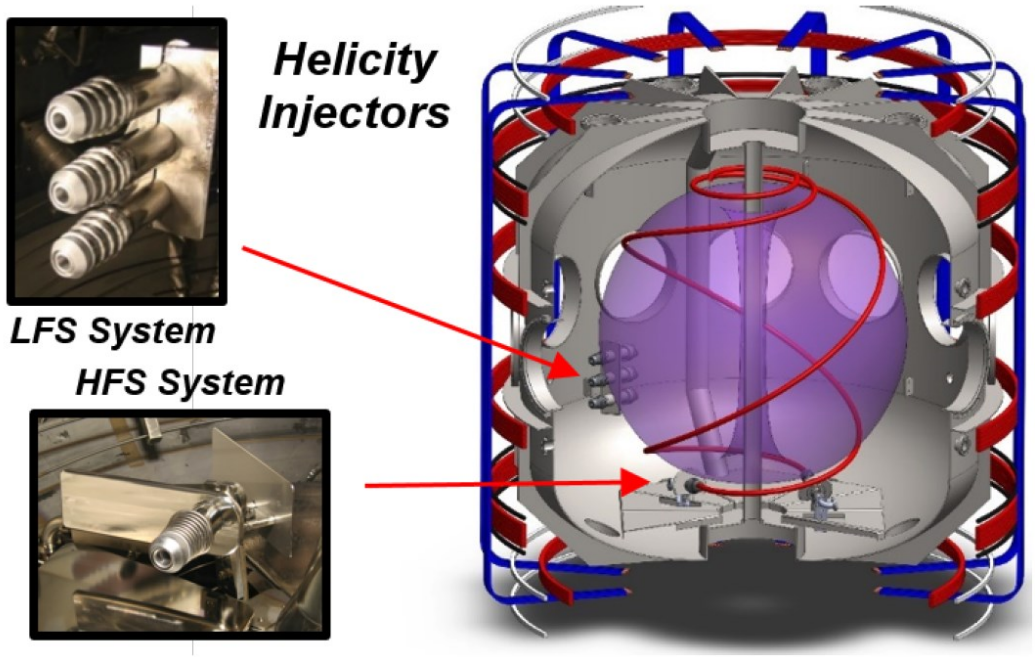

Figure 2.1: CAD model of LFS and HFS LHI systems implemented in Pegasus. A representative tokamak-like plasma and injected current path being extracted from the HFS system are also illustrated.

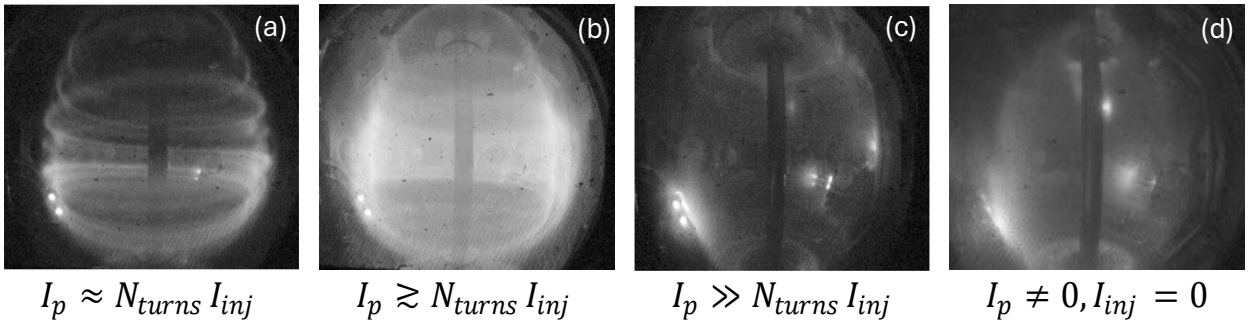

Figure 2.2: High-speed visible images of a typical LFS LHI startup plasma on Pegasus-III: (a) injected streams follow helical vacuum fields; (b) streams become unstable and reconnect; (c) plasma relaxes to a tokamak-like state; (d) tokamak plasma remains after injector shutoff.

Figure 2.2. First, a bias voltage is applied across the arc tube within the injector to initiate an arc plasma. The arc anode is then biased negatively with respect to the vacuum vessel to extract an electron current from the arc source. Initially, the extracted current follows the helical vacuum magnetic field lines (Figure 2.2(a)). These injected current streams become increasingly unstable as more current is extracted (Figure 2.2(b)). Under appropriate conditions, adjacent passes of the streams attract and undergo magnetic reconnection which relaxes the system to a tokamak-like state (Figure 2.2(c)). This plasma is referred to as "tokamak-like" to indicate the system is fundamentally 3D but the magnetic energy is predominantly axisymmetric which resembles a tokamak in a toroidally-averaged sense [29,49–51]. After this initial relaxation, the injectors and inductive effects continually supply helicity to grow and sustain the tokamak-like plasma. After termination of the LHI sources ($I_{inj}, V_{inj} \rightarrow 0$), the flux surfaces rapidly heal [23,50,52,53] leaving the desired tokamak plasma (Figure 2.2(d)) which may be sustained by other current drive methods [47,48,52].

2.3 Magnetic Relaxation

Magnetic relaxation is the general process through which the magnetic topology self-organizes to a more stable configuration (i.e. relaxed state) [35]. In general, relaxation theories rely on variational principles to predict the properties of this relaxed state. For example, Taylor relaxation theory which was introduced in Section 2.1 relies on the minimization of magnetic energy while conserving the total magnetic helicity. Taylor relaxation theory assumes there is sufficient

magnetic turbulence and/or fluctuations to drive the system toward the predicted force-free magnetic equilibrium (uniform λ).

Taylor relaxation theory has provided a useful framework for interpreting a variety of experimental observations. These include: conservation of helicity over timescales which magnetic energy is measured to decay [54,55]; characteristics of magnetic equilibrium in RFPs, including field reversal [35,56,57]; spheromak formation and magnetic field profiles [35,58,59]; and current-limiting behavior in toroidal and spherical systems [35,58]. Despite the success of the theory in qualitatively describing these experimental features, it possesses several shortcomings and cannot fully describe experimental observations [57,60,61]. Additionally, a fully relaxed state described by Taylor relaxation theory implies no confinement as $\nabla p = 0$ throughout the entire volume. Experiments generally observe non-uniform λ profiles. Taylor attributes this to excessive plasma resistivity impeding the relaxation process and leading to a partially relaxed state [35]. Additionally, experiments typically observe the relaxation to be driven by large-scale fluctuations rather than small-scale turbulence which is required within this framework.

Alternative theories have been proposed based on other variational principles to address the shortcomings of Taylor relaxation theory. One such theory proposed by Hameiri and Bhattacharjee argues that the rate of entropy production, not the magnetic energy, is the quantity to be minimized [62]. In this theory, finite plasma resistance dynamically relaxes the system toward a local minimum in the rate of entropy production. This theory attempts to describe the thermodynamics of the relaxation process which is not considered in Taylor relaxation theory. Under certain limiting assumptions, the minimum rate of entropy production theory recovers the force-free equilibrium predicted by Taylor relaxation theory.

The final relaxation theory that has been extensively explored is known as the minimum dissipation rate theory. Montgomery and Phillips initially proposed an alternative variational principle in which the rate of energy dissipation is minimized to determine the relaxed state [63]. Assuming an isothermal plasma, this theory is identical to the minimum rate of entropy production theory. Since the initial theory proposed by Montgomery and Phillips, the theory has been developed and applied to numerous experimental configurations, including RFPs [64–66], tokamaks [66], field-reversed configurations (FRCs) [67], spheromaks [68], as well as DC helicity injection in tokamaks [69,70]. A notable success of this theory compared to Taylor relaxation

theory is the prediction of non-uniform λ profiles in the relaxed states which are consistent with experimental observations.

Relaxation theories based on variational principles can provide a useful framework for interpreting experimental data but have inherent limitations. These limitations are predominately related to the underlying assumptions in the computation of these relaxed states which are often not representative of experimental conditions [60,62,71]. Additionally, the assumed boundary conditions can strongly influence results, and it is not always straightforward to identify conditions that adequately describe experiments [63,72,73].

More recently, resistive MHD computational tools are being utilized to understand the dynamics that drive relaxation processes. These high-fidelity computational tools can relieve the simplifying assumptions that are inherent in the variational principles to better describe experimental conditions. These resistive MHD simulations have predicted phenomena that are consistent with experimental observations. In MST, discrete relaxation events are associated with cyclic tearing mode activity (i.e. sawtooth cycle) [74,75] which is consistent with NIMROD simulations [76]. Spheromak experiments initiated by CHI have attributed system relaxation to a $n = 1$ kink mode [77–79] which is also reproduced in simulations [80–82], where n is the toroidal mode number. A similar $n = 1$ mode is also observed during CHI operations on STs and contributes to the relaxation process [83–85].

The understanding of the magnetic relaxation process during LHI is still developing. The initial relaxation from the helical injected current streams to a tokamak-like plasma is understood through NIMROD simulations [49–51]. In the simulations, bursts of low frequency ($f \sim 10$ kHz) $n = 1$ magnetic activity are generated by large-scale reconnection events between adjacent passes of the injected current streams. The dynamics of these events are illustrated in Figure 2.3 which shows λ isosurfaces during an individual event with positive (red) surfaces corresponding to current flowing from injectors and negative (blue) representing reversed current associated with reconnection. During these events, the injected streams attract and reconnect which subsequently releases a ring of current. This current ring diffuses inward and leads to an accumulation of poloidal flux as part of the magnetic relaxation process. Bursts of $n = 1$ magnetic activity at similar frequency ($f \approx 20 - 60$ kHz) and amplitude ($\tilde{b}/B \approx 5\%$) are also observed during LHI operations on Pegasus [12,23,86]. This $n = 1$ activity is consistent with line-tied kink motion of

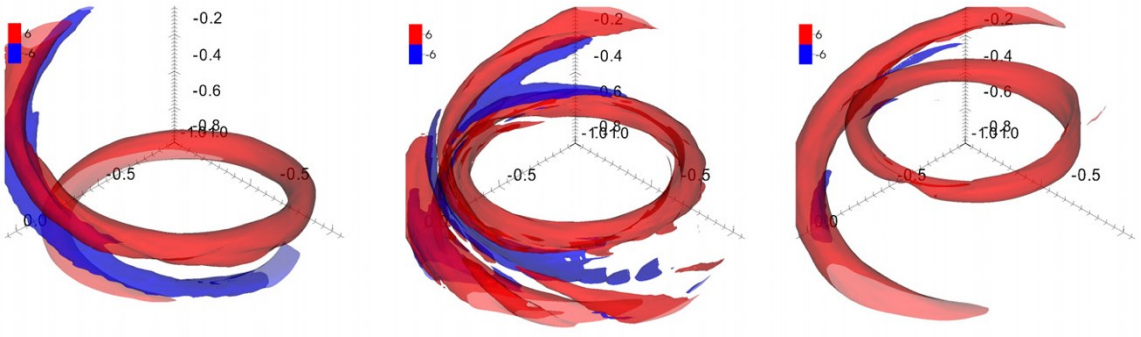

Figure 2.3: Evolution of λ during NIMROD simulations of LHI illustrating reconnection of injected current streams releasing an axisymmetric ring of current which diffuses inward. Time increases from left to right over the course of the single event depicted here. Positive (red) isosurfaces correspond to current flowing from injectors and negative (blue) surfaces represent reversed current associated with reconnection. This is Figure 1 from [50].

the injected current streams and is likely associated with the reconnection events predicted by NIMROD [12,87].

These bursts of $n = 1$ activity are commonly observed throughout LHI discharges on Pegasus and are typically accompanied by discrete jumps in I_p [12,87]. This behavior is illustrated in Figure 2.4 which shows the measured $I_p(t)$ and a representative LFS $\dot{B}_Z$ sensor over the span of four discrete bursts. The vertical dotted lines indicate the time of peak I_p during each discrete burst. The magnetic fluctuations grow in amplitude prior to the gradual rise in I_p and reach their maximum amplitude in the middle of this rise. The magnetic activity is then damped prior to reaching the peak I_p value. Further, the increases in I_p are approximately equal to I_{inj}. The representative example in Figure 2.4 illustrates that this behavior is cyclical but the period between these bursts varies. Typically, the bursts early in these discharges occur in rapid succession and are not always discernable as separate events. As I_p ramps throughout the discharge, the repetition rate decreases, and the bursts are more distinguishable as individual events [12,87].

NIMROD simulations also predict jumps in I_p with similar magnitude and relative timing to the bursts of $n = 1$ activity [51]. Further, the simulations also predict the rate of these large-scale reconnection events to decrease throughout the I_p ramp. As such, these bursts of $n = 1$ activity and associated I_p jumps can be viewed as indirect evidence of these large-scale reconnection events predicted by NIMROD. These events act as a current drive mechanism and drive relaxation during LHI plasmas [12,87].

Experiments on Pegasus suggest that additional processes contribute to magnetic relaxation during LHI. A subset of HFS LHI discharges experience an abrupt reduction in the amplitude of $n = 1$ magnetic activity measured by magnetic sensors located outside the LFS plasma edge and generally observe an increase in I_p and plasma density [12,46]. To date, the underlying mechanism for this abrupt reduction is not understood [23]. Still, the sustainment of the tokamak-like discharge with the significantly reduced $n = 1$ activity suggests that additional processes are providing current drive.

During these discharges with reduced $n = 1$ activity, higher frequency broadband magnetic fluctuations become dominant. This suggests that this activity is providing current drive and contributing to relaxation [12,46]. This is further supported by anomalous ion heating measured during LHI by passive impurity Doppler spectroscopy. This ion heating is attributed to reconnection activity that is present during LHI and is temporally correlated with the higher frequency, continuous broadband activity [53]. High-bandwidth magnetic fluctuation measurements have been used to characterize this broadband magnetic activity. The activity exhibits power-law behavior consistent with Alfvénic turbulence generated by the injected current streams [86]. An estimate of the toroidal current that can be driven by this turbulence via dynamo electromotive forces is comparable to the experimentally realized current densities [86]. In total,

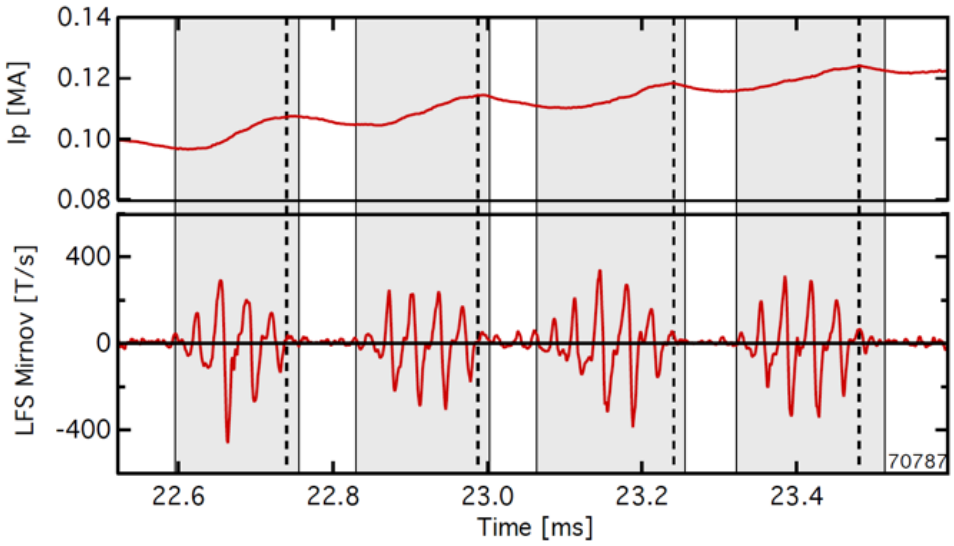

Figure 2.4: Bursts of $n = 1$ activity correlated with discrete increases in plasma current on Pegasus: (a) I_p and (b) representative LFS $\dot{B}_Z$ coil. Vertical shaded regions indicate the approximate burst lifetime. Vertical dotted lines indicated the time when each jump in I_p reaches its peak value. This is Figure 6.11 from [87].

these observations suggest that this broadband magnetic activity provides current drive in LHI discharges. This mechanism acts in conjunction with the large-scale reconnection events associated with the bursts of $n = 1$ activity to drive relaxation.

Developing a predictive understanding of the current drive mechanisms and relaxation process is a focus of LHI research. A hierarchy of physics models are being employed to develop this physics basis. The NIMROD simulations described earlier in this section provide insight into the underlying physics and fundamental current drive mechanisms. However, further computational studies are needed to continue to advance this understanding. While these efforts are undertaken, simpler models and tools are being used to guide the ongoing design and development of attractive LHI startup scenarios. To this end, the next two sections will describe steady-state I_p limits and a 0-D global power balance model which are used to guide the experiments undertaken in this thesis work.

2.4 Local Helicity Injection Global Current Limits

The plasma current that can be driven in LHI is constrained by the lower of two global limits. The first limit comes from magnetic helicity balance (equation 2.3). For the discrete LHI sources, the DC helicity injection rate, $\dot{K}_{DC}$, can be recast as [88]:

$$\dot{K}_{DC} = 2\Psi_T V_{LHI} = 2\Psi_T \sum_k \frac{V_{inj,k} A_{inj,k} B_{inj,k}}{\Psi_T} \tag{2.9}$$

where the summation is over each injector k, V_{inj} is the injector bias voltage, A_{inj} is the area of the injector surface, and B_{inj} is the magnetic field normal to the injector surface. V_{LHI} is an effective loop voltage for helicity injection which is analogous to an inductive loop voltage. Substituting this $\dot{K}_{DC}$ formulation into the magnetic helicity balance (equation 2.4) at steady-state ($dK/dt = 0$) results in the following global current limit [88]

$$I_p \leq \frac{A_p}{2\pi R_0 \langle \eta \rangle} (V_{LHI} + V_{IND}). \tag{2.10}$$

where $\langle \eta \rangle$ is the volume-averaged plasma resistivity and A_p is the plasma cross-sectional area.

The second global limit comes from the imposed boundary conditions of the relaxed plasma state. The Taylor relaxation process drives the system towards a minimal energy state characterized by a flat-λ profile. Per the discussion in the previous section, experiments typically

do not observe the force-free equilibria predicted by Taylor relaxation theory. Rather, non-uniform λ profiles are typically observed indicating only partial relaxation of the system. This suggests there is insufficient fluctuation activity and/or excessive dissipation to drive the system to a fully relaxed state.. Still, fluctuations will tend to redistribute the current in such a way to flatten the λ profile.

In DC helicity injection techniques, λ in the injection region must be higher than that of the core [22,54,59,89]. Therefore, DC helicity injection techniques are fundamentally limited by the properties of the injectors themselves, such that

$$\lambda_p \leq \lambda_{edge} \tag{2.11}$$

where λ_p and λ_{edge} are the λ in the driven core plasma and injection region, respectively [22,54,59].

The average λ in the core plasma ($\bar{\lambda}_p$) is given by

$$\bar{\lambda}_p = \frac{\mu_0 I_p}{\Psi_T}. \tag{2.12}$$

During LHI, the injectors set an average λ in the plasma edge region ($\bar{\lambda}_{edge}$). This can be approximated by

$$\bar{\lambda}_{edge} = \frac{\mu_0 I_{inj}}{\psi_{edge}} \approx \frac{\mu_0 I_{inj}}{2\pi R_{edge} w_{inj} B_{p,inj}} \tag{2.13}$$

where ψ_{edge} is the poloidal flux in the edge injection region. This is approximated to be $\psi_{edge} = 2\pi R_{inj} w_{inj} B_{p,inj}$ where $B_{p,inj}$ is the average poloidal magnetic field in the injection region which is assumed to be an axisymmetric sheet of poloidal flux centered at major radius R_{edge} with a characteristic radial width w_{inj} [52,88]. This approximation is motivated by high-speed visible images from LHI plasma on Pegasus (Figure 2.2) which suggest the discrete current streams rapidly mix to form a near-uniform current channel in the plasma edge [52,88]. Coaxial helicity injection experiments on the SSPX spheromak also demonstrated that the local λ near the electrodes was effectively averaged throughout the plasma edge [90].

A constraint on the total I_p that can be driven by LHI is found by substituting the $\bar{\lambda}_p$ and $\bar{\lambda}_{edge}$ approximations given by equations 2.12 and 2.13, respectively, into the constraint shown in equation 2.11. This limit is referred to as the "Taylor limit" (I_{TL}) and is given by

$$I_p \leq I_{TL} \approx \sqrt{\frac{\Psi_T I_{inj}}{2\pi R_{edge} w_{inj}(B_{p,inj}/I_p)}}. \quad (2.14)$$

To satisfy force balance, $B_{p,inj}$ is nearly linearly dependent on I_p. Therefore, the $(B_{p,inj}/I_p)$ term that appears in the Taylor limit is largely a function of the plasma geometry [29,88].

The primary scaling relations for the Taylor limit are $I_{TL} \propto \sqrt{B_T I_{inj}/w_{inj}}$. These scalings have been experimentally validated on Pegasus for $B_T \leq 0.15$ T and $I_{inj} \leq 5$ kA [88]. The w_{inj} scaling was tested by modifying the alignment of the injectors to the equilibrium magnetic field. A better aligned injector array is expected to have a narrower effective width of the edge region. This was consistent with the observed increase in $I_p(t)$ at otherwise fixed injector and plasma parameters [23,88].

2.5 0-D Power Balance Model

The helicity balance (equation 2.10) and the Taylor limit (equation 2.14) impose fundamental limits on LHI performance. However, these expressions are not sufficient to determine the I_p evolution. This motivated the development of a 0-D power balance model as a tool for predicting $I_p(t)$ by estimating V_{IND} in LHI discharges [29]. This model is used extensively throughout this work and will be briefly overviewed here. A more detailed discussion of this model is presented in [29].

This lumped-parameter, power balance circuit model uses the time-varying injector parameters, plasma shape, and assumed neoclassical resistivity as inputs to determine $I_p(t)$. The model is derived from applying Poynting's theorem at the plasma boundary and formulates the plasma dynamics as a series of voltages. The model solves the following fundamental circuit equation

$$V_{OH} + V_{PF} + V_{Le} + V_{Li} + V_{RTT} + V_{LHI} + V_R = 0 \quad (2.15)$$

where V_{OH}, V_{PF}, V_{Le}, and V_{Li} are the system voltages from ohmic induction, PF induction, external self-inductance, and internal inductance, respectively. The V_{RTT} term accounts for the effect of the moving plasma boundary on the internal energy storage by using the Reynolds' Transport Theorem. Lastly, V_{LHI} and V_R represent the effective loop voltage provided by the injectors and

the resistive dissipation, respectively. This equation can be simplified by combining V_{OH}, V_{PF}, V_{Le}, V_{Li}, and V_{RTT} into a single term which quantifies all the inductive effects, V_{IND}.

$$V_{IND} + V_{LHI} + V_R = 0 \tag{2.16}$$

Previous work by Barr et al. developed analytic formulae to quantify the inductive effects for the highly shaped, ultralow A Pegasus plasmas [29]. The V_{LHI} term is computed via equation 2.9. The helicity dissipation is assumed to be due to plasma resistivity and is defined to be

$$V_R = -I_p R_p = -I_p \left(\frac{2\pi R_0 \langle \eta \rangle}{A_p}\right) \tag{2.17}$$

where R_p is the plasma resistance.

Equation 2.16 can be recast into a first-order differential equation and numerically solved as an initial value problem for $I_p(t)$. Throughout the solution process, the model strictly enforces the Taylor limit given by equation 2.14.

The plasma resistivity is a large unknown in this analysis. Until a more detailed understanding of the energy confinement properties of LHI plasmas is developed, the resistivity is an input which is treated as a fitting parameter for interpretative modeling of LHI discharges. The resistivity is assumed to be constant throughout the discharge and takes the following form

$$\langle \eta \rangle = \langle M_{neo} \eta_{Spitzer} \rangle \tag{2.18}$$

where $\eta_{Spitzer}$ is the Spitzer resistivity and M_{neo} is a neoclassical resistivity enhancement factor. These can be calculated for arbitrary collisionality using the Sauter formulation [91]:

$$\sigma_{spitzer} = \frac{1}{\eta_{Spitzer}} = 1.9012 \times 10^4 \frac{(T_e[\mathrm{eV}])^{3/2}}{Z_{eff} N(Z_{eff}) \ln \Lambda_e}. \tag{2.19}$$

$$\frac{1}{M_{neo}} = \frac{\eta_{Spitzer}}{\eta_{neo}} = \frac{\sigma_{neo}}{\sigma_{Spitzer}} = 1 - \left(1 + \frac{0.36}{Z_{eff}}\right) f_{t,eff} + \frac{0.59}{Z_{eff}} f_{t,eff}^2 - \frac{0.23}{Z_{eff}} f_{t,eff}^3. \tag{2.20}$$

where $\ln \Lambda_e$ is the well-known Coulomb logarithm, Z_{eff} is the average ionic charge and $N(Z_{eff}) = 0.58 + 0.74/(0.76 + Z_{eff})$. The effective trapped particle fraction $f_{t,eff}$ is given by

$$f_{t,eff} = \frac{f_t}{1 + (0.55 - 0.1 f_t)\sqrt{\upsilon_{e*}} + 0.45(1 - f_t)\upsilon_{e*} Z_{eff}^{-3/2}} \tag{2.21}$$

where f_t is the trapped particle fraction and υ_{e*} is the electron collisionality which is given by

$$\upsilon_{e*} = 6.921 \times 10^{-18} q R Z_{eff} \ln \Lambda_e A^{-3/2} (n_e[m^{-3}])(T_e[eV])^{-2} \tag{2.22}$$

where n_e is the electron density in m^{-3} and T_e is in eV. For the typical Pegasus operating space, a nominal value of $M_{neo}Z_{eff} \leq 3$ has been assumed. The volume-averaged electron temperature $\langle T_e \rangle$ is then varied until $I_p(t)$ best matches experiment [29].

The 0-D power balance model has successfully reproduced both LFS and HFS LHI discharges on Pegasus with assumed $\langle T_e \rangle$ values. The 0-D model calculations shown in Figure 2.5 show good agreement with the measured $I_p(t)$ when assuming a fixed $\langle T_e \rangle = 36$ and 57 eV for the LFS and HFS discharges, respectively. These values are comparable to the available T_e profiles measured by the multi-point Thomson scattering diagnostic on Pegasus [30,46,92][1]. The LFS and HFS calculations assume a nominal $M_{neo}Z_{eff} = 1.5$ and 1, respectively, which is consistent with Z_{eff} inferred from experiments [30].

Figure 2.5 also shows the calculated Taylor limit and the system voltages representing various drive contributions for each of the scenarios. These calculations highlight fundamental differences between LFS and HFS discharges. The LFS LHI I_p evolution has a significant contribution from

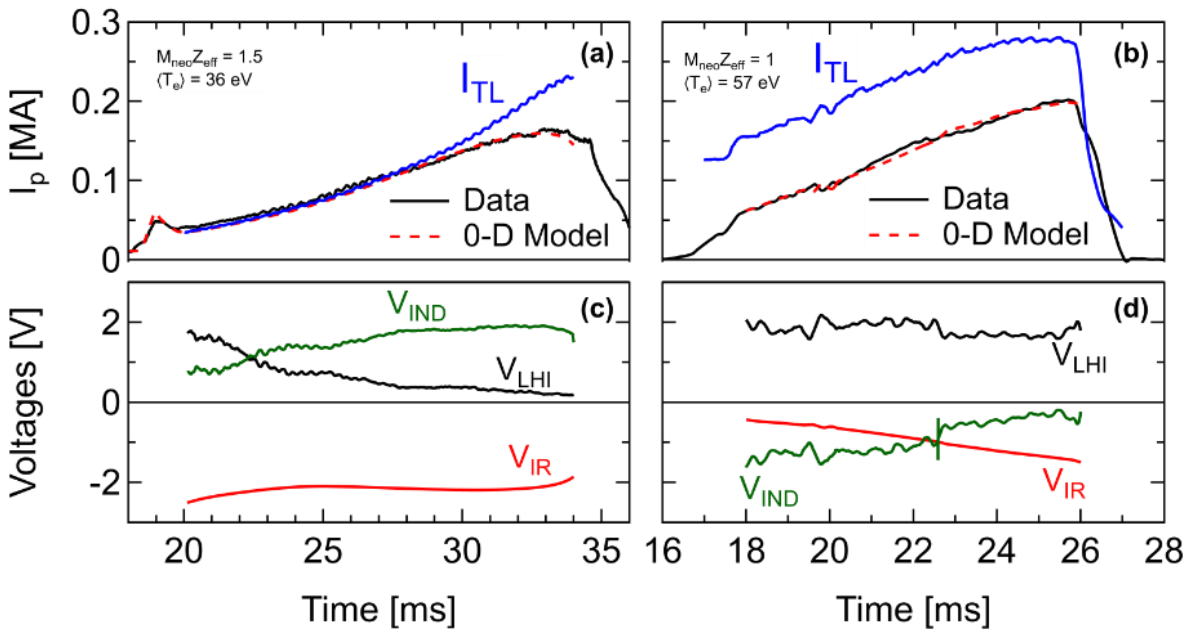

Figure 2.5: 0-D Power balance model comparison of LFS (a, c) and HFS (b, d) LHI discharges: (a,b) $I_p(t)$ and (c,d) system voltages. Adapted from [12].

[1] During this work, an error was identified in the Thomson scattering data processing routines which lead to a precise factor of 2 higher reported T_e than what it should have been. Errata are in the works but are not yet published for all these publications at the time of this dissertation. If no erratum has been published, then the stated T_e values are precisely twice as high as their actual values.

inductive effects and is also restricted by the Taylor limit early in the discharge. Whereas the HFS LHI scenario is driven entirely by the injector helicity input and is typically not impacted by the Taylor limit. These differences have significant implications for scaling LHI to higher I_p startup.

2.6 Scaling LHI to High Current Tokamak Startup

The path to high current LHI operation depends strongly on the injector geometry. For HFS LHI, the current is driven purely by the injector helicity input. To increase this input, the size of the system and/or the applied bias voltage must be increased ($V_{LHI} \propto N_{inj}A_{inj}V_{inj}$). However, increasing the system size must be compatible with physical space and initial relaxation requirements. Further, high applied bias voltages can lead to cathode spots which can damage injector hardware and be a source of impurities [23,46].

For LFS LHI, the dominant drive contribution is from inductive effects. Therefore, increasing the size and/or applied bias voltage only leads to marginal increases in achievable I_p [29]. A more effective approach for increasing I_p comes from manipulating the Taylor limit early in the discharge. LFS LHI discharges have an extended phase in which the I_p is sustained at the Taylor limit. This suggests that higher I_p can be driven by increasing the Taylor limit early in the discharge to utilize the available helicity input more effectively. This can be accomplished by optimized source design with a narrow current channel (w_{inj}), increased injector current (I_{inj}) and operating at higher toroidal field ($I_{TL} \propto \sqrt{B_T I_{inj}/w_{inj}}$). Figure 2.6 illustrates this approach through 0-D power balance model projections of the Pegasus-III LFS LHI system (to be described in Section 3.2). These projections assumed a fixed V_{LHI} ($A_{inj}V_{inj} = 16$ kV cm^2) and resistive dissipation ($M_{neo}Z_{eff} \approx 1.5$; $\langle T_e \rangle = 40$ eV). The Taylor limit is then increased by increasing B_T. At $B_T = 0.15$ T, the predicted I_{TL} (dotted line) is sufficiently low to limit the amount of I_p (solid line) that can be achieved for over half the discharge. As the I_{TL} is increased, the achieved I_p also increases throughout the discharge clearly demonstrating improved utilization of the fixed available helicity input provided by the injectors. At the $B_T = 0.60$ T level, $I_{TL} > I_p$ for much of the discharge meaning $I_p(t)$ is determined by the balance of the assumed helicity input and dissipation.

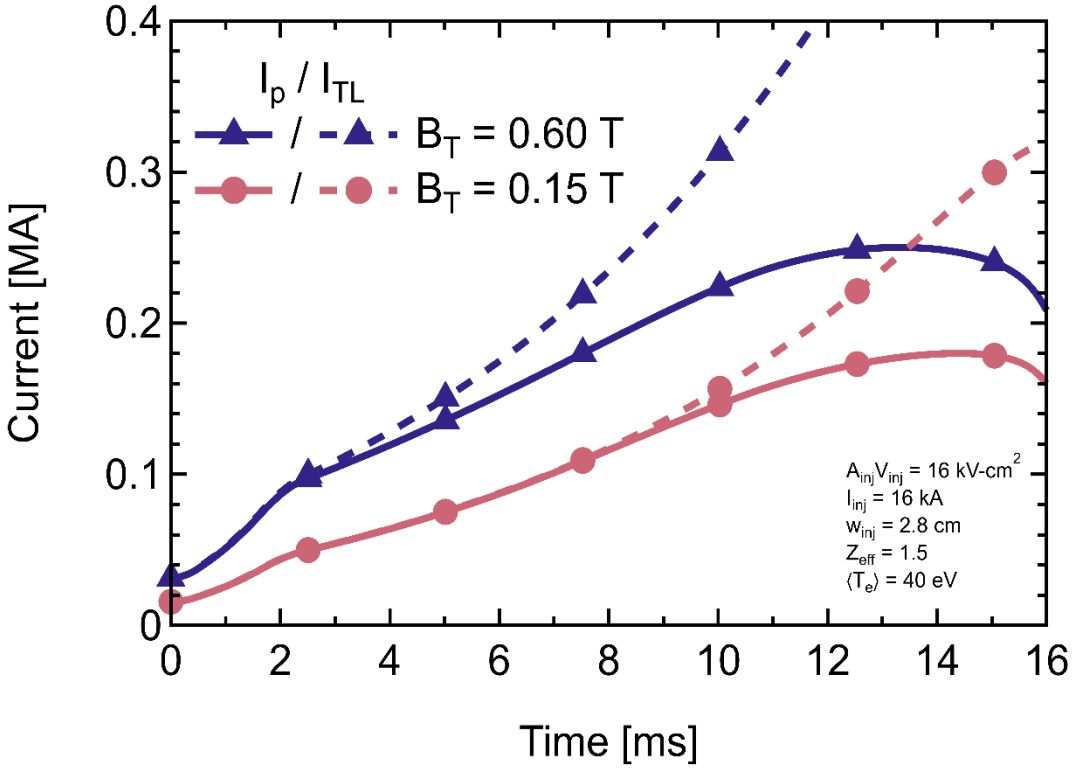

Figure 2.6: 0-D power balance model projections for LFS LHI startup on Pegasus-III with constant $A_{inj}V_{inj}$ = 16 kV cm^2 and varied B_T. Solid and dashed lines represent the projected I_p and I_{TL}, respectively.

Regardless of the injector configuration, reliable projections for LHI performance rely on understanding how the helicity dissipation scales to other devices and operating regimes. When operating below the Taylor limit, the balance of the helicity input and dissipation dictates I_p. Predictions from the 0-D power balance model strongly depend on the assumed plasma resistivity. This is demonstrated by the projected $I_p(t)$ in Figure 2.7 for a representative Pegasus LFS LHI discharge with different assumed $\langle\eta\rangle$. Here, a constant $M_{neo}Z_{eff} = 1.5$ is assumed which is consistent with previous estimates [30] and initial impurity transport modeling [93] for LHI discharges. The $\langle\eta\rangle$ is then varied via the assumed $\langle T_e\rangle$ which is constant throughout the evolution. As $\langle T_e\rangle$ increases, $\langle\eta\rangle$ decreases, and consequently I_p increases. The $I_p(t)$ predicted by the model best matches the measured $I_p(t)$ (solid black line) for $\langle T_e\rangle$~35 eV which is consistent with typical T_e profiles measured during LHI [30].

During the early part of the discharge, the Taylor limit is dictating the I_p evolution. As such, a modestly lower $\langle T_e\rangle$~30 eV would achieve an identical $I_p(t)$ for a decent portion of the discharge

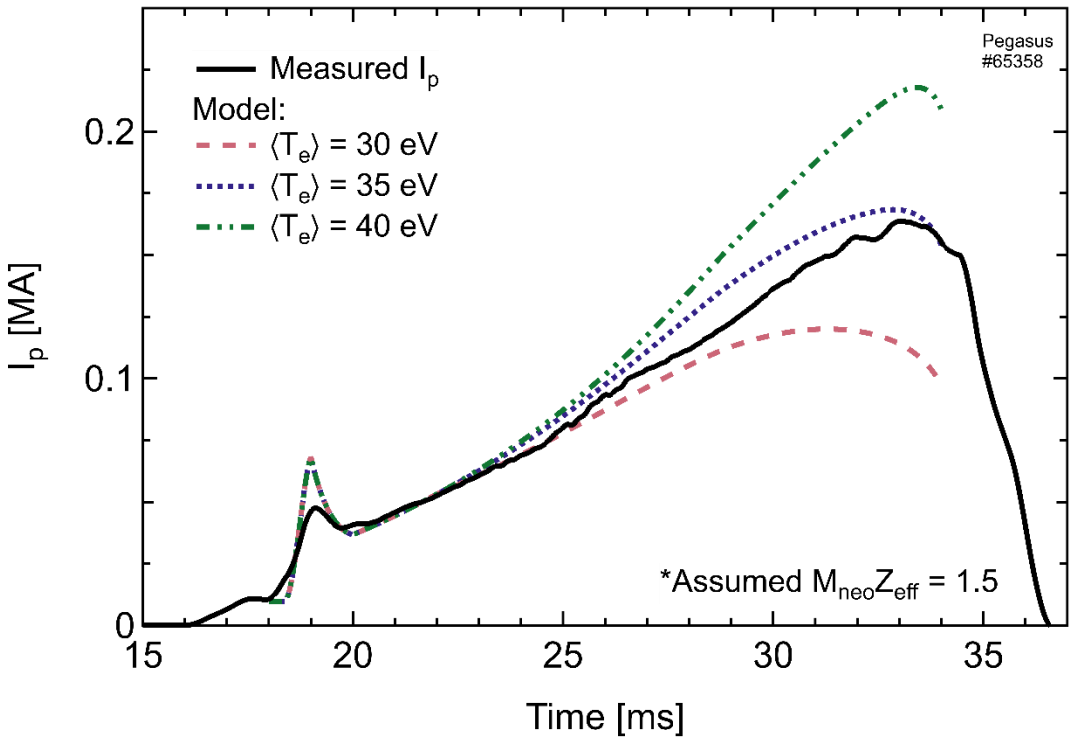

Figure 2.7: Sensitivity of predicted $I_p(t)$ from 0-D power balance model for different assumed $\langle\eta\rangle$. $\langle\eta\rangle$ is varied via $\langle T_e\rangle$ for an assumed fixed $M_{neo}Z_{eff} = 1.5$. Solid line represents measured $I_p(t)$ for Pegasus discharge #65358.

as illustrated in Figure 2.7. This suggests a lower input V_{inj} would be sufficient to achieve the same $I_p(t)$ during this phase and would be a more effective utilization of the available helicity input. Incorporating a self-consistent model for helicity dissipation into the dynamic power balance model would provide a tool to optimize LHI scenarios. More generally, reliable projections of LHI performance to MA-class devices require a validated model to quantify helicity dissipation.

2.7 Electron Temperature and Energy Confinement During Helicity Injection

Developing a predictive understanding for the electron temperature that can be attained during LHI is critical for projecting to MA-class devices for several reasons. First, the electron temperature strongly impacts the resistive dissipation of helicity ($\eta \propto T_e^{-3/2}$). This dissipation remains a significant uncertainty in projecting $I_p(t)$ as discussed in the previous section. Further, it also directly impacts the size and power supply capabilities required of an LHI system capable

of MA-class startup. The ability to achieve higher T_e would allow for a smaller and/or lower V_{inj} system for a fixed target I_p. Additionally, T_e can significantly impact the ability to transition an LHI discharge to alternative current drive sustainment techniques. For example, the efficiency of neutral beam current drive (NBCD) increases with T_e based on data from a range of tokamaks and stellarators [94]. This data indicates that $T_e \gtrsim 1\,\text{keV}$ is required to achieve $> 10\%$ coupling efficiencies. This is also consistent with simulations of a non-inductive NSTX startup scenario which suggest that $T_e > 1$ keV is required for sufficient coupling to direct NBCD [95].

The electron temperature that can be realized during LHI is impacted by a variety of factors, including thermal energy confinement, heating sources and sinks, and current drive mechanisms. The understanding of these aspects of LHI discharges is still being developed. Given the elementary understanding of LHI that presently exists, it is not feasible to adopt or develop a full transport model for LHI that is required for detailed predictions of $T_e(R)$. However, this section will present several observations from LHI experiments on Pegasus which have motivated the present belief that LHI confinement is a combination of neoclassical, anomalous, and stochastic transport processes. To provide context to these observations, this section will first present measurements from coaxial helicity injection (CHI) on a variety of devices.

2.7.1 Coaxial Helicity Injection in Spheromaks

Coaxial helicity injection was first developed as a plasma startup technique for spheromaks. A spheromak is a toroidal magnetic configuration that does not have a central column which leads to a vacuum wall that is topologically identical to a sphere. The absence of a central column also means there are no ohmic solenoid or toroidal field coils. The confining toroidal field is produced entirely from currents flowing in the plasma and is comparable in strength to the poloidal field [96]. Due to the lack of an ohmic solenoid, CHI was developed to initiate and drive plasma current.

The Sustained Spheromak Physics Experiments (SSPX) was a CHI-driven spheromak that focused on developing long-pulse ($\sim$4 ms) spheromaks with good energy confinement properties [78]. An example of a typical SSPX discharge is shown in Figure 2.8. Initially, a current pulse is driven such that $\lambda_{gun} = \mu_0 I_{gun}/\psi_{gun}$ exceeds a critical value (λ_{fc}) which causes the plasma to expand from the injection region to fill the vessel.

After the initial formation, the injector current is reduced for the sustainment phase of the discharge. If $\lambda_{gun} > \lambda_{fc}$ is maintained during the sustainment phase, then the current drive is active and repeated reconnection events occur which destroy flux surfaces and enhance thermal transport. It was found that the flux surfaces rapidly heal between reconnection events and allow T_e to rise. However, the time between reconnection events is sufficiently short to limit peak electron temperatures to ≤ 100 eV [78].

If the gun current is reduced such that $\lambda_{gun} < \lambda_{fc}$, then the current drive is shutoff and a transient quiescent phase can be achieved. This is accomplished by carefully tuning λ_{edge} and the q-profile as well as achieving clean vacuum conditions [78,97]. In this quiescent phase, the magnetic fluctuations are dramatically reduced ($dB/B_{edge} \leq 1\%$), as is the case in Figure 2.8. Further, careful tuning of the q-profile is required to transiently shift the resonant surfaces toward the plasma edge thereby enabling the formation of large, closed flux surfaces [98]. These closed flux surfaces provide a transport barrier which enables good energy confinement and the highest achieved peak T_e values.

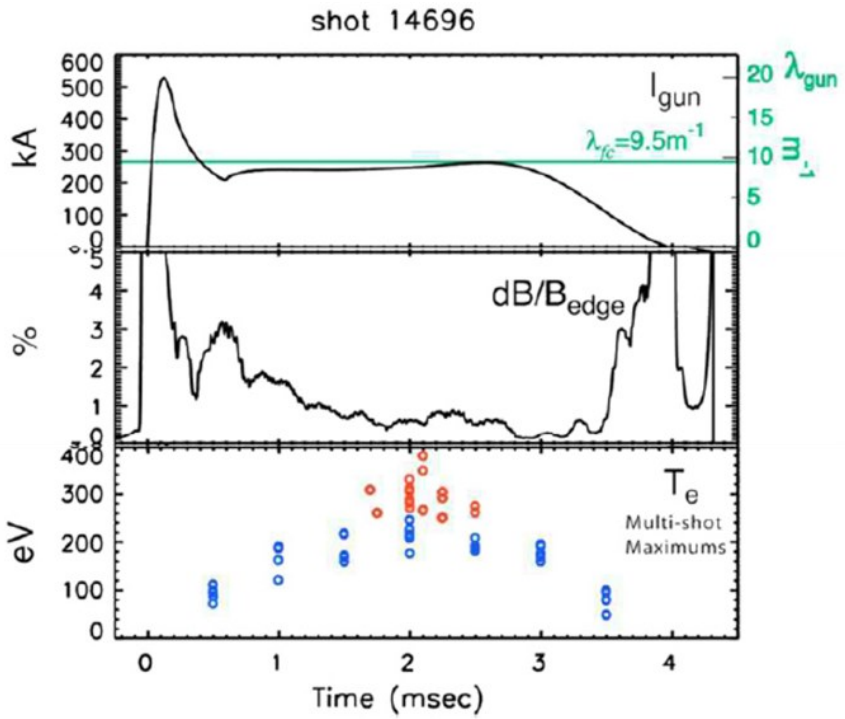

Figure 2.8: Example SSPX discharge evolution. Top-to-bottom: injector current ($\lambda_{gun} = \mu_0 I_{gun}/\psi_{gun}$), fluctuation level, and electron temperature. Adapted from [100].

The existence of closed or nearly closed flux surfaces is critical for achieving good thermal energy confinement. This is demonstrated in Figure 2.9 which compares NIMROD modeling and experimental T_e profiles [99]. The magnetic field line puncture plot (Figure 2.9(a)) shows a region of closed, nested flux surfaces that are surrounded by a region of chaotic magnetic field lines. The closed flux region results in good energy confinement and can support $T_e \geq 100$ eV (Figure 2.9(b)) which rapidly declines as the magnetic field lines transition to a chaotic topology and the thermal energy transport increases. This is also observed experimentally (Figure 2.9(c)) where the steep temperature gradient coincides with the transition to a chaotic topology. Ultimately, SSPX was able to attain peak $T_e \sim 500$ eV while operating in this transient quiescent regime [77].

Analysis of transport profiles in SSPX CHI discharges have demonstrated core thermal electron diffusivities comparable to tokamak L-mode values, $\chi_e < 10\ \mathrm{m}^2/\mathrm{s}$ [77,101]. Further,

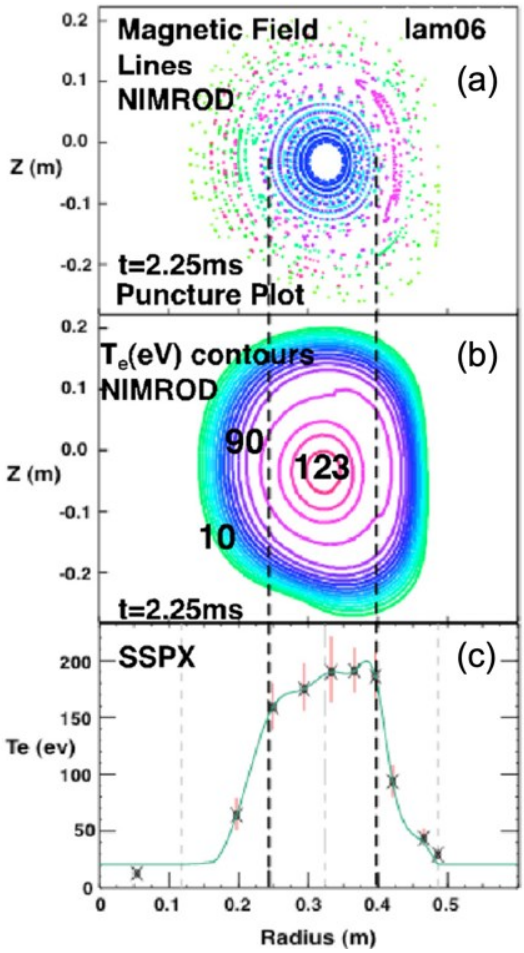

Figure 2.9: Closed flux surfaces predicted by NIMROD simulations of SSPX discharges enabling good energy confinement: (a) Magnetic field-line puncture plot and (b) T_e contours from NIMROD simulation; (c) radial T_e profile from SSPX shot 12560. Taken from [99].

Figure 2.10 shows the scaling of the experimentally measured χ_e as a function of T_e compared to various transport models. The best-fit power law to the experimental data shows that $\chi_e \propto T_e^{-5/2}$ [100]. Below 100 eV, the magnetic fluctuations are the highest and the measured χ_e are comparable to those predicted by the stochastic (RR) transport model developed by Rechester and Rosenbluth [102]. At intermediate temperatures ($100\ \text{eV} \leq T_e \leq 250\ \text{eV}$), the SSPX data is comparable to Bohm diffusion values, $D_{Bohm}[\text{m}^2/\text{s}] = T_e[\text{eV}]/16B[\text{T}]$. At the highest temperatures, the measured χ_e diverges from the other two models and begins to approach the ion classical diffusivity, $\chi_i = \rho_s^2/\tau_s$,where ρ_s is the ion gyroradius and τ_s is the ion collision time. These observations demonstrate that under appropriate conditions, plasmas formed by helicity injection can attain good core energy confinement and are not necessarily dominated by stochastic transport processes.

The good energy confinement properties and highest achieved core T_e are a result of a finely tuned transient operating space. During this transient quiescent period, the magnetic fluctuations are significantly reduced and the q-profile is tuned to enable formation of closed flux surfaces. Outside of these operating conditions, closed flux surfaces cannot be sustained and the T_e is set by the balance of ohmic heating and parallel thermal conduction along open magnetic field lines [98,99]. It is important to point out that these transient quiescent periods with good confinement properties cannot be sustained while actively driving the system ($\lambda_{gun} > \lambda_{fc}$). In this

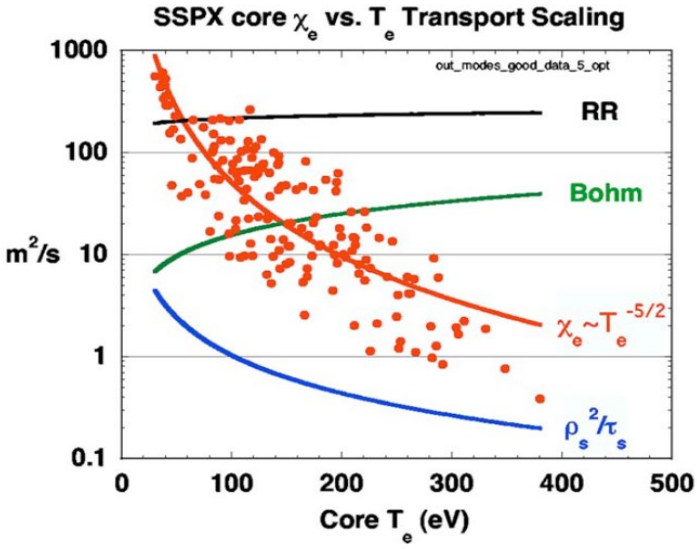

Figure 2.10: Scaling of core χ_e *vs* T_e in SSPX compared with various transport models. Power-law best fit through data shows $\chi_e \propto T_e^{-5/2}$.Taken from [100].

transient quiescent phase, there is insufficient reconnection activity and associated dynamo activity to sustain the equilibrium against resistive decay [98,99]. After years of experimental effort, SSPX found no evidence that it is possible to simultaneously sustain the plasma configuration against resistive decay and maintain good confinement properties [78].

2.7.2 Coaxial Helicity Injection in Tokamaks

The development of coaxial helicity injection for solenoid-free tokamak startup was first studied on the Helicity Injected Torus (HIT). Initially, CHI development focused on a technique known as sustained CHI. In this mode of operation, the injector circuit is continuously driven and injecting helicity for times longer than the plasma resistive decay timescale [103]. Sustained CHI discharges have demonstrated high current multiplication discharges on HIT [104] and several other devices such as HIT-II [39] and NSTX [38].

A common feature of sustained CHI plasmas is a hollow T_e profile with low core T_e. Figure 2.11 shows Thomson scattering measurements at various times during a sustained CHI discharge on HIT-II [105]. Throughout this discharge, the core (R_0~0.3 m) is sustained at $T_e \leq 40$ eV while the edge approaches T_e~150 eV at times. This hollow profile has been attributed to excessive

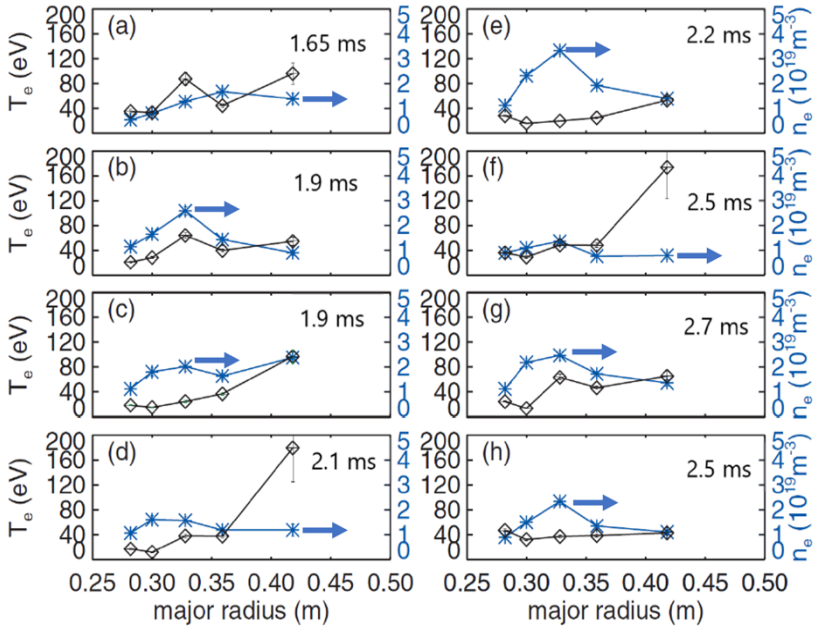

Figure 2.11: T_e (black diamonds) and n_e (blue stars) measurements for several similar sustained CHI discharges on HIT-II. Each time point represents an individual discharge. Adapted from [105].

impurity radiation which suppresses ohmic heating of core electrons. The excessive influx of impurities has hindered the viability of sustained CHI as a scalable tokamak startup technique. The impurities are thought to be sourced from the electrodes and contaminate the plasma [106]. These contaminants inhibit the ability to couple to subsequent current drive techniques that do not have sufficient heating power to overcome the radiated losses [103].

Despite the low core T_e of sustained CHI discharges, there is some evidence from Hamp et al. [105] that the core confinement is not significantly impacted by the driven edge current. Figure 2.12 shows an ohmic discharge (black) and the same ohmic discharge with CHI added (blue). The two discharges are programmed identically except in one discharge (blue) the CHI system is turned on at ~16 ms to drive edge current. After the addition of CHI, the plasma current, radiated power, and density all increase sharply. A comparison of the electron temperature and density profiles between the two discharges measured by Thomson scattering at t~18 ms is shown in Figure 2.12(d) and (e), respectively. The authors note that the ohmic (black) T_e measurements at $R = 28$ and 41 cm are interpreted to be > 200 eV and are omitted on the plot because of measurement uncertainty due to the low density. The authors claim that the addition of CHI to the ohmic plasma results in a dramatic drop in the edge T_e accompanied with an increase in the edge n_e. However, the core T_e and n_e are comparable between the two discharges. The authors suggest this indicates low energy transport from the core plasma to the stochastic edge region. Moreover, Hamp et al.

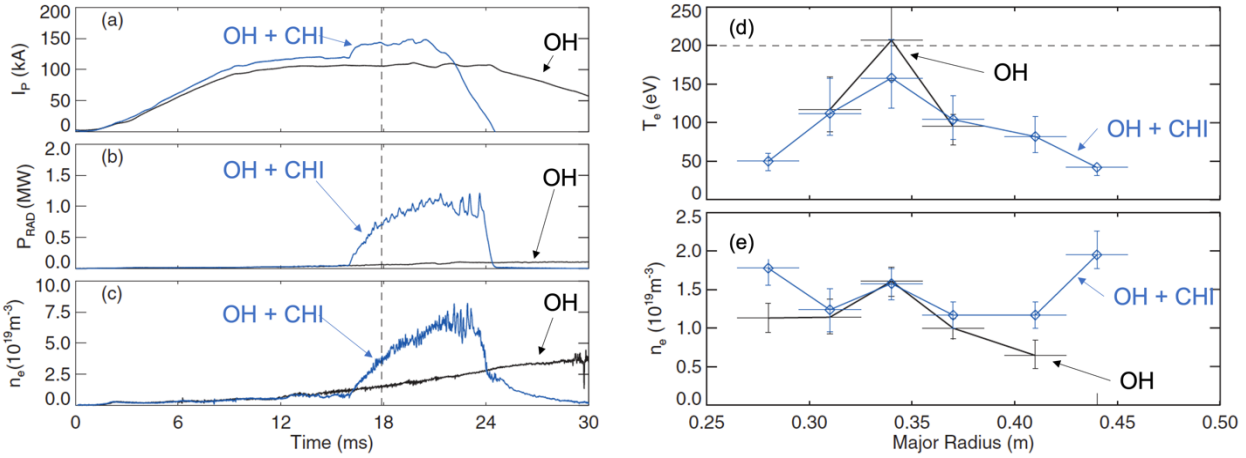

Figure 2.12: Comparison of OH-only and CHI-assisted OH discharges on HIT-II: (a) Plasma current, (b) radiated power, and (c) line-averaged n_e for OH-only discharge (black) and OH+CHI discharge (blue). Radial profiles of (d) T_e and (e) n_e measured by Thomson scattering at $t = 17.9$ ms (vertical dotted line). Adapted from [105].

use this evidence to contradict models presented by Boozer [107] and Moses [108] that closed flux regions cannot be sustained by helicity injection.

To address the impurity accumulation problem, an alternative mode of CHI operation was developed, known as transient CHI. In this mode, the injector current is rapidly shut off after initial plasma formation. In this way, there is less time for the electrodes to act as a source of impurities to mitigate impurity accumulation issues that are associated with the sustained CHI technique. The rapid shut off after initial plasma formation forces axisymmetric magnetic reconnection to occur which bypasses the need for toroidal asymmetries in the magnetic topology to facilitate magnetic relaxation [22,41,42]. This process forms a plasma consisting of closed flux surfaces that must then be coupled to alternative current drive schemes. This method has been successfully coupled to traditional ohmic current drive on both HIT-II [109] and NSTX [106,110]. Several examples of successful handoffs to ohmic induction on NSTX are shown in Figure 2.13 for different sized CHI power supplies [106]. The CHI system drives injector current for ~ 4 ms and produces a seed plasma with $I_p \leq 300$ kA. After this point, the CHI supply is rapidly shut off and the discharge is driven by ohmic induction. After an initial spike during the transient CHI seed plasma, the radiated power drops dramatically. This is indicative of a reduced influx of impurities compared to the sustained CHI technique. This enables the ability to couple the startup plasma to subsequent current drive sustainment methods.

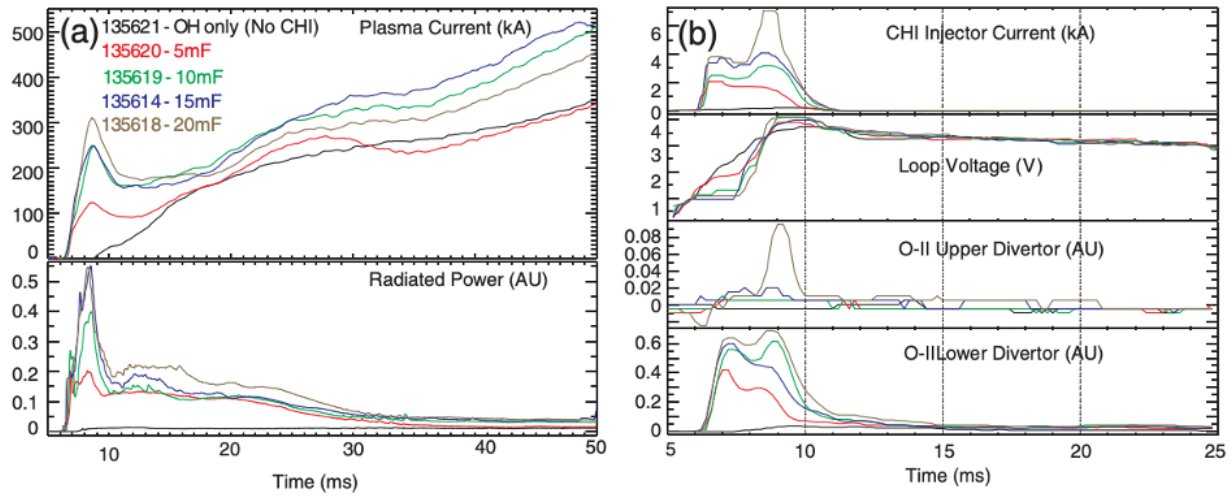

Figure 2.13: Overview of successful transient CHI to ohmic handoff on NSTX for different sized CHI power supplies. (a) shows I_p and radiated power traces, (b) shows I_{inj}, V_{OH}, and O-II impurity radiation from the upper and lower divertor regions. Taken from [106].

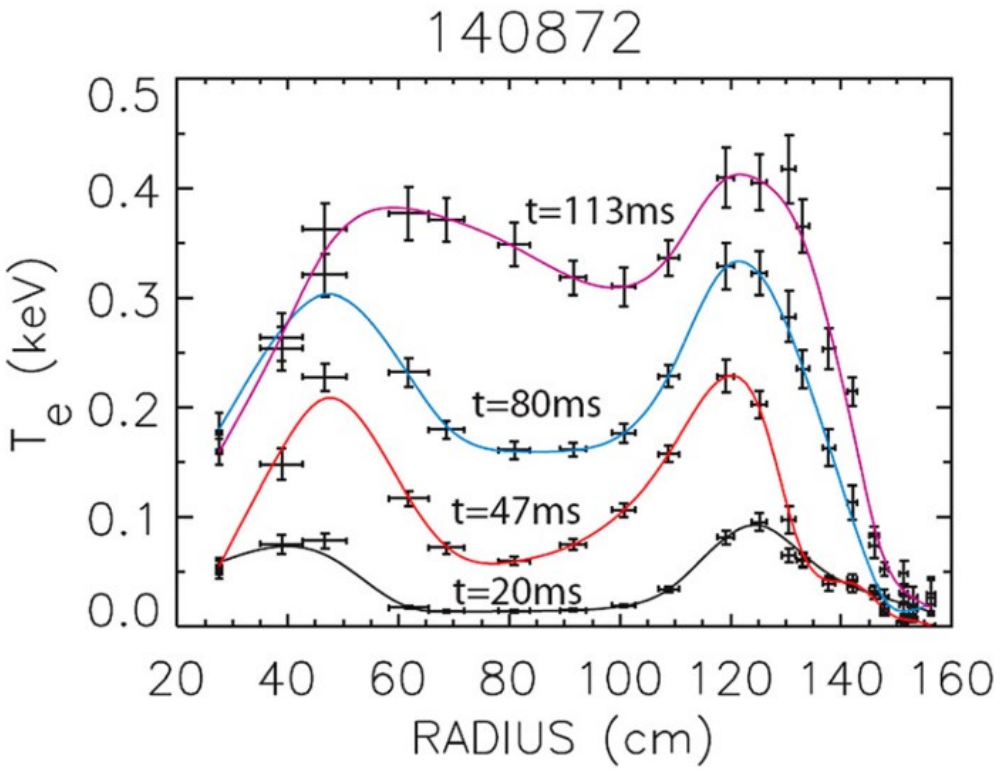

Figure 2.14: Time evolution of electron temperature profiles for a CHI-ohmic induction handoff discharge on NSTX. Taken from [40].

Despite the reduction in core impurity accumulation, transient CHI plasmas still exhibit hollow T_e profiles. This is demonstrated in Figure 2.14 which shows the time evolution of the T_e profile during an ohmic handoff shot on NSTX. Shortly after CHI supply is shutoff ($t = 20$ ms), the T_e profile is hollow with the core $T_e \sim 20$ eV. The initial hollowness of the CHI phase of the discharge is attributed to the relatively slow current diffusion from the plasma edge to the core as opposed to impurity radiation. This hollowness persists into the ohmic-only phase of the discharge, but eventually fills in with subsequent heating from ohmic induction and achieves $T_e > 300$ eV [40].

2.7.3 Local Helicity Injection on Pegasus

The existence of closed or nearly closed flux surfaces is required for good energy confinement properties. Tokamaks are generally comprised of nested flux surfaces and are dominated by neoclassical and anomalous transport. Regions of stochastic magnetic fields result in enhanced radial transport and degraded confinement properties. Although still an active area of research, there is evidence that the magnetic topology of LHI discharges can support regions of good energy

confinement. However, the presence of magnetic reconnection may also lead to stochastic regions. Therefore, energy confinement in LHI discharges may be impacted by a combination of traditional tokamak transport and stochastic transport processes.

Peaked electron temperature and pressure profiles are routinely achieved in LHI [92,111]. A common feature of strongly stochastic regions is a flattening of T_e profiles due to enhanced radial transport. Therefore, the observation of peak profiles suggests that LHI plasmas can support regions of good confinement and are not strongly globally stochastic.

Further, LHI can support core T_e comparable to ohmic L-mode discharges. Figure 2.15 shows I_p, n_e, and T_e measurements for similar HFS LHI and ohmic L-mode discharges developed at $B_T \approx 0.15$ T on Pegasus [30]. In this comparison, the HFS LHI (black triangles) and ohmic L-mode (red circles) each have peaked profiles with $T_{e,0} \approx 50$ eV. The relatively low T_e in the L-mode discharge on Pegasus compared to larger facilities, such as NSTX or MAST, is most likely due to the lower operating B_T point and comparatively smaller plasma volume. These factors lead to poorer energy confinement properties and will be discussed in greater detail in the next section. Still, the self-similar T_e profiles observed during LHI and ohmic L-mode discharges on Pegasus suggest a similar quality of core energy confinement. The reduced density of the LHI discharge was attributed to the lower available helicity input ($V_{LHI} \approx 1$ V) compared to the ohmic loop voltage ($V_{loop} \approx 3$ V) [92].

The magnetic activity present in LHI is localized inside the edge pressure gradient. This is demonstrated in Figure 2.16 which shows the radial profiles of the vertical magnetic field fluctuations ($\tilde{b}_z$) power and electron pressure (P_e) measured by an insertable probe and Thomson scattering, respectively [112]. The electron pressure begins to rise at $R \sim 70$ cm and then flattens to $P_e \approx 75$ Pa at $R \leq 60$ cm. Meanwhile, the peak of the $\tilde{b}_z$ power occurs near the top of the edge pressure gradient at $R \sim 60$ cm and then falls off at lower R. Although not explicitly shown in Figure 2.16(b), measurements from other discharges show the $\tilde{b}_z$ power dropping to ~ 0 as R approaches R_0 [86,112]. This demonstrates that the magnetic activity in LHI is localized to the plasma edge. This magnetic activity may be expected to create stochastic fields and enhance radial transport. However, the existence of edge gradients and peaked pressure profiles suggests that this localized edge magnetic activity does not destroy the confined core region.

The consideration of stochastic transport in LHI plasmas is motivated by the presence of magnetic reconnection. Magnetic reconnection breaks magnetic field lines and leads to regions of stochastic and/or chaotic magnetic fields. NIMROD simulations predict magnetic reconnection occurring in the plasma edge [50]. This aspect of the simulation was validated through the observation of anomalous ion heating during LHI on Pegasus [53]. Dedicated scans demonstrated

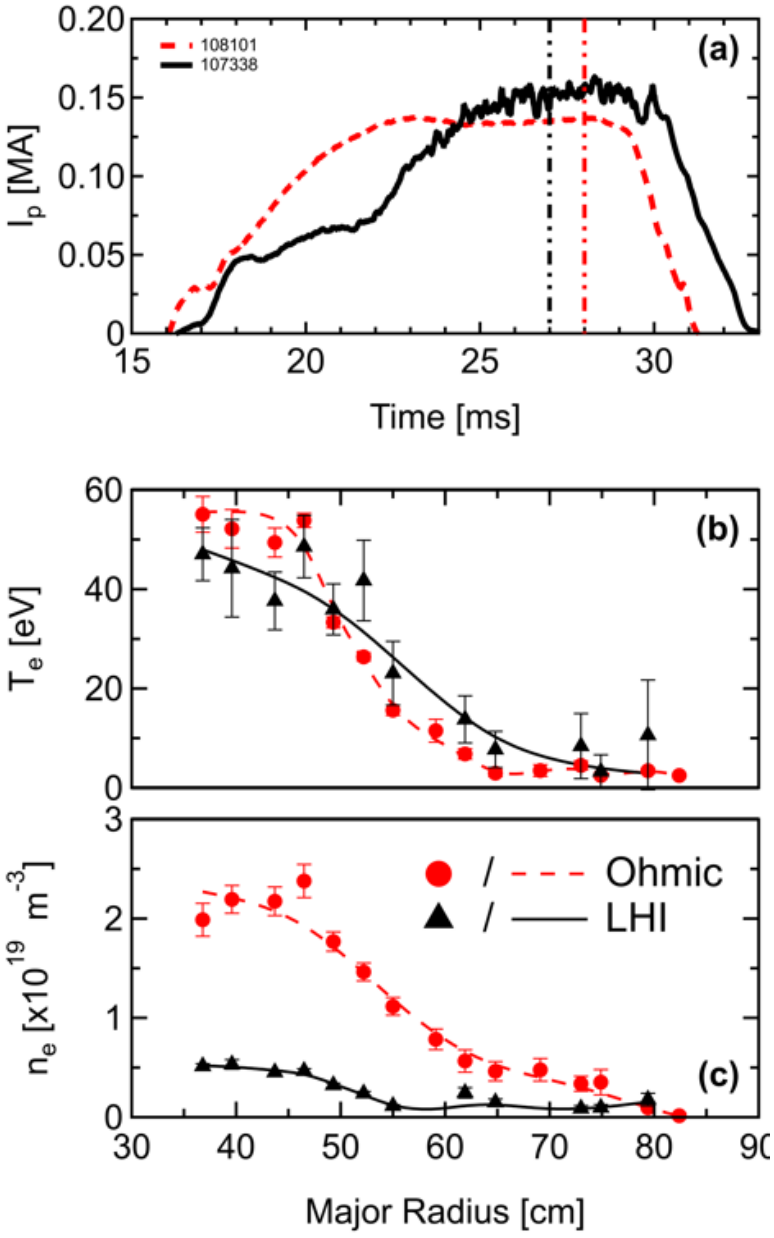

Figure 2.15: Comparison of electron kinetic profiles between similar LHI and ohmic L-mode discharges at $B_T \approx 0.15$ T on Pegasus: (a) $I_p(t)$, (b) $T_e(R)$ and (c) $n_e(R)$. Dotted vertical lines in (a) indicate the time that the T_e and n_e profiles were measured using Thomson scattering. Figure adapted from [30].

that the scaling of the ion heating was consistent with two-fluid reconnection theory ($\propto I_{inj}V_{inj}^{1/2}$). Additionally, the heating was found to be localized to the plasma edge where NIMROD predicts reconnection activity.

The apparent core confinement and localized reconnection at the plasma edge suggest that multiple confinement regimes may exist within the LHI plasmas. Previous work by Bodner [92] hypothesized a confined core plasma surrounded by a stochastic edge region during LHI discharges but this has yet to be confirmed. A similar transient configuration has been observed during CHI on SSPX as described in Section 2.7.1. Further, observations from CHI on HIT-II presented in Section 2.7.2 also suggest the existence of a confined core region surrounded by a stochastic edge.

Experimental observations in LHI have provided motivation for considering neoclassical, anomalous, and stochastic transport processes. It is reasonable to expect that anomalous tokamak

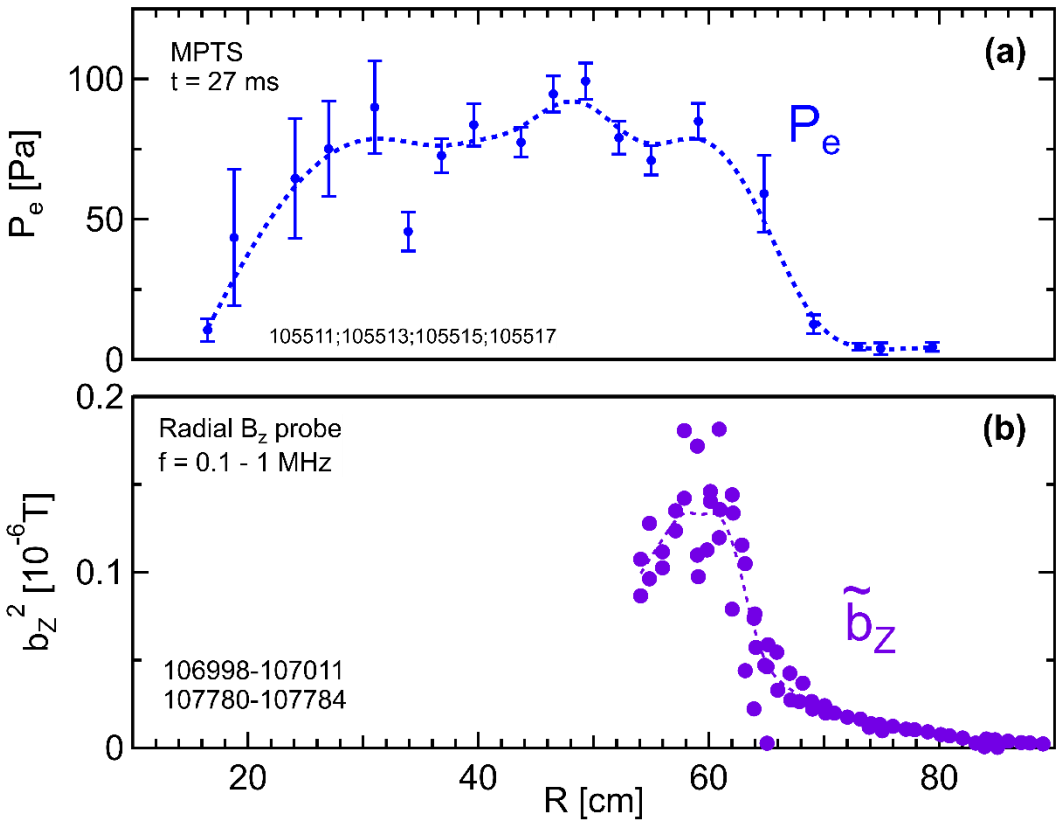

Figure 2.16: Radial profiles of (a) electron pressure and (b) integrated magnetic power from 0.1 to 1 MHz measured during a HFS LHI discharge with I_p~0.14 MA, B_T~0.045 T. Smoothing splines applied to the data points (dashed lines) are also shown. Figure adapted from [112].

transport sets an upper limit for confinement in LHI plasmas. Whereas globally stochastic transport represents a lower bound on LHI confinement. The transport governing LHI plasmas likely lies somewhere between these two extremes and may consist of multiple regions throughout the plasma volume.

2.8 Electron Confinement and Transport

The previous section provided evidence that both closed flux surfaces and stochastic magnetic fields may be present in LHI plasmas. In modern tokamaks, the magnetic topology is largely comprised of nested, closed flux surfaces. As such, neoclassical and anomalous processes dominate over stochastic effects [113]. In systems with magnetic reconnection and/or strong magnetic fluctuations, stochastic magnetic fields often dominate the transport and confinement [78,114,115]. This section will briefly introduce these confinement models. This discussion will be primarily focused on introducing estimates for global energy confinement scalings for various tokamak and stochastic confinement regimes. A broader discussion of plasma transport and confinement is outside the scope of the proposed work and will not be addressed here.

Additionally, LHI relies on driving open field line currents to provide a source of DC helicity injection. Some models [108,116] and simulations [51,98,99] of DC helicity injection systems predict the entire plasma volume consists of open field lines connected to the biased electrodes while actively driving the system. As such, a discussion on the electron temperature that can be sustained in an open field line topology will also be provided.

2.8.1 Tokamaks

Thermal energy confinement in a plasma is often characterized by a global energy confinement time, τ_E, which is defined as

$$\tau_E = \frac{W_k}{P_{in} - \frac{dW_k}{dt} - \frac{dW_M}{dt}} \tag{2.23}$$

where W_k and W_M are the stored plasma kinetic and magnetic energy. P_{in} is the input heating power. In a simple cylindrical plasma dominated by thermal diffusive losses, the confinement time can be approximated as

$$\tau_E \sim \frac{a^2}{\chi_e} \tag{2.24}$$

where χ_e is the cross-field thermal diffusion coefficient. In classical transport theory, χ_e is calculated by assuming this cross-field transport is due to coulomb collisions in a magnetized cylindrical plasma. In a toroidal confinement device, such as a tokamak, the geometry leads to further enhancements to this transport which is described by neoclassical transport theory [113,117]. The confinement times calculated from classical and neoclassical transport theories are much longer than what is observed experimentally. This large discrepancy is attributed to anomalous transport.

Anomalous transport is comprised of highly non-linear turbulence processes and is an active area of research. Despite the development of many sophisticated modeling tools [118–122], empirical scalings generated from multi-machine databases are typically used for predicting τ_E in present-day tokamaks. These empirical scalings are generally grouped into discrete tokamak operating regimes: the linear ohmic confinement (LOC) and the saturated ohmic confinement (SOC) regimes. The SOC regime is then further divided into the low confinement (L-mode) and high confinement (H-mode) regimes.

The LOC regime is characterized by the observation that τ_E increases linearly with n_e. At a critical density, $n_{e,crit}$, τ_E saturates as it enters the SOC regime. This behavior is demonstrated in Figure 2.17 with the critical density shaded in purple [123]. Experiments on a variety of machines at high A have identified that $n_{e,crit}$ depends on q, R, and B_T [124] and is typically approximated by the empirical relation [125]

$$n_{e,crit} = 0.65 \frac{A_i^{0.5} B_T}{qR} [10^{20}\ \mathrm{m}^{-3}] \tag{2.25}$$

where A_i is the ion mass in amu, B_T in T, safety factor q, and major radius R in m. Additional indicators of the LOC/SOC transition include intrinsic rotation reversal and changes in the turbulence characteristics. Many gyrokinetic simulations have identified that the turbulence in the LOC regime is dominated by trapped electron modes (TEMs), but ion- and electron- temperature gradient modes (ITG/ETG) are also active and important for electron thermal transport [124].

Confinement times in the LOC regime are well described by the neo-Alcator empirical scaling relation [124]

$$\tau_E^{neo-A} = 0.07 n_e q \kappa^{0.5} R^2 a\ [s] \tag{2.26}$$

with n_e in 10^{20} m^{-3}, R in m, and a in m.

Above the critical density, tokamaks transition into the saturated ohmic confinement regime where τ_E is more weakly dependent on n_e. Gyro-kinetic simulations have commonly identified that ITG modes are the dominant source of turbulent transport in this regime, but ETG modes also contribute to electron thermal transport [124]. The SOC regime includes both L-mode and H-mode plasmas. The plasma will initially begin in L-mode. The confinement time in L-mode is described by the ITER97L scaling [126]:

$$\tau_E^{ITER97Lth} = 0.023 \frac{M^{0.2} I_p^{0.96} R^{1.83} \kappa^{0.64} n_e^{0.4} B_T^{0.03} A^{0.06}}{P_L^{0.73}} \; [s] \qquad (2.27)$$

where M is the average isotopic mass number, plasma current I_p in MA, R in m, n_e in 10^{20} m^{-3}, B_T in T, and P_L is the "loss power" in MW. This loss power is the total heating power P with a correction for the time rate of change in the total stored energy dW/dt, $P_L \equiv P - dW/dt$.

Under appropriate conditions and sufficient heating power, an L-mode plasma can spontaneously transition into H-mode [113,127]. The H-mode is characterized by increased stored

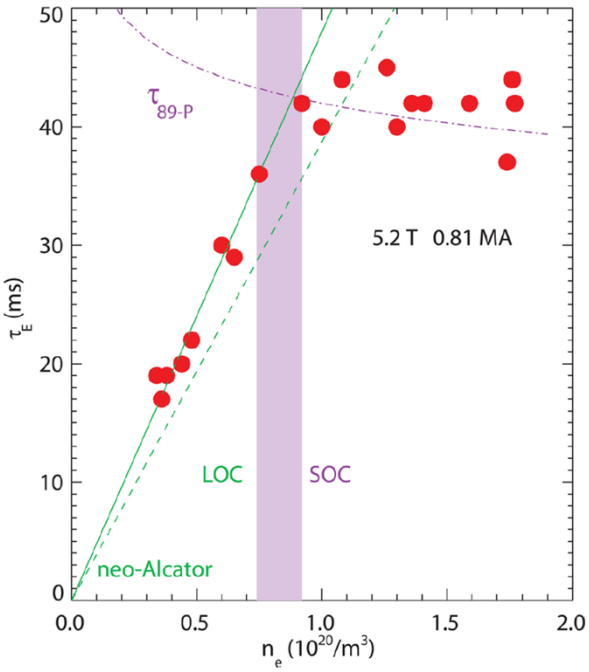

Figure 2.17: Transition from linear ohmic confinement (LOC) to saturated ohmic confinement (SOC) observed in Alcator C-Mod ohmic plasmas. The shaded purple region is the approximate critical density at which the LOC/SOC transition occurs. The dashed green line represents neo-Alcator scaling and the dashed purple line represents the ITER89-P L-mode scaling. Figured taken from [123].

energy due to the formation of an edge transport barrier. A commonly used empirical confinement time scaling for H-mode is the IPB98(y,2) [125]

$$\tau_E^{IPB98(y,2)} = 0.0562 \frac{I_p^{0.93} R^{1.39} \kappa^{0.78} n_e^{0.41} B_T^{0.15} A^{0.19} a^{0.58}}{P_L^{0.69}} \; [s] \tag{2.28}$$

with a in m and all other parameters are the same as in equation 2.27.

2.8.2 Spherical Tokamaks

Although the general picture is similar, there are some differences in the confinement and transport between spherical tokamaks and high A devices. These differences are especially important to consider for Pegasus, which operates at extremely low A.

At low densities, START [128], Globus-M [129], and NSTX [130] have all observed LOC behavior with τ_E increasing linearly with n_e up to a saturation point. For NSTX and START, this linear trend was observed above the predicted critical density derived from data at high A (equation 2.25). For typical NSTX parameters ($B_T = 0.3$ T, $R_0 = 0.85$ m, and $q = 3$), the critical density calculated by equation 2.25 is $n_{e,crit} \sim 1 \times 10^{19}$ m^{-3}. However, experiments have demonstrated τ_E increases with n_e up to $0.8 n_{e,gw}$, where $n_{e,gw}$ is the Greenwald density [130,131]. This Greenwald fraction ($n_e/n_{e,gw}$) corresponds to $n_e \leq 4 \times 10^{19}$ m^{-3} which is significantly higher than the predicted critical density. On START, the predicted $n_{e,crit} \sim 1 \times 10^{19}$ m^{-3} but the LOC regime was observed up to $n_e \sim 1 \times 10^{20}$ m^{-3} [132]. Additionally, the measured confinement times on START and Globus-M have also typically been larger than the neo-Alcator predictions [128,129].

At higher densities, the confinement times observed in STs also saturate and experience a degradation with heating power. On START, the confinement time predictions for L-mode discharges (equation 2.27) were generally in agreement with experimental observations [128]. However, ITER97L predictions for L-mode discharges on NSTX and MAST underestimated the experimental confinement times [133,134]. Further, there was a significantly weaker degradation with heating power in NSTX, $\tau_E \propto P^{-0.37}$ [134]. These differences are not particularly surprising because low A STs were not included in the multi-machine databases from which the ITER97L empirical scaling is derived [125].

The IPB98(y,2) (equation 2.28) scaling showed general agreement across the ST H-mode data [135]. However, there were significant scaling differences with the toroidal magnetic field and plasma current. Analysis of data from Globus-M [136], MAST [137], and NSTX [134] all differed from the IPB98(y,2) scaling ($\tau_E \propto I_p^{0.93} B_T^{0.15}$). Generally, the ST H-mode confinement time scalings showed a greater than linear scaling with B_T and a weaker I_p dependence. This is illustrated by an empirical scaling developed by Kurskiev et al. [138] from a database consisting of data from several STs:

$$\tau_E^{Low-A} = 0.066 \frac{I_p^{0.53} R^{2.66} \kappa^{0.78} n_e^{0.65} B_T^{1.05} A^{1.14}}{P_L^{0.58}} \; [s] \tag{2.29}$$

with the same unit conventions used in the IPB98(y,2) scaling. However, experiments on NSTX have observed that operating at lower collisionality recovered the B_T and I_p dependencies given by the IPB98(y,2) relation [139].

Despite the general agreement with empirical scalings, the transport characteristics of STs in the SOC regime are different from those observed in higher A tokamaks. The low A ST operating space can access high β equilibrium which can stabilize ITG and TEM turbulence [18]. However, the micro-tearing modes (MTM) and kinetic ballooning modes (KBM) are destabilized at sufficiently high β. These modes are typically not observed in high A equilibria. Along with ETG modes, these are considered candidates for describing electron thermal transport in ST plasmas [18,139,140]. Additionally, ETG modes have been found to be stabilized at decreasing plasma collisionality and the electron thermal transport is dominated by MTM/KBM modes [139].

2.8.3 Stochastic Magnetic Fields and Transport

Magnetic reconnection can break field lines and form a stochastic magnetic topology. Magnetic reconnection is a critical component to the magnetic relaxation process that exists during LHI [49,50] and is invoked by Taylor relaxation theory [35]. The chaotic structure of a stochastic magnetic field creates parallel paths for enhanced radial transport. This results in degraded confinement relative to systems with nested flux surfaces, such as standard tokamak confinement regimes.

An important paper by Rechester and Rosenbluth explored electron thermal transport in a tokamak with destroyed magnetic surfaces [102]. In this paper, thermal transport coefficients are

derived based on the Brownian motion of magnetic field lines for both collisional and collisionless regimes. Rechester and Rosenbluth showed that a magnetic flux tube can wander from its starting point,$\langle(\Delta r)^2\rangle$, as

$$\langle(\Delta r)^2\rangle = 2LD_M \tag{2.30}$$

where L is a characteristic distance along the flux tube and D_M is the magnetic diffusion coefficient which is

$$D_M = \sqrt{\frac{\pi}{2}}\left(\frac{\delta B_r}{B_T}\right)^2 L_c \tag{2.31}$$

where $\left(\frac{\delta B_r}{B_T}\right)$ is the relative radial magnetic field fluctuation amplitude and L_c is the parallel correlation length of the fluctuation [141].

In a strongly stochastic magnetic field, the radial thermal energy transport is dominated by electron transport along the field lines due to the faster thermal electron speed ($v_{th,e}$). Rechester and Rosenbluth argue that both the collisional and collisionless regimes are diffusive in nature. Thus, the radial thermal transport can be modeled by a diffusion coefficient [102]

$$\chi_e = \frac{(\Delta x)^2}{2\Delta t} \tag{2.32}$$

where Δx and Δt are the characteristic spatial and temporal step sizes, respectively.

In the context of stochastic transport, the characteristic spatial scales are the electron collisional mean free path, λ_{mfp}, and the magnetic connection length. In the collisionless regime ($L_c < \lambda_{mfp}$), an electron will travel $L = \lambda_{mfp}$ before colliding and will take $\Delta t = v_{th,e}/\lambda_{mfp}$. From equation 2.30, the radial displacement of the magnetic field line in this time will be $\langle(\Delta r)^2\rangle = 2\lambda_{mfp}D_M$. Plugging this radial displacement and Δt into equation 2.32 results in the collisionless radial thermal diffusion coefficient [102]

$$\chi_{e,collisionless} = D_m v_{th,e} \sim v_{th,e}\left(\frac{\delta B_r}{B_T}\right)^2 L_c \tag{2.33}$$

In the collisional regime ($L_c > \lambda_{mfp}$), electrons will exhibit many collisions before traveling the magnetic connection length. Therefore, the step-size is dictated by the balance of two processes: deformation of the field line and parallel diffusion. The consideration of these two processes leads to the following thermal diffusion coefficient:

$$\chi_{e,ccollisional} = \frac{D_M \chi_\parallel}{L_{c\delta}} \sim {v_{th,e}}^2 \tau_{col} \left(\frac{\delta B_r}{B_T}\right)^2 \quad (2.34)$$

where $\chi_\parallel$ is the parallel thermal conductivity and τ_{col} is the average time between collisions. The $L_{c\delta}$ is the magnetic connection length with a logarithmic correction factor which is given in equation 7 of [102].

The collisionless and collisional thermal diffusivities given by equations 2.33 and 2.34, respectively, depend on the relative magnitude of magnetic fluctuations. Dimensional analysis performed by Connor and Taylor found that the magnetic fluctuations scale with the Lundquist number S, $\delta B_r/B_T \sim S^{-1/2}$ [142]. The Lundquist number is defined as the ratio of the resistive diffusion time, τ_R, to the Alfvén time, τ_A:

$$S = \frac{\tau_R}{\tau_A} = \frac{\mu_0 a^2/\eta}{a/\left(B_T^2/\mu_0 \rho_0\right)^{1/2}} \quad (2.35)$$

where ρ_0 is the mass density. Experiments on the Madison Symmetric Torus tested this scaling and found that $\delta B_r/B_T \sim S^{-\alpha}$. However, α was limited to a range of $0.07 \leq \alpha \leq 0.18$ instead of $\alpha = 0.5$ [114].

Presently, there is no a priori information on δB_r in LHI discharges. Thus, the χ_e relations given in equations 2.33 and 2.34 can only provide relative scalings and not absolute predictions.

2.8.4 T_e Sustained on Open Magnetic Field Lines

DC helicity injection techniques rely on driving current along open magnetic field lines. These open field line currents originate from the biased electrodes and will necessarily intersect the wall and/or a designated current return structure. The electron temperature that can be sustained along such open field lines is dictated by the balance of ohmic heating and parallel heat losses conducted to the wall. Simple analytic models for this balance indicate that the maximum electron temperature $T_{e,max}$ that can be sustained along these open field lines is dependent on the current density driven along the field line J_{inj} and the length of the magnetic field line L_{inj}, $T_{e,max} \propto \left(J_{inj} L_{inj}\right)^{2/5}$ [116,143]. Applying this simple estimate to typical parameters for CHI-driven spheromaks yields T_e on the order of tens of eV [116] which is comparable to Thomson scattering data in the open field line region as well as values predicted by NIMROD simulations [98,99].

More recent work by Moses et al. develops a model for $T_{e,max}$ in DC helicity injection plasmas [108]. The model asserts that all driven current in the plasma volume must, at least intermittently, be connected to the biased electrodes. Therefore, thermal and particle transport is governed by the balance of ohmic heating with thermal and advective power flow along open magnetic field lines that are connected to the biased electrodes. This leads to $T_{e,max}$ within the plasma volume being limited to some fraction of the applied bias voltage $T_{e,max} \leq V_{inj}/C_0$, where $C_0 \approx 2.5 - 4$. The range in this limit arises from a variety of assumptions that are considered by Moses et al. which yields similar results but different ratios between $T_{e,max}$ and V_{inj}. The authors also note that additional radiative losses can result in an even lower observed T_e for a given applied V_{inj} [108].

2.9 Simple Steady-State Confinement Model

Validated models for predicting LHI performance must be developed for scaling the technique to MA-class tokamak startup. The 0-D power balance model, described in Section 2.5, has been developed for this purpose to model $I_p(t)$ in LHI discharges. However, the 0-D power balance model has practically no predictive capability without an accurate estimate of the helicity dissipation in LHI plasmas. A working model for determining the electron temperature and hence $\langle\eta\rangle$ in LHI would constrain the helicity dissipation in the 0-D model and enable more relevant $I_p(t)$ predictions.

A full transport analysis is needed to fully understand the confinement properties of LHI plasmas and quantify the amount of helicity dissipation. However, this sort of analysis is not feasible at this point due to open questions regarding energy sources/sinks in LHI plasmas and presently limited information on bulk ion kinetic profiles. Until a more complete physical understanding of LHI develops, it is worthwhile to consider more simplistic models to characterize the scaling of I_p and T_e during LHI. To this end, a simple steady-state confinement model will be used to assess how well LHI I_p scalings are characterized by estimates consistent with conventional global confinement times.

The steady-state confinement model is based on calculations developed by McCool [144] to self-consistently calculate the I_p, V_{LHI}, and $T_{e,0}$ for an assumed confinement time scaling. This

calculation is used to determine the variation in achievable I_p for an imposed drive voltage. For assumed density and temperature profile shapes, the model balances the heating power with losses from radiation and anomalous transport.

$$P_{in} = \left(V_{LHI} I_p + P_{aux}\right)(1 - F_{RAD}) = \frac{W_k}{\tau_E} \tag{2.36}$$

where P_{aux} is the auxiliary heating power, $F_{RAD} \equiv P_{rad}/P_{in}$ is the radiated power fraction. A variety of confinement time scalings are under consideration because LHI transport is likely impacted by a combination of neoclassical, anomalous, and stochastic transport processes.

For standard tokamak confinement regimes, these confinement times are calculated from standard empirical scaling laws built from multi-machine databases, such as those which were presented in Sections 2.8.1 and 2.8.2. These empirical scalings provide absolute τ_e estimates. Thus, the I_p scaling estimates for standard tokamak confinement regimes contain no free parameters.

As discussed in Section 2.7.3, there is evidence that LHI plasmas are not strongly globally stochastic, and the stochasticity may be localized to the plasma edge. However, a partially stochastic model has not been developed for LHI plasmas. In the absence of a more sophisticated model, a globally stochastic confinement model is assumed to provide a worst-case estimate. In a globally stochastic plasma, the confinement time estimates are based on the stochastic transport model derived by Rechester and Rosenbluth which was presented in Section 2.8.3. With $\tau_E \sim a^2/\chi_e$, the balance between heating power and transport losses for a globally stochastic plasma in a collisional or collisionless regime becomes

$$\text{Collisional: } \left(V_{LHI} I_p + P_{aux}\right)(1 - F_{RAD}) \sim \frac{n_e T_e {v_{th_e}}^2 \tau_{col} S^{-2\alpha}}{a^2} \tag{2.37}$$

$$\text{Collisionless: } \left(V_{LHI} I_p + P_{aux}\right)(1 - F_{RAD}) \sim \frac{n_e T_e v_{th_e} L_c S^{-2\alpha}}{a^2}. \tag{2.38}$$

Here, the stored energy scales as $W_k \sim n_e T_e$, the stochastic magnetic fluctuations are assumed to scale with the Lundquist number ($\delta B_r/B_T \sim S^{-\alpha}$), and τ_{col} is the average time between collisions. It can be shown that equations 2.37 and 2.38 can be recast into the following I_p scaling relations [92,145]:

$$\text{Collisional: } I_p \propto \frac{V_{LHI}^{5/2}}{\left(\frac{\delta B_r}{B_T}\right)^{3/2}} \sim V_{LHI}^{5/2} S^{3\alpha/2} \tag{2.39}$$

$$\text{Collisionless:} I_p \propto \frac{\left(\frac{\delta B_r}{B_T}\right)^2}{V_{LHI}^2} \sim V_{LHI}^{-2} S^{-2\alpha}. \quad (2.40)$$

The collisionless scaling model provides a non-intuitive and seemingly unphysical result. In particular, the I_p is predicted to increase with increasing magnetic fluctuation amplitude. This contrasts with the expectation that increased magnetic fluctuations should increase transport leading to degraded confinement and performance. Previous work by Perry suggested that invoking a non-Spitzer resistivity could provide a more sensible scaling by allowing the stochastic magnetic field to increase the electron momentum loss [145]. However, this collisionless model has not been extensively considered as LHI discharges are generally approximately collisional [30,92,145]. Further, the next section will illustrate that LHI plasmas have demonstrated a robust linear increase in I_p with V_{LHI} which entirely contradicts the expected collisionless scaling given by equation 2.40. For these reasons, the collisionless scaling will not be discussed further.

These power balance equations only provide relative I_p scalings because no absolute τ_E estimates are provided by the stochastic model. Therefore, the stochastic scalings do not provide predictable absolute values of I_p. To compare the stochastic predictions with data, the relative stochastic estimates are normalized to an arbitrary experimental reference.

An example of this normalization is demonstrated in Figure 2.18 which shows I_p estimates from the steady-state confinement model assuming a collisional stochastic scaling at various values of α. The curves are normalized to a HFS LHI discharge at $I_p \approx 120$ kA, $B_T \approx 0.15$ T, and $\langle n_e \rangle \approx 6 \times 10^{18}$ m^{-3} which is indicated by the blue dot. A consequence of this normalization is that each of the curves is forced through this operating point and can skew the I_p scaling estimates. Further, it is unclear how applicable a given normalization is when other input parameters are varied significantly from the chosen experimental reference.

Figure 2.18 also presents the I_p scaling as a function of a geometry-normalized voltage, V_{NORM}. This is done to isolate injector contributions and remove geometric shaping effects. This V_{NORM} only depends on injector parameters and is defined to be [92]

$$V_{NORM} \equiv V_{LHI} \frac{A_p}{R_0}. \quad (2.41)$$

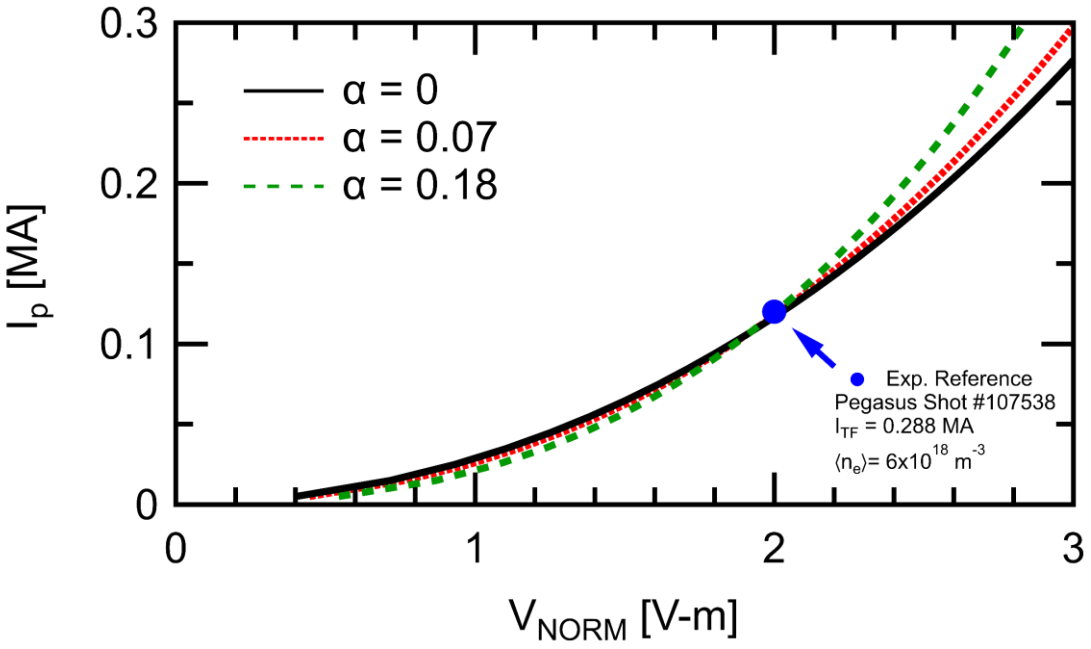

Figure 2.18: I_p scaling for collisional stochastic confinement model at different values of α.Blue dot represents the experimental reference data point used for normalization.

2.10 I_p Scaling Trends Observed During LHI on Pegasus

A series of steady-state HFS LHI discharges were developed to investigate the scaling of LHI current drive [92]. These discharges scanned V_{NORM} at low toroidal field (B_T~0.045 T) on Pegasus. The result was a robust offset linear I_p scaling V_{NORM} [46,92]. This data is shown in Figure 2.19 along with I_p predictions assuming neo-Alcator and globally stochastic confinement scalings [92]. The large uncertainty in the scaling predictions comes from the rough estimate of auxiliary power from reconnection heating. The estimates are based on work by Burke et al. which found that the ion heating scaled with $I_{inj}V_{inj}^{1/2}$ [53].

Within the context of the simple steady-state confinement model, the blue shaded region in Figure 2.19 represents estimates using neo-Alcator scaling with no free parameters. Given the simplistic nature of these estimates, the consistency between the data and neo-Alcator (LOC) scaling estimates is somewhat striking. Even in LHI discharges operating at low B_T and characterized by hollow T_e profiles, the observed scaling is within the bounds of simple ohmic

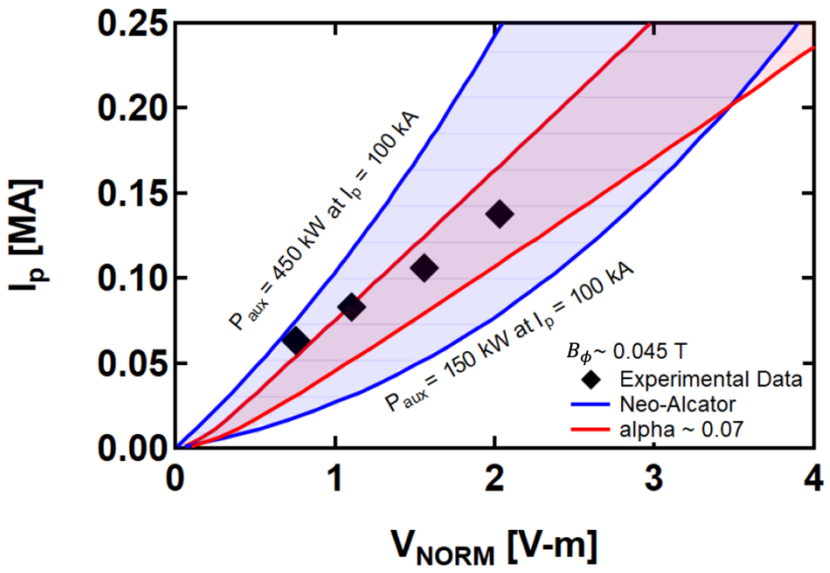

Figure 2.19: Comparison of experimental data (black dots) with predicted I_p scaling assuming neo-Alcator (blue) and globally stochastic (red) confinement. The shaded regions represent the range of assumed auxiliary reconnection heating power [92].

confinement estimates [92]. On the other hand, the agreement between experiment and the globally stochastic scaling estimate is unsurprising due to the normalization. Still, the relative variation with V_{NORM} is consistent with the data over the limited parameter range that was investigated.

Realistically, this experiment was unable to distinguish the I_p-scaling of LHI between ohmic-like or globally stochastic-like confinement estimates. However, it does provide motivation for using simple global confinement estimates as a potentially useful benchmark for future LHI experiments. Still, further tests are required over a wider parameter space to explore the relevance of using these global confinement scalings to characterize LHI plasmas.

2.11 Expected Qualitative Scaling Trends

Energy confinement in LHI plasmas may be influenced by several competing transport processes and vary throughout the plasma volume. However, a working confinement model describing these interactions has not been developed and is outside the scope of this work. For simplicity, the calculations presented in this section assume LHI plasmas are dominated by a single global confinement scaling. The predicted trends will be compared against Pegasus-III experiments that

will be discussed in Chapter 6 to assess if any of the proposed global confinement scalings are useful for characterizing the T_e and I_p trends observed during LHI.

Prior to presenting these predicted I_p trends, it is important to recall the limitations of the simple steady-state confinement model. First, the steady-state model is ill-equipped to model LFS LHI discharges which typically rely on dynamic shape evolution to provide significant inductive drive. Additionally, the calculation is based on global power balance and thus does not include any profile effects. Finally, the assumption of conventional confinement scalings does not imply that LHI discharges are dominated by the same physical transport processes. Instead, the comparison of LHI data to various confinement scalings is attempting to identify a useful benchmark to characterize the scaling of I_p and T_e in LHI plasmas.

Despite the simplicity of the model, previous work presented in Section 2.10 found that the observed I_p scaling on Pegasus was within the bounds of ohmic-like confinement estimates, albeit with a very wide range of uncertainty. Here, the model is used to estimate predicted trends for ohmic-like confinement scaling in Pegasus-III. Such predictions are only meaningful if the simple model provides reasonably accurate estimates for tokamak operating points. As such, the model calculations have been benchmarked against data from a variety of tokamaks to provide credibility to the standard tokamak scalings estimates that will be presented in this section. These comparisons are provided in Appendix A. Overall, the simple model shows good agreement with data across a variety of machines.

The steady-state confinement model is used to examine the predicted I_p scaling dependencies on B_T and n_e in Pegasus-III. The B_T and n_e dependencies are of particular interest because of their experimental accessibility for dedicated parameter scans via the toroidal field rod current and external fueling, respectively. In addition, varying these parameters should provide an opportunity to distinguish between competing confinement models presently under consideration for characterizing LHI plasmas. As outlined in Section 2.8, the standard tokamak and stochastic confinement time estimates have different dependencies for B_T and n_e. This should correspond to different predicted I_p scaling trends which can be compared to experimental data.

The expected I_p scaling relations for variations in B_T, n_e, and V_{LHI} at otherwise fixed parameters can be extracted for the various confinement models using the τ_E estimates provided

in Section 2.8. For simplicity, the power balance relation given by equation 2.36 can be simplified by assuming $P_{aux} = F_{RAD} = 0$ and $W_k \sim n_e T_e$ which yields

$$I_p V_{LHI} = \frac{n_e T_e}{\tau_E}. \tag{2.42}$$

Using Ohm's law and assuming Spitzer resistivity, T_e can be represented as a function of I_p and V_{LHI}:

$$T_e \sim \left(\frac{I_p}{V_{LHI}}\right)^{2/3}. \tag{2.43}$$

Equation 2.43 can be substituted into equation 2.42 along with the empirical tokamak confinement times presented in Section 2.8 for a LOC (τ_E^{neo-A}, equation 2.26) and SOC ($\tau_E^{ITER97Lth}$, equation 2.27) confinement scaling. This leads to the following relative I_p scalings:

$$\text{LOC: } I_p \sim B_T V_{LHI}^{5/3} \tag{2.44}$$

$$\text{SOC: } I_p \sim n_e^{1.1} V_{LHI}^{-1.7} B_T^{-0.1}. \tag{2.45}$$

The relations given by equations 2.44 and 2.45 also use $q \sim B_T / I_p$ and $P_L \sim I_p V_{LHI}$ which appear in the neo-Alcator and ITER97L empirical relations, respectively. The LOC scaling relation (equation 2.44) does not depend on n_e due to $\tau_E^{neo-A} \propto n_e$ but does linearly increase with B_T due to $\tau_E^{neo-A} \propto B_T$. In contrast, the SOC scaling relation (equation 2.45) has a much weaker B_T dependence as the ITER97L empirical scaling has a very weak B_T dependence ($\tau_E^{ITER97Lth} \propto B_T^{0.03}$). Additionally, the degradation of confinement with increasing input power in the SOC regime ($\tau_E^{ITER97Lth} \propto P_L^{-0.73}$) gives rise to the inverse relationship between I_p and V_{LHI}. This is notably inconsistent with the rather robust observation of I_p increasing with V_{LHI} that was presented in the preceding section.

This same approach can be applied to the relative τ_E scaling predicted by the collisional stochastic model described in Section 2.8.3. A power balance equation (2.37) was presented in Section 2.9 for this model which is repeated here for context:

$$\left(V_{LHI} I_p + P_{aux}\right)(1 - F_{RAD}) \sim \frac{n_e T_e {v_{th_e}}^2 \tau_{col} S^{-2\alpha}}{a^2}. \tag{2.46}$$

This equation can be simplified by once again assuming $P_{aux} = F_{RAD} = 0$ and using the relation for T_e given in equation 2.43. The relative I_p scalings of interest can be extracted from equation

2.46 by expressing $v_{th_e} \sim T_e^{1/2}$, $\tau_{col} \sim T_e^{3/2} n_e^{-1}$, and $S \sim T_e^{3/2} B_T n_e^{-1/2}$ which leads to the following relation[2]

$$I_p \sim V_{LHI}^{\frac{10/3-2\alpha}{4/3-2\alpha}} B_T^{\frac{2\alpha}{4/3-2\alpha}}. \quad (2.47)$$

Similar to the LOC scaling relation, this collisional stochastic scaling does not have any density dependence due to $\tau_{col} \sim n_e^{-1}$. This relation also indicates more favorable scalings are possible with higher values of α (i.e. stronger dependence of magnetic fluctuations on inverse Lundquist number). For the range of α that have been observed experimentally (MST [114]: $0.07 \leq \alpha \leq 0.18$), the I_p scaling with V_{LHI} is quite strong (V_{LHI} exponent:$\sim 2.7 - 3.1$). Further, there is a favorable B_T scaling, however, it is still quite weak for the typical range of α (B_T exponent:$\sim 0.1 - 0.4$).

At present, the scaling of magnetic fluctuations with Lundquist number or other parameters is not well-characterized for LHI discharges. Therefore, the forthcoming analysis will assume a conservative value of $\alpha = 0.07$ but more work is needed to provide more definitive conclusions or predictions of performance. Additionally, this stochastic scaling only provides relative variations and not absolute I_p estimates. As such, comparing the stochastic scaling to the tokamak confinement scalings (equations 2.44 and 2.45) may be misleading. For example, equation 2.47 predicts I_p to increase more strongly with V_{LHI} than either the LOC or SOC scaling relations. Still, the confinement will be improved in a tokamak-like confinement regime as opposed to a globally stochastic regime which would ultimately lead to improved performance.

Figure 2.20 shows estimates from the steady-state confinement model for the various candidate confinement scalings. These calculations assume $A = 1.2$, $R_0 = 0.4$ m, $\kappa = 2$, $M_{neo} = 2.4$, $Z_{eff} = 1$, $T_i/T_e = 2$, and $F_{RAD} = 10\%$. The plasma shape was chosen to be representative of a full-size LFS LHI discharge on Pegasus-III. For this plasma geometry, the normalized helicity input from the LFS system is limited to $V_{NORM} \lesssim 1.5$ V-m. The remaining parameters are similar to what has been assumed in previous work by Bodner et al. [30]. An input $P_{aux} = 300$ kW is assumed from auxiliary reconnection heating which predominantly heats the ions and has been

[2] The Lundquist number scaling given in this equation is derived by assuming Spitzer resistivity ($\eta \sim T_e^{-3/2}$) when calculating $\tau_R = a^2/\eta \sim T_e^{3/2}$ and $n_i \approx n_e$ when calculating $\tau_A = a/(B_T^2/\mu_0\rho_0)^{1/2} \sim n_e^{1/2}/B_T$.

previously estimated for LHI discharges on Pegasus from impurity ion spectroscopy measurements [53].The P_{aux} is assumed to be constant because I_{inj} and V_{inj} are fixed across the B_T and n_e scans ($P_{aux} \propto I_{inj}V_{inj}^{1/2}$). Within this simple model, the relative partitioning of the total heating power to the ion and electron populations is set by the assumed T_i/T_e ratio. Previous LHI studies have typically observed $T_i/T_e \geq 1$ [11,53]. This simple partitioning of the heating power couples this auxiliary input heating, which is predominantly deposited in the ion population, to the electron population. This can allow for this ion heating source to alter the predicted plasma resistance and I_p via T_e.

With these assumptions, the steady-state confinement model was used to estimate the I_p scaling as a function of B_{T0}, $\langle n_e \rangle$, and V_{NORM} throughout the operating space accessible on Pegasus-III. These estimates are shown in Figure 2.20. The relative stochastic I_p scalings have been normalized to the neo-Alcator estimate which is indicated by the gold dot in each plot to compare the trends more easily to the standard tokamak confinement scalings.

Figure 2.20(a) shows steady-state I_p calculated by the steady-state confinement model as a function of B_{T0} over the toroidal field accessible in Pegasus-III. These calculations assume$V_{NORM} = 0.75$ V − m and $\langle n_e \rangle = 1 \times 10^{19}$ m^{-3} which is comparable to densities that have been achieved in previous LHI discharges on Pegasus [92]. These estimates follow the expected

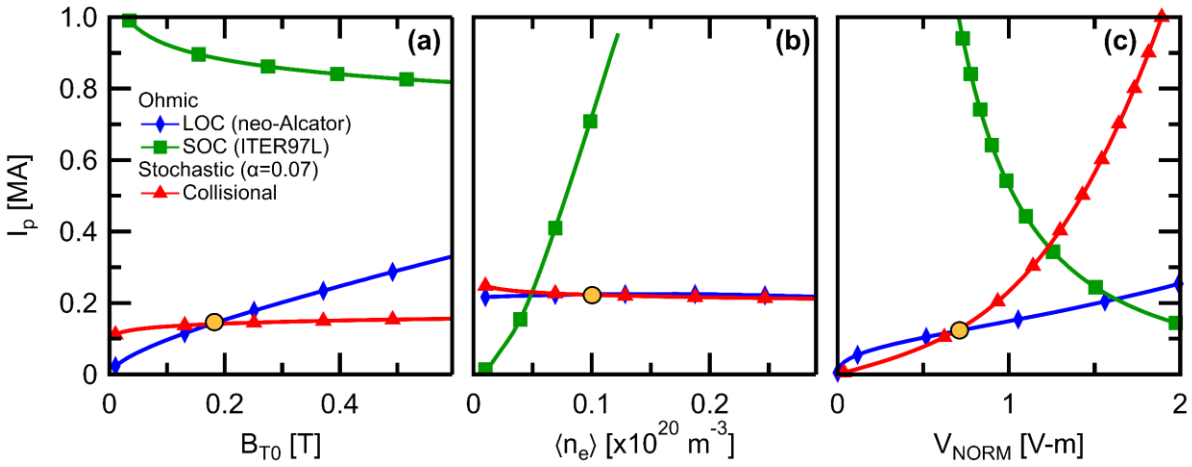

Figure 2.20: Pegasus-III steady-state I_p estimates as a function of (a) B_{T0} at (b) $\langle n_e \rangle$ and (c) V_{NORM} for different assumed confinement scalings at otherwise fixed parameters. The gold circlerepresents the normalization point for the relative stochastic scaling.

scaling behavior derived earlier in this section. Namely, the LOC scaling predicts I_p to linearly increase with B_T whereas the SOC and stochastic scalings are rather insensitive to B_T variations.

Figure 2.20(b) shows I_p scaling estimates as a function of $\langle n_e \rangle$ for the same selection of assumed confinement scalings. These calculations also assume $V_{NORM} = 0.75\ \mathrm{V-m}$ as well as $B_{T0} = 0.3\ \mathrm{T}$. Again, the model estimates demonstrate the scaling behavior derived earlier in this section. Namely, The SOC confinement scaling predicts a nearly linear increase in I_p with $\langle n_e \rangle$ whereas both the LOC and stochastic models do not show any $\langle n_e \rangle$ dependence.

Figure 2.20(c) shows I_p scaling estimates as a function of V_{NORM} while assuming $B_{T0} = 0.3\ \mathrm{T}$ and $\langle n_e \rangle = 1 \times 10^{19}\ \mathrm{m}^{-3}$. Previous HFS LHI experiments on Pegasus which were described in the preceeding section found that I_p increasedlinearly with V_{NORM} [46,92]. These experimental observations are consistent with both the LOC and stochastic scalings which exhibit I_p increasing with V_{NORM}. Further, these are inconsistent with the SOC scaling model which predicts I_p to decrease as V_{NORM} is increased. Still, it is worthwhile to consider the SOC as the previous work on Pegasus was limited to a narrow operating space. Therefore, it is possible that the behavior of LHI confinement may change as the operating space is expanded in Pegasus-III.

Table 1 summarizes the expected I_p and $\langle T_e \rangle$ scaling trends if any one of the confinement scalings are relevant for describing LHI. This table illustrates that each confinement scaling has a unique combination of qualitative dependencies on V_{NORM}, B_T, n_e. This suggests a discrete set of experimental scans can be used to assess if any one of these confinement scalings is consistent with the observed LHI I_p and T_e scaling. These qualitative trends will be compared to experimental observations presented in Chapter 6 to determine if any of these confinement scalings are useful for characterizing the observed I_p and T_e trends during LHI discharges.

	I_p and $\langle T_e \rangle$ trends for increasing		
Confinement Scaling Estimate	**V_{NORM}**	**B_T**	**n_e**
LOC	↑	↑	—
SOC	↓	—	↑
Collisional stochastic	↑	—	—

Table 1: Summary of qualitative I_p and $\langle T_e \rangle$ scaling trends for various assumed confinement scaling estimates

2.12 Exploring the Scaling Properties of LHI on Pegasus-III

The previous sections introduced the LHI technique and raised several outstanding physics issues that must be addressed to reliably project LHI performance to MA-class devices. First, the physics basis for LHI has been limited to the low toroidal field of Pegasus. Second, an understanding of the T_e scaling in LHI plasmas is needed to inform helicity dissipation predictions in different operating regimes. At present, this is limited to assessing the relevance of using global confinement estimates for describing LHI performance. Third, predictive models for LHI performance must be developed and validated. This thesis work advances these areas through a combination of model development and experimental campaigns. These efforts are focused on the following topics:

1. Assess the expected Taylor limit scaling in the expanded Pegasus-III operating space.
    a. Does increasing I_{TL} lead to more effective utilization of the helicity input and higher I_p as predicted by the 0-D power balance model?
    b. Does the expected $I_{TL} \propto \sqrt{B_T I_{inj}}$ scaling continue to hold at increased B_T and I_{inj}?
    c. Can injector design be leveraged to directly alter I_{TL} via w_{inj}?
    d. How do LHI discharges behave when provided excess helicity input at $I_p = I_{TL}$?
2. Continued development of the 0-D power balance model.
    a. Does extending the 0-D power balance model to include a self-consistent $T_e(t)$ via global confinement τ_E scalings provide a useful tool for analyzing discharges developed on Pegasus or Pegasus-III?
    b. Are the $I_p(t)$ and $T_e(t)$ predicted by the 0-D power balance model for any of the candidate global confinement scalings consistent with experimental observations during LHI?
3. Characterize the scaling of I_p and T_e with B_T and n_e during LHI.

a. Are the observed trends consistent with any candidate global confinement estimates?

b. Can the observed trends distinguish between the candidate global confinement scaling models?

To address these topics, this thesis work leverages the expanded operating space and enhanced LHI system on Pegasus-III which will be discussed in the next chapter. Chapter 4 provides an overview of code development undertaken throughout this work to improve preexisting global power balance and fast boundary reconstruction codes. These codes are used extensively in the analysis of the experimental campaigns described in Chapter 5 and Chapter 6 to explore the questions enumerated above.

Chapter 3
The Pegasus-III Toroidal Experiment

Pegasus is an ultralow aspect ratio spherical tokamak [146]. Over the course of this work, a major facility upgrade was completed to improve the capabilities in the third phase of its operation, also referred to as Pegasus-III [31]. This upgrade is accompanied with a shift in the program research focus. Its mission will be to compare, contrast, and combine promising solenoid-free plasma startup techniques on a dedicated experiment. This will initially be enabled by installation of a next generation LHI system, novel CHI electrodes, and an EBW heating and current drive system. This thesis work focuses solely on advancing LHI. This chapter will introduce the Pegasus-III facility, the LHI system, and diagnostics relevant for this work. Further details on the facility are provided in publications describing the electromechanical design of the TF assembly [31], digitally-controlled power systems [147], CHI system [148], and diagnostic suite [149,150].

3.1 The Pegasus-III Machine

A side-by-side comparison of the previous Pegasus facility and the upgraded Pegasus-III facility is shown in Figure 3.1. Additionally, Table 2 compares operational parameters of the two facilities. The centerpiece of the upgrade is a slightly larger solenoid-free center stack assembly, which includes a new 24-turn toroidal field electromagnet. Along with enhanced mechanical support, this new magnet enables an increase in B_T up to 0.6 T at a typical magnetic axis of $R_0 = 0.39$ m. To

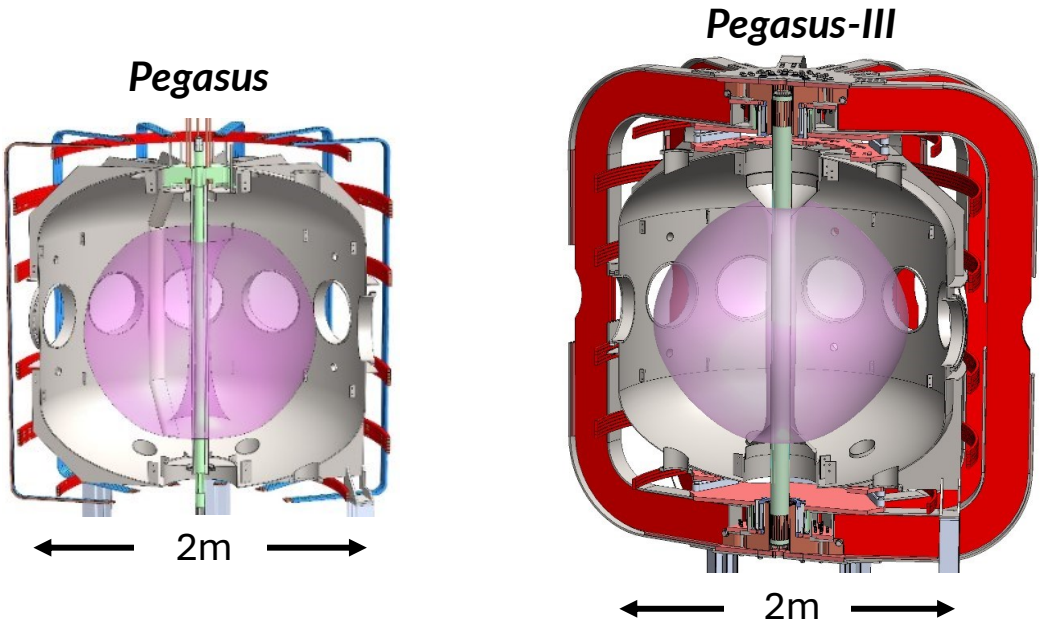

Figure 3.1: Comparison of Pegasus and upgraded Pegasus-III facility.

accommodate the larger center-stack assembly, a new inner vacuum wall was installed that extends the inner plasma boundary slightly from 5.5 to 7 cm. This modest increase in the inner plasma boundary still retains access to the ultra-low A operating space ($A \geq 1.22$). The PF coils primarily responsible for maintaining force balance were unchanged and can support plasmas with $I_p \leq$ 0.3 MA. A new divertor coil assembly was also designed and installed. The design and requirements of this new assembly was primarily driven by requirements of the planned CHI system [148]. However, these new divertor coils were not used to develop the discharges studied in this work.

An expansion of the stored energy driving the magnetic coil sets enables pulse lengths up to 100 ms. The coils are driven by IGBT (Integrated Gate Bipolar Transistor) switching power supplies with digital pulse width modulation (PWM) controllers [147].

The fueling and pumping systems were largely unchanged. The deuterium working gas is supplied by PV-10 piezoelectric valves located on the LFS and HFS of the machine as well as dedicated valves for each LHI injector. Typical base pressures of 10^{-9}– 10^{-8} Torr are achieved using a turbomolecular pump, a cryogenic pump, and titanium gettering wall conditioning.

Parameter	Pegasus	Pegasus-III
$\boldsymbol{\Psi_{solenoid}}$ [mWb]	40	0
$\boldsymbol{I_{TF}}$ [MA]	0.288	1.15
TF turns	12	24
$\boldsymbol{R_{inner}}$ [cm]	5.5	7.0
Max $\boldsymbol{B_T}$ on axis [T]	0.15	0.60
$\boldsymbol{B_T}$ flattop [ms]	25	50-100
$\boldsymbol{A}$	1.15	1.22

Table 2: Comparison of Pegasus and Pegasus-III operational parameters

3.2 LHI System

Pegasus-III utilizes washer-stack plasma sources located on the low-field side of the device for LHI operations [23]. The LFS LHI configuration was chosen because of its more attractive properties for scaling to larger, higher field devices. First, the outboard midplane is more conducive to the design of a retractable, port-mounted structure that could be removed after plasma startup. Second, the increased Taylor limit early in the LFS discharge evolution provides an attractive path to high current startup on higher field devices. On the contrary, the HFS operating space is more restricted at higher B_T because of competing requirements for injector stream clearance and initial tokamak relaxation [23].

Figure 3.2 shows a cross-section of the washer-stack stabilized arc sources that were installed for initial Pegasus-III operations and used throughout this work. The figure also includes simplified arc and bias circuits. First, a voltage (V_{arc}) is applied across the arc cathode and injector aperture which acts as the arc anode. Then deuterium gas is fed into the arc tube and ionized to establish an arc discharge current (I_{arc}). A bias voltage (V_{inj}) is then applied between the injector aperture (bias cathode) and the vacuum vessel to extract electrons and inject current (I_{inj}) along magnetic field lines.

The injector structure shown in Figure 3.2 is a result of a source development campaign on Pegasus to mitigate against harmful plasma-material interactions (PMI) [23,46,151]. The conical shaped tungsten frustum mitigates erosion of the insulators from high-power unipolar arcs, known as cathode spots. The molybdenum frustum shield further mitigates cathode spot formation by

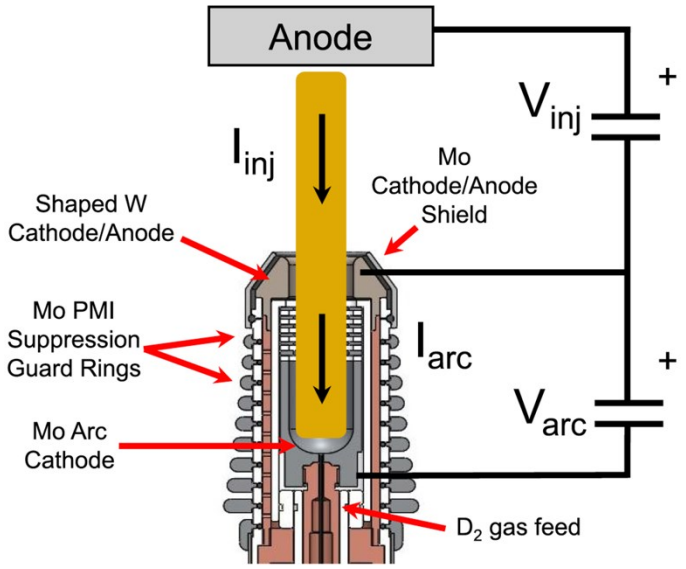

Figure 3.2: Cross-section and circuit schematic of an LHI injector. Taken from [23]

reducing the local plasma density. The floating molybdenum shield rings protect against arc-back currents to nearby limiter surfaces. These technological advances have increased the longevity of the plasma sources and achieved bias voltages up to power supply limits ($V_{inj} < 2$ kV) [23].

The LFS LHI system on Pegasus-III consists of two two-injector arrays of 4 cm^2 circular aperture injectors. The two arrays are located just below the outboard midplane and toroidally separated by 180°. Each injector is capable of supplying 4 kA of current at bias voltages greater than 1 kV. This power is supplied to each injector by independent arc and bias circuits. These circuits maintain a pre-programmed current waveform through active feedback control via digital PWM.

The power supply configuration for the LHI system is described in detail in [147] and is schematically shown in Figure 3.3. Each injector has its own dedicated arc and bias power supply which are controlled independently. The arc current is provided by a two-quadrant IGBT H-bridge driven by a 900 V capacitor bank. The bias current is supplied by a multi-level Buck converter (MLBC) power supply which is comprised of a two-quadrant IGBT H-bridge in series with a two-quadrant IGCT H-bridge. The IGCT bridge provides a maximum DC voltage of 1.8 kV. The IGBT can then modulate this DC level on sub-ms timescales by the bank voltage $\pm V_{IGBT}$ (max $V_{IGBT} =$ 900 V) by PWM control. The RCD clamp serves to damp voltage transients and provide a more smoothly varying V_{inj} to the injector. The crowbar uses a silicon-controlled rectifier (SCR) to

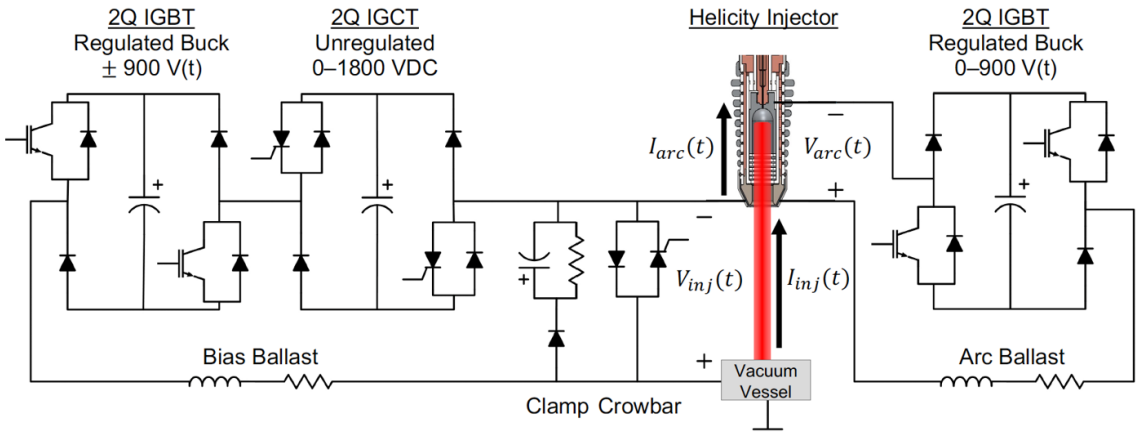

Figure 3.3: Schematic of Pegasus-III LHI power supply: multi-level buck converter bias power supply (left), protection circuits (center) and arc power supply (right) configured for LHI operation. Taken from [147].

divert power away from the injector at the pre-programmed discharge termination or in a fault scenario. The bias and arc currents are stabilized by a series ballast resistance and inductance.

Each of the injector circuits are outfitted with several diagnostics to monitor performance. High voltage Picoscope TA057 differential probes measure voltage and current for the arc (V_{arc}, I_{arc}) and bias (V_{inj}, I_{inj}) circuits for each injector. These probes are digitized by a Picoscope 5442D oscilloscope. This enables high-frequency voltage and current measurements (up to 25 MHz) over the entire pulse duration.

3.3 Diagnostic Capabilities

The Pegasus-III facility features an expanded set of diagnostics to assess the physics of LHI discharges. This section summarizes the diagnostics that are utilized throughout this work which includes various magnetic and optical diagnostics. The magnetic diagnostics were also used extensively for various analysis techniques throughout this work. This section provides an overview of two such techniques: magnetic equilibrium reconstruction analysis with the KFIT code and power spectral density analysis.

3.3.1 Optical Diagnostics

Numerous optical diagnostics will be deployed on Pegasus-III to visualize the plasmas as well as quantify their temperature, density, impurity content, and radiated power. This section provides a brief survey of the diagnostics relevant to this work.

A multi-point Thomson scattering (MPTS) system provides single-time point measurements of $n_e(R)$ and $T_e(R)$ at 24 radial locations spanning $R = 15 - 85$ cm on the vessel midplane [92,152,153]. The system is capable of measuring T_e from 10 to 1000 eV and n_e from 0.1 to 5×10^{19} m^{-3} [153]. Multi-shot averaging over repeated plasma shots is used to achieve typical error around $\sim 5 - 10$ eV and $\sim 1 - 3 \times 10^{18}$ m^{-3} [92]. The time evolution of the T_e and n_e profiles can be obtained by shifting the sampling time over repeat discharges.

A microwave interferometer system (MIF) provides time-resolved measurements of line-integrated n_e along a single viewing chord. This system is similar to what is described in [154]. However, the system on Pegasus uses a zero-bias microwave power detector rather than a mixer diode and has an altered beam path [155]. For Pegasus-III, a new 5 cm interferometer mirror has been incorporated into the design of the core armor assembly [149].

To identify the primary impurity ions, a SPRED spectrometer is deployed which provides time-resolved measurements of line radiation emitted from the plasma [150]. The imaging system collects data at a rate of 1.25 kHz enabling several spectra to be collected over the short-pulse ($t \lesssim 10$ ms) Pegasus-III discharges in this work. The installed grating covers a spectral region from $\sim 10 - 110$ nm with a ~ 0.33 nm wavelength resolution.

An absolute extreme ultra-violet (AXUV) photodiode array provides an estimate of the total radiated power with temporal and spatial resolution [150]. Due to variations in the diode sensitivity across the photon energy spectrum, the P_{rad} inferred from the array can be underestimated. Still, these diodes were chosen over traditional foil bolometers because of the enhanced time response to resolve the short-pulse Pegasus-III discharges and their compact size enabled the design of a multichannel array with high spatial resolution. The 32-channel array has viewing chords that cover most of the plasma volume ($R = 12 - 90$ cm) with a ~ 3 cm spatial resolution along the machine midplane ($Z = 0$). The processing electronics provide an effective bandwidth of 60 kHz, however a $5 - 10$ kHz low-pass filter is typically applied during data processing to remove high-frequency oscillations. The emissivity profiles are obtained through Abel inversion of the viewing chords using the onion-peeling algorithm.

A high-speed Phantom 12 visible camera images the entire plasma volume through a fisheye lens. These images are used for observing injector stream dynamics, PMI throughout the vessel, and provide estimates of the plasma shape and position.

3.3.2 Magnetic Diagnostics

The Pegasus-III machine magnetic diagnostic array consists of various magnetic pickup coils and flux loops mounted around the vacuum vessel. The details of the Pegasus-III magnetic diagnostic suite is discussed in greater detail in [149]. The physical location of these measurements is shown in Figure 3.4.

The magnetic pickup coils measure the local $\dot{B}$ around the vacuum vessel. These coils are used to gather information about the magnetic fluctuation activity around the vessel as well as provide constraints to equilibrium reconstructions. These coils are distributed around the vessel in various toroidal and poloidal arrays.

There are two toroidal arrays of pickup coils (green diamonds in Figure 3.4) which measure $\dot{B}_Z$ at the HFS machine midplane and just below the LFS midplane ($Z \approx -15$ cm). The LFS and HFS arrays each contain six sensors which are non-uniformly toroidally spaced to enable mode identification up to $n = 12$ and 10, respectively.

There are also two poloidal arrays of pickup coils (blue squares in Figure 3.4) which measure the poloidal field around the plasma boundary. One array has 21 coils distributed vertically along the central column which are oriented to measure $\dot{B}_Z$. The other array has 13 coils distributed along

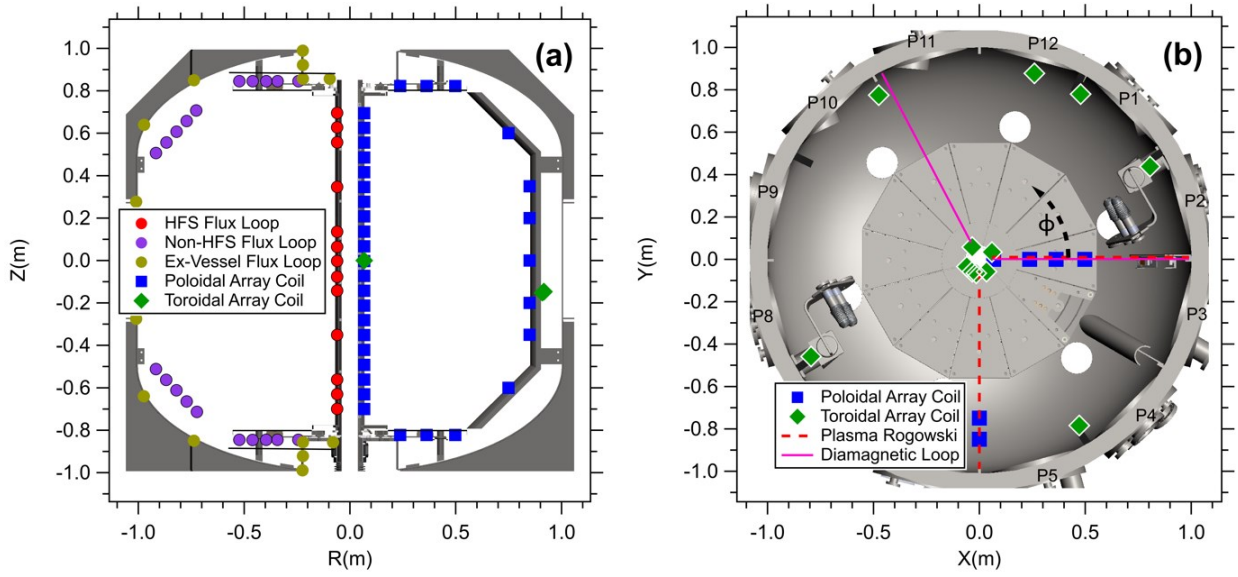

Figure 3.4: Pegasus-III magnetic diagnostic layout: (a) side view and (b) top-down view. Adapted from [82].

the LFS boundary and on the upper and lower divertor regions. These coils are oriented to measure various components of $\dot{B}_p$ depending on their position.

There are several arrays of magnetic flux loops distributed inside and outside the vacuum vessel. These flux loops measure the large-scale B_z evolution and provide constraints for equilibrium reconstructions. Each flux loop is comprised of a single-turn toroidal loop and produces a signal proportional to the total magnetic flux normal to the enclosed loop area. These coils are oriented such that B_z is normal to the loop area.

One set of 13 flux loops is distributed vertically on the central column (HFS Flux Loop, red circles in Figure 3.4). The uneven vertical spacing was chosen to increase the sensitivity to changes in the plasma shape for constraining equilibrium reconstructions.

Another set of 20 flux loops is distributed on the top, bottom, and LFS regions of the machine (Non-HFS Flux Loop, purple circles in Figure 3.4).

The final set of 16 flux loops are external to the vacuum vessel (Ex-Vessel Flux Loop, gold circles in Figure 3.4). These are distributed along the LFS vessel wall and are important for constraining the wall currents induced in the conducting vacuum vessel for equilibrium reconstructions.

There are two plasma Rogowski coils which measure the total toroidal plasma current throughout the discharge. These Rogowski coils follow the contour of the vacuum vessel and are aligned to the poloidal plane ($\hat{n} \parallel \hat{\phi}$). They are located at two different toroidal angles which are indicated by the dashed red lines in Figure 3.4(b). The toroidal separation is meant to provide additional information on any toroidal asymmetries that are present. These may be expected to exist during LHI due to the presence of the injected open field line currents.

There are also three flux loops oriented to measure the toroidal magnetic flux (i.e. diamagnetic loop). Like the Rogowski coils, these flux loops follow the contour of the vacuum vessel and are also aligned to the poloidal plane ($\hat{n} \parallel \hat{\phi}$). These loops are also distributed toroidally around the machine as indicated by the solid pink lines in Figure 3.4(b). Two of these diamagnetic loops are co-located with the plasma Rogowski coil nominally located at $\phi = 0$. The other diamagnetic loop is again toroidally separated to provide additional information on any toroidal asymmetries that are present. These diamagnetic loops can provide valuable constraints on the total plasma stored energy during equilibrium reconstruction.

3.3.3 KFIT Equilibrium Reconstruction Code

MHD equilibrium reconstruction analysis is a standard technique used to determine various properties of a toroidal plasma. In axisymmetric toroidal systems, this process identifies a solution to the Grad-Shafranov equation (1.8) that best matches the available magnetic diagnostics subject to a set of boundary conditions. The KFIT Grad-Shafranov solver [156,157] is used for generating equilibria and performing reconstruction analysis on Pegasus.

The KFIT code is separated into two discrete parts: a free boundary Grad-Shafranov equilibrium solver and a Levenberg-Marquadt χ^2 minimizer. The inputs to the Grad- Shafranov solver module are I_p, $p' = dp(\Psi)/d\Psi$, $GG'(R) = G(R)(dG(R)/d\Psi)$, currents from external magnetic field coils and induced in the conducting vessel wall, and an initial guess for the plasma shaping. A filament model is used to estimate the significant wall currents induced during the discharge [156,157]. The p' and GG' profiles are typically parameterized with n_p-order polynomial functions of the form:

$$f(\psi_N) = f_0 + \sum_{i=1}^{n_p} f_i\left(\psi_N^{i-1} - \psi_N^{n_p}\right) \tag{3.1}$$

for $0 \leq \psi_N \leq 1$ where ψ_N is the normalized poloidal flux:

$$\psi_N = \frac{\Psi - \Psi_0}{\Psi_{LCFS} - \Psi_0} \tag{3.2}$$

with Ψ_0 and Ψ_{LCFS} being the poloidal flux at the magnetic axis and last-closed-flux-surface (LCFS), respectively. The coefficients f_i are free parameters that are varied throughout the fitting process.

The solution to the Grad-Shafranov equation is computed on a 2D (R, Z) solution grid for a single time point using PDE relaxation methods. After these methods converge, the code returns self-consistent solutions for the poloidal flux, toroidal current density, and magnetic field. From these, a variety of equilibrium properties are derived, including: I_p, LCFS shaping moments (R_0, Z_0, a, κ, δ), magnetic stored energy W_m, kinetic stored energy W_k, normalized internal inductance ℓ_i, poloidal beta β_p, and safety factor profile $q(\psi_N)$.The Grad-Shafranov equilibrium solver module can be used independently to generate model equilibria in the Pegasus geometry and operating regime.

For reconstruction analysis, the Grad-Shafranov solver is coupled to a Levenburg-Marquadt minimization algorithm provided by the proprietary programming language of Igor Pro. Reconstruction analysis seeks to identify the Grad-Shafranov solution that best matches the available measurements. The χ^2 figure-of-merit is minimized to determine the best fit to the available measurement in a least squares sense. χ^2 is computed for each trial solution and is defined as

$$\chi^2 = \sum_{i=1}^{N_{meas}} \left(\frac{M_i - \hat{M}_i}{\sigma_i}\right)^2 \tag{3.3}$$

where the summation is performed over all N_{meas} measurements M_i with uncertainty σ_i and $\hat{M}_i$ is the synthetic measurement derived from the trial equilibrium solution. In practice, the set of measurement constraints is comprised of the available magnetic flux loops, pickup coils, diamagnetic loop, and plasma Rogowski coil.

This reconstruction process is repeated several times throughout the discharge if time-resolved equilibrium analysis is desired. At each time point, the Pegasus wall model is utilized to update the coil currents and the corresponding estimates of the induced wall currents [156,158]. Depending on the desired time step, these currents and the associated equilibrium solution may be a suitable initial guess for the subsequent time point if they are not expected to change significantly on that timescale. Additionally, the measurement constraints are updated to reflect the diagnostic signals at the desired time.

Functionally, this process can be repeated for the entirety of the discharge. In practice, performing reconstructions when the plasma current is comparable or smaller than the total amount of induced wall currents has proved troublesome [156,158]. This is typically most relevant for early in Pegasus discharges as the I_p is ramping up and the induced wall currents have not had sufficient time to decay away.

3.3.4 Power Spectral Density Analysis

The magnetic diagnostic suite, particularly the $\dot{B}$ coils, also provides information on the magnetic fluctuation activity. The interpretation of these fluctuation quantities is aided by the use of well-established power spectral density (PSD) analysis techniques to extract information from noisy and/or complex time-dependent signals [159].

This work primarily used the cross-power P_{xy}, cross-phase θ_{xy}, and coherence γ_{xy}^2 functions to aid in the interpretation of the fluctuating quantities in the frequency domain. For two time-dependent signals $x(t)$ and $y(t)$, these quantities are computed from the complex cross-spectral density function defined as

$$G_{xy}(f) = \frac{2}{NT}\sum_{k=1}^{N} X_k^*(f,T)Y_k(f,T) \tag{3.4}$$

where $X_k(f,T)$ and $Y_k(f,T)$ are the finite Fourier transforms of $x(t)$ and $y(t)$, respectively, where the signals have been segmented into N equally spaced sections of length T [159]. The cross-power and cross-phase functions are then defined as:

$$P_{xy}(f) = \left|G_{xy}(f)\right| = \sqrt{G_{xy}^*(f)\cdot G_{xy}(f)} \tag{3.5}$$

$$\theta_{xy}(f) = \tan^{-1}\left[\frac{\mathrm{Im}[\hat{G}_{xy}(f)]}{\mathrm{Re}[\hat{G}_{xy}(f)]}\right] \tag{3.6}$$

where $\mathrm{Im}\left[G_{xy}(f)\right]$ and $\mathrm{Re}\left[G_{xy}(f)\right]$ functions refer to the imaginary and real components of the complex G_{xy} quantity, respectively. The coherence of the signals is defined as

$$\gamma_{xy}^2(f) = \frac{\left|G_{xy}(f)\right|^2}{G_{xx}(f)G_{yy}(f)}. \tag{3.7}$$

Coherence is a normalized quantity which represents how well-correlated the two input signals are to each other with $\gamma_{xy}^2 = 1$ representing perfect correlation and $\gamma_{xy}^2 = 0$ completely uncorrelated.

The cross-phase quantity is also used in the determination of the toroidal and poloidal mode number of instabilities through the "phase-slope" method. The magnetic perturbation $\tilde{b}$ takes the following form:

$$\tilde{b} \sim e^{i(m\theta + n\phi - 2\pi f t)} \tag{3.8}$$

where m and n are the poloidal and toroidal mode numbers, respectively. Under appropriate symmetry, these mode numbers can be inferred from sets of $\dot{B}$ sensors located in a plane with varying physical angles. In this work, the n is determined by comparing the cross-phase between sensors located at constant R, Z in the machine but varying toroidal location ϕ_{phys}. The analysis is performed by plotting θ_{xy} vs ϕ_{phys} for each sensor in the array and identifying the best-fit linear, integer slope to the data. This integer slope is the n for the instability at the frequency of interest. In a high-A, circular cross-section tokamak, m can be identified in a similar manner. However, in

highly-shaped, low-A tokamaks alternative techniques and/or corrections to the sensor poloidal location are required for m-determination [158].

Chapter 4
Advancing Analysis Capabilities for LHI Plasmas

Chapter 2 provided an overview of the local helicity injection technique and some available tools for projecting performance to larger devices. Continued improvements to these tools are required to improve the understanding of LHI plasmas and enable reliable projections to larger facilities. To this end, this chapter outlines code development and validation that was performed throughout this work.

4.1 Extended 0-D Power Balance Model

Reliable projections for LHI performance rely on understanding how the helicity dissipation scales to other devices and operating regimes. The 0-D power balance model is very sensitive to the assumed resistive dissipation as discussed in Section 2.6. Global confinement scaling models are being explored as a potential approach to estimate the dissipation during LHI discharges. Initial work outlined in Section 2.10 showed that such an approach may be useful to describe the experimentally observed I_p scaling. Further, Section 2.11 outlined qualitative I_p and T_e scaling trends for different assumed models using a simple steady-state confinement model. However,

typical high-performance LFS LHI discharges are dynamic scenarios which have significant inductive effects and are ill-described by a steady-state model.

This motivates extending the 0-D power balance model to incorporate global confinement estimates. Such an extension provides a tool for assessing how well global confinement models describe LHI plasmas. If a suitable global confinement model is identified, then it would enable more reliable projections of LHI performance.

4.1.1 Derivation of Extended Model

The original development of the 0-D power balance model was discussed at length in Section 2.5 with more detail found in [29,87]. This circuit model is summarized by the balance of various system voltages shown in equation 2.15 which is repeated here for convenience

$$V_{OH} + V_{PF} + V_{Le} + V_{Li} + V_{RTT} + V_{LHI} - V_R = 0 \tag{4.1}$$

where the inductive voltages from PF induction, external self-inductance, internal inductance, and a net surface voltage arising from the application of Reynolds' transport theorem [160,161] for a time-changing plasma boundary are computed by

$$V_{PF} = -\frac{\partial}{\partial t}(\pi R_0^2 B_V M_V) \tag{4.2}$$

$$V_{Le} = -L_e \frac{\partial I_p}{\partial t} - I_p \frac{\partial L_e}{\partial t} \tag{4.3}$$

$$V_{Li} = -L_i \frac{\partial I_p}{\partial t} - \frac{I_p}{2} \frac{\partial L_i}{\partial t} \tag{4.4}$$

$$V_{RTT} = \oiint_{S_p} \frac{B_p^2}{2\mu_0} \vec{v}_b \cdot \hat{n} dA \tag{4.5}$$

where B_V and M_V are the uniform vertical field required for force balance and a mutual inductance-like parameter. L_e is the plasma external self-inductance which accounts for the plasma current's own contribution to the plasma boundary surface flux. L_i is the plasma internal inductance which is related to the stored internal magnetic energy $W_m = L_i I_p^2/2$. The net surface voltage arising from the Reynolds' transport theorem V_{RTT} is computed via the surface integral over the plasma boundary S_p which is moving with a local velocity $\vec{v}_b$. The B_p on this surface is computed using an analytic finite-A approximation derived by Miller et al. [162]. The model computes these quantities by using analytic formulae which have been calibrated to be suitable for the low-A

Pegasus operating space [29,87]. With these definitions, equation 4.1 can be recast into a first-order ODE for $I_p(t)$:

$$\frac{dI_p}{dt} = -\frac{\frac{1}{2}\frac{dL_i}{dt} + \frac{dL_e}{dt} + \left(\frac{\langle \eta_p \rangle 2\pi R_0}{A_p}\right) + \frac{d}{dt}\left[\pi R_0^2 \left(\frac{B_V}{I_p}\right) M_V\right] - \frac{V_{RTT}}{I_p}}{\pi R_0^2 \left(\frac{B_V}{I_p}\right) M_V + L_i + L_e} I_p + \frac{V_{OH} + V_{LHI}}{\pi R_0^2 \left(\frac{B_V}{I_p}\right) M_V + L_i + L_e} \tag{4.6}$$

The previous implementation of the 0-D model numerical solves equation 4.6 using a Runge-Kutte algorithm provided in the Igor Pro software package from WaveMetrics, Inc. It also strictly enforces the global Taylor limit throughout the solution process using the following formulation:

$$I_P \leq I_{TL} \approx \sqrt{\frac{\Psi}{(B_{pol,inj}/I_p)} \frac{I_{inj}}{2\pi R_{edge} w_{inj}}}. \tag{4.7}$$

This limit is implemented by artificially enforcing $\frac{dI_p}{dt} \leq 0$ when at $I_p = I_{TL}$. The initial condition on I_{p0} is taken to be equal to the calculated I_{TL} at the beginning of the time of interest. For interpretative analysis, it can also be set to the measured I_p at the point when the calculation is chosen to begin.

As discussed in Sections 2.5 and 2.6, the predictive capability of this model is limited because of the uncertainty on the dissipation term. Functionally, the plasma resistivity is assumed to be constant throughout the discharge and treated as a free parameter during interpretative analysis to best match the experimental $I_p(t)$ within reasonable bounds. However, reliable projections require a suitable model to estimate this dissipation throughout the discharge. Assuming resistive dissipation $\eta \propto T_e^{-3/2}$, incorporating a self-consistent $T_e(t)$ evolution into the model could dramatically improve the dissipation estimates. Such information can be added to this global model by providing additional information on the stored kinetic energy.

This can be done by adding an additional equation into the system which describes the evolution of the total stored kinetic energy. The time rate of change of the plasma stored kinetic energy depends on the balance of total heating power with anomalous transport and radiation losses:

$$\frac{d}{dt}[W_k] = I_p^2 R_p + P_{aux} - P_{rad} - \frac{W_k}{\tau_E}. \tag{4.8}$$

The stored kinetic energy is calculated by the following volume integral

$$W_k = \int \frac{3k_B}{2}(n_e T_e + n_i T_i) dV \tag{4.9}$$

where n_i and T_i are the ion density and temperature, respectively. This integral can be recast into the following form:

$$W_k = \frac{3k_B}{2} V_p (\langle n_e \rangle \langle T_e \rangle_n + \langle n_i \rangle \langle T_i \rangle_n) \tag{4.10}$$

where V_p is the plasma volume, $\langle T_e \rangle_n$ and $\langle T_i \rangle_n$ are the density-weighted volume-averaged electron and ion temperatures which are defined to be

$$\langle T_{e,i} \rangle_n \equiv \frac{\langle n_{e,i} T_{e,i} \rangle}{\langle n_{e,i} \rangle} = \frac{\iiint n_{e,i} T_{e,i} dVol}{\iiint n_{e,i} dVol} \tag{4.11}$$

This can be further simplified by assuming the ion and electron density profiles have identical shape $\hat{n}$ and differ by a fixed n_i/n_e ratio determined by quasi-neutrality. Another simplifying assumption is that T_i and T_e profiles have identical profile shape $\hat{T}$ and only differ by a fixed T_i/T_e ratio such that

$$T_e = T_{e0} \hat{T} \tag{4.12}$$

$$T_e = T_{i0} \hat{T} = T_{e0} \frac{T_i}{T_e} \hat{T} \tag{4.13}$$

which leads to the following simplified form of the stored kinetic energy:

$$W_k = \frac{3k_B}{2} V_p \langle n_e \rangle \langle T_e \rangle_n \left(1 + \frac{n_i}{n_e} \frac{T_i}{T_e}\right). \tag{4.14}$$

Plugging this relation and the other previously defined quantities into the power balance relation in (4.8) and re-arranging yields the following first-order ODE for $\langle T_e \rangle_n$

$$\frac{d(\langle T_e \rangle_n)}{dt} = \frac{2}{3k_B G} \left[P_{aux} - P_{rad} + I_p^2 R_p - \frac{3k_B}{2} \langle T_e \rangle_n \left(\frac{G}{\tau_E} + \frac{dG}{dt} \right) \right]. \tag{4.15}$$

where $G \equiv \langle n_e \rangle V_p [1 + (n_i T_i / n_e T_e)]$ is a grouping of parameters defined for simplicity. This can be expressed in terms of T_{e0} instead of $\langle T_e \rangle_n$ by applying the chain rule in the following way

$$\frac{d(\langle T_e \rangle_n)}{dt} = \frac{d}{dt} \left[\frac{n_{e0} T_{e0} \iiint \hat{n} \hat{T} dVol}{\langle n_e \rangle} \right] = \frac{d}{dt} [C T_{e0}] = \frac{dT_{e0}}{dt} C + T_{e0} \frac{dC}{dt} \tag{4.16}$$

where $C \equiv \left(n_{e0} \iiint \hat{n} \hat{T} dVol \right) / \langle n_e \rangle$ is again defined for convenience. Finally, equation 4.15 can then be recast as

$$\frac{dT_{e0}}{dt} = \frac{2}{3k_B G C} \left[P_{aux} - P_{rad} + I_p^2 R_p \right] - T_{e,0} \left[\frac{1}{\tau_E} + \frac{1}{G} \frac{dG}{dt} + \frac{1}{C} \frac{dC}{dt} \right]. \tag{4.17}$$

Equations 4.6 and 4.17 form a coupled set of first-order ODEs that can be solved numerically which provide a self-consistent solution for $I_p(t)$ and $T_{e0}(t)$. These ODEs along with the Taylor limit constraint given by equation 4.7 comprise the extended 0-D power balance model. This extended model uses the same inputs as the previous model implementation, which includes: plasma shape evolution ($R_0(t)$, $a(t)$, $\kappa(t)$, and $\delta(t)$), normalized internal inductance $\ell_i(t)$, toroidal field $B_T(t)$, ohmic loop voltage $V_{OH}(t)$, $Z_{eff}(t)$, neoclassical enhancement factor $M_{neo}(t)$, and injector parameters relevant for defining V_{LHI} and I_{TL} ($I_{inj}(t)$, $V_{inj}(t)$, $A_{inj}(t)$, $w_{inj}(t)$, and $R_{inj}(t)$). The additional equation also necessitates a variety of new time-varying inputs: electron profile evolution $n_e(t)$, temperature profile shape evolution $\hat{T}(t)$, ion-to-electron temperature ratio evolution $\frac{T_i}{T_e}(t)$, total radiated power $P_{rad}(t)$, and auxiliary heating power $P_{aux}(t)$.

An assumed scaling model is also a required input to estimate τ_E during the calculation. In this work, this takes the form of empirical confinement scalings that are under consideration which were outlined in Section 2.8. However, alternative scalings can be implemented if any are found to be adequately descriptive of LHI plasmas.

The expanded model provides the ability to test the viability of scaling models in high-performance dynamic LHI scenarios. However, rigorous tests require elimination of free parameters through diagnostic constraints. The plasma shape evolution is inferred from the ShapeFIT fast boundary reconstruction code which will be discussed later in this chapter. The electron kinetic profiles can be constrained by MPTS measurements. Additionally, the microwave interferometer diagnostic can provide line-integrated electron density evolution $\bar{n}_e(t)$. The suite of impurity diagnostics are being used to better characterize the impurity content during LHI to provide $Z_{eff}(t)$ and $P_{rad}(t)$ [150]. Unfortunately, the bulk ion channel of the kinetic energy is presently not well-diagnosed in Pegasus-III which limits the ability to constrain the $\frac{T_i}{T_e}(t)$ and $P_{aux}(t)$ inputs. However, previous measurements of impurity ion temperatures $T_{i,Z}$ indicate that auxiliary reconnection ion heating typically leads to $\frac{T_i}{T_e} \geq 1$ and scales like $I_{inj}V_{inj}^{1/2}$ [11,53]. Further, the auxiliary power from this reconnection heating is on the order of $P_{aux}{\sim}300$ kW for typical LHI parameters on Pegasus [53]. These observations can be used to inform the assumed values used in this work but are an avenue for future improvement.

4.1.2 Validation of Extended Model

To validate the output of the modified code, time-constant inputs were provided to the extended 0-D model and compared against results from the simple steady-state confinement model described in Section 2.9. Despite the simplicity of the steady-state model, it has proven to be descriptive of published operating points from various tokamaks as detailed in Appendix A. This at least provides confidence that the estimates it provides are reasonably accurate. Therefore, benchmarking the extended 0-D model with calculations from the steady-state confinement model provides an initial validation of the modified code.

An example comparison between the extended 0-D model and the steady-state confinement model is shown in Figure 4.1. Specifically, it shows the I_p, T_{e0}, and τ_E outputs over a 200 ms simulation domain along with the expectations from the steady-state model indicated by the horizontal black dotted lines. These calculations assume a neo-Alcator confinement scaling. Two

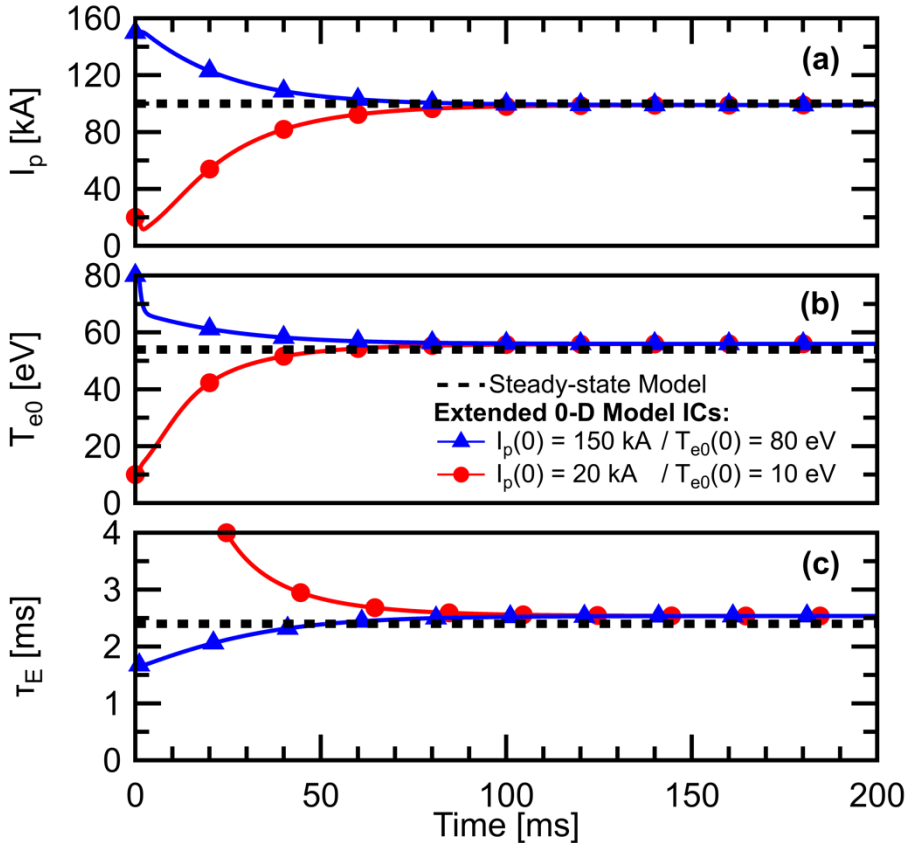

Figure 4.1: Comparison of extended 0-D power balance model and simple steady-state confinement model outputs for identical input parameters: (a) I_p, (b) T_{e0}, and (c) τ_E. Two 0-D model calculations are shown for different I_p and T_{e0} initial conditions.

different sets of initial conditions are shown which lead to different evolutions at early times. As the system evolves from these disparate starting points, the calculations eventually converged to a steady-state operating condition that agrees well with the values predicted by the steady-state confinement model. Similar agreement was also observed for other L-mode and H-mode confinement scalings.

The expanded 0-D model also reasonably recreates ohmically-driven Pegasus discharges. Specifically, the model was compared against a Pegasus ohmic discharge that was extensively documented and analyzed [48]. The model used inputs that were consistent with the experimental values. The plasma shape evolution was inferred from ShapeFIT. The remaining inputs were constrained by measurements and/or equilibrium reconstruction analysis. Figure 4.2 shows several of these inputs along with their experimental values. The ohmic loop voltage was measured directly by a flux loop located on the central column. The remaining quantities were inferred through the aid of equilibrium reconstructions. The $\langle n_e \rangle$ and P_{rad} quantities were computed by mapping the measured radial profiles to flux surfaces to calculate the necessary integrals over the plasma volume. In the absence of a direct measurement, Z_{eff} is estimated using an approach outlined by Bodner et al. [30]. This approach maps the measured $T_e(R)$ to flux surfaces and rigorously computes the neoclassical plasma resistance for a uniform Z_{eff} through the Sauter formulation [91] discussed in Section 2.5. The value of Z_{eff} is then determined by matching the computed R_{neo} with the effective measured plasma resistance $R_p = V_{OH}/I_p$. The error bars in Figure 4.2(c) are representative of the propagated uncertainty in the MPTS measurements. Given this uncertainty, the $M_{neo}Z_{eff}$ input to the 0-D model calculation was varied within these bounds to better match the output $I_p(t)$ and $\langle T_e \rangle(t)$.

The early phase of the discharge ($t < 23$ ms) was not as well-constrained and required assumptions on various quantities. The density is assumed to ramp linearly during the initial I_p ramp and then holds at $\langle n_e \rangle \approx 1 \times 10^{19}$ m^{-3} which is set by the $\langle n_e \rangle$ measured by MPTS at $t = 23$ ms. The $\ell_i(t)$ is assumed to be constant prior to 23 ms and equal to the first reconstructed value $\ell_i(23\text{ ms}) \approx 0.25$. Prior to 23 ms, the $M_{neo}Z_{eff}$ quantity is assumed to follow a linear slope comparable to the data trend inferred at later times but was varied to improve model $I_p(t)$ agreement. Finally, measurements of the bulk ion properties were not available and thus the T_i/T_e ratio is not well-constrained. Here, a constant $T_i/T_e = 0.4$ is assumed throughout the discharge.

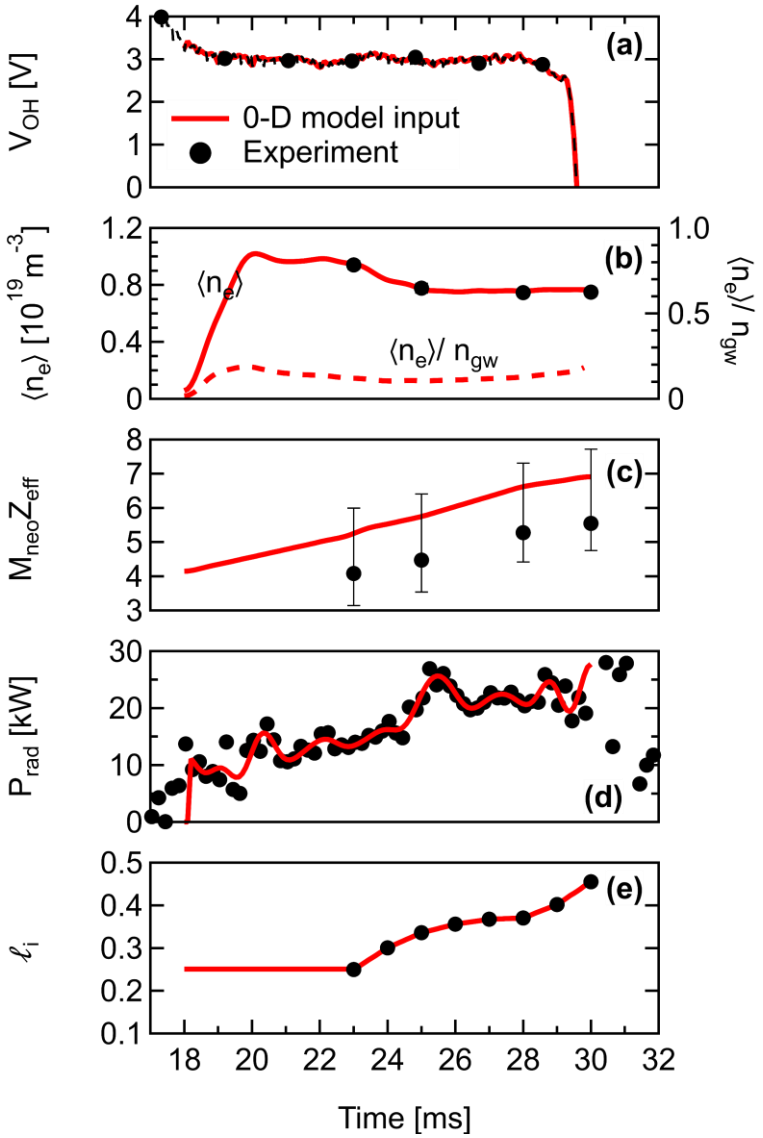

Figure 4.2: Comparison of extended 0-D power balance model inputs and their experimental values: (a) V_{OH}, (b) volume-averaged n_e (left) and corresponding Greenwald fraction (right), (c) $M_{neo}Z_{eff}$, (d) total P_{rad}, and (e) ℓ_i.

This is reasonable given ohmic heating predominantly heats the electron population leading to $T_i/T_e < 1$ [113,125,163]. Further, impurity ion temperatures measured during ohmically-driven Pegasus discharges indicate that $T_i/T_e \lesssim 0.5$ [47,53].

The confinement time was assumed to follow neo-Alcator scaling given by equation 2.26. This is justified for this discharge because both NSTX [131] and Globus-M [129] have observed neo-Alcator-like scaling for $n_e/n_{e,GW} \lesssim 0.8$. In this discharge, the densities are such that $\langle n_e \rangle/n_{e,GW} \lesssim 0.2$ throughout as shown in the right axis of Figure 4.2(b).

Figure 4.3 compares the outputs of the 0-D model calculation to experimental values. Specifically, it shows the time evolutions of I_p, $\langle T_e \rangle$, τ_E, and β_p which are all self-consistently calculated for the assumed neo-Alcator τ_E scaling. The error bars for $\langle T_e \rangle$ in Figure 4.3(b) are a result of the propagated uncertainty in MPTS data and its mapping to the flux surfaces via a weighted Akima spline fit. The error bars in Figure 4.3(d) for β_p are derived from a Monte Carlo uncertainty analysis for the equilibrium solution as described in [156]. The experimental τ_E is

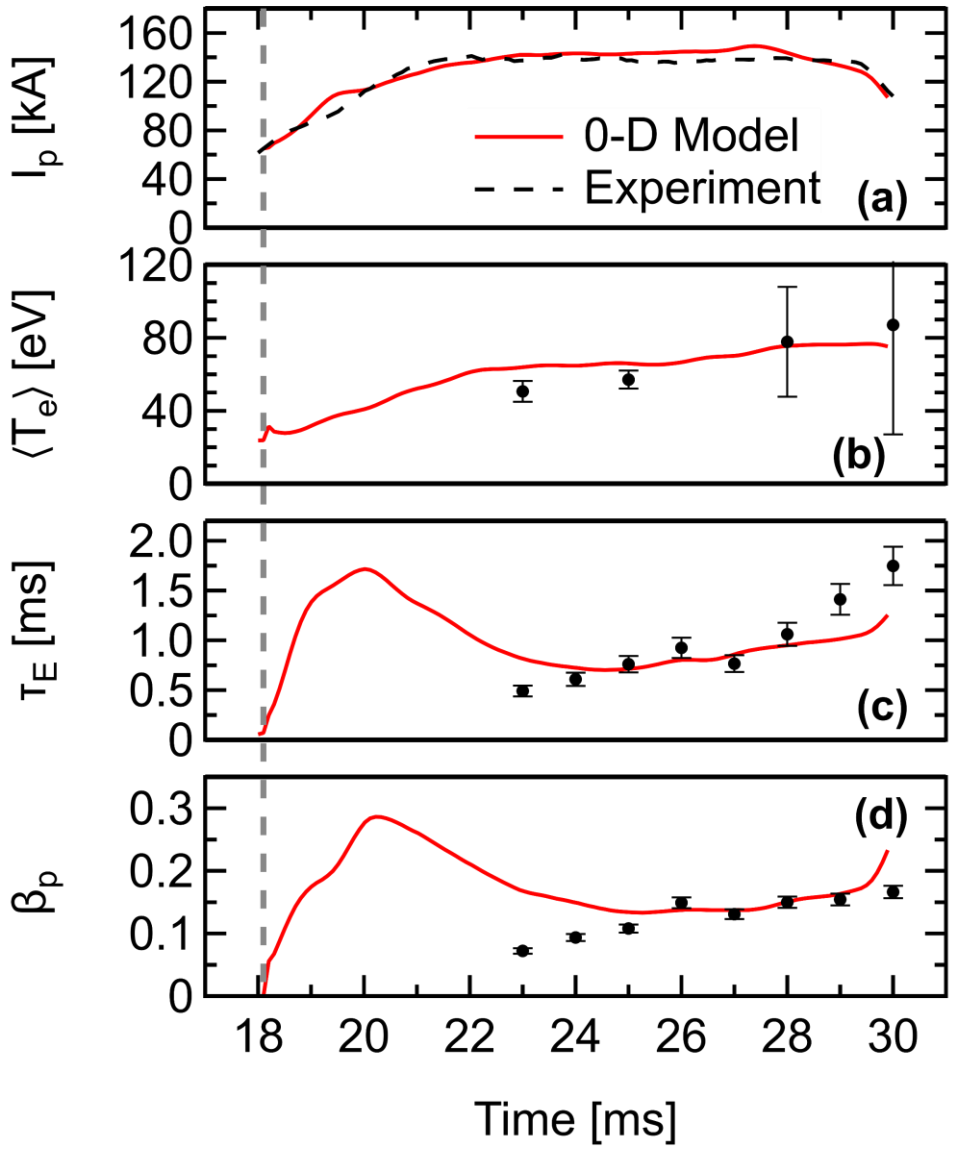

Figure 4.3: Comparison of extended 0-D power balance model outputs and their experimental values: (a) I_p, (b) volume-averaged T_e , (c) τ_E, and (d) β_p. The vertical dashed line indicates the start of the 0-D model calculation.

calculated by equation 2.23 with $P_{in} = I_p V_{OH} - P_{rad}$. The W_K, $\frac{dW_K}{dt}$, and $\frac{dW_M}{dt}$ terms are computed from the time-resolved equilibrium reconstructions with the propagated parameter uncertainty derived from the Monte Carlo uncertainty analysis representing the error bars in Figure 4.3(c). In general, the model agrees well with the experimental values for much of the discharge. Further, the τ_E agreement is consistent with the expectation that the neo-Alcator scaling should be descriptive of this ohmically-heated discharge operating at $n_e/n_{e,GW} \lesssim 0.8$.

The agreement demonstrates that the expanded 0-D model can reasonably describe Pegasus discharges for which the inputs are well-constrained and there is a suitable confinement scaling model. Thus, interpretative analysis of LHI discharges with experimentally constrained model inputs can be a useful tool for attempting to identify a suitable global confinement scaling model. If such a scaling model can be identified, then this tool can also more reliably project the performance of LHI systems because of the improved estimate of the dissipation via the self-consistent $T_e(t)$ calculation.

4.2 ShapeFIT Fast Plasma Boundary Reconstruction Code

Time-evolving equilibrium reconstruction analysis of Pegasus discharges using the KFIT equilibrium code discussed in Section 3.3.3 can be a time-consuming endeavor. Further, the full Grad-Shafranov equilibrium is not always required when only an estimate of the plasma boundary evolution is needed. A fast boundary reconstruction code called ShapeFIT has been previously developed to provide an alternative method for inferring the plasma shape evolution in a less time-intensive manner [29,87]. It has proven to be useful as a control room tool capable of estimating the plasma shape between discharges during scenario development. Further, it is also used to provide plasma shaping moment inputs to the 0-D power balance model. In this work, ShapeFIT has been extended and the resulting analysis refined for LHI discharges.

4.2.1 Algorithm description

Numerous filament and finite-element models have been developed for fast plasma boundary reconstruction analysis [164–167]. These techniques represent the plasma as a set of discrete current sources to estimate the plasma shape without solving for the Grad-Shafranov equilibrium. The plasma boundary is estimated by determining the current distribution that best matches the

available magnetic diagnostic constraints in a least-squares sense. This best-fit plasma current distribution and the external coil currents are then used to compute Ψ on the solution grid. Finally, the plasma boundary can be extracted from $\Psi(R, Z)$ based on the defined limiter geometry.

Filament and finite-element models can be further separated into two groups based on the kernel geometry that is used. Fixed current filament (FCF) methods define a fixed kernel geometry to describe the plasma current distribution. Whereas variable current filament (VCF) methods allow the position of the kernel filaments to vary throughout the fitting process.

The original ShapeFIT implementation is a filament model using the VCF approach [29,87]. It also incorporates a circuit model for the wall currents that are induced in the Pegasus vacuum vessel [156,157]. This enables boundary reconstruction in the presence of wall currents induced by the PF coils and plasma current. The wall currents induced by the plasma currents are dynamically calculated and updated as the filament plasma model varies throughout the fitting process.

The code was developed to allow for flexibility in designing new filament kernels. However, a standard kernel consisting of four filaments is typically used. The geometry and free parameter definitions for this kernel are shown graphically in Figure 4.4. The measured toroidal plasma current is distributed between the four filaments. This distribution is constrained such that each element carries current in the same direction. The filaments move rigidly relative to the central filament carrying I_1 located at $(R, Z) = (R_c, Z_c)$. The top and bottom filaments carrying I_0 can

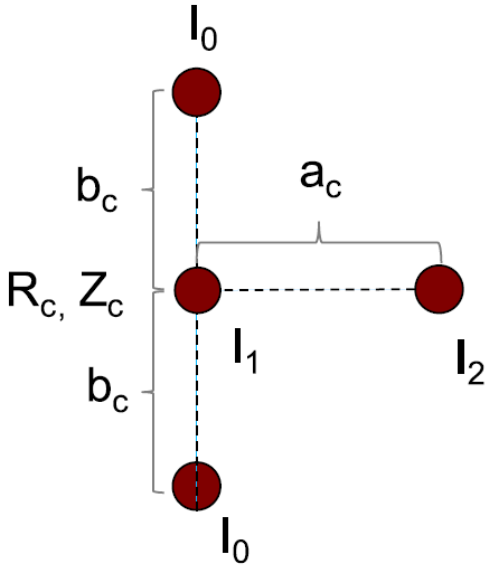

Figure 4.4: Standard $N = 4$ VCF kernel parameterization used for ShapeFIT. Taken from [29].

move vertically relative to the central filament with the distance free parameter designated as b_c. The right-most filament carrying I_2 can move radially outward with the distance free parameter designated as a_c. In total, this results in seven fit parameters: $R_c, Z_c, a_c, b_c, I_0, I_1,$ and I_2. Additional constraints are imposed on these parameters during the fitting process to ensure numerical stability and limit results to physically meaningful solutions. These are summarized in greater detail in [87].

The fitting process begins once the discharge exceeds a specified threshold toroidal current (typically $15 - 25$ kA). Prior to exceeding this threshold, the plasma is treated as a stationary single current filament near the center of the vacuum vessel to provide a zeroth-order estimate of the wall currents induced by the non-zero plasma current. Once the current threshold is exceeded, a single filament fit is used to generate an initial guess for the first fit with the desired filament kernel (i.e. four filaments). The fitting process then proceeds for the rest of the discharge at a user-specified fixed time step (typically 100 μs). After the first time point, each fit uses the best-fit solution from the previous time point as an initial guess.

At each time point, the model filaments are fit based on the calculated field and flux contributions to all the magnetic measurement constraints using a Levenberg-Marguardt χ^2-minimizer. After converging to the best-fit current distribution, the induced wall currents are recalculated using the fitted plasma filaments and time-varying PF coil currents. If a fit at any time point fails to converge, the standard time-step is halved, and the fit is repeated until a converged solution is achieved. If the fit continues to fail until a user-specified minimum time step, then the algorithm continues to the next time point. This process continues for the duration of the discharge.

Finally, $\Psi(R, Z)$ is calculated from the fitted plasma filaments, the PF coils, and the induced wall currents using well-established Greens' function calculations which map these respective current sources to the solution grid assuming these sources are axisymmetric current loops [168]. A boundary search algorithm is then used along with the defined machine limiter geometry to identify a contour of constant $\Psi(R, Z)$ representing the plasma boundary. The algorithm identifies the largest closed flux contour that is bounded by the limiter geometry. Shaping moments are then derived from this boundary contour using the formulation developed by Luce et al. [169].

This implementation of ShapeFIT was previously benchmarked against KFIT magnetic equilibrium reconstructions for a series of ohmic-induction driven discharges on Pegasus [29,87]. This analysis found that boundary moments estimated by ShapeFIT agreed reasonably well with the fully reconstructed equilibrium. Discrepancies between ShapeFIT and KFIT in R_0, Z_0, and a

were comparable to the inherent error in the KFIT reported values ($\sim 1.5 - 2$ cm) and $5 - 10\%$ in κ and δ.

4.2.2 Output uncertainty

A Monte Carlo analysis engine was developed in this work to estimate errors in the output shaping moments calculated by ShapeFIT due to uncertainties in the magnetic diagnostic constraints used during fitting. For each analyzed discharge, a large number (typically $\sim 100 - 200$) of trial fits are conducted with random Gaussian noise added to the diagnostic constraints. The width of the Gaussian noise distribution is set to the characteristic diagnostic uncertainty for the magnetics. These uncertainties have been estimated for both the Pegasus [156] and Pegasus-III [149] magnetics suites.

The uncertainty in the fitted shaping moments at each time point is quantified through statistical analysis of all N trials in the Monte Carlo study. An example of this output is shown in Figure 4.5 for an $N = 200$ trial Monte Carlo analysis of Pegasus-III LHI discharge #4898. The distribution of κ values at each time point in the discharge is shown in Figure 4.5(b). Early in the discharge there is a wider variance in the fitted values. This variance reduces throughout the I_p ramp corresponding to less uncertainty in the output. Figure 4.5(c) shows histograms of the fitted values at three discrete times at the beginning, middle, and end of the I_p ramp corresponding to the vertical shaded bars in Figure 4.5(a) and (b). The solid lines represent a Gaussian distribution fitted to the binned data. The standard deviation σ of the Gaussian fit to the data represents the uncertainty in the ShapeFIT output. This clearly narrows as the discharge progresses later in time. This is expected as the plasma component of the magnetic diagnostic signals will increase with I_p thereby increasing its signal-to-noise ratio. The plasma size is also growing in time and comes into closer proximity to the magnetic diagnostics which further increases this signal-to-noise ratio and provides stronger constraints on the plasma shape. The other shaping moments exhibit similar behavior albeit with different relative amounts of variance in the fitted values.

This data can be further reduced into a relative error for the shaping moments as a function of time for a given discharge. The relative error at each time point is defined as $\sigma_i / \bar{M}_i$ where σ_i and $\bar{M}_i$ are the standard deviation and mean of the i-th output parameter (*i.e.* R_0, a, κ, etc.) for the Monte Carlo analysis. The relative error for several shaping moments along with the toroidal flux

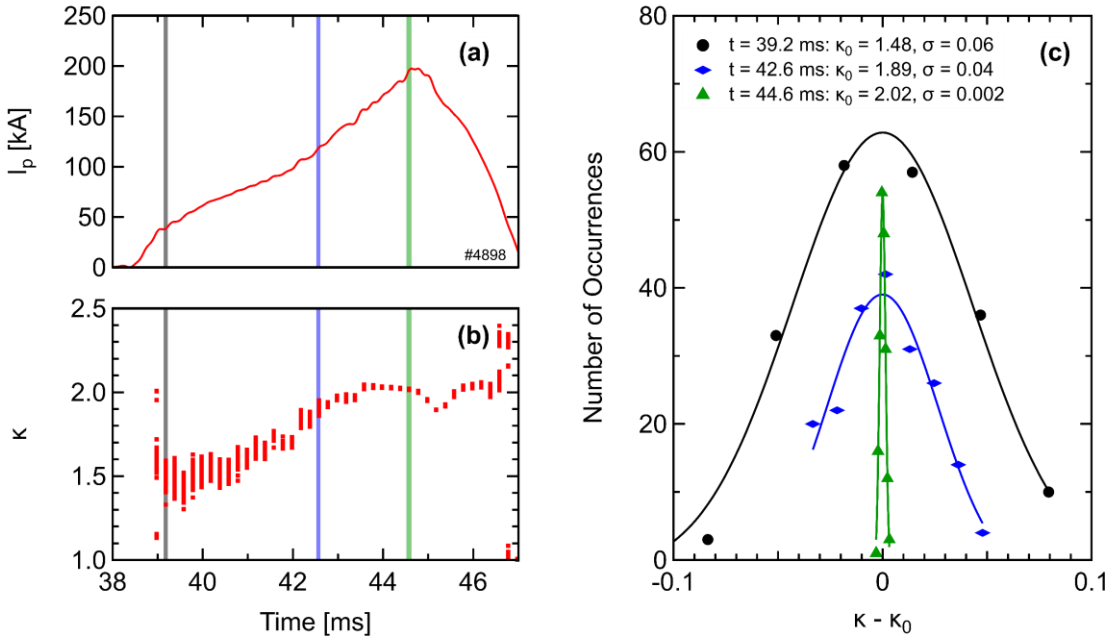

Figure 4.5: Representative ShapeFIT Monte Carlo analysis: (a) plasma current and (b) elongation for $N = 200$ trials throughout Pegasus-III discharge #4898. (c) Histograms showing number of occurrences of elongation values shifted in the trials at three discrete times in the discharge indicated by the vertical shaded bars in (a) and (b). The histograms have been shifted by the central value (κ_0) for clarity.

calculated by ShapeFIT for Pegasus-III discharge #4898 is shown in Figure 4.6. The relative error for each parameter decreases as the discharge progresses and for most parameters is $\leq 5\%$ for the entire discharge. The triangularity parameter is not as well constrained early in the discharge but does fall below 5% at later times. In addition to the time-dependent nature, the relative error is also dependent on the number of constraints and diagnostic uncertainty used in the ShapeFIT analysis. This necessitates performing this Monte Carlo analysis on each ShapeFIT calculation of interest to quantify the output parameter uncertainty over the entirety of a given discharge.

In addition to random error associated with diagnostic uncertainty, there are also sources of systematic uncertainty that have been identified. An important source relevant for this work is the choice of diagnostic constraints. The ShapeFIT solution is highly dependent on the number and location of available diagnostic constraints. This is demonstrated in Figure 4.7(c) where the toroidal flux for discharge #4898 are shown for two different ShapeFIT solutions. The only input differences between these solutions are the diagnostic constraints. The "full set" shown in Figure 4.7(a) uses all available magnetic diagnostics as constraints which is comprised of flux loops and pickup coils distributed around the vessel. The "reduced set" shown in Figure 4.7(b) uses only a

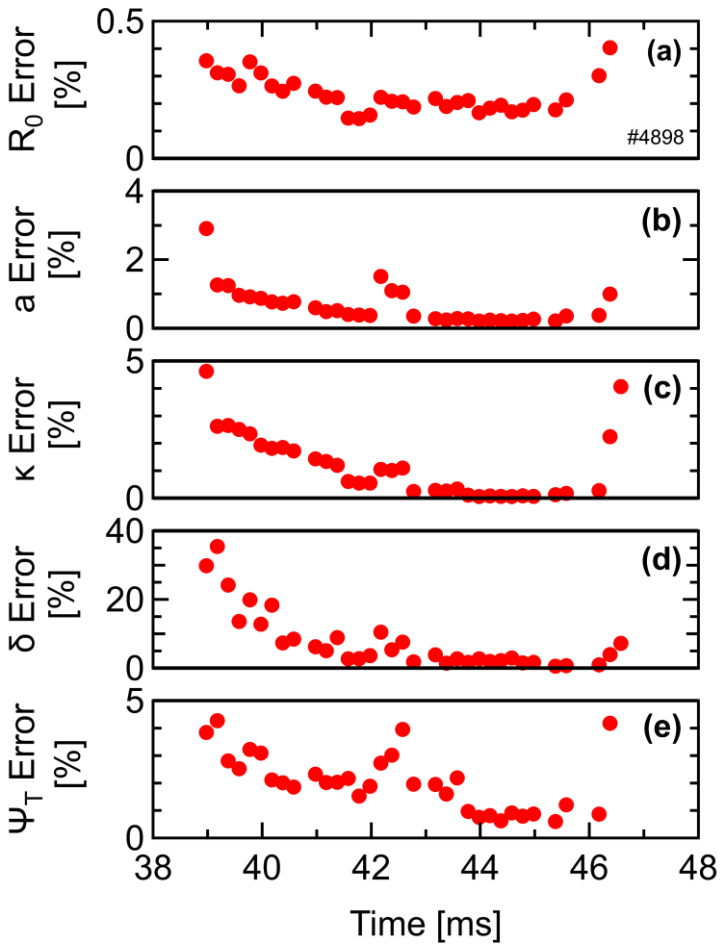

Figure 4.6: ShapeFIT output relative uncertainty for Pegasus-III discharge #4898: (a) major radius, (b) minor radius, (c) elongation, (d) triangularity and (e) toroidal flux.

subset of the magnetic diagnostics suite and is primarily comprised of flux loops located on the top, bottom, and outboard area of the machine with only a handful of pickup coils.

The inferred plasma boundary from these two ShapeFIT solutions are systematically different in several ways. First, the output uncertainty is higher in the solution which had fewer diagnostics as illustrated by the larger error band shown in Figure 4.7(c). This is unsurprising because a set of diagnostics which covers more of the poloidal cross-section should provide a stronger constraint on the inferred plasma boundary. The other primary difference is the systematically higher toroidal flux computed later in time when using the full set of available magnetic diagnostics. This is a result of the ShapeFIT solution inferring a boundary that is systematically larger and located at lower major radius. Early in time, the plasma shape is similar and within the random error of each of the fitted outputs.

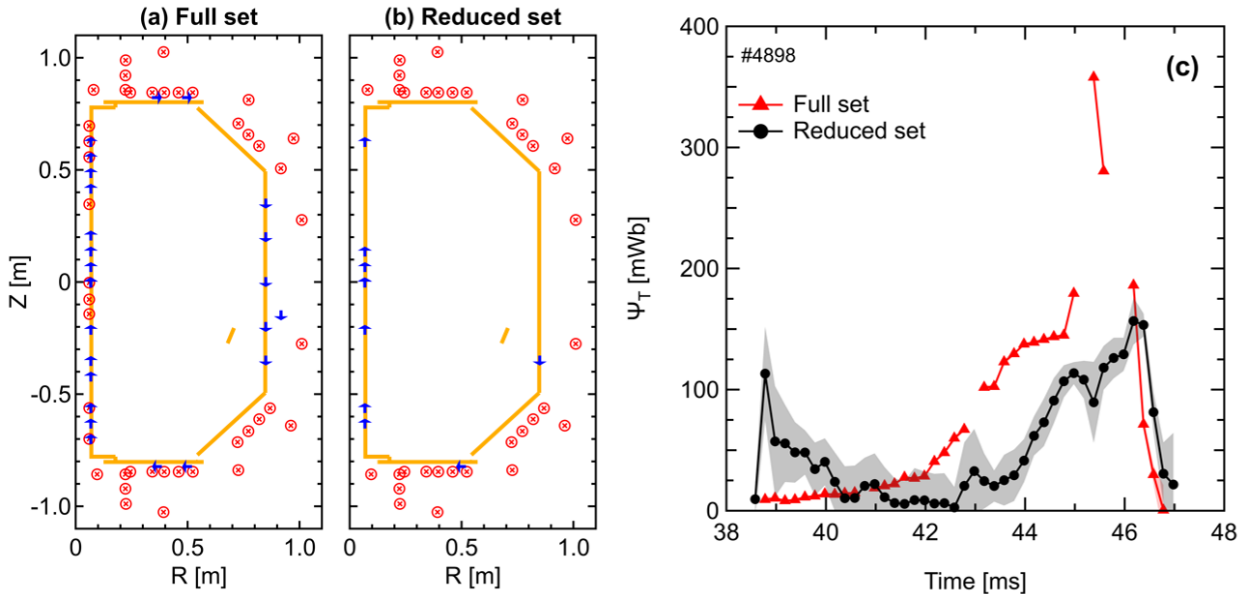

Figure 4.7: Comparison of ShapeFIT output for different sets of diagnostic constraints: Poloidal cross-section of Pegasus-III displaying the layout of (a) all available magnetic diagnostics and (b) a reduced array used as constraints ShapeFIT along with the calculated (c) toroidal flux for each ShapeFIT solution of Pegasus-III discharge #4898. The red circles indicate flux loops and the blue arrows indicate pickup coils and their nominal orientation. The error bars in (c) are derived from the Monte Carlo analysis and in some cases may be smaller than the marker size itself.

In general, including more diagnostic constraints provides a more physically accurate estimate of the plasma boundary. This is illustrated in Figure 4.8 which shows a comparison of ShapeFIT solutions to a high-speed visible image of the plasma during the decay of Pegasus-III discharge #4898. This time point is just after the injectors have been shut off ($I_{inj} = 0$) so that the plasma boundary is more readily discernible in the high-speed visible imaging shown in Figure 4.8(a). The ShapeFIT solutions using the full and reduced set of diagnostic constraints are shown in Figure 4.8(b) and (c), respectively. There is a significant difference in the predicted plasma boundary with the full diagnostic set predicting a plasma that is limited on the central column with a $\sim$7 cm gap between the injector structures which are outlined in green. Whereas the solution that utilized a reduced set of constraints is limiting on the injector structures and is in much closer proximity to the main rail limiter at $R = 0.85$ m. Overall, the boundary predicted by the full diagnostic appears to be more representative of the plasma seen in the high-speed image which has a clear gap between the decaying plasma and the injector structures.

This is further supported by comparing the ShapeFIT boundaries to the boundary predicted by a KFIT equilibrium reconstruction. This comparison is shown in Figure 4.9 during the decay of

Pegasus-III discharge #4898 at $t = 46$ ms (same time as visible image in Figure 4.8 (a)). The flux contours are from the KFIT solution with the predicted boundary indicated by the thick black contour. For reference, the plasma boundary predicted by KFIT for the full and reduced set of diagnostic constraints were very similar. For clarity, only the solution from the full set of diagnostic constraints is shown here. The boundaries predicted by ShapeFIT with the full and reduced diagnostic set are shown in the dashed red and dotted blue contours, respectively. Just as with the high-speed visible image at this time point, the ShapeFIT solution using the full set of diagnostic constraints has better qualitative agreement with the boundary predicted from KFIT. However, ShapeFIT appears to overestimate the plasma size during the decay of this LHI plasma.

The systematic difference in ShapeFIT solutions with the choice of diagnostic sets is generally not of great consequence because it is best practice to use as many constraints as possible to provide a more physically accurate reconstruction of the plasma boundary. However, this issue is unavoidable when trying to compare the reconstructed boundary of Pegasus and Pegasus-III plasmas. The number of magnetic diagnostics available on Pegasus was more limited due to damaged diagnostics and inadequate noise immunity. These issues were addressed in the Pegasus-III facility resulting in a larger set of available magnetics [149]. The reduced diagnostic set in

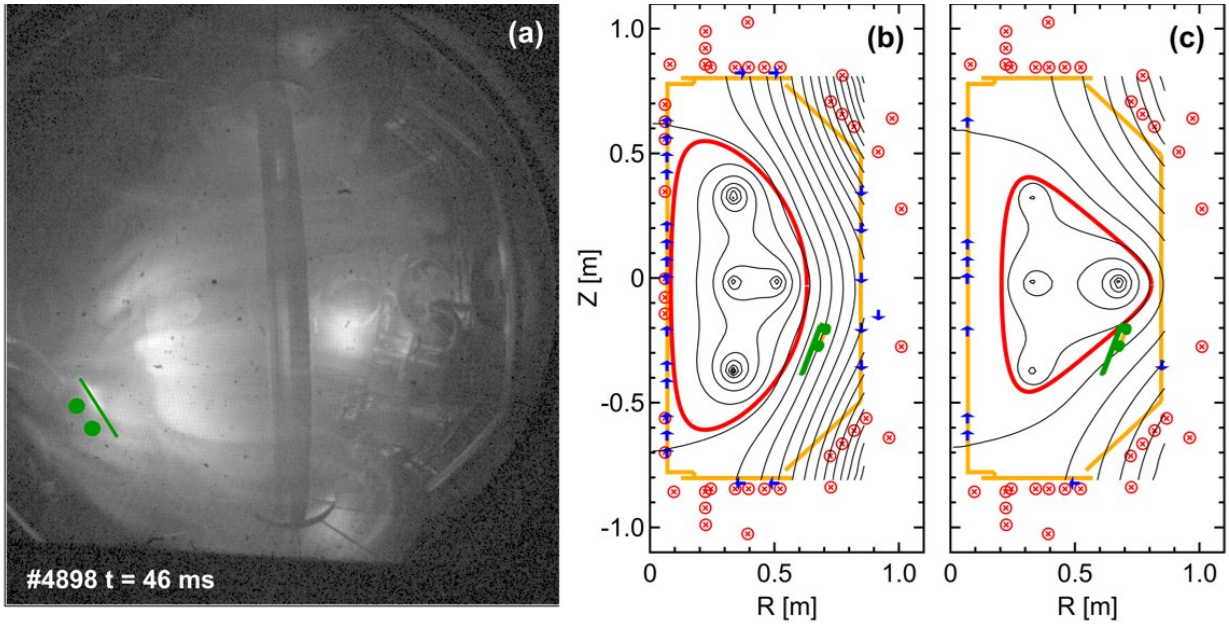

Figure 4.8: Representative comparison of high-speed visible imaging and ShapeFIT solutions for different sets of diagnostic constraints: (a) high-speed visible image and ShapeFIT solutions using the (b) full and (c) reduced set of diagnostics during the decay of Pegasus-III discharge #4898 at $t = 46$ ms. The nominal injector location is shown in the green shapes in each image. Flux contours are depicted in the (b) and (c) with the red contour indicating the predicted plasma boundary.

Figure 4.7(b) was selected to be representative of the typical diagnostics that are available for reconstructing Pegasus discharges. This comparable, reduced set of diagnostics is used to reconstruct the boundary of Pegasus-III plasmas when comparing to Pegasus discharges to reduce the effect of this systematic error. In this way, it is at least possible to determine if a Pegasus and Pegasus-III discharge possess qualitatively similar plasma shapes even if the details of the shape may be inaccurate in an absolute sense.

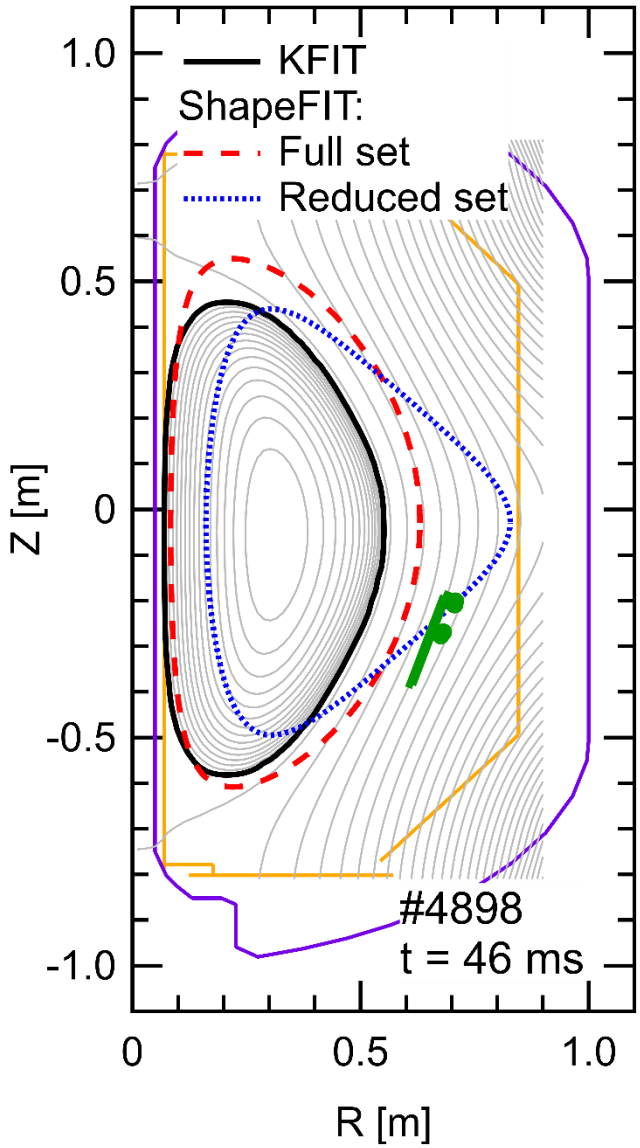

Figure 4.9: Representative comparison of plasma boundary predicted by KFIT and ShapeFIT during the decay of Pegasus-III discharge #4898 at $t = 46$ ms. Flux contours (thin gray) are from KFIT. The nominal injector location is indicated by the green markgers.

Another source of uncertainty that exists in the ShapeFIT boundary reconstruction of LHI plasmas is the disagreement with the equilibrium reconstructions calculated by KFIT. ShapeFIT has systematically inferred plasma boundaries that are larger than those predicted by KFIT. This is demonstrated in Table 3 which compiles the toroidal flux computed by ShapeFIT and KFIT across several LFS LHI scenarios. Due to limitations of KFIT, these reconstructions are limited to the end of their respective discharges when the plasma has reached its full size and is limiting on the central column. Still, they cover a wide Pegasus-III parameter space: $70\ \text{kA} \leq I_p \leq 200\ \text{kA}$, $0.15\ \text{T} \leq B_T \leq 0.3\ \text{T}$, and $3\ \text{kA} \leq I_{inj} \leq 12\ \text{kA}$. Across this set of reconstructions, ShapeFIT systematically overestimates Ψ_T by $\gtrsim 30\%$.

This set of reconstructions was also used to quantify the systematic errors in the inferred shaping moments relative to KFIT. The average offset error and standard deviation in these shaping parameters is shown in Table 4. For reference, the table also includes these values for a similar comparison to ohmically-driven discharges on Pegasus that was performed by Barr et al. [33,99]. Unsurprisingly, the relative offset error for each parameter is larger for LHI discharges which is indicative of a larger systematic error between the two reconstruction methods. This may be related to the kernel being somewhat less applicable for LHI discharges than OH discharges. Additionally, the injected open field line currents that exist during LHI can introduce systematic errors in both reconstruction methods [170] but may have different levels of impact that lead to the larger discrepancies shown here. The standard deviation in these parameters is also somewhat higher during analysis of LHI discharges. Still, these errors are comparable to the intrinsic error in the KFIT output itself which is $1.5 - 2$ cm for R_0 and a and 10% for κ and δ [156].

					Calculated Ψ_T		
Shot	**Time [ms]**	**I_p [kA]**	**B_T [T]**	**I_{inj} [kA]**	**ShapeFIT [mWb]**	**KFIT [mWb]**	**ShapeFIT relative error [%]**
3598	45.5	78	0.15	2.7	190	134	+42
	46	87		2.8	206	132	+56
3799	45.5	75	0.15	3.0	210	129	+63
	46	81		3.0	205	138	+49
4593	46.5	159	0.15	7.2	239	149	+60
4958	44.5	172	0.23	12.0	296	219	+35
	45	168		11.5	271	214	+27
4898	44.5	203	0.30	11.9	400	300	+33
	45	200		11.4	384	295	+30

Table 3: Calculated Ψ_T from ShapeFIT and KFIT for several Pegasus-III LHI discharges

	OH		**LHI**	
Parameter	**Average Error**	**Standard deviation**	**Average Error**	**Standard deviation**
R_0 [cm]	+1.5	1.1	+4	2
Z_0 [cm]	+1.7	2.5	+2	4
a [cm]	+1.0	1.2	+4	2
κ	-0.03	0.12	-0.2	0.2
δ	-0.03	0.03	-0.06	0.02

Table 4: Comparison of ShapeFIT errors in shaping moments relative to KFIT for ohmic and LHI discharges. Analysis for OH discharges is from work by Barr et al. [29,87].

Chapter 5
Taylor Limit Studies on Pegasus-III

LFS LHI discharges have an extended phase in which the I_p is sustained at a global limit imposed by the magnetic relaxation process, referred to as the Taylor limit. This suggests that higher I_p can be driven by increasing this limit early in the discharge to utilize the available helicity input more effectively. The scaling of this limit has been previously explored on Pegasus and observed a robust $\propto \sqrt{B_T I_{inj}/w_{inj}}$ scaling [88]. As discussed in Section 2.6, this scaling can be leveraged to develop higher current LHI plasmas through injector design (I_{inj}, w_{inj}) and/or operating at higher B_T.

The expanded operating space of Pegasus-III enables definitive tests of this path to higher I_p in an operating space increasingly more relevant to MA-class facilities. The previous Taylor Limit scaling studies were conducted in a relatively small operating space on Pegasus which was limited by facility ($B_T \leq 0.15$ T) and injector capabilities ($I_{inj} \leq 5$ kA and $A_{inj} = 2$ cm^2 per injector). Upgrades to the facility ($B_T \leq 0.6$ T) and an enhanced injector system ($I_{inj} \leq 16$ kA and $A_{inj} = 4$ cm^2 per injector) enable this scaling to be tested over an expanded operating space.

This chapter will describe experiments focused on studying the properties of LHI plasmas operating at the Taylor limit. The discussion focuses on the observed scaling of the Taylor limit in the expanded operating space and the properties of discharges that have excess helicity to sustain the plasma at $I_p = I_{TL}$.

5.1 Taylor Limit B_T Scaling in Expanded Operating Space

To test the scaling of the Taylor limit with B_T, a series of self-similar discharges at various B_T levels were designed on Pegasus and Pegasus-III. In these experiments, the discharges were designed to have identical injector parameters and plasma shape evolutions to isolate variations in the Taylor Limit solely due to the B_T variation. Additionally, discharges at increased input helicity via higher V_{inj} were developed to verify the discharge was operating at the presumed Taylor limit.

This experiment was first performed on Pegasus using two 2 cm^2 circular aperture injectors located just below the outboard midplane [171]. In this scan, B_T was varied from 0.04 to 0.15 T corresponding to a two-fold variation in the expected Taylor limit. The injector parameters (V_{inj} and I_{inj}) and plasma shape evolutions were well-matched across all discharges. The measured trajectories across these discharges are shown in Figure 5.1(a). Here, the traces have been time-shifted to align the initial relaxation event corresponding to the transition from the purely helical current streams to the tokamak-like state ($t - t_{relax} = 0$). As B_T is increased, the plasma initially relaxes to higher I_p due to the increased Taylor limit. This increased Taylor limit then results in a higher I_p trajectory for the remainder of the discharge demonstrating more effective use of the fixedV_{LHI}. Further, the increase in I_p is consistent with the expected increase from the Taylor limit. This is illustrated in Figure 5.1(b) in which the $I_p(t)$ at each B_T level is normalized by $\sqrt{B_T}$ ($I_{TL} \propto$

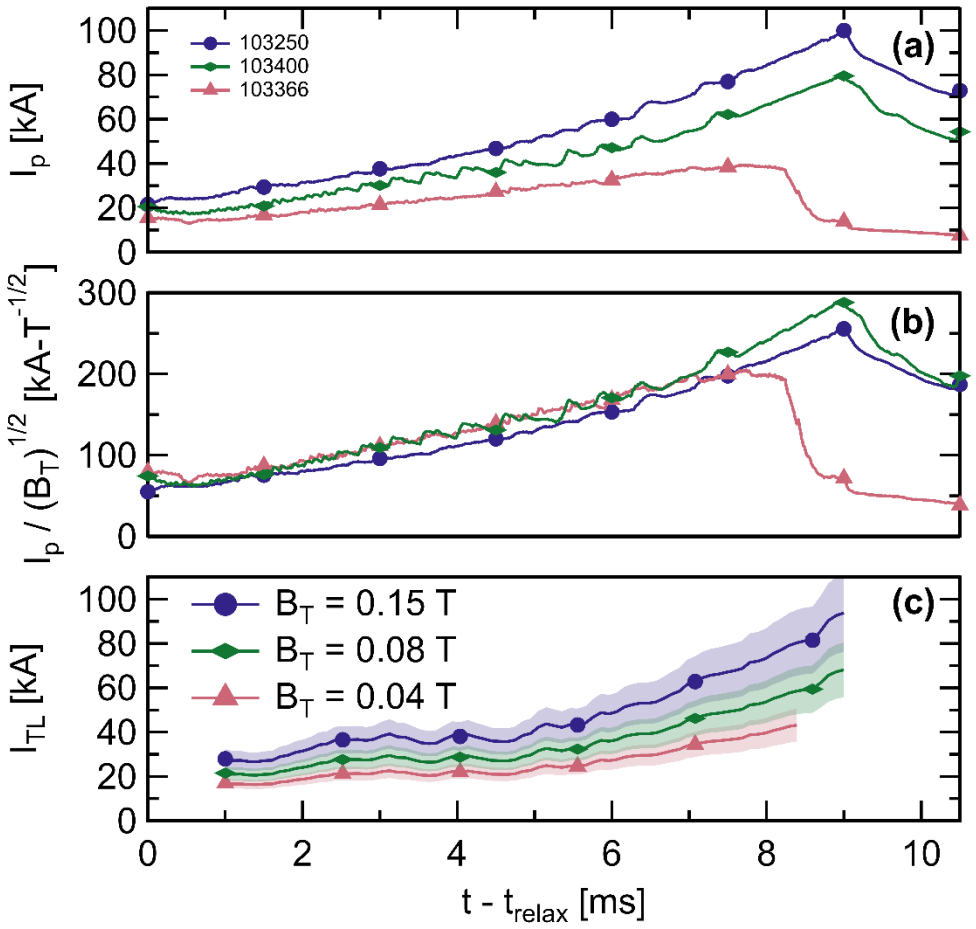

Figure 5.1: Overview of B_T scan on Pegasus up to 0.15 T: (a) I_p, (b) normalized I_p, and (c) predicted I_{TL}.

$\sqrt{B_T}$). With this normalization, the I_p trajectories coincide for most of the discharge evolution. This suggests that the Taylor limit is dictating $I_p(t)$ over this series of discharges. The discrepancy at the end ($t - t_{relax} > 8$ ms) of the lowest B_T scenario is due to the plasma decoupling from the injectors prior to injector shutoff leading to the significant roll-over and decay in I_p.

The predicted Taylor limit for these discharges is shown in Figure 5.1(c). This Taylor limit calculation uses the self-similar plasma shape evolution inferred from ShapeFIT. It also assumes a constant w_{inj} throughout each discharge which is equivalent to the injector diameter $d_{inj} = 1.6$ cm. The error bands on this calculation represent a 20% uncertainty arising from the uncertainty in the input shaping moments inferred from ShapeFIT. This will be discussed in greater detail in Section 5.4. Generally, the measured $I_p(t)$ agrees well with the predicted Taylor limit within its uncertainty which provides additional support that the Taylor limit is dictating the I_p evolution in these discharges.

This experiment served as a proof-of-principle demonstration for the plan to access higher I_p in Pegasus-III. It illustrates the feasibility of leveraging the facility and injector parameters to increase the Taylor limit and achieve higher I_p. This guided the design specifications for the Pegasus-III LHI system described in Section 3.2. Testing this approach to achieve higher current LHI plasmas was a primary focus of the initial experimental campaigns following commissioning the new facility up to $B_T = 0.3$ T.

To test the model projections, another series of discharges was developed at several B_T levels using the new four 4 cm^2 circular aperture injector array described in Section 3.2. In this scan, B_T was varied from 0.15 to 0.3 T to overlap with the previous Pegasus operating space and extend up to the maximum accessible B_T during this operational campaign. Just like in the previous Pegasus experiment, the injector parameters and plasma shape (inferred from the ShapeFIT code) are well-matched across all the discharges to isolate changes in I_{TL} due solely to the B_T variation.

The resulting trajectories for the discharges in this scan are shown in Figure 5.2(a). The behavior of the I_p trajectories follow the same behavior as the Pegasus experiments at lower B_T. As B_T is increased, the plasma initially relaxes to higher I_p due to the increased Taylor limit. This increased Taylor limit then results in a higher I_p trajectory for the remainder of the discharge demonstrating more effective use of the fixed V_{LHI}. Additionally, $I_p \approx 210$ kA is achieved at $B_T = 0.30$ T which exceeds previous LFS LHI operations on Pegasus.

The increase in I_p is consistent with the expected $I_{TL} \propto \sqrt{B_T}$ scaling. This is illustrated in Figure 5.2(b) where the $I_p(t)$ is normalized by $\sqrt{B_T}$ for each discharge. Just as in the lower B_T Pegasus scenarios, the normalized I_p trajectories coincide for the entirety of the discharge which suggests that the predicted scaling continues to be applicable in this operating space. In total, the $I_{TL} \propto \sqrt{B_T}$ scaling has proven to robustly describe LHI plasmas over a factor of eight variation in B_T.

The predicted evolution of the Taylor limit for these discharges is shown in Figure 5.2(c). This Taylor limit calculation uses the self-similar plasma shape evolution inferred from ShapeFIT and assumes a constant $w_{inj} = d_{inj} = 2.3$ cm. The predicted $I_{TL}(t)$ shows good agreement with the measured $I_p(t)$ within the uncertainty in the estimate. This demonstrates that the Taylor limit

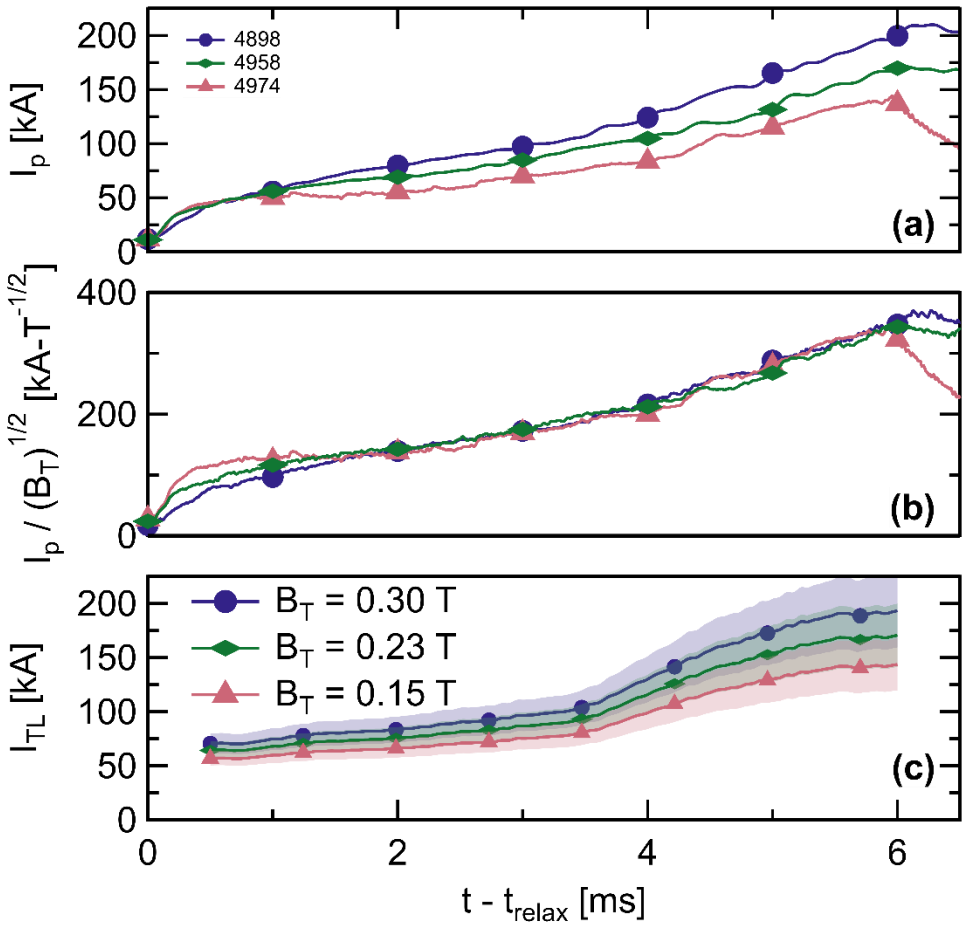

Figure 5.2: Overview of B_T scan on Pegasus-III up to 0.30 T: (a) I_p, (b) normalized I_p, and (c) predicted I_{TL}

calculation used within the 0-D model continues to provide reasonably accurate estimates in this expanded operating space. Further, this also indicates that the Taylor limit still inhibits the achievable $I_p(t)$ in these scenarios. Therefore, additional increases in I_p can likely be realized by further increasing this limit through facility and/or injector design.

A discharge with increased helicity input was developed to confirm that the Taylor limit is still clamping $I_p(t)$ at the highest B_T level. Previous experiments on Pegasus used the ohmic solenoid to provide an additional source of helicity input via magnetic induction to probe the Taylor limit during LHI discharges [88]. This approach is not available on Pegasus-III due to the removal of the ohmic solenoid. Instead, an alternative approach is utilized in this work to provide a similar test. Here, a complementary discharge was developed with identical parameters that influence the Taylor limit (i.e. B_T, I_{inj}, and shape) but had higher helicity input due to increased V_{inj}. The injector impedance is set by the arc and/or edge neutral fueling [171]. Reducing the injector neutral fueling increases the injector impedance and enables higher V_{inj} at fixed I_{inj} via feedback control.

This approach was used to develop the two complementary discharges which are summarized in Figure 5.3. The discharges are nominally identical except that the "over-driven" (#4905) discharge has a lower throughput from the injector neutral fueling valves which leads to the higher V_{inj} at otherwise fixed I_{inj}. On average, the over-driven discharge has roughly 25% more V_{inj} throughout the first ~ 5 ms of the I_p ramp relative to the "baseline" scenario (#4898). Despite the increased helicity input, the discharges have very similar $I_p(t)$ and shape evolution during this period. This is especially true for the first ~ 3 ms of the ramp where Ψ_T is well-matched and I_p is essentially indistinguishable. At later times, Ψ_T is somewhat higher in the over-driven discharge. This is accompanied by a marginal increase in the realized I_p due to the increased I_{TL} from the mismatched plasma shape evolutions ($I_{TL} \propto \sqrt{\Psi_T}$). Ultimately, the over-driven discharge reaches a comparable I_p and plasma size before decoupling ~ 1 ms before the baseline discharge. In these discharges, there is not a significant difference in the observed magnetic fluctuation activity. This is illustrated by a representative LFS $\dot{B}_Z$ sensor shown in Figure 5.3(d) which measures comparable fluctuation amplitude throughout both discharges until the plasma decouples at the end of their respective I_p ramps.

The observation of comparable $I_p(t)$ at an increased helicity input and otherwise similar parameters is indicative of the discharge following a trajectory dictated by the Taylor limit. Thus,

the Taylor limit continues to restrict the achievable I_p in this increased B_T operating space over much of the discharge.

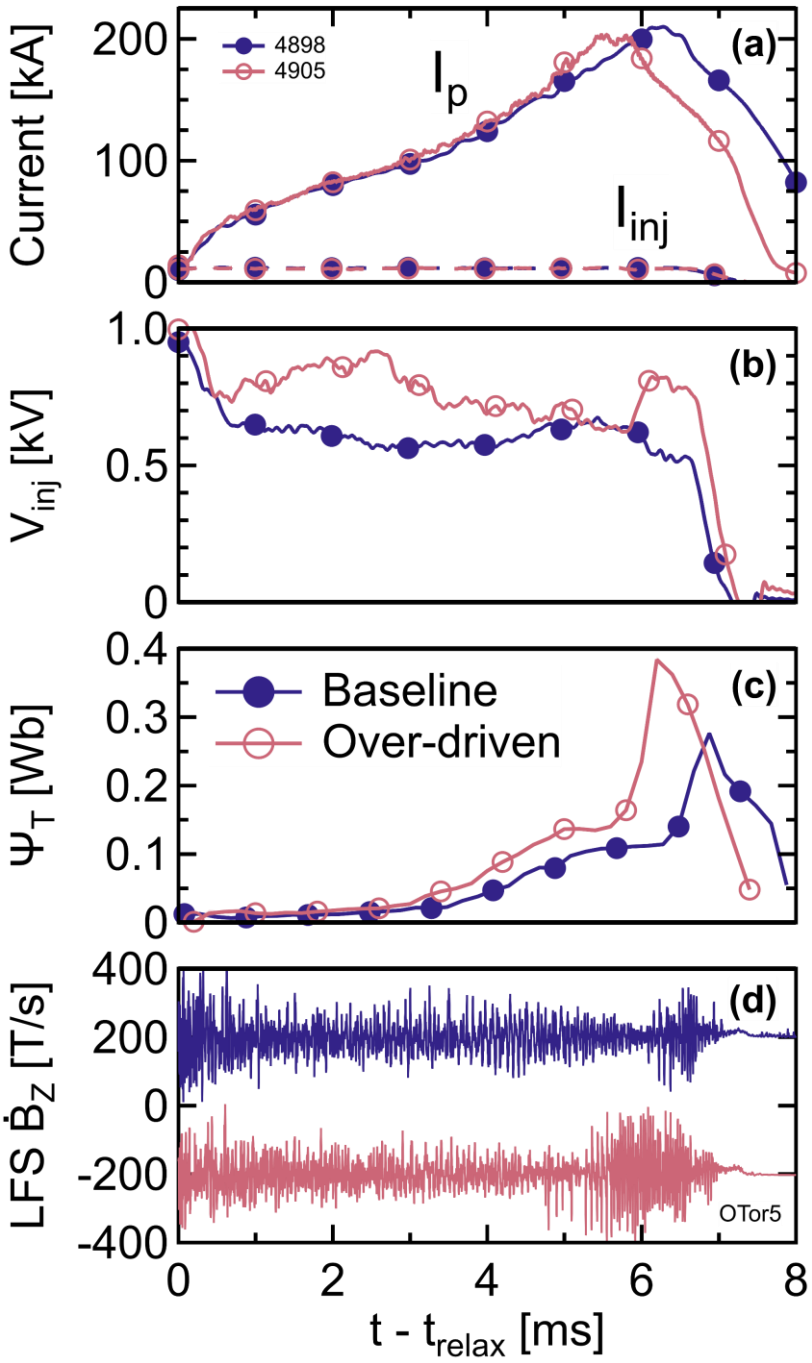

Figure 5.3: Overview of baseline (#4898) and over-driven (#4905) discharges at $B_T = 0.3$ T: (a) I_p and I_{inj}, (b) V_{inj}, (c) toroidal flux, and (d) representative LFS $\dot{B}_Z$ signal. Signals in (d) have been vertically offset for clarity.

5.2 Taylor Limit I_{inj} Scaling in Expanded Operating Space

The enhanced LHI system deployed on Pegasus-III also enabled the expected $\sqrt{I_{inj}}$ scaling of the Taylor limit to be tested over an expanded operating space. LHI operations on Pegasus were limited to $I_{inj} \leq 8$ kA with the dedicated I_{inj} scaling studies limited to ≤ 5 kA [23,88].

The new Pegasus-III LHI system is capable of supplying $I_{inj} \leq 16$ kA. However, most LHI operations thus far have remained around $I_{inj} = 3$ kA/inj (or 12 kA total) due to excessive PMI that has been observed at higher current. The cause of this is hypothesized to be related to non-optimal installation of local limiters near the injectors. The design of these structures is presently being modified to address this issue and enable more reliable operation at the full 16 kA capability. Nonetheless, the $I_{inj} \leq 12$ kA operating space explored in this work still represents a significant extension compared to previous work on Pegasus.

A subset of Pegasus-III discharges developed at $B_T = 0.15$ T with varying levels of I_{inj} ranging from $3 - 12$ kA is shown in Figure 5.4. The plasma shape evolution varied significantly between these discharges. This is shown in Figure 5.4(b) which plots the $\left(\Psi_T/\left(B_{p,inj}/I_p\right)\right)^{1/2}$ quantity inferred from ShapeFIT. This quantity explicitly appears in the estimate of the Taylor limit given by equation 2.14 and primarily depends on the plasma shape [29,88]. The variation in plasma shape evolutions and I_{inj} both contribute to the observed variations in $I_p(t)$ shown in Figure 5.4(c) as well as the Taylor limit. Therefore, the variation in plasma shape must be accounted for to assess if the expected $I_{TL} \propto \sqrt{I_{inj}}$ scaling continues to hold in this expanded operating space.

Another effect that needs to be accounted for is the variation in the amount of toroidal windup current I_{windup} from the injected current streams due to the varying levels of I_{inj}. The amount of I_{windup} can be estimated by assuming a simple model in which the injected current strictly follows $\vec{B}$ and has a uniform current density along its helical path which is localized to the LFS plasma edge [170]. In this model, $I_{windup} = GI_{inj}$ where G is a geometric windup factor which describes the number of toroidal transits of the helical injected current stream. The details of this correction are very dependent on the assumed structure of the streams which are outside the scope of this work. Therefore, a simple assumption of a geometric windup factor $G = 2$ will be used based on

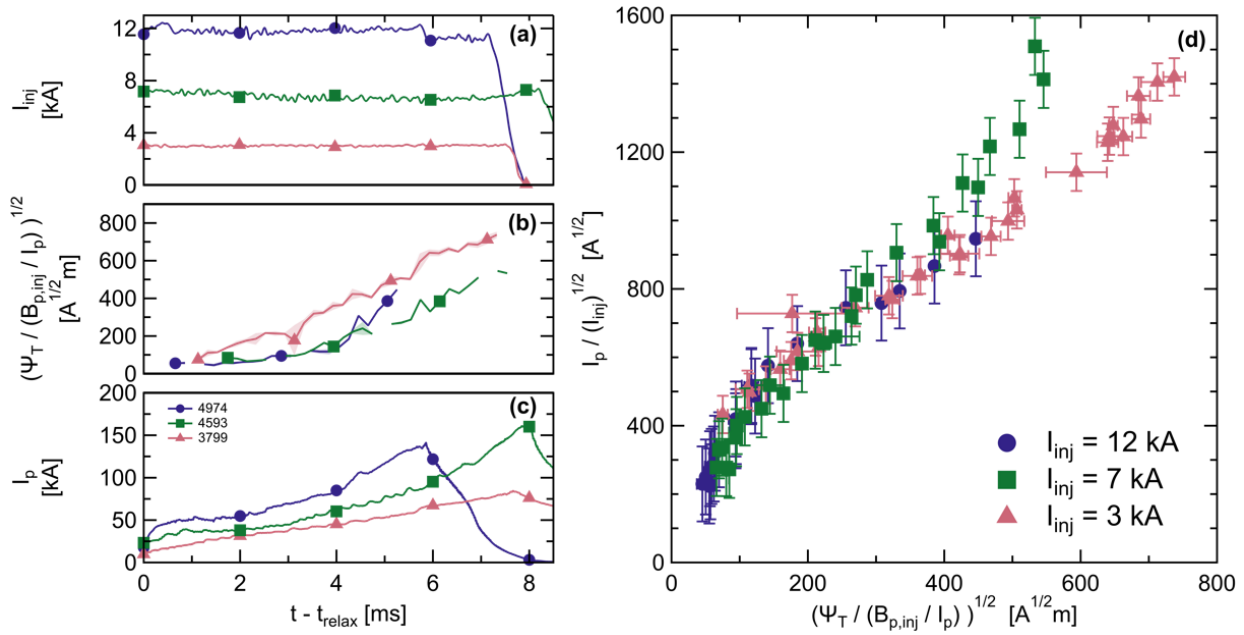

Figure 5.4: Overview of Pegasus-III discharges with varying levels of I_{inj} at $B_T = 0.15$ T: (a) I_{inj}, (b) $\left(\Psi_T/\left(B_{p,inj}/I_p\right)\right)^{1/2}$ metric, (c) I_p and (d) normalized I_p as a function of $\left(\Psi_T/\left(B_{p,inj}/I_p\right)\right)^{1/2}$.

the observation that the field-line pitch typically allows for $1-2$ toroidal passes of the injected current stream between the injector aperture and the top of the vessel [29,52,170]. This observation is generally true throughout these discharges as the field line pitch outside the LFS plasma edge does not change significantly. This $I_{windup} = GI_{inj} \approx 2I_{inj}$ estimate is uniformly subtracted off the measured $I_p(t)$ to provide a first-order correction for the variation in I_{windup} across these discharges.

Figure 5.4(d) plots the $I_p(t)$ normalized by $\sqrt{I_{inj}}$ as function of $\left(\Psi_T/\left(B_{p,inj}/I_p\right)\right)^{1/2}$ for the different scenarios to account for the expected variation in the Taylor limit due to the plasma shape. The vertical error bars are derived from the uncertainty in the I_{windup} estimate and reflect an assumed $\pm I_{inj}$ uncertainty to reflect the coarse nature of this I_p correction. The horizontal error bars arise from the propagated random error in Ψ_T and $B_{p,inj}$ quantities which are extracted from ShapeFIT analysis of these discharges. The uncertainty in these quantities is derived from the Monte Carlo uncertainty analysis described in Section 4.2.2 to determine the random error due to the uncertainty in the magnetic diagnostics that are used as ShapeFIT constraints.

The data presented in Figure 5.4(d) generally agrees within the respective uncertainties across this wide variation in I_{inj}. These discharges utilized the same injector installation and thus the R_{edge} and w_{inj} parameters which appear in the Taylor limit (equation 2.14) are expected to be similar. Therefore, the agreement of the data indicates the $I_{TL} \propto \sqrt{I_{inj}}$ scaling continues to robustly describe LHI plasmas over this factor of four variation in I_{inj} up to 12 kA. Thus, providing confidence in continued performance improvements as the I_{inj} capability is further increased.

This data significantly expands the range over which the $I_{TL} \propto \sqrt{I_{inj}}$ scaling has been demonstrated. This is illustrated in Figure 5.5 which plots I_p as a function of the $\sqrt{I_{inj}}$ for a variety of Pegasus (star) and Pegasus-III (circle) discharges with self-similar plasma shape and $R_0 \approx$ 50 cm. The Pegasus data is from previous Taylor limit scaling studies which varied from 1 to 5 kA [88]. Both sets of data show a clear linear trend. Further, the datasets overlap and are

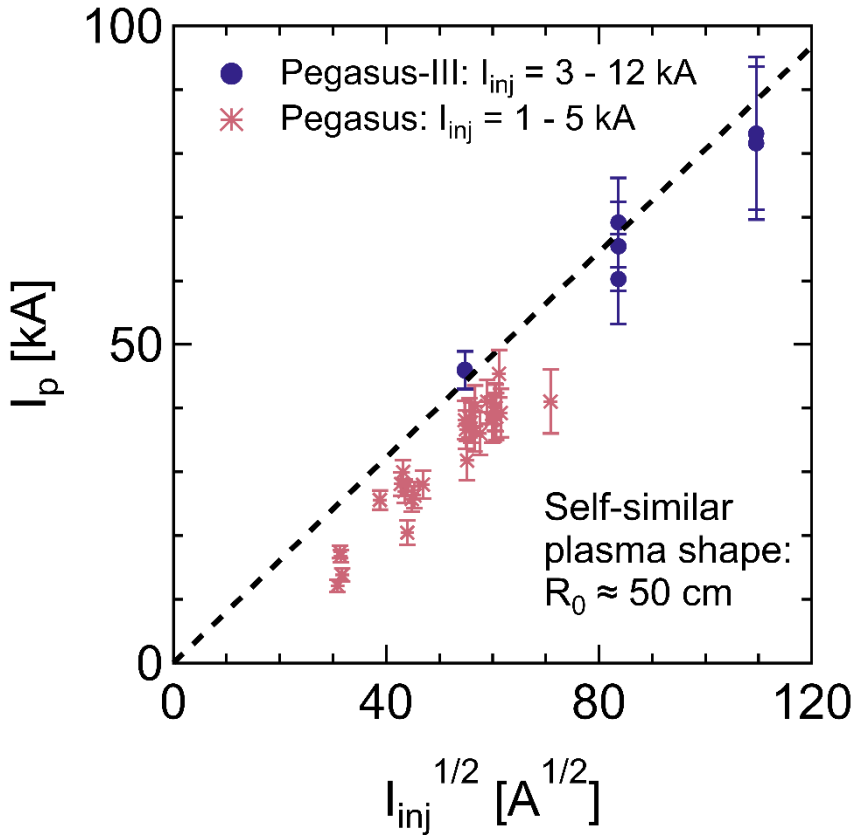

Figure 5.5: Scatterplot of I_p vs $\sqrt{I_{inj}}$ for times when $R_0 \approx 50$ cm in Pegasus and Pegasus-III discharges. Pegasus data is from studies presented in [88].

consistent with each other when $I_{inj} \approx 3$ kA. In total, the Pegasus and Pegasus-III data spans 1 kA $\leq I_{inj} \leq$ 12 kA and follows a robust linear relationship in agreement with the expected $I_{TL} \propto \sqrt{I_{inj}}$ scaling.

5.3 Inferred w_{inj} Across Different Injector Geometries

The majority of LFS LHI operations on Pegasus utilized circular aperture injectors with $A_{inj} = 2$ cm^2. The inferred w_{inj} for these injectors was ~2 cm which is slightly larger than the physical injector diameter $d_{inj} = 1.6$ cm [29,52,88]. The projections for the larger 4 cm^2 circular injectors deployed on Pegasus-III assumed that the nominal $w_{inj} \approx 2$ cm should scale proportionally with the increased injector diameter, resulting in $w_{inj} \approx 2.8$ cm. However, the extent of this edge current region has not yet been directly measured, and it is not clear how additional physical processes such as plasma instabilities, magnetic shear, or particle drifts impact this width. For example, previous work on Pegasus identified that misalignment of the injector array to the magnetic equilibrium flux surfaces can result in larger effective w_{inj} [88]. This illustrated the importance and care needed during the injector design and installation to properly align the injectors to the planned plasma equilibrium. Future injector design can also be informed by understanding the impact the width of the injector aperture has on the effective w_{inj}.

The Pegasus and Pegasus-III LHI systems utilized arrays of circular aperture injectors with nominal diameters of 1.6 cm and 2.3 cm, respectively. A detailed comparison of these injector installations is provided in Figure 5.6. A head-on view of both injector sets is shown in Figure 5.6(a) along with the nominal d_{inj}. Figure 5.6(b) shows the (R, Z) location of these arrays along with representative poloidal flux contours and plasma boundary inferred from ShapeFIT for a typical LHI discharge generated by these injector configurations. The w_{inj} parameter is the width of the injected poloidal flux that intercepts the injectors and is taken at the plasma midplane ($Z = Z_0$). The bounding poloidal flux contours of this injection region for the Pegasus and Pegasus-III are indicated by the thick solid and dotted lines in Figure 5.6(b), respectively. The arrays were installed in similar positions and were both reasonably well-aligned to the poloidal flux contours. Therefore, the inferred variation in w_{inj} between the two injector arrays when mapping the injector aperture to the poloidal flux contours is predominately set by the d_{inj} ratio.

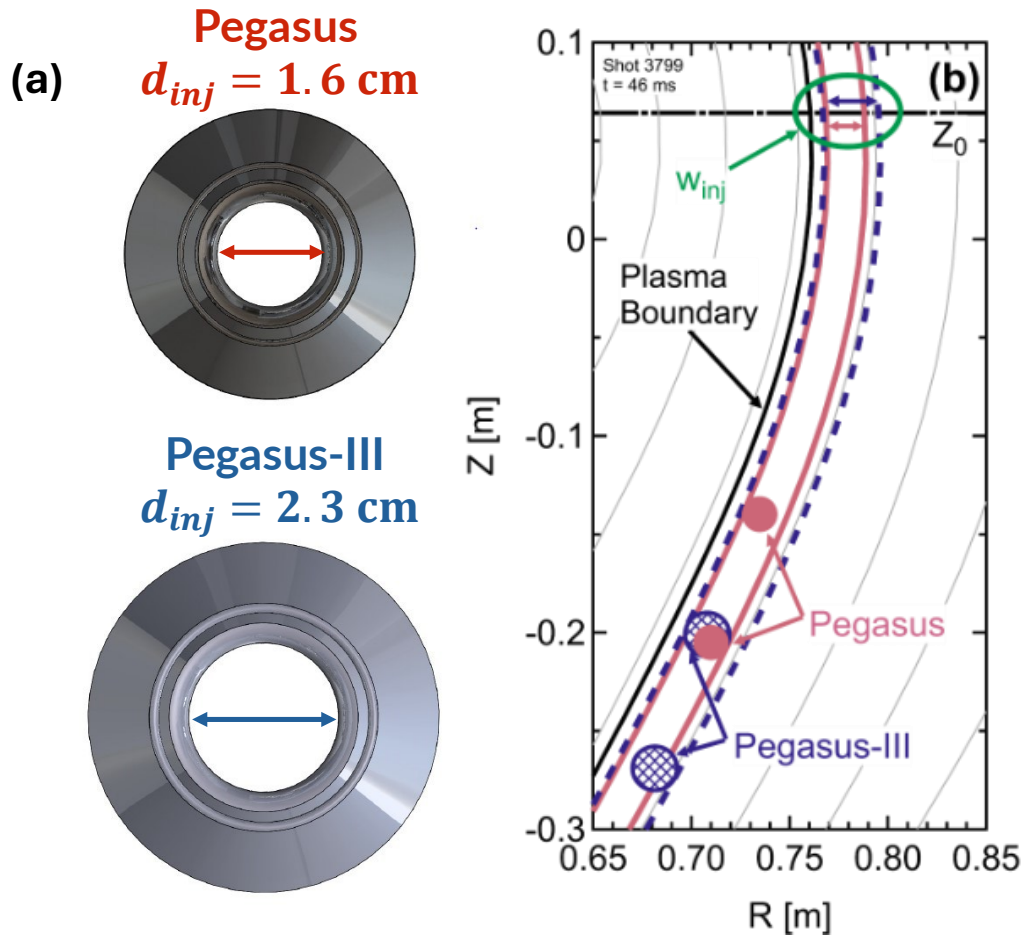

Figure 5.6: Comparison of Pegasus ($d_{inj} = 1.6$ cm) and Pegasus-III ($d_{inj} = 2.3$ cm) injector arrays: (a) head-on view of injectors with d_{inj} indicated and (b) poloidal position of injectors near representative plasma boundary and poloidal flux contours inferred from ShapeFIT.

A subset of the previously discussed Pegasus and Pegasus-III scaling studies are used to assess the impact of injector aperture on w_{inj}. The discharges were selected to have self-similar plasma shape evolutions and I_{inj} to minimize potential variations in w_{inj} from other plasma shaping and/or beam-related effects. These effects along with other processes (e.g. magnetic shear, plasma instabilities and transport) may modify the effective w_{inj}. However, these effects are not investigated here.

Figure 5.7 shows scatterplots of I_p as a function of $\left(\Psi_T I_{inj}/\left(B_{p,inj}/I_p\right)\right)^{1/2}$ for the Pegasus and Pegasus-III datasets. The effective w_{inj} of the arrays can be inferred from the slope of these scatterplots. For clarity, the Taylor limit formulation given by equation 2.14 is repeated here:

$$I_{TL} \approx \sqrt{\frac{1}{2\pi R_{edge} w_{inj}}} \sqrt{\frac{\Psi_T I_{inj}}{(B_{p,inj}/I_p)}} \tag{5.1}$$

which scales linearly with $\sqrt{\Psi_T I_{inj}/\left(B_{p,inj}/I_p\right)}$. Plotting the data in this way effectively accounts for any variations in the Taylor limit due to differences in plasma shape, B_T, and I_{inj}. Further, the previously discussed $I_{windup} = 2I_{inj}$ correction to I_p is also employed here. The vertical error bars correspond to the uncertainty in the I_{windup} correction. The horizontal error bars are derived from the propagated uncertainty of the Ψ_T and $B_{p,inj}$ quantities inferred from the ShapeFIT analysis.

As expected, the data in Figure 5.7 clearly exhibits a linear trend for both sets of injectors. Further, the slope of the data is $\propto \left(R_{edge} w_{inj}\right)^{-1/2}$. Due to the similar injector installation position for both arrays, R_{edge} is comparable in all cases. Therefore, the slope is effectively $\propto w_{inj}^{-1/2}$. The

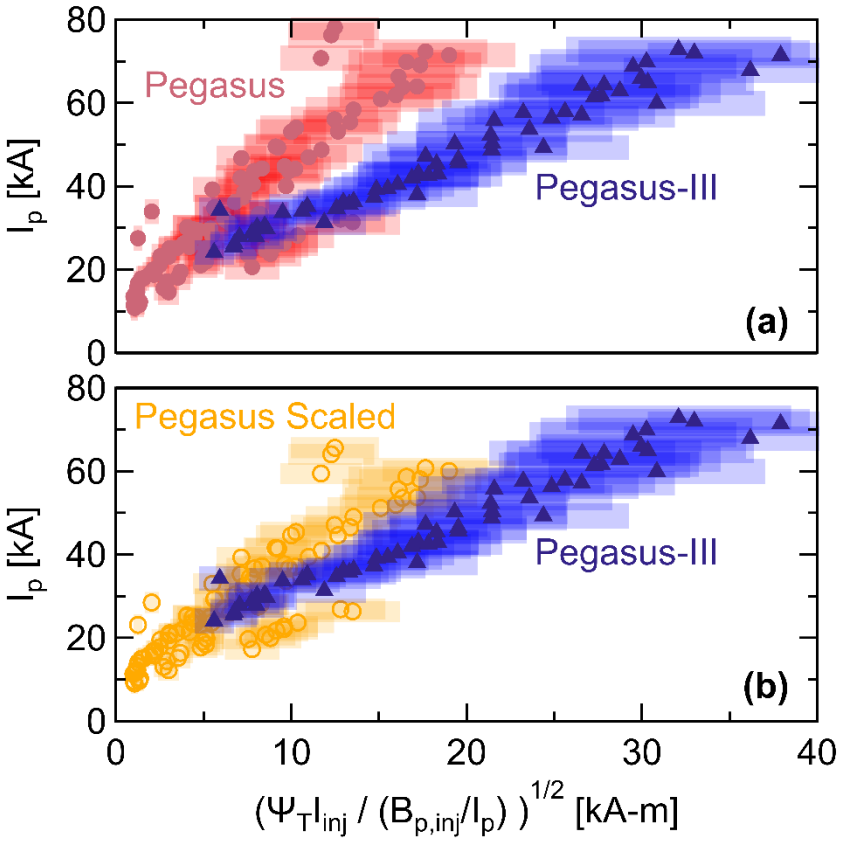

Figure 5.7: Scatterplots of I_p vs $\left(\Psi_T I_{inj}/\left(B_{p,inj}/I_p\right)\right)^{1/2}$ for the Pegasus and Pegasus-III injector arrays with different d_{inj}. The Pegasus data in (b) is scaled by the expected $I_{TL} \propto w_{inj}^{-1/2}$ ratio assuming $w_{inj} \sim d_{inj}$.

two data sets have different slopes and vary outside of their respective uncertainties for $I_p > 40$ kA which indicates a statistically significant variation in their effective w_{inj}. The narrower injector set used on Pegasus ($d_{inj} = 1.6$ cm) has a steeper slope in Figure 5.7(a) corresponding to a narrower effective w_{inj}. This demonstrates that injector design can be leveraged to optimize the Taylor limit by utilizing a narrower current channel.

The variation in the inferred w_{inj} is consistent with $w_{inj} \sim d_{inj}$. This is illustrated in Figure 5.7(b) where the Pegasus data ($d_{inj} = 1.6$ cm) has been scaled by the expected difference in the Taylor limit relative to the Pegasus-III data assuming $w_{inj} \sim d_{inj}$ (i.e. $(1.6\text{ cm}/2.3\text{ cm})^{1/2} \approx 0.83$). This scaled data exhibits significant overlap with the Pegasus-III dataset within their respective error bars. This is consistent with the expected behavior based on the mapping of the injector apertures to the flux surfaces shown in Figure 5.6(b) in that the variation in the inferred w_{inj} is predominately set by d_{inj}.

5.4 Quantitative Assessment of I_{TL} Calculation

The preceding sections outlined a variety of experiments which validated the expected scaling relations of the Taylor limit in the expanded Pegasus-III operating space. This same data is used here to validate the quantitative calculations of the Taylor limit provided by equation 2.14 over an expanded operating space compared to previous work on Pegasus [29,88].

Early in LFS LHI discharges, $I_p(t)$ is constrained by the Taylor limit for an extended period which largely dictates the I_p that can be ultimately achieved [29]. As such, projections of LHI systems that are subject to an extended Taylor limited phase can be significantly impacted by the uncertainty of the Taylor limit estimation. The simplified model originally developed by Battaglia et al. [88] has proven to robustly describe the scaling of LHI discharges as highlighted earlier in this chapter. However, accurate projections require robust quantitative agreement in addition to the scaling behavior. Previous validation work by Barr et al. [29] did show reasonable agreement to Pegasus data.

The I_{TL} calculation shows good agreement across the Pegasus-III operating space. Figure 5.8 shows a comparison of I_{TL} calculated by the model to the measured I_p for three Pegasus-III discharges which broadly span the parameter space explored in this work (3 kA $\leq I_{inj} \leq$ 12 kA

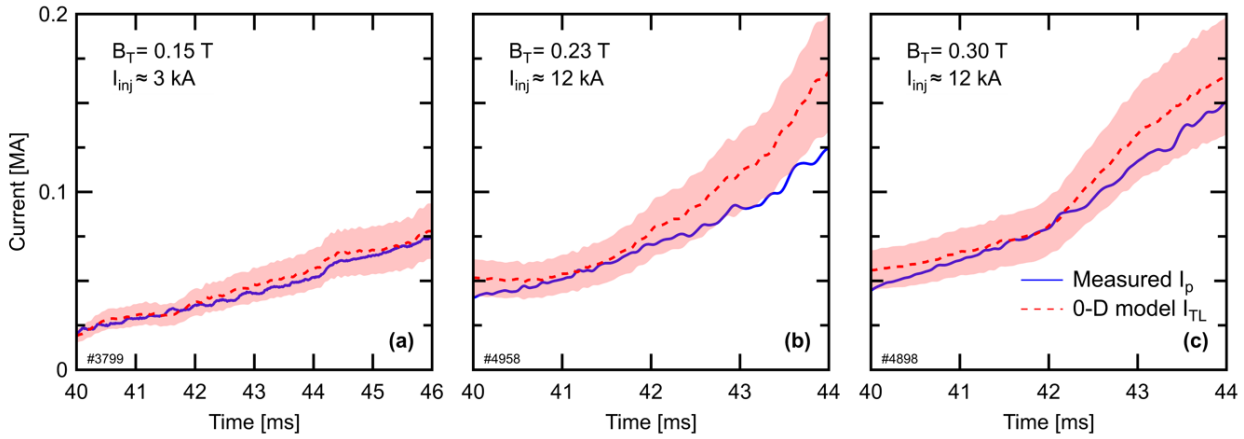

Figure 5.8: Comparisons of I_p (solid) and I_{TL} calculated by 0-D model (dashed) for discharges spanning Pegasus-III operating space. Shaded region represents $\pm 20\%$ uncertainty on I_{TL} calculation.

and $0.15\ \text{T} \leq B_T \leq 0.30\ \text{T}$). Once again, $I_{windup} = 2I_{inj}$ is subtracted from I_p as a first-order correction for the geometric windup current. Here, w_{inj} is assumed to be the nominal injector diameter $d_{inj} \approx 2.3$ cm.

The error band for the I_{TL} estimate shown in Figure 5.8 is motivated by the systematic errors inherent to the plasma boundary predicted by ShapeFIT. As discussed in Section 4.2.2, ShapeFIT systematically overestimates Ψ_T by ~40%, on average, compared to the reconstructed equilibria. This translates to a ~20% uncertainty when propagated to the Taylor limit estimate using the plasma shape evolution inferred from ShapeFIT analysis ($I_{TL} \propto \sqrt{\Psi_T}$). Admittedly, the analysis described in Section 4.2.2 is limited to the end of LHI discharges and may not necessarily reflect the systematic uncertainties throughout the entire discharge evolution. However, reconstructions during the early phase of these LHI discharges at lower I_p are challenging and not presently available. Therefore, this ~20% uncertainty in the I_{TL} estimate is assumed to be representative throughout these discharges to provide some context when quantitatively comparing to the measured $I_p(t)$.

Generally, the estimated I_{TL} and measured $I_p(t)$ shown in Figure 5.8 agree within this assumed uncertainty. This is consistent with the scaling observations discussed in previous sections which indicated that $I_p(t)$ in these Pegasus-III discharges were dictated by the Taylor limit (i.e. $I_p(t) = I_{TL}(t)$). The agreement also indicates that the present Taylor limit formulation (equation 2.14) provides quantitatively accurate estimates of I_{TL} given the uncertainty in the shaping moments

inferred from ShapeFIT. This gives confidence that theI_{TL} calculation is a useful tool for projecting LHI performance as the operating space continues to be expanded on Pegasus-III and beyond. Also, it highlights that further validation of these estimates would benefit from improved accuracy in the inferred plasma boundary during LHI discharges by ShapeFIT or some other boundary reconstruction method.

5.5 Magnetic Activity in Discharges Over-driven at Taylor Limit

The Taylor limit has proven to be a robust global I_p limit during LHI discharges throughout this work and in previous studies [29,88]. For scaling to higher I_p, it is desirable to increase the Taylor limit to fully utilize the available helicity input. However, the properties of discharges with excess helicity input (i.e. over-driven) at the Taylor limit have not been previously characterized. This work provides an array of discharges that are suitable to begin this characterization. The remainder of this chapter highlights observations from this initial characterization and potential implications for LHI scenario development.

Throughout the course of the scaling studies discussed earlier in this chapter, complementary discharges with excess helicity input were developed to probe the Taylor limit. These discharges possessed identical parameters that influence the Taylor limit (i.e. B_T, I_{inj}, and shape) but higher helicity input $V_{LHI} \propto A_{inj}V_{inj}$. The injector impedance is set by the arc and/or edge neutral density which can be coarsely adjusted via injector neutral fueling rates [171]. Reducing the injector neutral fueling increases the injector impedance and enables higher V_{inj} at fixed I_{inj} via power supply feedback control. This enabled the creation of discharges at fixed I_{TL} and varied amounts of V_{inj}. Generally, these discharges were observed to remain clamped at $I_p = I_{TL}$, despite the increased helicity input. Therefore, they provide the ability to characterize the properties of discharges which are over-driven at the Taylor limit.

A pair of discharges which demonstrate this behavior are shown in Figure 5.9. Both discharges were sustained at the Taylor limit for their entire duration. This is shown in Figure 5.9(a) which plots the identical I_p trajectories which agree with the Taylor limit predicted by the 0-D model. The "baseline" discharge (#3799) was sustained by $V_{inj} \approx 400$ V throughout its I_p ramp as shown

in Figure 5.9(b). The "over-driven" discharge (#3598) had a reduced amount of injector fueling which led to a factor of $\sim 1.5-3$ increase in V_{inj} relative to the baseline scenario. This results in a higher helicity input provided by the injectors as indicated by the increased V_{LHI} shown in Figure 5.9(c) Despite the increased helicity input in the over-driven discharge, the $I_p(t)$ is identical in both discharges which illustrates the Taylor limit acts as a robust absolute I_p limit.

The magnetic fluctuation activity is qualitatively different in these two cases. Figure 5.9(d) and (e) show the vertical magnetic field fluctuations normalized by the local toroidal magnetic field strength $\tilde{b}_Z/B_T$. These fluctuations are measured by representative $\dot{B}$ coils located outside the plasma edge on the LFS and HFS vessel wall at the machine midplane. The signals have been vertically offset for clarity. Early in the I_p ramp, the fluctuations measured in each discharge are of a comparable amplitude. In the over-driven discharge, the discrete bursts of activity persist throughout the entire discharge at a relatively consistent magnitude. However, these bursts are less pronounced in the baseline discharge beginning at ~ 41 ms and continue to decrease in amplitude for the remainder of the discharge. This observed difference in the amplitude of the magnetic fluctuations motivates a more detailed analysis.

The magnetic activity in these discharges possess similar spectral features which have been commonly observed during LHI and characterized in previous work [12,86–88,112,172]. Figure 5.10 shows representative PSD spectra measured from pickup coils located on the LFS and HFS of the machine. These spectra represent data averaged over the $t = 43-44$ ms period in each discharge. There is a characteristic $n = 1$ mode at $f_{n=1} = 20-40$ kHz observed on the LFS magnetics which is associated with line-tied kinking of the injected current streams [12,86,87]. This feature is not observed on HFS magnetics. Both the LFS and HFS magnetics observe an $n = 0$ low-f ($\lesssim 10$ kHz) peak attributed to bulk plasma motion. Further, the poloidal phase shift between the LFS and HFS magnetics for this $n = 0$ component is consistent with radial plasma motion [87,88,172]. Additionally, these features sit atop a spectrum of broadband magnetic turbulence which has previously been shown to be consistent with kinetic Alfvén wave turbulence [86,112]. Unfortunately, higher bandwidth measurements were not available to assess the MHD content at higher frequencies which has been previously correlated to current drive [86,112] and reconnection activity [171].

There is a notable frequency shift of the $n = 1$ mode ($f_{n=1}$) between these two discharges. Previous work has shown that $f_{n=1} \propto v_A$ where v_A is the local Alfvén velocity in the edge injection region [87]. As discussed previously, the neutral fueling was reduced in the over-driven discharge to increase V_{inj} relative to the baseline. Thomson scattering measurements indicate this resulted in an approximately factor of four reduction in the edge electron density. Assuming

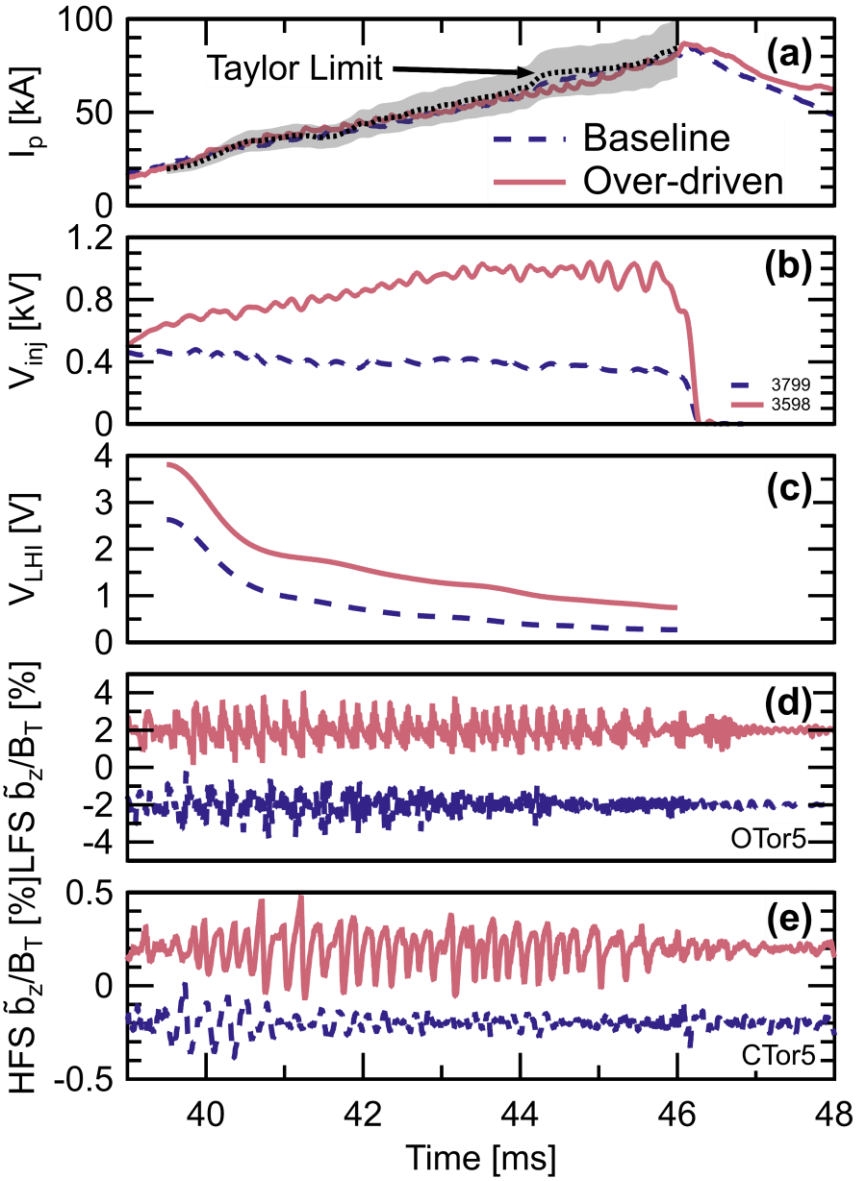

Figure 5.9: Overview of discharges sustained with varying amounts of helicity input: (a) I_p and predicted Taylor limit, (b) V_{inj}, (c) V_{LHI} and normalized vertical magnetic field fluctuations measured by a representative $\dot{B}$ coil outside the (d) LFS and (e) HFS plasma edge. The signals in (d) and (e) are vertically offset by $\pm 2\%$ and $\pm 0.2\%$ for clarity, respectively.

quasineutrality, this leads to roughly a factor of two increase in v_A in the over-driven discharge. As expected, this increase in v_A is consistent with the observed increase in $f_{n=1}$ in the over-driven discharge.

The increased magnetic fluctuation power is predominately concentrated in the low frequency ($3 - 12$ kHz) spectral region. This spectral region is highlighted by the vertical gray shaded region in Figure 5.10. The power in this region is roughly an order of magnitude higher in the over-driven discharge relative to the baseline during this period on both the LFS and HFS sensors. This suggests that this low frequency activity may be related to the amount of helicity input provided by the injectors while being sustained at $I_p = I_{TL}$.

This observation is further supported by tracking the power that resides within this low frequency magnetic activity along with the amount of helicity input provided by the injectors. The over-driven discharge has more V_{inj} and V_{LHI} as shown in Figure 5.9(b) and (c), respectively.

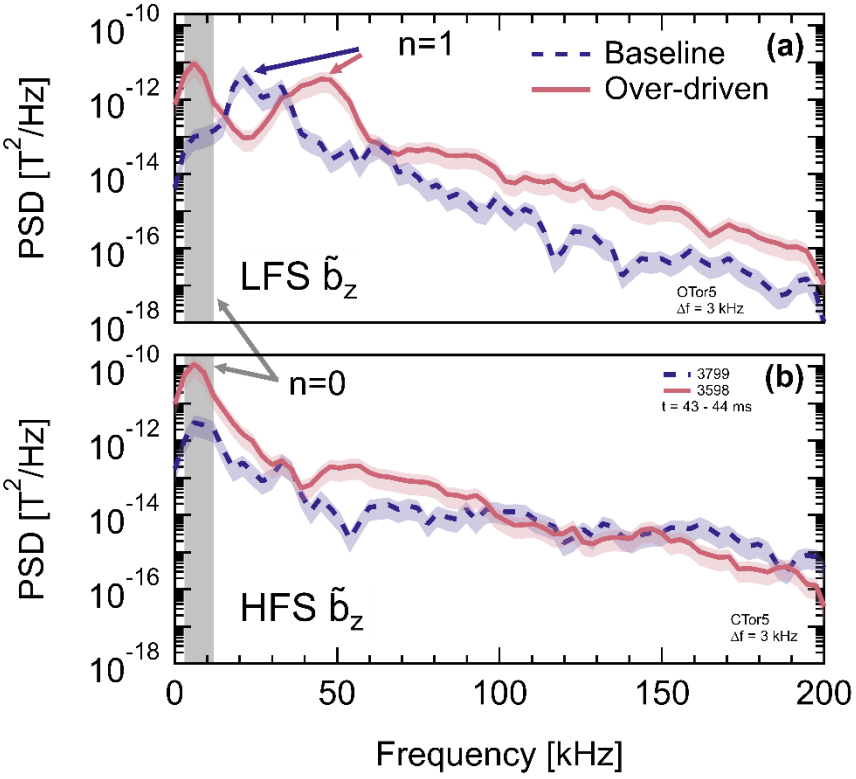

Figure 5.10: Magnetic field fluctuation power spectral density in baseline (dotted) and over-driven (solid) discharges as measured by representative $\dot{B}$ coils located outside the (a) LFS and (b) HFS plasma edge. The $\tilde{b}_Z$ data is averaged over the $t = 43 - 44$ ms period.

Figure 5.11(a) and (b) shows the integrated magnetic fluctuation power $\tilde{b}_z^2$ in the low frequency range ($3-12$ kHz) measured by a representative sensor located outside the LFS plasma edge throughout both discharges as a function of V_{LHI}. The fluctuation power is calculated every 0.5 ms by integrating the PSD which is averaged over a 1 ms time window centered around the time of interest. Similarly, the V_{LHI} value for each data point represents the average value over the same 1 ms time windows. The uncertainty in $\tilde{b}_z^2$ is derived by propagating the integrated uncertainty of the PSD over the $3-12$ kHz spectral range. The horizontal error bars for V_{LHI} represent the standard deviation over each averaging window.

The power in these low frequency magnetic fluctuations is correlated with the amount of helicity input when sustained at $I_p = I_{TL}$. Figure 5.11(a) illustrates that the measured $\tilde{b}_z^2$ increases with V_{LHI}. A similar trend is observed in both discharges. At lower helicity input, there is an offset linear trend which may suggest there is a threshold amount of V_{LHI} needed to drive this increased low-f activity. Interestingly, the power appears to rollover and saturate as the system is strongly over-driven at $V_{LHI} \gtrsim 2$ V.

The low frequency component of $\tilde{b}_Z$ has a 180° phase shift between LFS and HFS sensors consistent with abrupt radial plasma motion [87,88,173]. This large-scale motion should result in highly correlated fluctuation measurements around the plasma boundary. The cross-power and

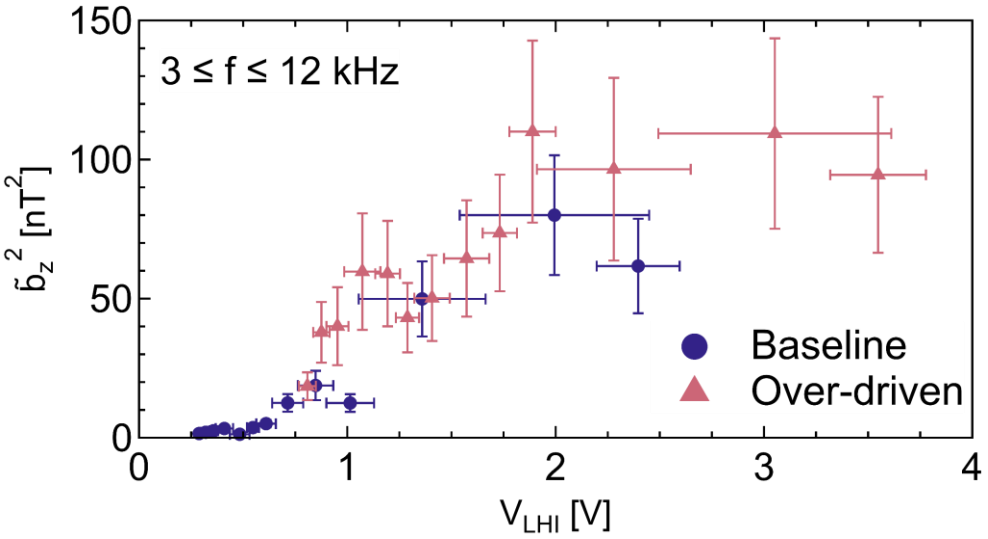

Figure 5.11: Comparison of integrated power in low frequency ($3-12$ kHz) $\tilde{b}_Z$ as a function of V_{LHI} throughout the baseline (circle) and over-driven (triangle) discharges. $\tilde{b}_Z$ measured by representative $\dot{B}$ coil located outside the LFS plasma edge and averaged over 1 ms periods.

coherence quantities described in Section 3.3.4 are used to quantify this correlation. These quantities are shown in Figure 5.12 for the entire poloidal diagnostic array during the $39 - 40$ ms (Figure 5.12(a,c)) and $43 - 44$ ms (Figure 5.12(b,d)) periods of both discharges. The sensor poloidal angle θ_{phys} is in machine coordinates defined from the outboard midplane relative to the center of the machine and is shown schematically in Figure 5.12(e). Here, a diagnostic located on the LFS device midplane ($\theta_{phys} = 0°$) is used as the reference for this analysis. Early in the I_p ramp, the discharges exhibit similar levels of power with a similarly high degree of correlation ($\hat{\gamma}^2 \geq 0.7$) over most of the poloidal plane. In the baseline discharge, the cross-power decreases significantly as the discharge proceeds. Further, the fluctuations become significantly less correlated later in the I_p ramp as indicated by the drop in coherence on all sensors in the later time window. In contrast, the fluctuations in the over-driven discharge are highly correlated throughout and increase in power as the discharge proceeds. This behavior illustrates that these fluctuations are likely caused by large-scale events based on the high level of coherence around the entire

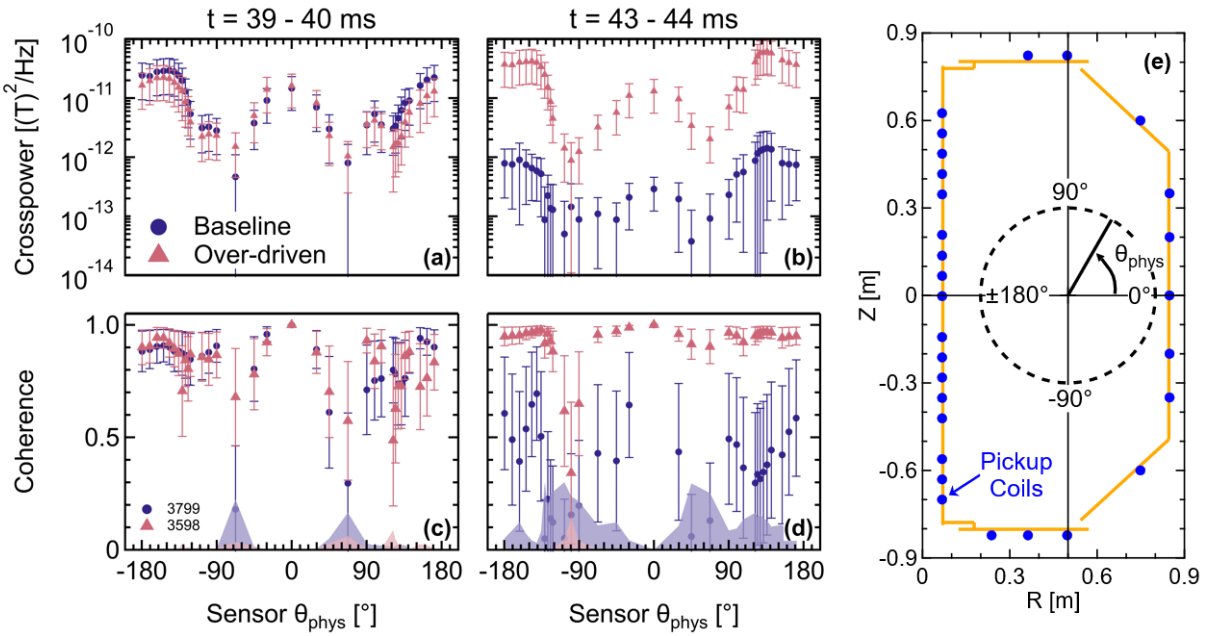

Figure 5.12: Poloidal distribution of the cross-power and coherence for low frequency ($3 - 12$ kHz) $\tilde{b}_Z$ during the (a, c) $39 - 40$ ms and (b, d) $43 - 44$ ms periods in the baseline and over-driven discharges. (e) poloidal location of sensors and definition of θ_{phys}. A midplane LFS pickup coil ($\theta_{phys} = 0$) is used as reference sensor. Shaded region at the bottom of the coherence plots indicates the bias error.

plasma perimeter. Further, this large-scale phenomenon persists while there is a sufficient level of helicity input.

These discharges exhibit intermittent bursts of $n = 1$ activity which have been observed in previous LHI studies [12,87,88]. These bursts are also accompanied by the lower frequency $n = 0$ activity discussed previously. The peak amplitude of the bursts occurs just prior to discrete increases in I_p that are on the order of I_{inj}. These bursts have been used in previous work [87] as indirect evidence of large-scale reconnection events which are predicted by NIMROD simulations [49,50]. In these simulations, bursts of magnetic activity and discrete increases in I_p were a result of large-scale reconnection events. During these events, adjacent passes of the injected current streams reconnect and release an axisymmetric ring of current which diffuses inward. This current drive mechanism acts to transport current from the injected current streams into the plasma core thereby relaxing the system.

These mechanisms correspond to different characteristic frequencies in the simulations. The abrupt movement of the injected current stream associated with the reconnection event occurs around the experimental $n = 1$ frequency ($f \sim 20$ kHz). The lower-f activity ($f \sim 6$ kHz) is associated with the slower timescale of the stream reorienting itself to the magnetic field following release of the current ring. Additionally, the release of the inward diffusing axisymmetric current ring would appear as a radial plasma motion consistent with the experimentally observed $n = 0$ radial motion.

The behavior of these bursts is summarized in Figure 5.13. The measured I_p and a representative LFS $\dot{B}$ signal are shown for the baseline and over-driven discharges in Figure 5.13(a) and (b), respectively. Here, a period containing several bursts in each discharge is chosen to illustrate their features. The bursts of $\dot{B}$ signal are preceded by the discrete increases in I_p which are approximately equivalent to $I_{inj} \approx 3$ kA in these discharges. A noticeable difference between the two discharges is the rate at which these bursts occur. During this time window, the period between bursts in the over-driven discharge is roughly half that of the baseline discharge. This can be quantified by defining a burst period ΔT_{burst} which represents the time between successive burst events and is defined visually in Figure 5.13(a).

This period between bursts of $n = 1$ activity is correlated to the amount of helicity input provided by the injectors. The ΔT_{burst} was tracked throughout both discharges and is shown in

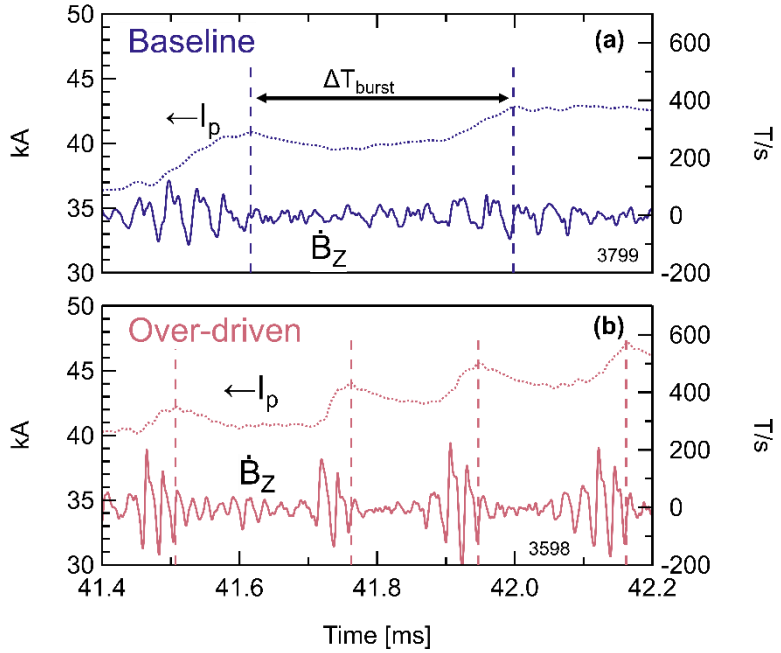

Figure 5.13: Comparison of I_p (dotted, left axes) and representative LFS $\dot{B}_Z$ signal (solid line, right axes) during period of bursty $n = 1$ magnetic activity in (a) baseline and (b) over-driven discharges. ΔT_{burst} is also visually defined.

Figure 5.14 as a function of V_{LHI}. This plot illustrates that ΔT_{burst} is shorter as the system is increasingly over-driven. This behavior is observed in both discharges. In the baseline discharge, the bursts stop occurring at ~43.5 ms which is when V_{LHI} falls below 0.5 V for the remainder of the discharge. In the over-driven discharge, the bursts persist throughout and V_{LHI} is maintained above 0.75 V. These observations illustrate that the rate of these bursts is correlated to the amount of helicity input. Assuming these burst events are indicators of large-scale reconnection events, these events occur more often as the system is increasingly over-driven at the Taylor limit. Additionally, the observation that the bursts are not apparent in the baseline discharge at $V_{LHI} <$ 0.5 V supports the notion that these events require the system to be sufficiently over-driven.

The aforementioned observations were made throughout discharges in which the plasma and Taylor limit were dynamically evolving. So, it is fair to question if other factors besides the helicity input were influencing these trends. observation of increased power in low frequency magnetic fluctuations and an increased rate of $n = 1$ bursts were observed over a range of helicity input. Figure 5.15 provides an overview of a series of Taylor-limited discharges with self-similar I_{inj}, B_T and shape evolutions. Figure 5.15(a) shows the $I_p \sim I_{TL}$ trajectories in these discharges. The V_{inj} was varied by modifying the injector fueling and is shown in Figure 5.15(b). Figure 5.15(c) and

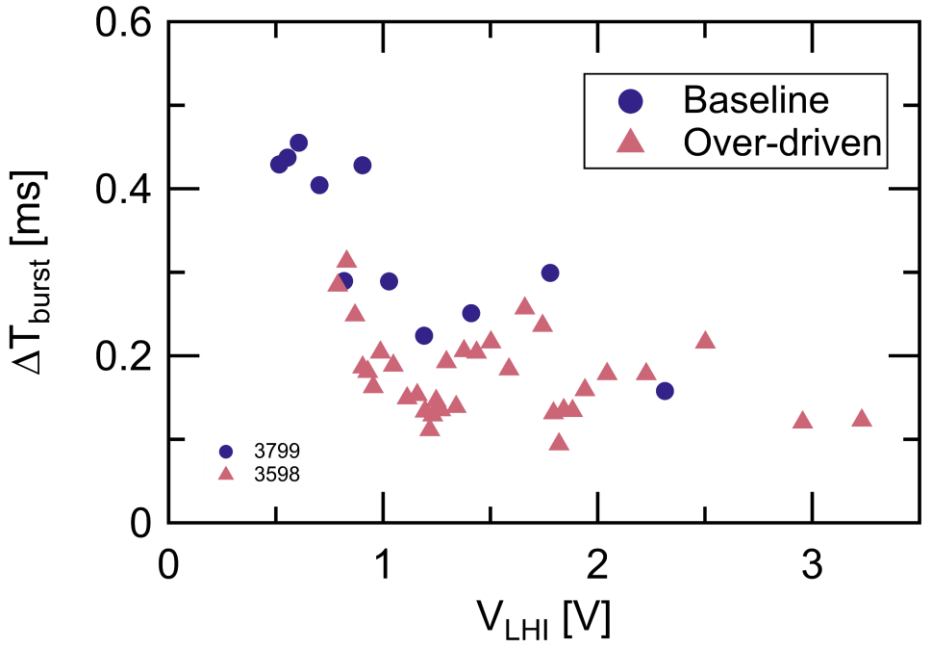

Figure 5.14: Comparison of ΔT_{burst} throughout baseline (circle) and over-driven (triangle) discharges.

(d) show the low frequency ($3-12$ kHz) $\tilde{b}_z^2$ measured by a representative $\dot{B}$ coil outside the LFS plasma edge and the average ΔT_{burst}, respectively, as functions of V_{LHI} during the $41-43$ ms time window. This time window is indicated by the shaded region in Figure 5.15(a) and (b). The error bars in Figure 5.15(c) and (d) correspond to the uncertainty derived during the $\tilde{b}_z^2$ PSD calculation and the standard error of the ΔT_{burst} mean, respectively.

These data demonstrate correlations with the amount of V_{LHI}. As V_{LHI} is increased, the power in the low-f magnetic fluctuations increases and the period between bursts of $n=1$ magnetic activity decreases as illustrated in Figure 5.15(c) and (d), respectively. These trends are similar to those presented in Figure 5.11 and Figure 5.13. This suggests that these trends are not related to the dynamics of these discharges or the evolving Taylor limit but are likely related to the amount of helicity input.

It is important to note that the increased low frequency magnetic fluctuations and presence of $n=1$ bursts are not solely determined by the amount of V_{LHI}. In these discharges, this behavior was generally observed when the injectors provided $V_{LHI} \gtrsim 0.5$ V. However, the bursts were not prevalent in all discharges throughout this work and have been absent in previous LHI operating regimes [12,46]. For example, the bursts were entirely absent from the discharges described in the

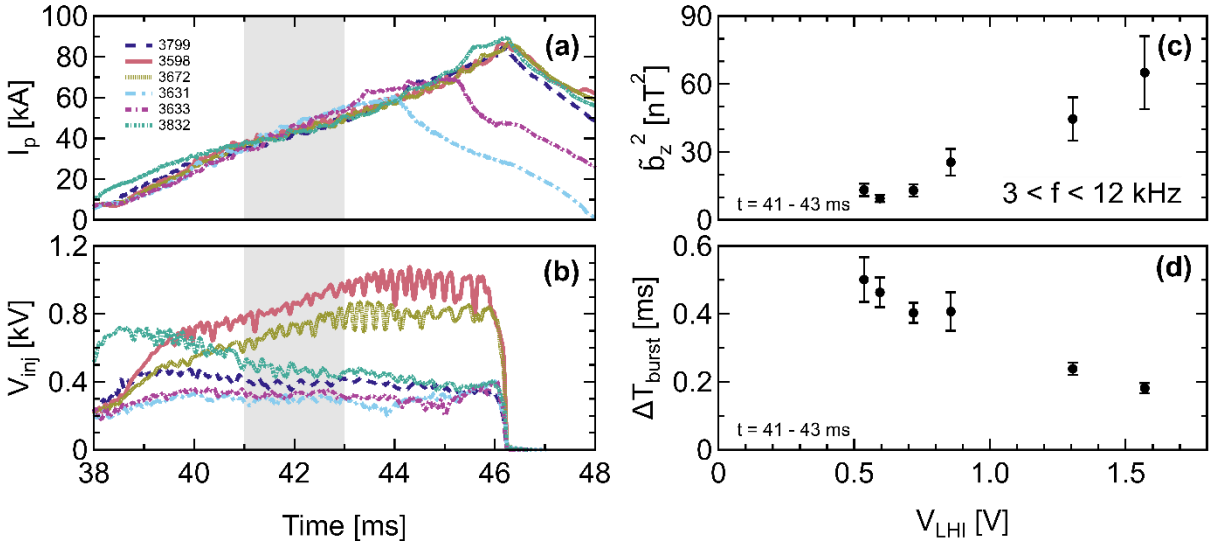

Figure 5.15: Comparison of low-f $\tilde{b}_z^2$ and ΔT_{burst} for similar discharges with varying levels of V_{inj}. (a) I_p and (b) V_{inj} evolutions for the various discharges. (c) integrated power in low frequency (3-12 kHz) $\tilde{b}_Z$ measured by a representative LFS $\dot{B}$ coil and (d) average ΔT_{burst} as a function of V_{LHI} during the $41 - 43$ ms time window. Shaded region in (a) and (b) correspond to this averaging window.

Pegasus-III B_T scan described in Section 5.1. Those discharges were all sustained at $I_p = I_{TL}$ and provided $V_{LHI} > 0.5$ V throughout their entire evolution. These discharges operated at a higher Taylor limit and potentially different amounts of excess helicity input. Here, the excess helicity input refers to the amount of helicity provided to the system from all sources above what would be needed to sustain $I_p = I_{TL}$. It is important to note that these discharges also had a comparable or larger amount of inductive drive (V_{IND}) relative to V_{LHI}. This provides an additional helicity source which also varies throughout these scenarios. This will be discussed in more detail in the following section.

All else being equal, the amount of excess helicity input increases with V_{LHI}. Therefore, the amount of excess helicity input in the baseline and over-driven discharges discussed in this section covary with V_{LHI}. However, it is not possible to accurately quantify the amount of excess helicity input in these discharges because it depends on the amount of helicity dissipation in the system. This is difficult to accurately quantify with the current limited understanding of impurity concentrations in LHI discharges. Nonetheless, the amount of helicity input provided to the system while sustained at the Taylor limit does lead to an increased rate of bursts of $n = 1$ activity and increased power in low frequency magnetic fluctuations in these discharges. These observations

are consistent with an increased rate of large-scale reconnection events as the system is increasingly over-driven.

The increased rate of large-scale reconnection events leads to an apparent increase in the core current density. This is indicated by an increase in the normalized internal plasma inductance ℓ_i when the system is over-driven at $I_p = I_{TL}$. The KFIT equilibrium reconstruction code was used to infer the time-evolving magnetic equilibrium near the end of the baseline and over-driven discharges. Figure 5.16(a) shows the I_p (left) and I_{inj} (right) near the end of both discharges. These reconstructions only used external magnetic diagnostics as constraints. Therefore, the details of the internal profiles are not uniquely determined. However, the relative peaking of the current profile can be meaningfully interpreted via ℓ_i in these highly shaped plasmas [174]. Figure 5.16(b) shows the reconstructed ℓ_i in both discharges near peak I_p. The error bars represent a $\pm 9\%$ uncertainty which was determined from previous characterization of the KFIT output uncertainty using a Monte Carlo error analysis [156]. The reconstructed ℓ_i is roughly 50% higher in the over-driven discharge while the injectors are on ($I_{inj} \neq 0$). This is indicative of a less hollow current profile with more current driven in the core of the plasma. As the injectors are shut off ($I_{inj} \to 0$), the reconstructed ℓ_i converges to self-similar values and agree within its uncertainty when $I_{inj} = 0$. This suggests that the higher ℓ_i is related to the system being over-driven while the injectors are on and providing excess helicity input.

The increased amount of current driven in the plasma core leads to a more uniform λ profile. Figure 5.16(c) shows the reconstructed $\lambda(\Psi_N)$ for each discharge just prior to injector shutoff ($t = 46$ ms) corresponding to the shaded period in Figure 5.16(a,b). The λ in the outer half of the plasma ($\Psi_N \gtrsim 0.5$) is comparable in both discharges with the over-driven discharge being marginally lower. The λ in the core ($\Psi_N \approx 0$) of the over-driven discharge is roughly twice the baseline discharge. Although the details of $\lambda(\Psi_N)$ are not uniquely determined in this analysis, the relative flattening of the λ profile in the over-driven discharge is meaningful given the less hollow current profile indicated by the increased ℓ_i. This flatter λ profile is indicative of a greater degree of relaxation.. In these discharges, this increased level of relaxation appears to be driven by the increased rate of large-scale reconnection events which are more effectively transporting current from the plasma edge into the core.

Despite the variation in profile shape, the volume-averaged λ (i.e. λ_p) is not significantly different in these discharges. This is important when considering the Taylor limit formulation given by equation 2.10 is derived from the $\lambda_p \leq \lambda_{edge}$ constraint. Here, λ_p and λ_{edge} represent average values over the plasma and edge injection regions, respectively. The average value of set by the injectors in the edge injection region is given by

$$\lambda_{edge} = \mu_0 \frac{I_{inj}}{\psi_{p,inj}} = \mu_0 \frac{I_{inj}}{2\pi R_{edge} w_{inj} B_{p,inj}}. \tag{5.2}$$

The computed values of λ_p agree well with this λ_{edge} estimate which assumes $w_{inj} = d_{inj} =$ 2.3 cm. This is indicataed by the horizontal dashed line in Figure 5.16(c) which represents $\lambda_p \approx \lambda_{edge} \approx 1.05\ \mathrm{m}^{-1}$. This agreement between the reconstructed λ_p and estimated λ_{edge} provides some credibility to the assumptions used to during the Taylor limit formulation for LHI. This is further supported by the good quantitative agreement between the predicted Taylor limit and measured $I_p(t)$ throughout the discharges described earlier in this chapter.

The robust agreement with this Taylor limit formulation indicates that the global I_p constraint is enforced even if a true Taylor state (i.e. uniform λ) is not achieved. Relaxed states with non-uniform λ are commonly observed in other experiments [57,60,70,175]. Still, the more uniform profile is indicative of the system approaching a more fully relaxed state due to the increased level of magnetic fluctuations. In these cases, this relaxation appears to be driven by the increased rate of large-scale reconnection events.

Finally, an implication of this increased amount of current driven in the core when the system is over-driven suggests an avenue for current profile control during LHI discharges. This can potentially be utilized to better tailor these startup scenarios. To date, LHI has been characterized by a hollow current profile and consequently low amount of core ohmic heating ηJ^2. This likely contributes to the low core T_e and occasionally hollow profiles which have been observed during LHI discharges [30]. These features may be addressed by over-driving these Taylor limited discharges to increase the core ohmic heating, assuming that the increased magnetic activity does not have an otherwise negative impact on the measured T_e. Therefore, this remains a potential path to be explored in future optimization of LHI startup scenarios.

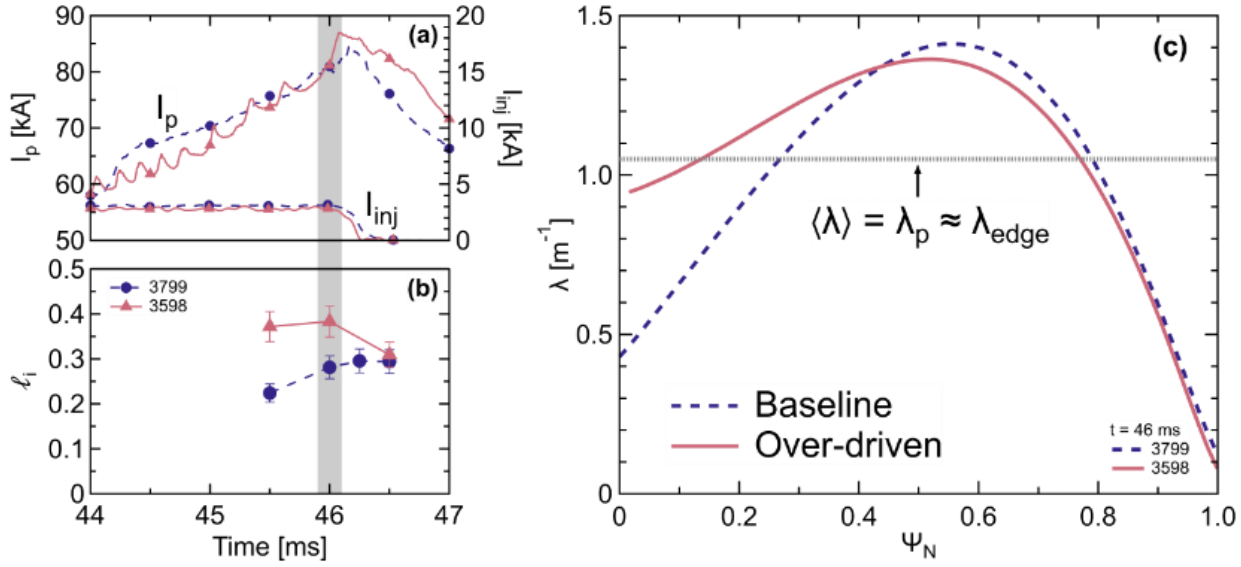

Figure 5.16: Comparison of magnetic equilibrium of baseline and over-driven discharge: (a) I_p (left) and I_{inj} (right), reconstructed (b) ℓ_i, and (c) λ profile at end of I_p ramp. Reconstructed λ profile corresponds to $t = 46$ ms indicated by the vertical shaded region in (a) and (b). Horizontal dotted line in (c) indicates calculated $\langle\lambda\rangle = \lambda_p$ and estimated λ_{edge} given by equation 5.2.

5.6 Helicity Dissipation in Discharges Over-driven at Taylor Limit

The previous section illustrated the robust nature of the Taylor limit in clamping $I_p(t)$ even with excess helicity input. This was accompanied by an increased level of magnetic activity as well as an increase in the plasma inductance. The resistive dissipation of helicity also needs to be considered to understand how the excess helicity input is balanced in these over-driven scenarios. This will be assessed in the over-driven and baseline discharges that were discussed at length in the preceding section.

Despite increased magnetic activity, higher T_e was measured in the over-driven discharge. The T_e and n_e profiles measured just prior to injector shutoff ($t = 46$ ms) in the over-driven and baseline discharges are shown in Figure 5.17(a) and (b), respectively. The lower n_e for the over-driven discharge is not surprising because the injector neutral fueling was significantly reduced to increase the V_{inj}. Additionally, the modestly higher $T_e(R)$ is also not surprising based on previous observations that higher V_{inj} and lower n_e typically lead to higher T_e in studies of HFS LHI

discharges [30]. Here, the increased T_e is most notable closer to the plasma edge, resulting in an increasingly hollow T_e profile which have also been observed in previous work [30,46,111].

The Spitzer $R_{Spitzer}$ and neoclassical R_{neo} plasma resistances can be calculated at the end of the I_p ramps in these discharges where MPTS data and equilibrium reconstructions are available. The Sauter formulation [91] described in Section 2.5 is used to compute $R_{Spitzer}$ and R_{neo} by mapping the MPTS profiles shown in Figure 5.17 to flux surfaces and computing f_t and ν_{e*} exactly for the low-A equilibrium. The resulting η_{neo} distributions along with the resistances are shown in Figure 5.18 assuming a uniform $Z_{eff} = 1$ profile in both cases. In general, the neoclassical effects become more important as collisionality decreases. Therefore, the over-driven discharge has a more significant neoclassical enhancement due to the higher T_e and lower n_e which leads to lower collisionality. This is especially noticeable near the edge of the over-driven discharge where η_{neo} is $\sim 25 - 50\%$ higher relative to the edge of the baseline discharge. As a result, R_{neo} is comparable in both discharges with the over-driven discharge being somewhat more resistive despite the significantly lower classical $R_{Spitzer}$.

Despite this marginally increased R_{neo}, additional resistive dissipation is required to explain the identical $I_p(t)$ with the increased helicity input. Differences in impurity content could contribute additional dissipation since the previous calculations assumed a uniform $Z_{eff} = 1$. Unfortunately, a direct measurement of Z_{eff} is challenging in the Pegasus-III operating space and is not presently available for these discharges [150]. However, the 0-D power balance model can be used to get an estimate of how much of an increase in Z_{eff} would be needed to balance the added helicity input in the over-driven discharge.

For this estimate, the 0-D model is initialized with self-similar plasma shape evolutions inferred from ShapeFIT along with the experimentally measured I_{inj} and V_{inj}. Due to the lack of MPTS measurements and reconstructions early in the discharge, $\langle\eta\rangle$ and ℓ_i will be assumed to be constant throughout both discharges. The $\langle\eta\rangle$ in each discharge is set to match the $\langle\eta_{neo}\rangle$ shown in Figure 5.18. Based on the difference in ℓ_i observed in Figure 5.16(b), $\ell_i = 0.3$ and $\ell_i = 0.4$ is assumed for the baseline and over-driven scenarios, respectively. The reconstructed ℓ_i at the end of both discharges shown in Figure 5.16(b) was slightly lower than these assumed values because higher ℓ_i was correlated with more frequent bursts of $n = 1$ activity. Both discharges exhibit more frequent $n = 1$ bursts earlier in their I_p ramps which may suggest an even higher ℓ_i. This gradually

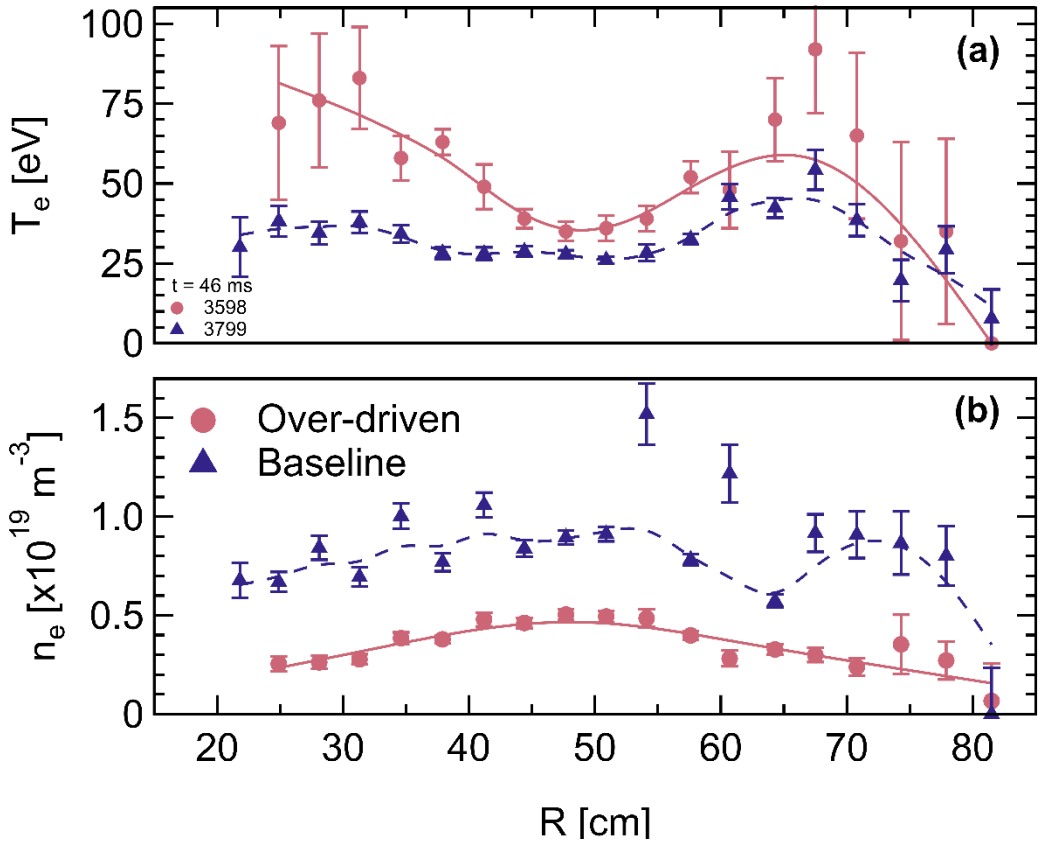

Figure 5.17: Comparison of electron kinetic profiles near at end of baseline (triangle) and over-driven (circle) discharges: (a) T_e and (b) n_e measured by MPTS near peak I_p. Profiles were collected at $t = 45.5$ ms and 46 ms for the baseline and over-driven discharges, respectively. Lines represent weighted spline fits to the MPTS data.

decreasing ℓ_i is consistent with previous work [29,88]. Unfortunately, equilibrium reconstructions are not presently available at these earlier times to confirm this assumption. Instead, a constant ℓ_i slightly higher than what was reconstructed at the end of the discharges is assumed here for simplicity.

The results of this calculation are summarized in Figure 5.19. The three sets of curves represent different cases: baseline discharge with $Z_{eff} = 1$; over-driven discharge with $Z_{eff} = 1$; and over-driven discharge with $Z_{eff} = 1.4$. In all cases, there is sufficient input drive from the combination of V_{LHI} and V_{IND} to sustain $I_p = I_{TL}$ with the assumed dissipation which agrees well with the experimentally realized I_p in Figure 5.19(a). There is some variation in the V_{IND} between the scenarios due to the different assumed ℓ_i. The over-driven scenarios have lower V_{IND} due to a larger back-emf from the ramping I_p. By construction, the V_R is also comparable in the $Z_{eff} = 1$

scenarios. However, the increased V_{LHI} in the over-driven scenario leads to a larger amount of excess drive voltage V_{excess} relative to the baseline scenario. The V_{excess} quantity is defined to be

$$V_{excess} \equiv V_{LHI} + V_{IND} + V_R. \tag{5.3}$$

When operating in a helicity-limited regime, this quantity will be zero as the input drive is perfectly balanced by the resistive dissipation. At the Taylor limit, it represents how strongly the system is being over-driven. It is important to point out that the absolute magnitude of this metric completely depends on the assumed resistive dissipation which is not well-constrained in this exercise. Still, within the simplicity of this model it is a useful metric to identify how much extra dissipation is needed to account for the increased V_{LHI} in the over-driven scenario. In this case, a 40% increase in Z_{eff} is needed to recover a similar amount of predicted V_{excess}.

This modest increase in Z_{eff} is feasible given the experimental observations. AXUV diode measurements suggest that there is an increased impurity concentration in the over-driven

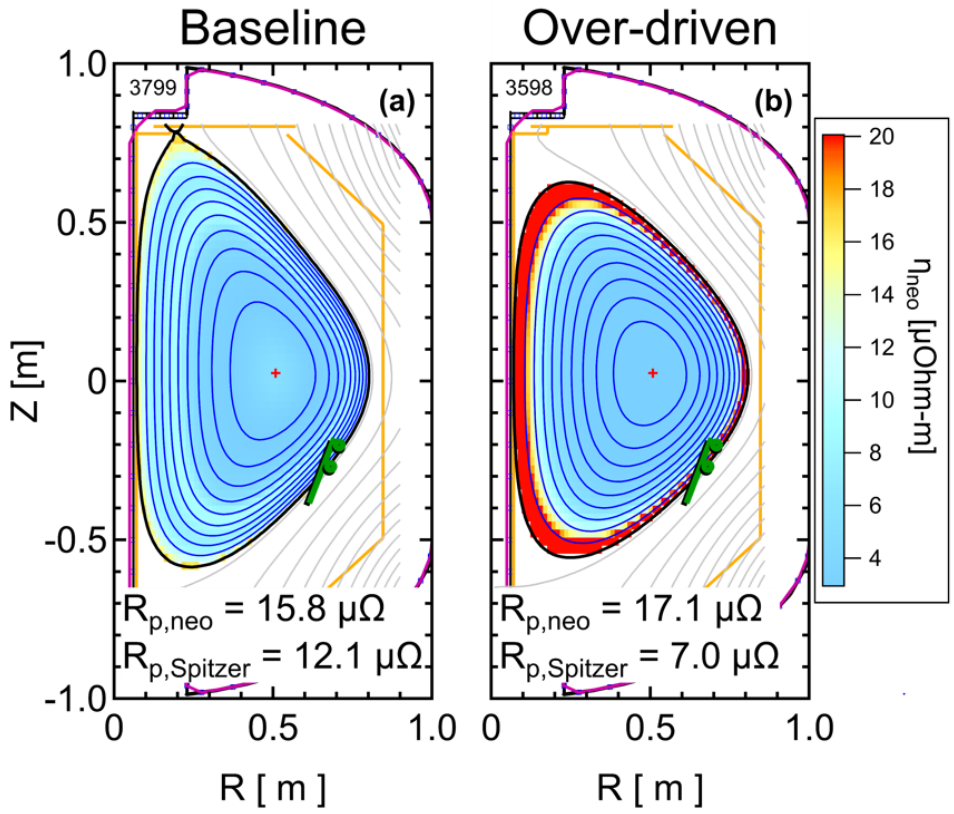

Figure 5.18: Comparison of $\eta_{neo}(R,Z)$ distributions near peak I_p for the (a) baseline and (b) over-driven discharges using the MPTS profiles shown in Figure 5.17. The computed Spitzer and neoclassical resistances are also shown for each case.

discharge. Figure 5.20 shows a representative channel from the AXUV diode array for both discharges. This specific channel was selected to provide a representative time evolution because its nominal tangency radius $R_{tan} \approx 45$ cm samples a large portion of the plasma volume for much of the discharge. The signal is a proxy for the power radiated from the plasma which scales with the electron and impurity densities $P_{rad} \propto n_e n_Z$. Despite the lower measured n_e, the over-driven discharge has comparable or higher signal throughout. This suggests that there is an increase in the impurity concentration. Inferring Z_{eff} from these measurements requires more sophisticated transport modeling which is outside the scope of this work but is an ongoing focus of LHI research. Preliminary impurity transport calculations suggest that the measured AXUV signals on Pegasus-III are consistent with $Z_{eff} < 2$ [93]. This is consistent with the 40% increase in Z_{eff} needed to balance the excess V_{LHI} between these discharges that is suggested by the 0-D model.

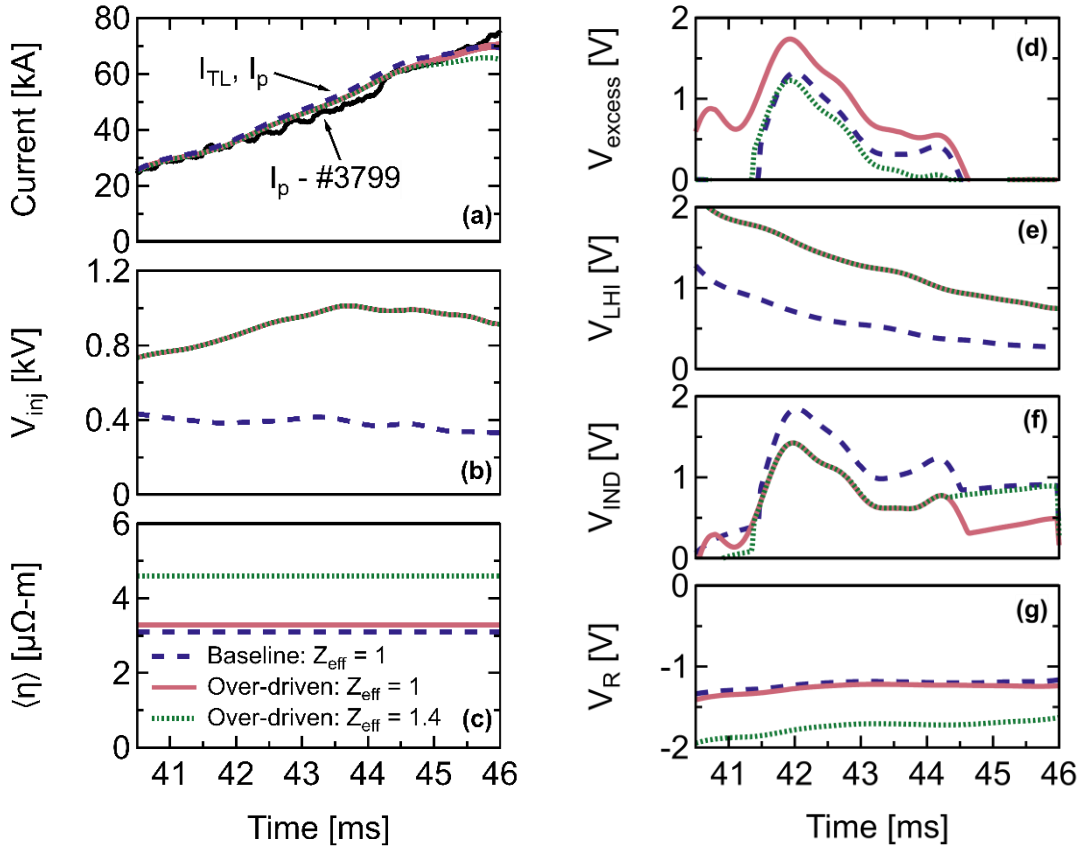

Figure 5.19: Summary of 0-D model calculations with different amounts of helicity input and dissipation. (a) I_p, I_{TL} from 0-D model and measured I_p from baseline discharge (#3799). Model inputs: (b) V_{inj} and (c) volume-averaged resistivity. System voltages: (d) excess voltage to sustain $I_p = I_{TL}$, (e) V_{LHI} ,(f) V_{IND}, and (g) V_R.

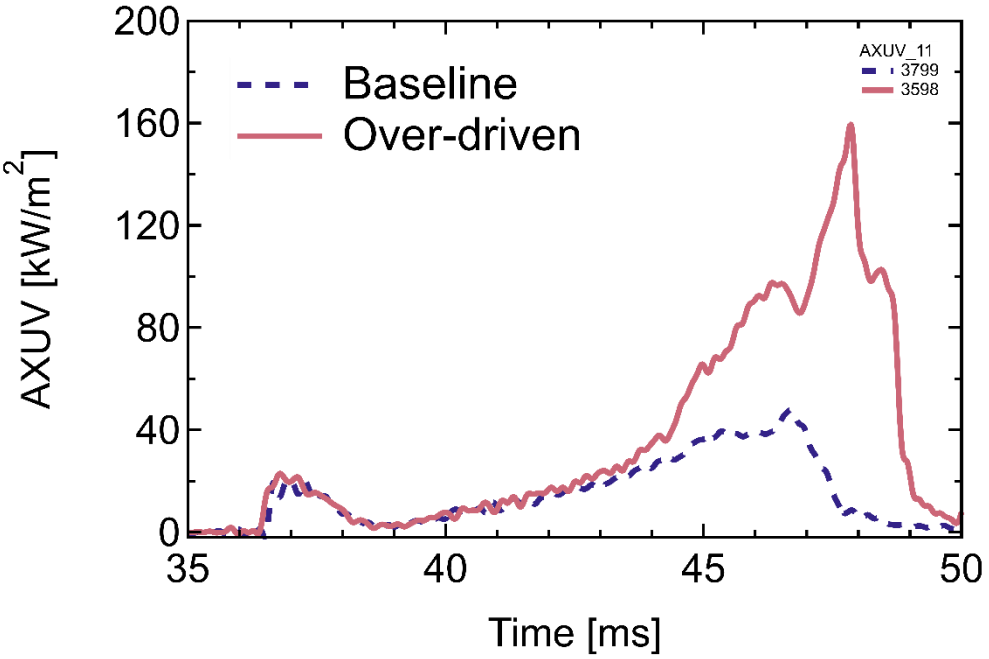

Figure 5.20: Comparison of representative AXUV signal from baseline and over-driven discharges. AXUV signal collected from tangential viewing chord with $R_{tan} \approx 45$ cm.

In total, the observed I_p clamp in these scenarios can be reasonably attributed to increased plasma inductance and neoclassical enhancement in the over-driven discharge. The increased inductance leads to a larger back-emf response to the $\dot{I}_p$ which reduces the net inductive drive. Further, the neoclassical enhancement nullifies the reduced $R_{Spitzer}$ from the higher measured T_e leading to a comparable R_{neo} when assuming $Z_{eff} = 1$. Together, these effects can effectively balance the excess drive from the higher V_{LHI} in the over-driven scenario by assuming a modest increase in Z_{eff}. Such an increase in Z_{eff} is qualitatively consistent with an increase in the impurity concentration inferred from AXUV measurements.

Chapter 6
Helicity Dissipation Scaling Studies in Pegasus-III

Future LHI systems on larger, higher B_T devices expect to operate in a regime in which the Taylor limit is sufficiently high to not impede performance. In this operating regime, the I_p is dictated by the balance of helicity input and dissipation. The 0-D power balance model described in Sections 2.5 and 4.1 was developed to interpret and predict discharges in this regime. However, the predictive capability of this model is limited without a more refined understanding of how the helicity dissipation scales to other operating regimes.

Previous LHI studies on Pegasus identified a robust linear I_p scaling with V_{LHI} [30,46]. This behavior was consistent with both ohmic-like and globally stochastic-like confinement estimates [30]. That data suggested that global confinement estimates may be useful for scaling LHI performance. However, it was unable to differentiate between these competing models which have very different implications for scaling LHI to a MA-class startup system. Further, these studies were performed in a narrow, low B_T operating space that is not particularly relevant for higher B_T facilities, including the new Pegasus-III operating space. As such, an expansion of those previous studies is needed to further characterize the scaling of helicity dissipation during LHI to improve the ability to project future systems.

This chapter will describe experiments focused on characterizing the scaling of dissipation in LHI plasmas. To expand on previous work, this chapter will discuss a series of parametric B_T and n_e scans in LHI discharges. The observed trends in I_p and T_e will be assessed in the context of expectations from global confinement scaling models presented in Section 2.11.

6.1 Fiducial LFS LHI Flattop Discharge

Traditional empirical tokamak confinement scalings are typically comprised of discharges that are sustained in transport equilibrium with minimal variation in the total stored energy ($dW/dt = 0$). This can be challenging to achieve in the short pulse start-up plasmas that are the focus of this work. Nonetheless, the baseline discharge for the subsequent parametric scans that are discussed throughout this chapter were developed to have I_p, plasma shape, and injector parameters held relatively constant for several milliseconds. Further, the Taylor limit needs to be sufficiently high such that $I_p(t)$ is dictated by the balance of helicity input and dissipation. The baseline discharge (#7145) that was ultimately developed is summarized in Figure 6.1. There is a $\sim$6 ms I_p flattop that extends from $42 - 48$ ms. During this time, the I_{inj} and V_{inj} are well-controlled via active feedback control and injector fueling to be sustained at 6.5 kA and 350 V, respectively.

The plasma shape has a little more variation as indicated in Figure 6.1(e) which shows the plasma boundary estimated from ShapeFIT at several times during the I_p flattop. The plasma is slowly growing towards a larger, low-A plasma throughout the flattop. The plasma shape control of these discharges is challenging for a variety of reasons, including: induced wall currents that decay on a characteristic $\sim$10 ms timescale, pre-programmed magnetic field coil waveforms, and maintaining plasma in force balance near the injectors.

This challenge is exacerbated with the added requirement to sustain a flattop I_p below the Taylor limit. This requires the sustainment of a relatively large plasma to increase the Taylor limit ($I_{TL} \propto \sqrt{\Psi_T}$) to a sufficiently high value which does not dictate $I_p(t)$. At these larger plasma sizes, the effective loop voltage provided by the injectors is greatly diminished ($V_{LHI} \propto 1/\Psi_T$). This makes it challenging to sustain an appreciable I_p flattop when developing a steady-state scenario which entirely removes the significant helicity input provided by magnetic induction in these LFS

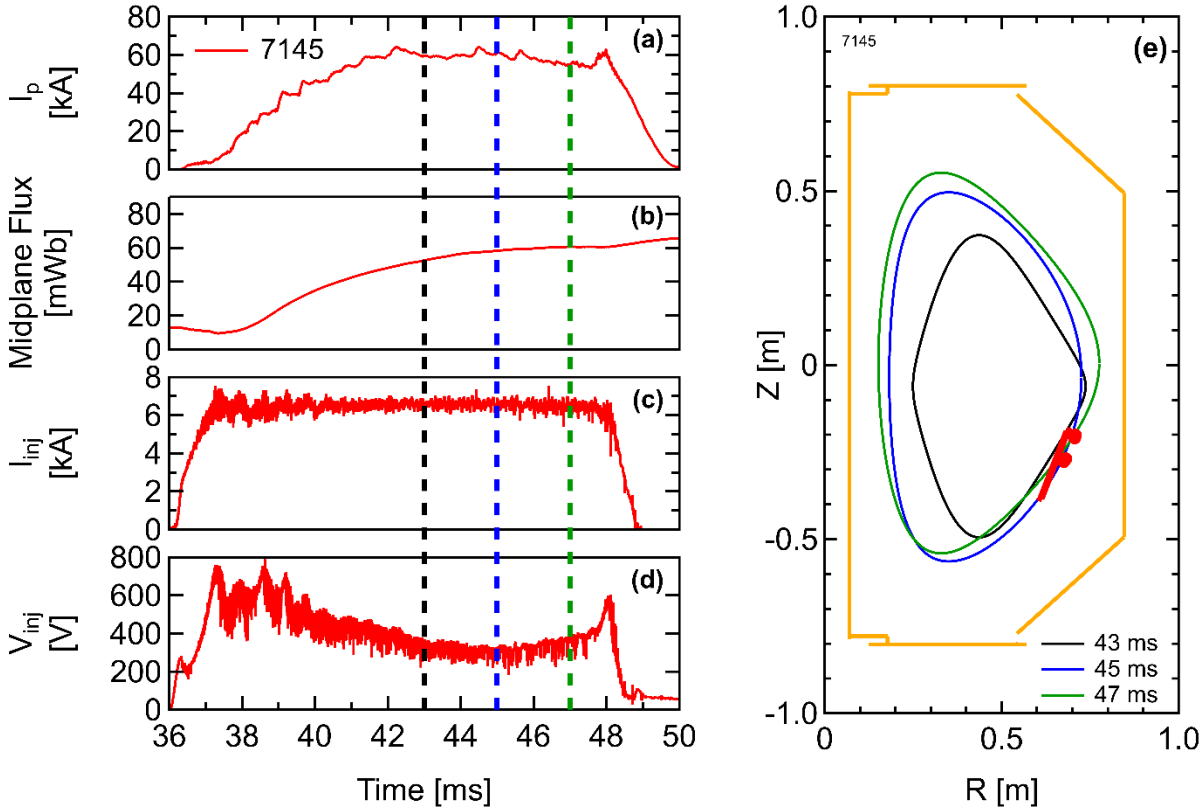

Figure 6.1: Overview of fiducial flattop discharge (#7145): (a) I_p, (b) midplane poloidal flux, (c) I_{inj}, (d) V_{inj} and (e) comparison of plasma boundary at several points during I_p flattop. Vertical dashed lines in (a-d) correspond to the times at which MPTS measurements were taken as well as the plasma boundaries shown in (e). The red circles and lines in (e) indicate the nominal injector limiting surfaces.

LHI discharges. Therefore, the gradually evolving plasma shape and midplane flux in this target were a compromise between run-time constraints and realizing the ideal target.

As such, the baseline discharge that was developed in this work still has a significant contribution of helicity input from magnetic induction. This is illustrated by the interpretive 0-D power balance model analysis summarized in Figure 6.2. Like previous work by Barr et al. [29], this analysis assumes a constant $\langle\eta\rangle$ throughout which was varied to best match the measured $I_p(t)$. Ultimately, the model agrees well with the experimentally measured $I_p(t)$ shown in Figure 6.2(a) with an assumed $\langle\eta\rangle \approx 6\ \mu\Omega - \mathrm{m}$ which is consistent with a Spitzer-like resistivity assuming $Z_{eff} = 1$ and $\langle T_e\rangle = 25$ eV. Additionally, Figure 6.2(a) also shows the predicted Taylor limit with its 20% uncertainty which is significantly higher than the realized I_p. This illustrates that the balance of helicity input and dissipation is governing $I_p(t)$ as opposed to the Taylor limit. Further,

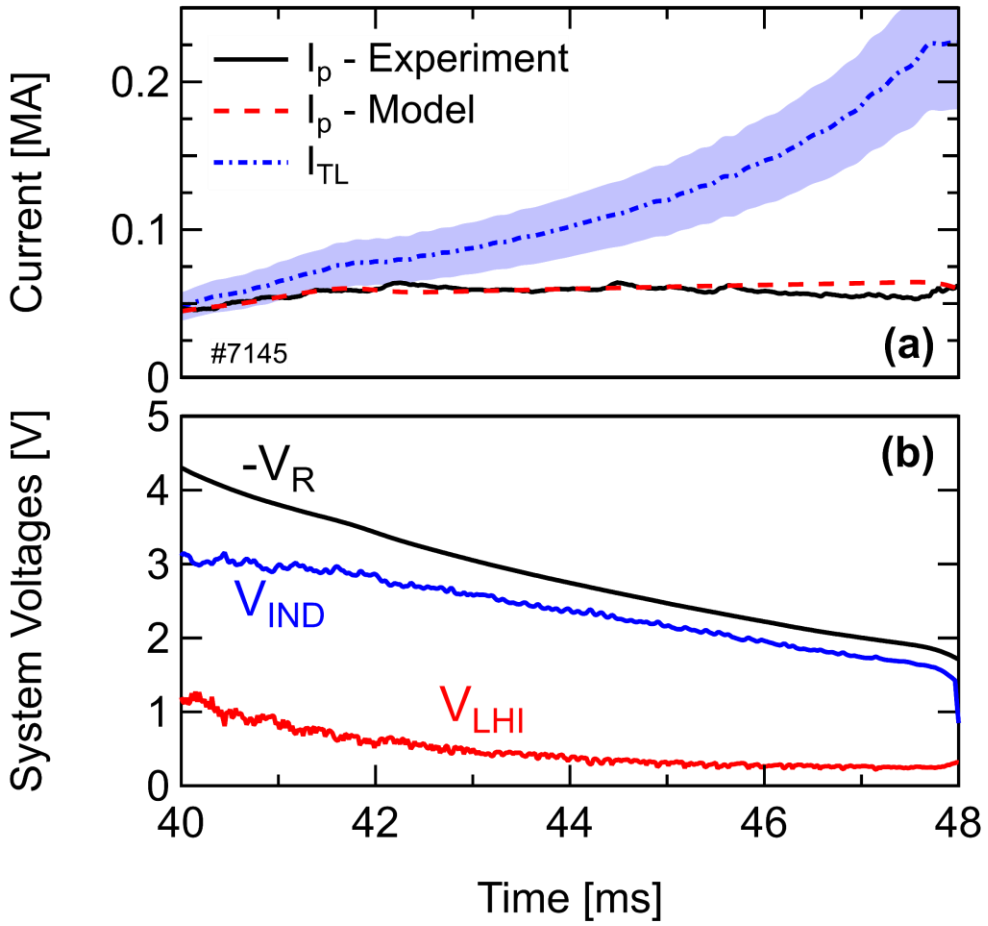

Figure 6.2: Interpretative 0-D power balance analysis of Pegasus-III discharge #7145: (a) Measured I_p and predicted I_p and $I_{TL}$from 0-D model; (b) system voltages calculated by 0-D model representing dissipation, inductive effects, and effective injector helicity input. Shaded region in (a)represents a 20% uncertainty band in the calculated I_{TL}.

the helicity input is predominantly provided by magnetic induction (V_{IND}) arising from the gradually evolving shape evolution. This is illustrated in Figure 6.2(b) where V_{IND} provides $2-3$ V whereas the injector helicity input (V_{LHI}) is generally < 1 V.

Despite the slowly evolving plasma shape, the stored kinetic energy is similar throughout the flattop. Figure 6.3 shows the electron temperature, density, and pressure profiles measured by the MPTS diagnostic at various times corresponding to the vertical dashed lines in Figure 6.1(a-d). There is a notable difference in the n_e profile at 43 ms which drastically falls off on the HFS around $R\sim25$ cm compared to the later time points. This is consistent with the plasma shape evolving and the HFS plasma edge moving to lower R during this period. Referring to Figure 6.1(e), ShapeFIT estimates the inboard edge at 43ms to be around $R\sim25$ cm which coincides with

the measured n_e fall off. At the later time points, the plasma grows, and the estimated LFS plasma edge extends below the lowest radial measurement of the MPTS diagnostic ($R = 21.8$ cm). Additionally, the rather poor density control leads to a gradual increase in n_e throughout the flattop and a corresponding decrease in T_e. This is primarily observed inboard of the plasma centroid ($22 \lesssim R \lesssim 40$ cm). However, the stored electron kinetic energy illustrated by the P_e profile is relatively flat at $\sim$70 Pa throughout the flattop. Unfortunately, measurements of the bulk ion population are not presently available to assess the total stored kinetic energy of the plasma.

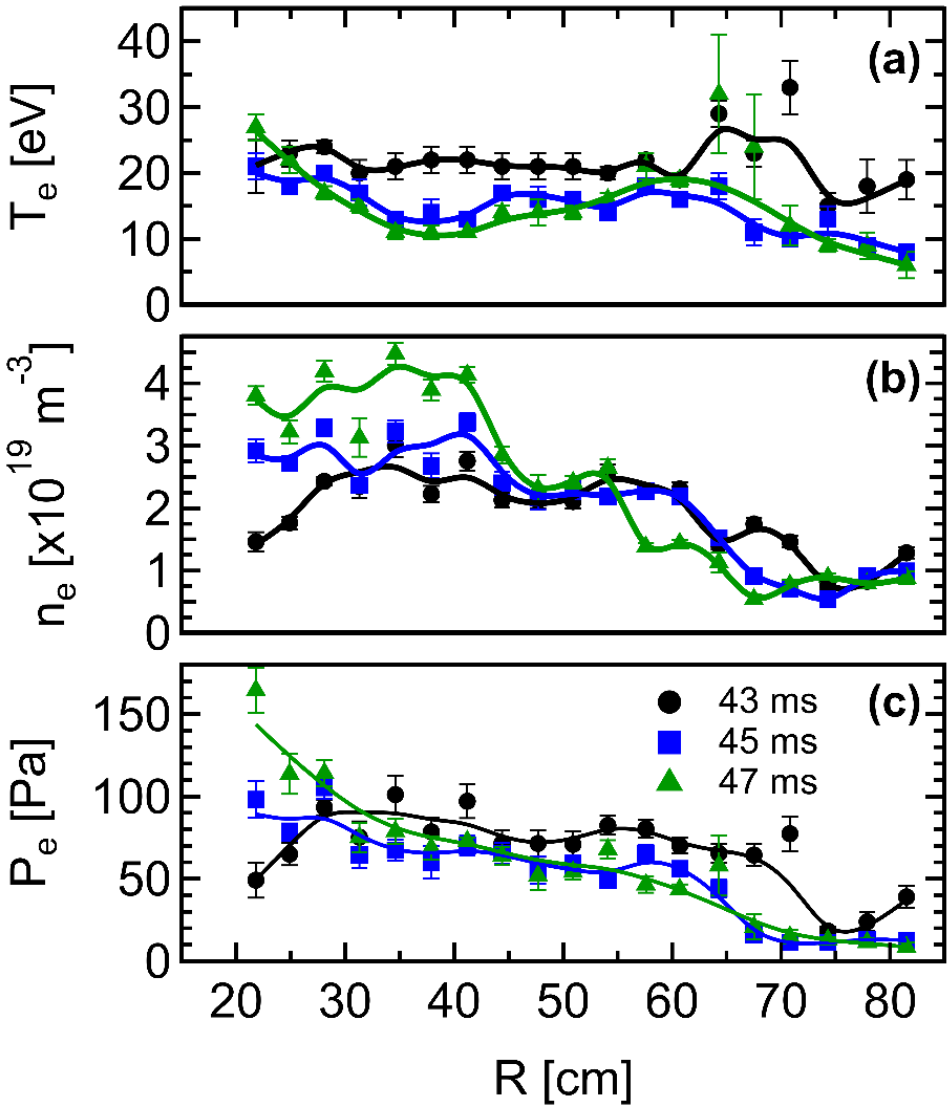

Figure 6.3: MPTS measurements during various times during flattop of discharge #7145: Electron (a) temperature, (b) density, and (c) pressure profiles. Solid lines are uncertainty weighted spline fits to the data.

6.2 B_T Scan in LFS LHI Flattop Discharges

Understanding the scaling of helicity dissipation with B_T is critical for reliable projections of power plant relevant LHI systems. These facilities will operate at significantly higher B_T than what is accessible on Pegasus-III. For standard ST ohmic confinement scalings, this increased B_T can significantly improve plasma performance in a variety of ways, including enhanced energy confinement. If such improvements are also realized in LHI plasmas they could significantly impact the size and scope of an LHI system required to drive MA-class startup plasmas. In contrast, stochastic confinement scaling models are not as favorable and imply different considerations for future LHI systems. These uncertainties and the shortcomings of previous B_T scans on Pegasus [92] motivate a dedicated B_T scan on Pegasus-III to better characterize this behavior.

In this work, LHI discharges were developed at $B_T = 0.15$ and 0.23 T on Pegasus-III. The fiducial $B_T = 0.15$ T discharge was discussed at length in the previous section. The higher B_T scenario was developed to maintain an I_p flattop with injector parameters, plasma shape, and n_e similar to the fiducial discharge. These discharges are summarized in Figure 6.4. As discussed in the previous section, development of these discharges can be a time-consuming process given the limited Pegasus-III plasma control capabilities. Due to limited experimental run-time, the higher B_T discharge was sustained for a shorter I_p flattop of approximately 3 ms duration which can be seen in Figure 6.4(a). The I_{inj} and V_{inj} were well-matched in these scenarios as illustrated in Figure 6.4(b) and (c), respectively. Additionally, the relative level of magnetic fluctuation activity was also similar throughout the flattop. This is shown in Figure 6.4(d) which plots $\tilde{b}_Z/B_T$ measured by a representative $\dot{B}$ coil located outside the LFS plasma edge at the midplane of the machine. In the higher B_T discharge, there is an increase in $\tilde{b}_z/B_T$ at around 45 ms which is likely related to the plasma beginning to decouple from the injectors. A similar increase in $\tilde{b}_z/B_T$ is also observed at the end of the lower B_T discharge just prior to injector shutoff.

The plasma shape was comparable throughout the flattop. This is demonstrated in Figure 6.5 which compares the evolution of the R_0, a, and κ inferred from ShapeFIT. These moments were selected because they appear in the empirical tokamak τ_E scalings which were presented in Section 2.8. The shape was well-matched between the discharges within the uncertainty in the ShapeFIT output. This uncertainty is representative of the typical accuracy of the ShapeFIT output relative

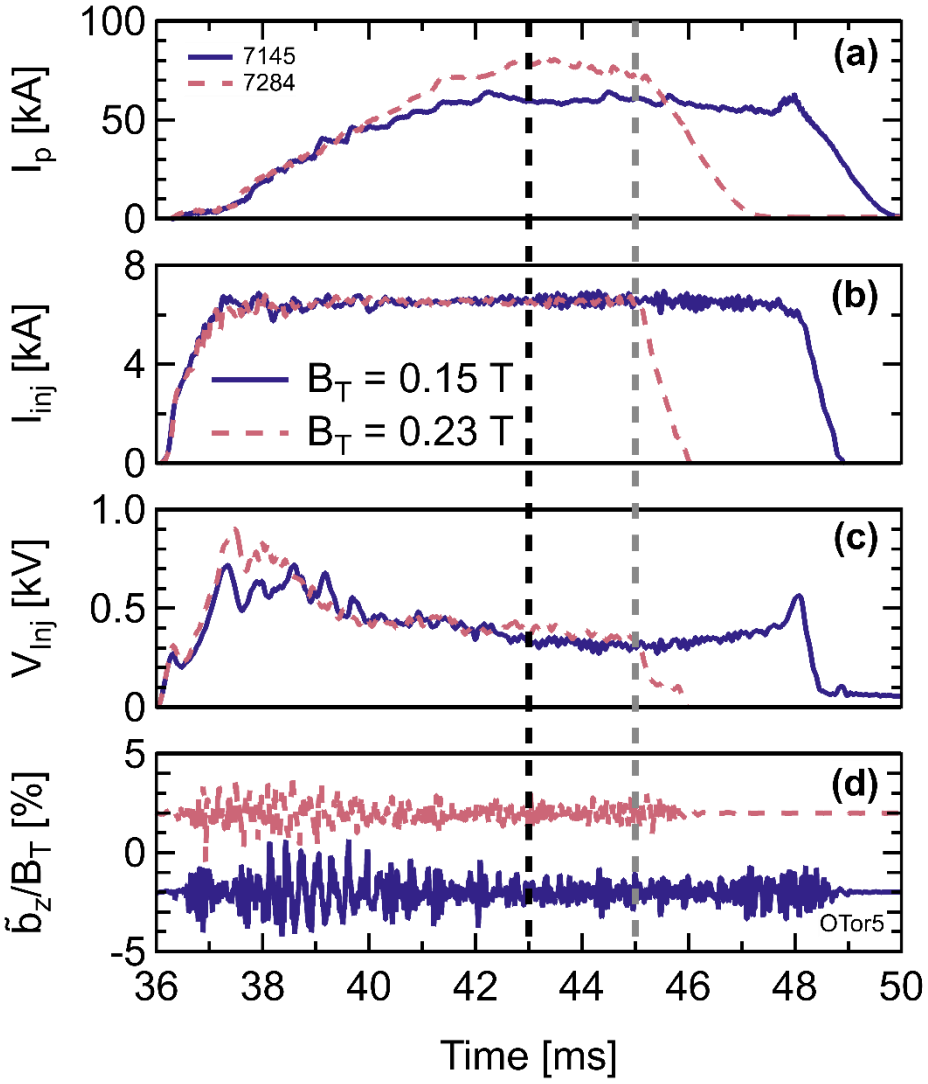

Figure 6.4: Overview of Pegasus-III discharges at different B_T levels: (a) I_p, (b) I_{inj}, (c) V_{inj}, and (d) normalized $\tilde{b}_Z$. Vertical dashed lines indicate times that MPTS were taken in each discharge. The signals in (d) have been vertically offset ($\pm 2\%$) for clarity.

to shape inferred from a KFIT equilibrium reconstruction which was discussed in Section 4.2.2. Specifically, it uses the average error in the ShapeFIT output relative to KFIT which was tabulated in Table 4 using a small set of reconstructions coarsely spanning the Pegasus-III operating space.

The density was also well-controlled across these scenarios as indicated in Figure 6.6. The density profiles for each discharge are shown in Figure 6.6(a) and (b) for $t = 43$ and 45 ms, respectively. The solid lines are weighted spline fits to the MPTS data. As desired, the density profiles in both discharges are well-matched and generally agree within the measurement uncertainty for much of the radial profile.

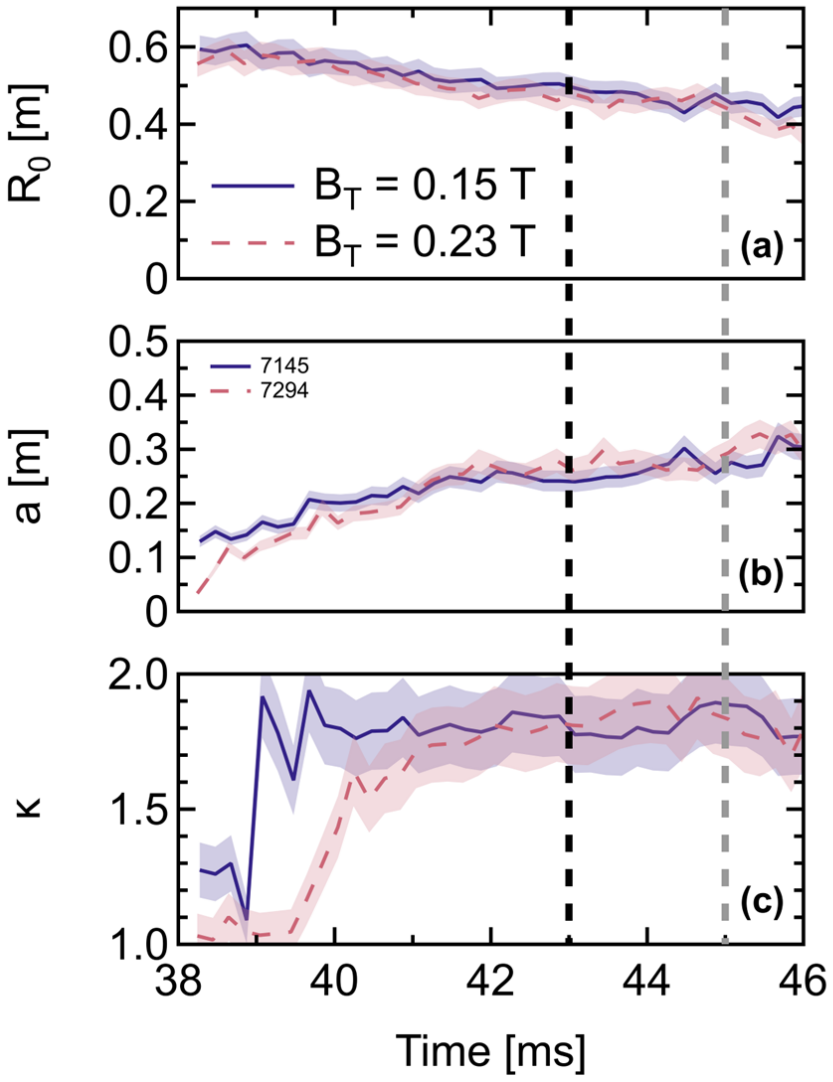

Figure 6.5: Overview of plasma shape evolution in discharges developed at different B_T levels: (a) major radius, (b) minor radius, and (c) elongation. Vertical dashed lines indicate times at which MPTS profiles are available in both discharges.

With the parameters of interest well-controlled, the observed trends in the measured I_p and T_e can be interpreted as primarily a result of the variation in B_T. First, there is an observed increase in the flattop I_p in the higher B_T scenario. This increase is likely not due to an increase in the I_{TL} as the calculated I_{TL} in the lower B_T discharge was significantly higher than the measured I_p (see Figure 6.2). The measured T_e in these discharges is comparable throughout the flattop. This is demonstrated by the T_e profiles measured by MPTS at $t = 43$ and 45 ms in Figure 6.6(c) and (d), respectively. At 43 ms, both profiles are flat at $T_e \sim 20$ eV and largely agree within the

measurement uncertainty across most of the radial profile. At 45 ms, there is a little more discrepancy between the two scenarios beyond the measurement uncertainty for several points in the profile. However, these typically correspond to measurable differences in density. With the higher B_T discharge having somewhat higher density and lower T_e at those points. Still, despite these small differences the profiles are very comparable between the discharges which suggests that the increased B_T is not having a significant impact on T_e in these discharges. This corresponds to a negligible variation in the total stored electron kinetic energy as indicated by the comparable P_e profiles shown in Figure 6.6(e) and (f). In total, the 50% increase in B_T does not appear to have a dramatic effect on the electron energy confinement in these discharges.

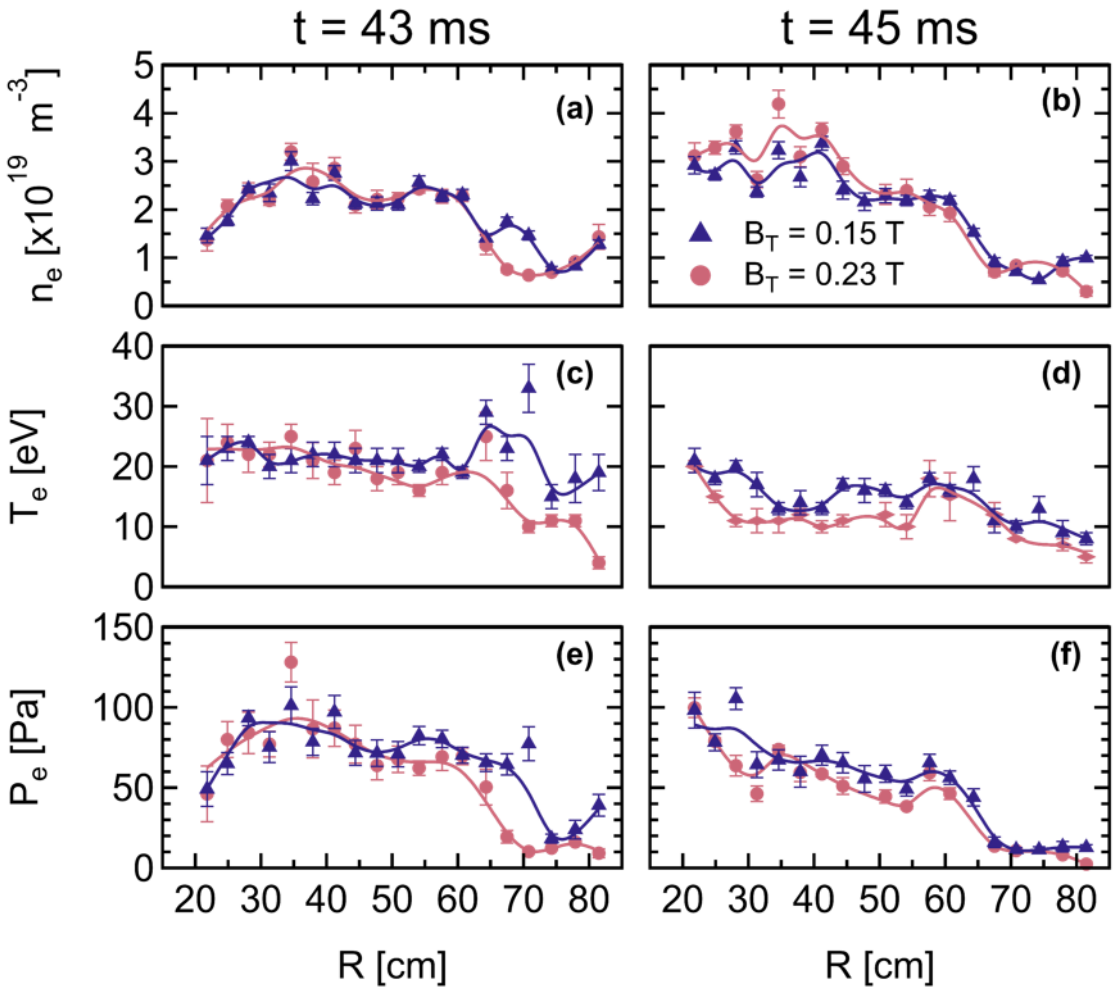

Figure 6.6: Comparison of electron kinetic profiles at different times during the flattop in discharges at different B_T levels: (a,b) n_e, (c,d) T_e and (e,f) P_e profiles measured by the MPTS diagnostic at $t = 43$ ms (a,c,e) and $t = 45$ ms (b,d,f). Solid lines are uncertainty weighted spline fits to the data.

6.3 n_e Scan in LFS LHI Flattop Discharges

Density is another parameter that can have a significant impact on the scaling of helicity dissipation. Over the course of LHI studies on Pegasus, higher I_p plasmas were typically attained at lower electron densities for a given set of operational parameters [30]. However, a systematic density scan has not been previously performed to characterize this dependence in LHI plasmas. Additionally, density plays an important role in differentiating between the competing confinement scaling models. This section describes a dedicated density scan on Pegasus-III designed to characterize the impact on the achieved I_p and T_e.

Figure 6.7 summarizes a series of flattop LFS LHI discharges developed at different densities on Pegasus-III. These discharges were all adapted from the baseline scenario developed at $B_T = 0.15$ T which was discussed in Section 6.1. From this baseline discharge, the throughput of the main chamber and injector neutral fueling PV10 valves were decreased/increased to create low/high density scenarios. These discharges were developed to have self-similar injector parameters. The I_{inj} was well-controlled by the current feedback-controlled power supply as shown in Figure 6.7(b). However, there was some variation in the V_{inj} evolution shown in Figure 6.7(c) as the throughput of the fueling valves were varied. Specifically, the injector fueling valves are tightly coupled to the injector impedance through their impact on the electron beam density $n_b \propto I_{inj}/V_{inj}^{1/2}$ [171]. This most clearly impacts the low-density discharge during the I_p ramp which initially has significantly higher V_{inj}. During the I_p flattop, V_{inj} is comparable across all three discharges when the MPTS diagnostic collected data. These collection times are indicated by the vertical dashed lines in Figure 6.7. Due to the limited development time, the low-density discharge was not extended sufficiently long to collect MPTS data at 45 ms. The magnetic fluctuation activity was also similar during the flattop portion of each discharge. This is illustrated in Figure 6.7(d) which shows comparable amplitude $\tilde{b}_z/B_T$ measured by a representative $\dot{B}$ coil located outside the LFS plasma edge at the midplane of the machine. The low- and high- density traces have been vertically offset by $\pm 4\%$ for clarity, respectively.

The plasma shape was also similar during the flattop of each scenario. Figure 6.8 shows the R_0, a, and κ inferred from ShapeFIT for each discharge. Generally, the inferred shaping moments agree within their respective uncertainties indicating that the plasma shape was well-matched

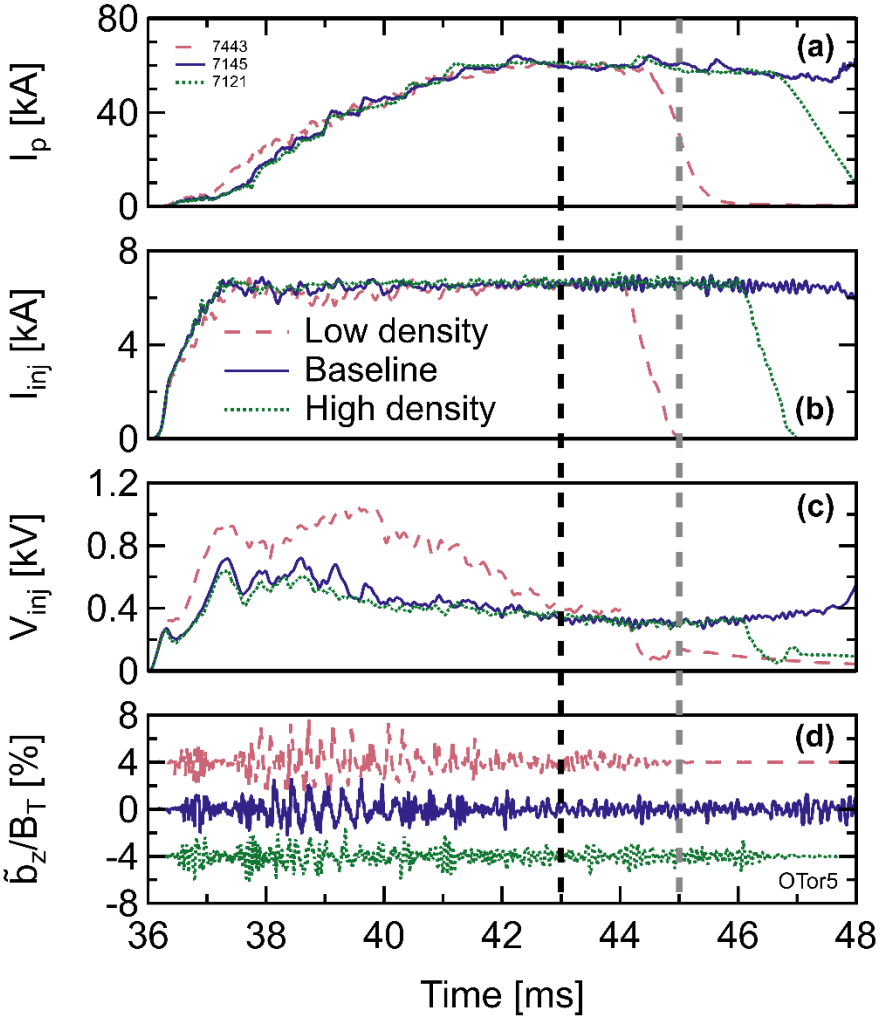

Figure 6.7: Overview of discharges developed at $B_T = 0.15$ T with different densities: (a)I_p, (b) I_{inj}, (c) V_{inj}, and (d) normalized $\tilde{b}_Z$. Vertical dashed lines indicate times that MPTS were taken in each discharge. The low- and high-density traces in (d) are vertically offset ($\pm 4\%$) for clarity.

across these discharges. As discussed in the previous section, the uncertainty indicated by the error bands in Figure 6.8 are representative of the typical accuracy of the ShapeFIT output relative to the shaping moments inferred from a KFIT equilibrium reconstruction. This self-similar plasma shape evolution was also achieved with identical PF programming resulting in the inductive drive contributions being comparable across the discharges.

The neutral fueling valves were used as actuators to alter the density. Adjusting the throughput of these valves was able to achieve discharges that had roughly a factor of two variation in the n_e measured via the MPTS diagnostic. This is illustrated in Figure 6.9(a) and (b) which shows the measured $n_e(R)$ in each scenario at 43 and 45 ms, respectively. Profiles were collected for all

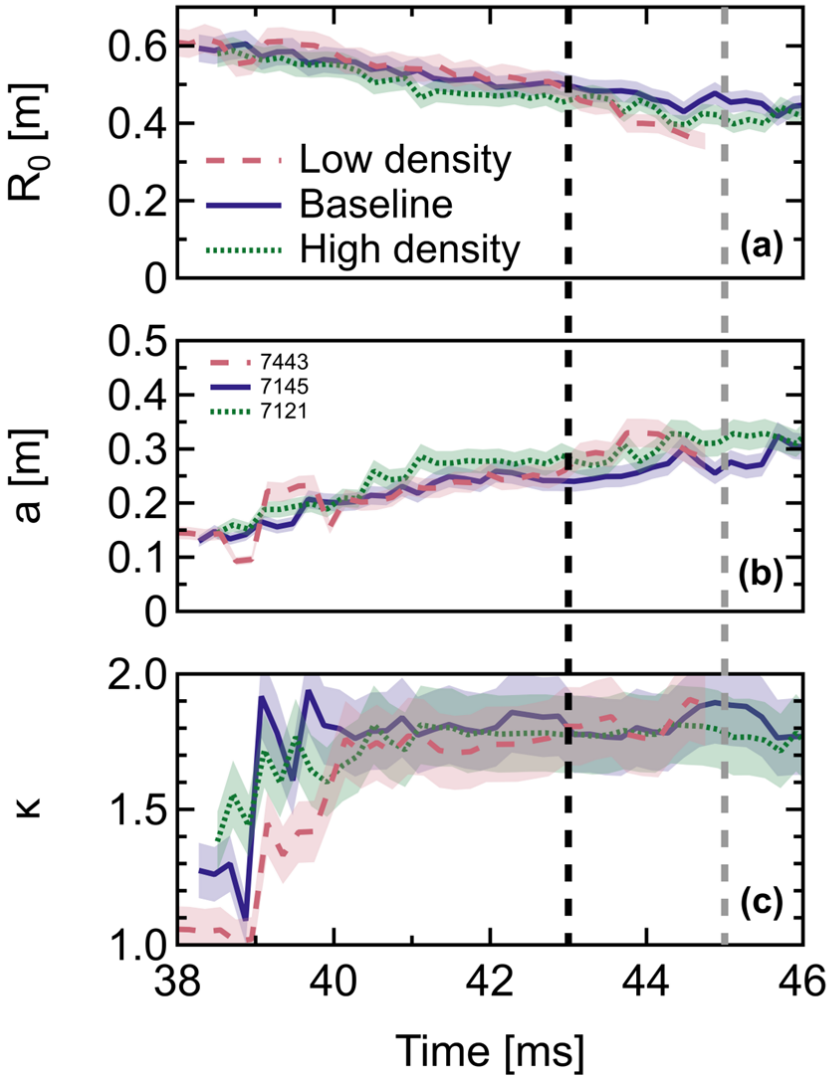

Figure 6.8: Overview of plasma shape evolution in Pegasus-III discharges with different densities at $B_T = 0.15$ T: (a) major radius, (b) minor radius, and (c) elongation. Vertical dashed lines indicate times that MPTS measurements were taken in each discharge.

three discharges at the earlier time point and clearly show a peaked density profile for each scenario. The central density ranges from $\sim 1.5 \times 10^{19}$ m^{-3} up to $\sim 3 \times 10^{19}$ m^{-3} across the scan. MPTS data was not collected at the later time point in the lower density scenario, but peaked density profiles are still observed for the baseline (blue triangles) and high density (green diamonds) scenarios. The density in these discharges is somewhat higher than the earlier time point but there is still a clear distinction between the two profiles outside of their respective measurement uncertainties. There is not a clear drop in density on the inboard side at the later time point likely

due to the gradual increase in the plasma shape resulting in the inboard plasma edge extending below the radial coverage of the MPTS diagnostic.

With the parameters of interest well-controlled, the observed trends in the measured I_p and T_e can be interpreted as primarily a result of the variation in n_e. First, the flattop I_p level shown in Figure 6.7(a) was unchanged across this density scan and maintained at $I_p \approx 60$ kA. Further, the measured T_e in these discharges is also comparable throughout the flattop. This is demonstrated by the T_e profiles collected at $t = 43$ and 45 ms in Figure 6.9(c) and (d), respectively. The profiles at each time point are self-similar with many points agreeing within measurement uncertainty. Despite the measurable variation in density, the profiles are all flat to slightly hollow with $T_e \approx$

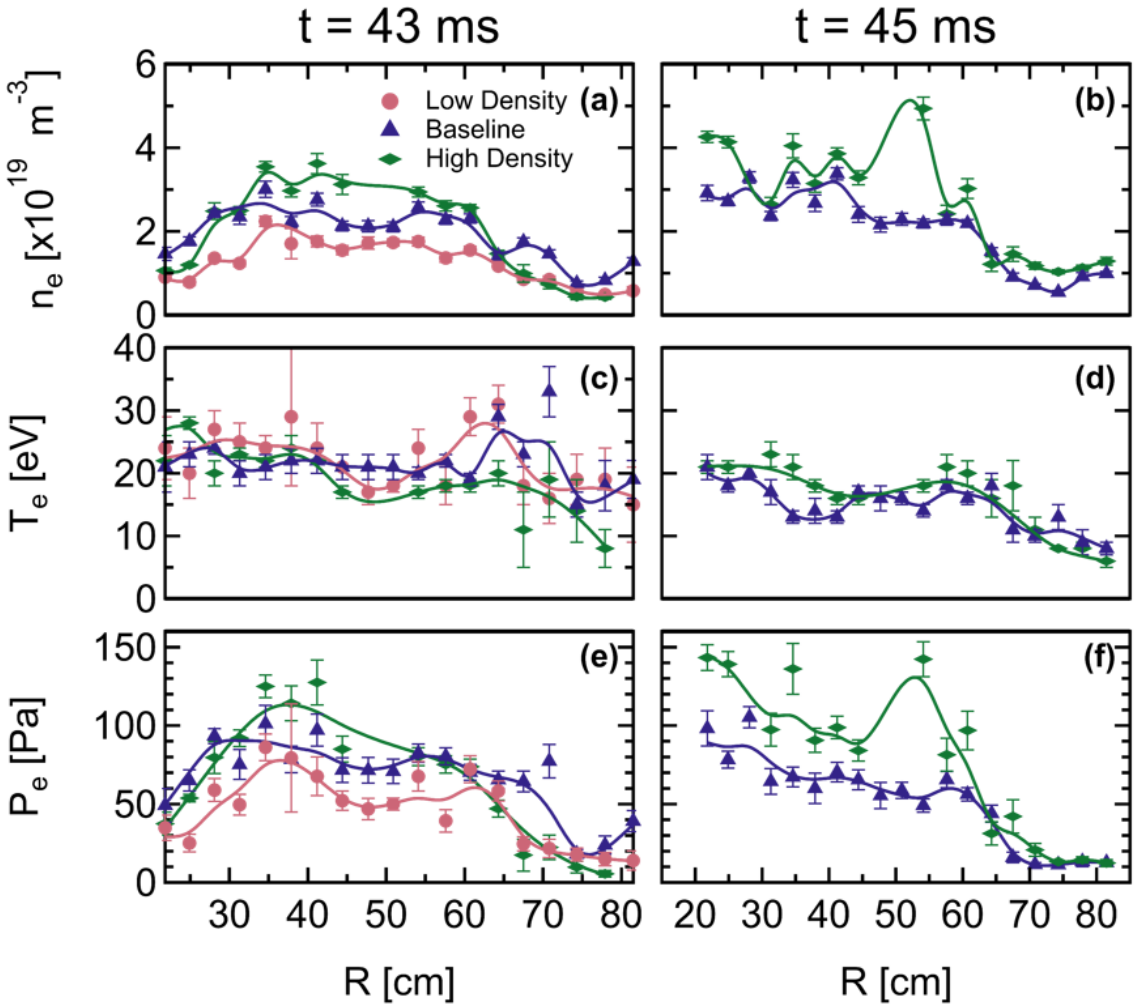

Figure 6.9: Comparison of electron kinetic profiles at different times during the flattop in discharges developed at $B_T = 0.15$ T with different densities: (a,b) n_e, (c,d) T_e and (e,f) P_e profiles measured by the MPTS diagnostic at $t = 43$ ms (a,c,e) and $t = 45$ ms (b,d,f). Solid lines are uncertainty weighted spline fits to the data.

$15-25$ eV. This suggests that the density is not significantly impacting the $T_e(R)$ or energy confinement properties of these discharges. As such, the stored electron kinetic energy increases with increasing density as shown by the P_e profiles in Figure 6.9(e) and (f).

Similar behavior was also observed in a smaller dataset at higher B_T. During the development of the $B_T = 0.23$ T discharge outlined in the previous section, a higher density discharge was also realized that was virtually identical. A comparison of these discharges is shown in Figure 6.10 with the "low density" discharge being the $B_T = 0.23$ T discharge discussed in the previous section. Figure 6.10(a) shows that both discharges were sustained at $I_p \approx 80$ kA with the higher

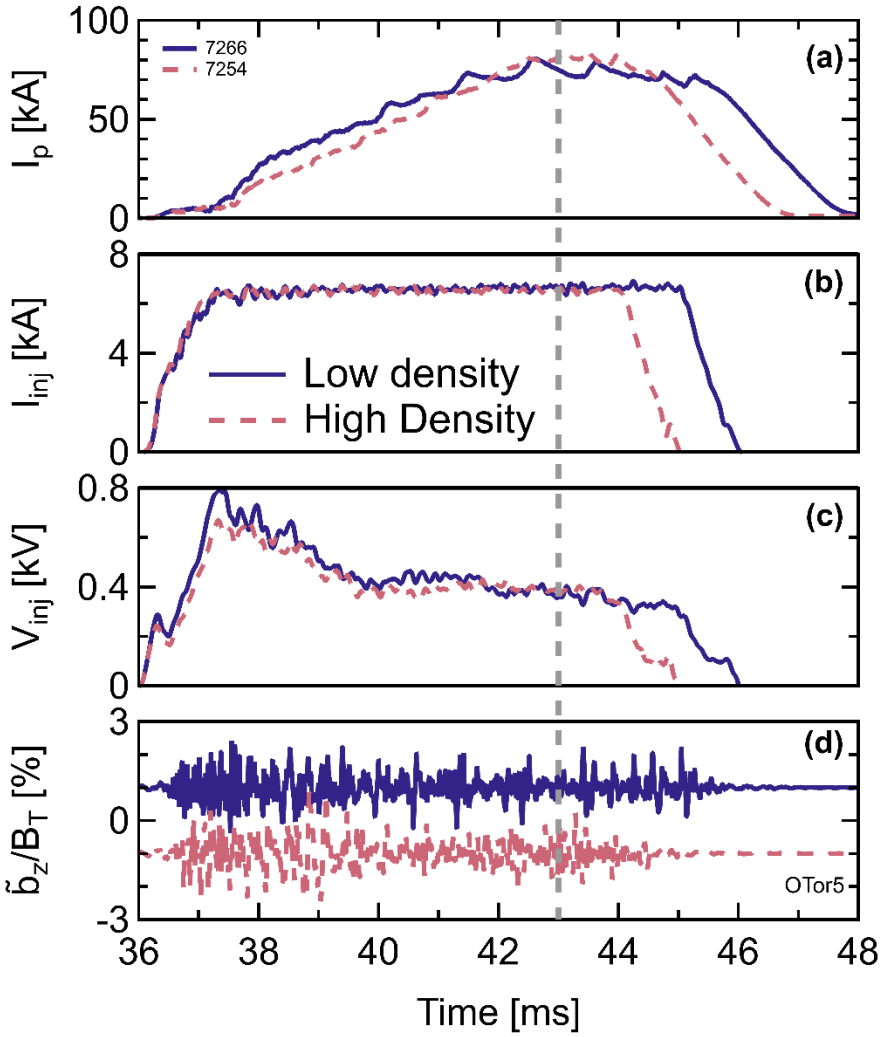

Figure 6.10: Overview of discharges developed at $B_T = 0.23$ T with different densities: (a)I_p, (b) I_{inj}, (c) V_{inj}, and (d) normalized $\tilde{b}_Z$. The vertical dashed line indicates the time when MPTS data was collected during each discharge. The traces in (d) are vertically offset ($\pm 1\%$) for clarity.

density discharge having a shorter flattop duration because runtime was not dedicated to the development of this scenario. The injected current and voltage shown in Figure 6.10(b) and (c), respectively, were well-matched throughout both discharges. Additionally, the amplitude of the magnetic fluctuations was also comparable as illustrated by the measured $\tilde{b}_Z/B_T$ shown in Figure 6.10(d). The PF coil programming was unchanged between these scenarios resulting in a similar plasma shape evolution in these discharges.

The primary difference in these discharges was a reduction in the throughput of the neutral fueling valves in the "low density" scenario. This resulted in a measurable difference in the density illustrated in Figure 6.11(a) which shows the n_e profiles measured by the MPTS diagnostic early

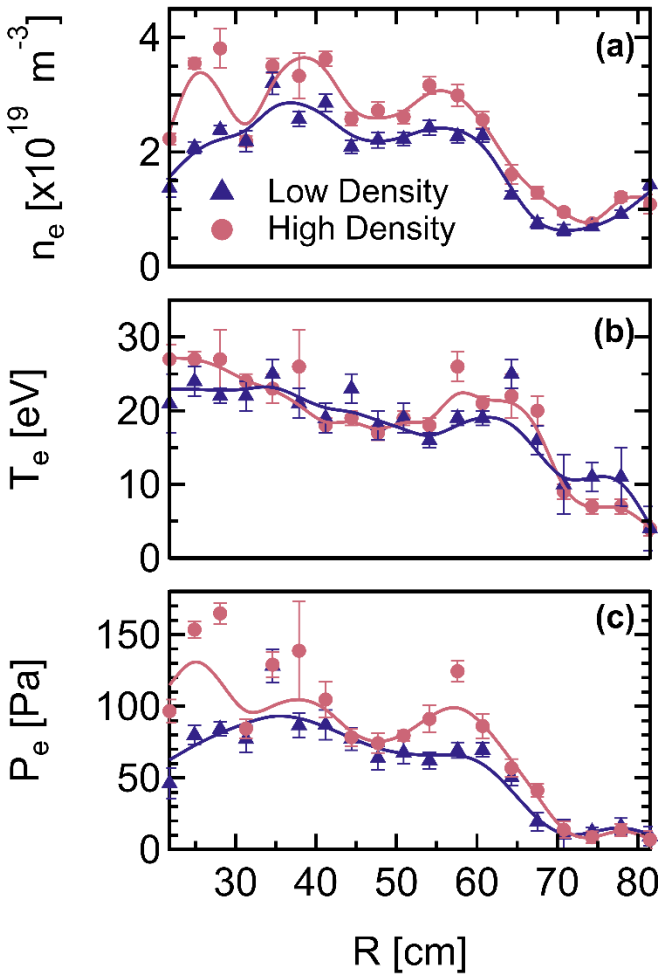

Figure 6.11: Comparison of electron kinetic profiles during the flattop in discharges developed at $B_T = 0.23$ T with different densities: (a) n_e, (c) T_e and (e) P_e profiles measured by the MPTS diagnostic at $t = 43$ ms. Solid lines are uncertainty weighted spline fits to the data.

in the flattop at $t = 43$ ms. There is a systematic separation in the n_e profiles outside of their respective error bars. Despite this difference in density, the temperature profiles shown in Figure 6.11(b) generally agree within the measurement uncertainty across the radial profile. These profiles are again relatively flat at T_e~20 eV like the data at $B_T = 0.15$ T. Additionally, the increased n_e does lead to an increase in the total stored electron kinetic energy as indicated by the increase in $P_e(R)$ shown in Figure 6.11(c).

Overall, the systematic variations in the density explored in this work did not observe significant changes to the measured T_e profiles. This was true for datasets collected at both $B_T = 0.15$ and 0.23 T. This observation may suggest that the energy confinement properties in LHI are not significantly impacted by variations to the density. However, it is important to acknowledge that the scenarios presented in this work are at higher density than previous LHI studies which typically operated with core density $n_{e,0} \leq 2 \times 10^{19}$ m^{-3} [30]. Further, scenarios operated at the higher end of this regime typically observed hollow T_e profiles with the core T_e around 20 eV which is comparable to what was observed in this work [30]. The explanation for these hollow T_e profiles was insufficient core heating to overcome the core radiation losses. The radiated power increases with density $P_{rad} \propto n_e$. Therefore, it is possible that the higher density scenarios studied in this work are limited by excessive radiation and not an intrinsic property of the transport processes that exist in LHI discharges. This will be further discussed in the next section.

6.4 Impact of Increased Plasma-Material Interactions and Radiated Power

Characterization of the impurities present during LHI discharges is an active area of focus on Pegasus-III. The impurity content dictates Z_{eff} and can lead to increased resistive dissipation which balances the helicity input thereby limiting the I_p that can be driven by LHI. Impurity ions can also lead to additional energy losses within the plasma through various radiation processes, such as Bremsstrahlung and line radiation. These radiative losses can reduce the T_e and further lead to enhanced resistive dissipation [5,176]. Hence, proper impurity control is critical for the development of a viable LHI startup scenario and subsequent handoff to alternative sustainment methods. This idea was illustrated in CHI experiments on NSTX which required PMI mitigation

to reduce the impurity content and radiated power to achieve successful coupling to subsequent inductive current drive [106].

A full investigation and characterization of the impurity content and transport during LHI is outside the scope of this work. Such investigations are ongoing in parallel [93,150] and are not discussed in detail here. Instead, a limited discussion is presented to illustrate the impact that the impurities generated from excessive PMI have on the interpretation of the results described in the preceding sections.

A persistent feature of initial LHI operations on Pegasus-III and during the discharges discussed previously in this chapter was PMI on injector surfaces. Examples of this interaction can be seen in the high-speed visible images shown in Figure 6.12. Generally, there are a variety of limiting surfaces that are contributing to the visible emission. The persistent feature of interest resides on the local injector limiter and is outlined by a red box in each image. In these discharges, only two of the four injectors are being actively driven, and the PMI feature is only observed on the local limiter structures associated with that array. When the other injectors are operated, a similar feature is also observed on the local limiter structure associated with the second set of injectors. The exact cause of this interaction is not yet precisely known. However, the working

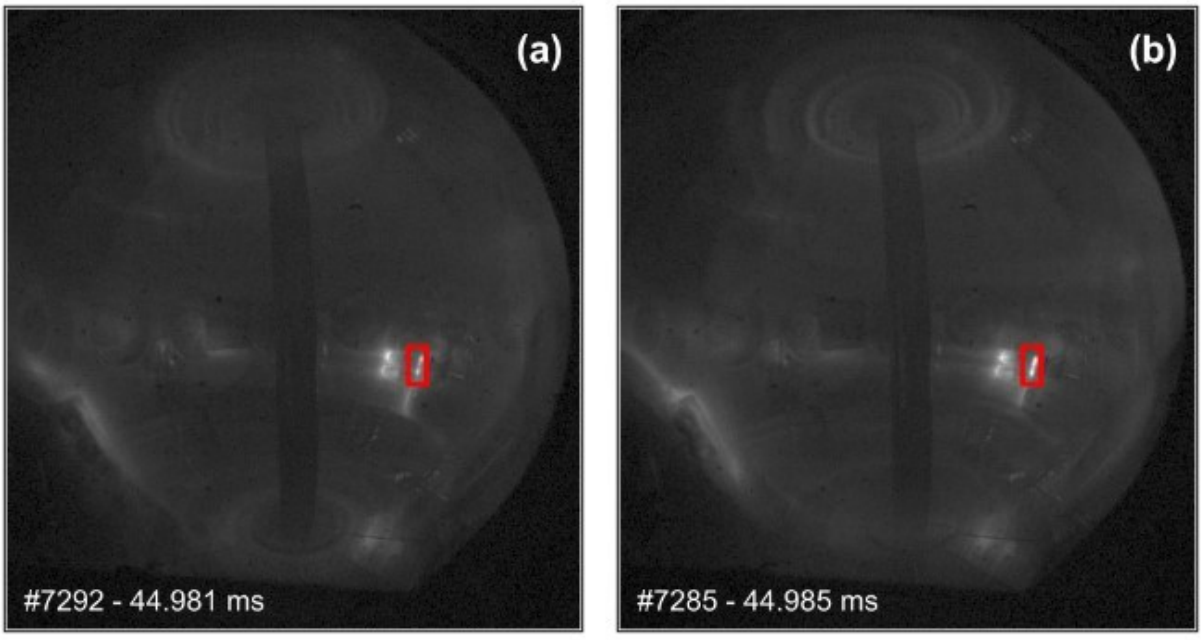

Figure 6.12: High-speed visible image from Pegasus-III discharges (a) #7292 and (b) #7285 at $t \approx 45$ ms. The persistent PMI feature that is the focus of the discussion is indicated by the red box in each image.

hypotheses are that the injectors are slightly misaligned to the equilibrium magnetic field and/or the injector limiter is improperly designed. These can allow injected current to flow along magnetic field lines that connect the biased injector surfaces to a grounded surface, which in this case would be the local limiter surface. A redesign of these limiting structures is underway and will be tested in upcoming campaigns to reduce this PMI.

Considerable runtime was devoted to efforts focused on mitigating this interaction, but a robust operating space was not identified. Still, the behavior of the interaction did vary across the operating space and led to measurable differences in the impurity content and plasma performance. Anecdotally, the interaction did appear to reduce in intensity when the injector power $P_{inj} = I_{inj}V_{inj}$ was reduced through the programming of the power supply and/or injector neutral fueling. However, there are additional variables that impact this interaction. A particular example is shown in Figure 6.13 which provides an overview of two discharges. The discharges have identical injector parameters as well as nominally identical PF coil programming and throughput of the neutral fueling valves. Despite this identical programming, the discharges experienced a bifurcation in the I_p evolutions shown in Figure 6.13(a).

A primary difference between these discharges is the amount of PMI on the local injector limiter. To visualize this, the two images shown in Figure 6.12 correspond to these discharges at $t = 45$ ms. The "reduced PMI" and "baseline" discharges described in Figure 6.13 correspond to Figure 6.12(a) and (b), respectively. Qualitatively, the baseline discharge has an increased amount of visible light emitted from the local injector limiter. This is quantified in Figure 6.13(d) which is the total number of counts measured by the high-speed camera within the same viewing region that is indicated by the red outline in Figure 6.12. The intensity of the emitted visible light from the local injector limiter in the baseline discharge is roughly twice that of the discharge with reduced PMI. It is not clear if this difference in PMI is a contributing cause of the bifurcation or merely a side effect. Still, the difference in PMI does have a measurable effect on the amount of radiated power. This is demonstrated in Figure 6.13(e) which compares an estimate for the volume-averaged radiated power density $\langle p_{rad} \rangle$. This estimate is derived from mapping the Abel-inverted radiated power density profile $p_{rad}(R)$ from the AXUV diode array. This $p_{rad}(R)$ is then mapped to the flux grid determined by ShapeFIT and then averaged over the plasma volume. The reduced PMI discharge generally has less than half the amount of $\langle p_{rad} \rangle$ relative to the baseline discharge.

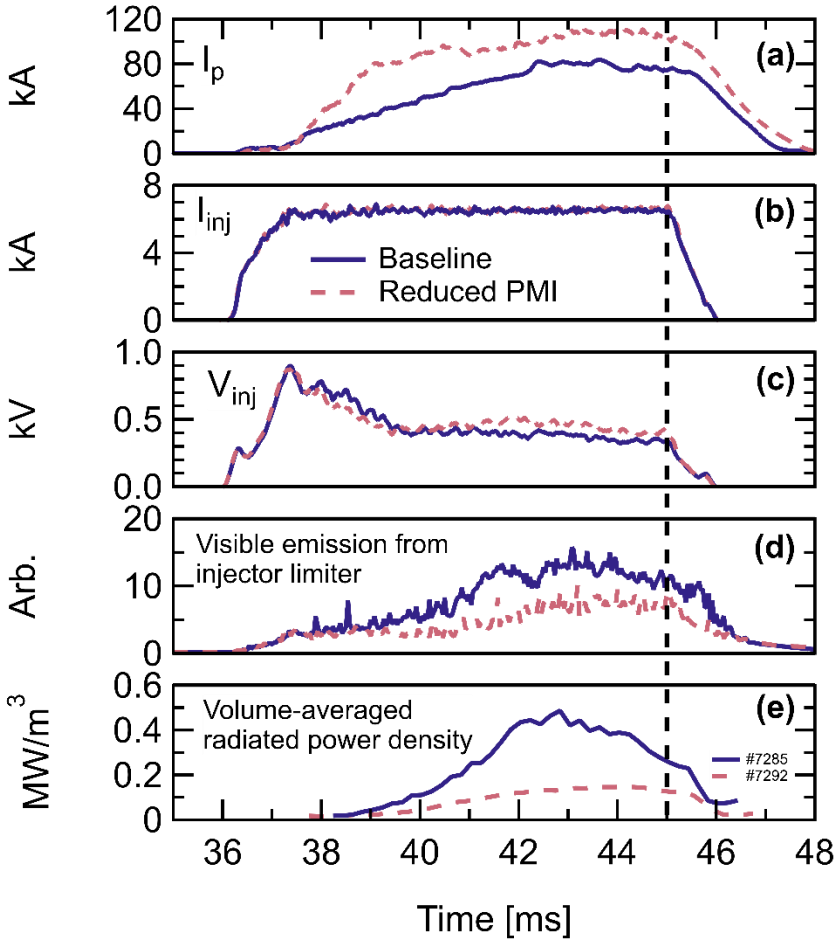

Figure 6.13: Overview of bifurcated discharges with identical programming: (a) I_p, (b) I_{inj}, (c) V_{inj}, (d) intensity of visible emission from local injector limiter PMI, and (e) estimated volume-averaged radiated power density. Vertical dashed line corresponds to the time of the visible high-speed images shown in Figure 6.12.

This indicates that the bifurcation to the reduced PMI scenario has less radiated power and is likely contributing to the higher achieved I_p.

The electron density is similar in each discharge which suggests an increased impurity concentration in the plasma. Figure 6.14(b) shows the $n_e(R)$ measured by the MPTS diagnostic late in both discharges at $t = 45$ ms. Despite the similar density, $\langle p_{rad} \rangle$ is higher throughout the baseline discharge. This implies an increase in the impurity density n_Z as the radiated power scales linearly with both the electron and impurity densities ($P_{rad} \propto n_e n_Z$). Assuming quasi-neutrality is satisfied (i.e.$n_i \approx n_e$), higher n_Z at fixed n_e also implies an increased Z_{eff} and an associated increase in the plasma resistance. Further, the radiated power density profile shown in Figure 6.14(c) indicates that the increase in radiated power is predominately concentrated near the LFS

plasma edge. This is consistent with the observed increased PMI on the local injector limiter in the baseline discharge providing a larger source of impurities near the plasma edge.

The different PMI characteristics and their apparent impacts on P_{rad} and implied impurity concentration directly impacts the achieved I_p and T_e in these discharges. In the reduced PMI discharge, the T_e profile shown in Figure 6.14(a) is systematically higher than the baseline discharge across much of the plasma volume. Specifically, the volume-averaged electron temperature for the baseline and reduced PMI discharge is 14 eV and 23 eV, respectively. All else being equal, this corresponds to the reduced PMI discharge having roughly half the plasma resistance compared to the baseline discharge when assuming Spitzer-like resistivity ($\eta \propto T_e^{-3/2}$). This is consistent with the higher I_p sustained in the reduced PMI discharge at otherwise fixed

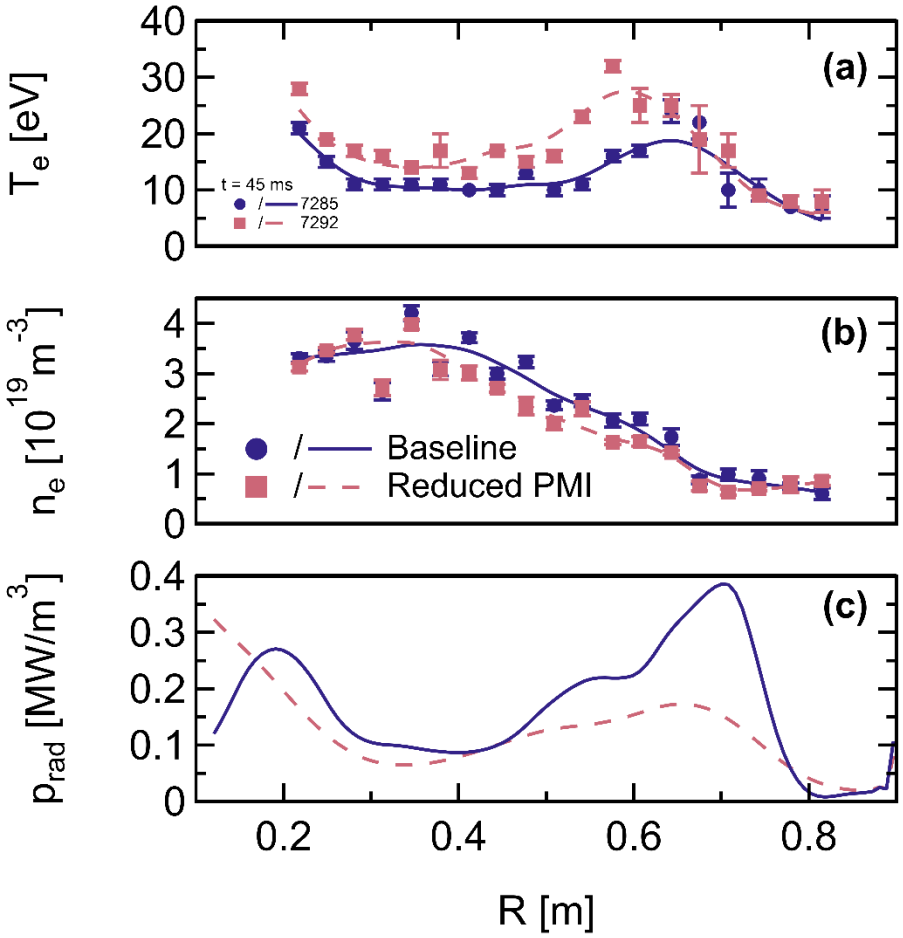

Figure 6.14: Comparison of radiated power and electron kinetic profiles in bifurcated discharges with different PMI characteristics: (a) n_e (b) T_e, and (c) radiated power density radial profiles measured at $t = 45$ ms.

helicity input. However, there are additional factors that are not fully accounted for in this simple analysis as the I_p flattop in the reduced PMI discharge is approximately a factor of ~1.4 higher than the baseline discharge. This is less than the factor of ~2 variation that would be expected from the variation in Spitzer resistivity alone. Still, the observation of increased T_e and I_p when the PMI is reduced is a suggestive result that demonstrates the importance of proper impurity control and PMI mitigation in the development of high performance LHI startup scenarios.

It is also important to understand the potential impact of this PMI in the context of the B_T and n_e scans presented in the previous sections. Specifically, the PMI and any subsequent effects on the impurity content of the plasma were not explicitly controlled during these experiments. Differences in the impurity content can affect the interpretation of the trends that were observed and can lead to misinterpretation of the results if not properly considered. The remainder of this section will revisit the P_{rad} measurements throughout those scenarios to provide additional context to the observed I_p and T_e variations.

First, the B_T scan discussed in Section 6.2 is revisited. The I_p trajectories of those discharges are shown in Figure 6.15(a). Figure 6.15(b) compares the estimated volume-averaged radiated power density throughout these discharges. The higher B_T discharge has higher $\langle p_{rad} \rangle$ throughout the I_p ramp. However, the $\langle p_{rad} \rangle$ is comparable during the flattop portion of both discharges. Recall from the discussion in Section 6.2, n_e was also well-matched throughout the I_p flattop. Therefore, this suggests that the impurity concentration is comparable in these discharges. Still, this is a considerable amount of radiated power that dynamically evolves throughout each discharge. This bears consideration while interpreting the observed I_p and T_e trends because excessive radiation can dominate over other transport losses in the global power balance. For instance, previous LHI studies on Pegasus observed hollow T_e profiles which were reasonably attributed to an excessive amount of core radiation compared to the limited core ohmic heating [30].

The measured P_{rad} during the discharges that comprise the density scans presented in Section 6.3 suggest a difference in the impurity content. Figure 6.16 shows the I_p and estimated volume-averaged radiated power density evolutions for each discharge within the density scan performed at $B_T = 0.15$ T. There is a difference in $\langle p_{rad} \rangle$ across the discharges with the lowest density scenario having significantly higher radiated power than the other two discharges. A deviation in

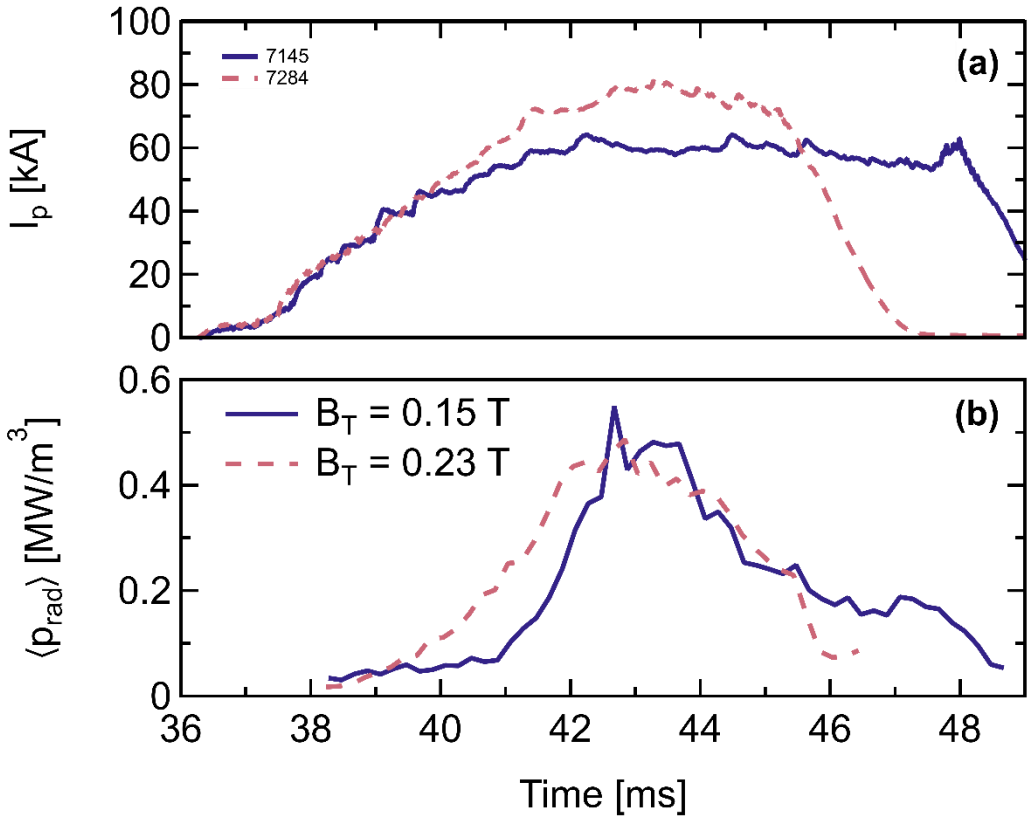

Figure 6.15: Comparison of radiated power in discharges that comprise the Pegasus-III B_T scan described in Section 6.2: (a) I_p and (b) volume-averaged radiated power density estimated from the AXUV diode array.

the measured P_{rad} is expected because $P_{rad} \propto n_e$. However, in these discharges there is an inverse relationship with density.

The inverse relationship is more clearly illustrated in Figure 6.17 which plots $\langle p_{rad} \rangle$ as a function of the core n_e measured by the MPTS diagnostic at $t = 43$ ms. The n_e at $R \approx 48$ cm is taken to be representative of the plasma core based on the average inferred R_0 from ShapeFIT in these discharges. The observed increase in $\langle p_{rad} \rangle$ as n_e decreases implies the impurity density is increasing as the density is lowered. This is consistent with the increased intensity of PMI observed on the local injector limiter structures during the lower density discharge which is likely providing a larger influx of impurities. The variation in radiation did not lead to any significant differences in the measured T_e profiles shown in Figure 6.11(a). Still, the relatively high level of radiated power could be dominating the power balance and masking changes in transport losses. Further, higher impurity concentration is likely leading to a higher Z_{eff} and consequently higher resistive

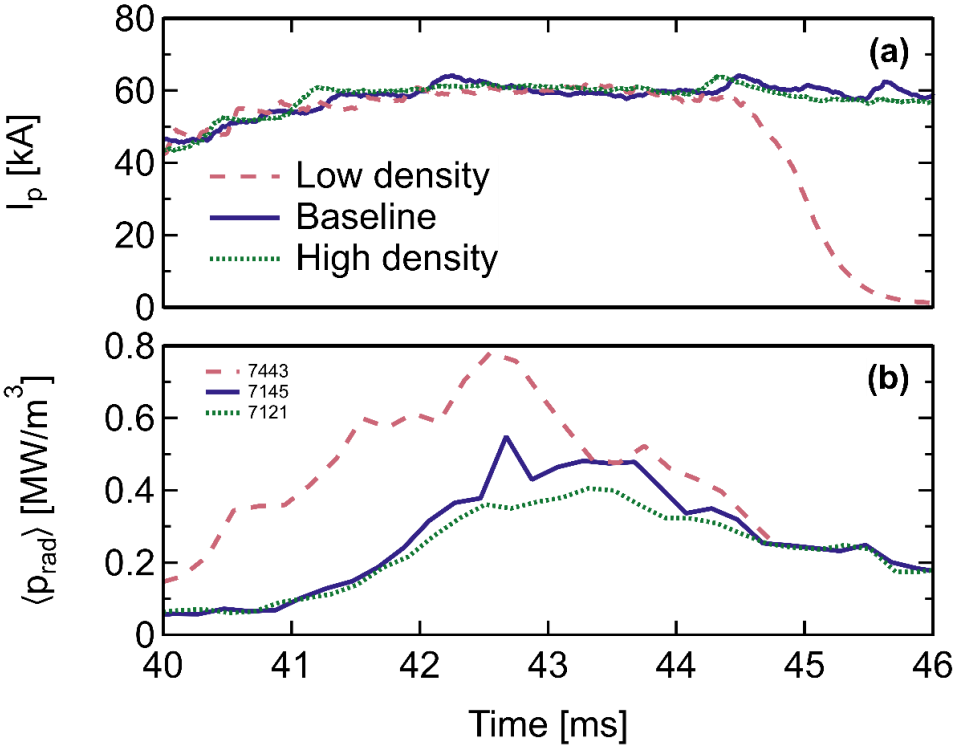

Figure 6.16: Comparison of radiated power in discharges that comprise the density scan at $B_T = 0.15$ T scan described in Section 6.3: (a) I_p and (b) estimated volume-averaged radiated power density from the AXUV diode array.

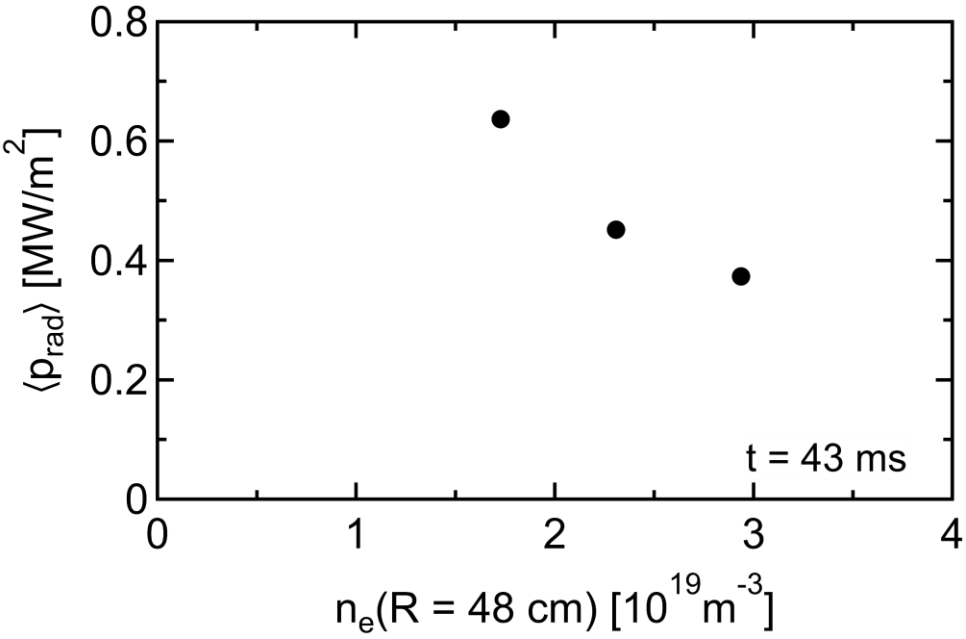

Figure 6.17: Estimated volume-averaged radiated power density as a function of the core n_e measured at $t = 43$ ms throughout the density scan performed at $B_T = 0.15$ T. Core n_e values correspond to MPTS measurements near the plasma core ($R \approx 48$ cm).

dissipation. This could contribute to the fixed I_p that was observed despite the roughly factor of two variation in n_e across these scenarios.

6.5 Comparison of Experimental Observations to Confinement Scaling Models

In Section 2.11, the expected I_p and T_e scaling trends for different assumed global confinement models were computed for hypothetical B_T, n_e, and V_{NORM} scans in the Pegasus-III operating space. These expectations are repeated here in Table 5 along with the observed experimental trends. The experimental B_T and n_e trends are inferred from the scans presented in Sections 6.2 and 6.3, respectively. The experimental V_{NORM} trends are informed by previous Pegasus studies performed by Bodner et al. [30].

These studies have indicated that I_p and T_e increases with V_{NORM} but are relatively unaffected by variations in n_e. Additionally, I_p increased with B_T while T_e was relatively unaffected. Referring to Table 5, these qualitative trends are not entirely consistent with any of the candidate confinement models but most closely follow the expectations from either the empirical neo-Alcator scaling and a globally collisional stochastic scaling model. This is consistent with previous work which found the relative trend of I_p with V_{NORM} to be consistent with these models when accounting for an estimate of the anomalous reconnection ion heating [30].

	I_p and $\langle T_e \rangle$ trends w/		
Confinement Scaling Estimates	**Increasing V_{NORM}**	**Increasing B_T**	**Increasing n_e**
LOC	↑	↑	—
SOC	↓	—	↑
Collisional stochastic	↑	—	—
Experimental observations	↑	I_p: ↑ $\langle T_e \rangle$: —	—

Table 5: Summary of I_p and $\langle T_e \rangle$ scaling trends for various assumed standard tokamak and globally stochastic confinement scalings along with the experimentally observed trends.

This simple interpretation of the observed trends is challenged by the observation of significant and variable amounts of P_{rad} throughout the discharges discussed in this work. The predicted qualitative trends summarized in Table 5 assume a constant radiated power fraction. Additionally, the radiated power fraction was assumed to be low ($F_{rad} \approx 10\%$) which is consistent with values used by Bodner et al. [30]. Further, P_{rad} varied throughout the I_p flattop which makes a steady-state model ill-suited for analyzing these discharges. As such, the extended 0-D power balance model developed in this thesis work and described in Section 4.1 is used to assess the impact of P_{rad} in these discharges in the context of these global confinement scalings.

The model inputs used in this analysis are consistent with the experimentally available measurements. The plasma shape evolution is inferred from ShapeFIT. The injector parameters (V_{inj} and I_{inj}) were measured directly from injector power supply diagnostics and w_{inj} is assumed to be $d_{inj} \approx 2.3$ cm. The n_e is assumed to linearly ramp during the I_p ramp and then remain steady during the flattop at values consistent with the limited MPTS profiles. The AXUV diode array was used to estimate $P_{rad}(t)$ by mapping the Abel-inverted emissivity profile [177] to the flux grid determined by ShapeFIT and integrating over the plasma volume. The remaining inputs were not well-constrained with the present diagnostic capabilities and/or limited available equilibrium reconstructions during LFS LHI discharges. Therefore, reasonable time-constant values are assumed for ℓ_i, T_i/T_e, Z_{eff}, and P_{aux}. These quantities are assumed to be consistent with previous LHI operations [11,30,53,88,93]: $\ell_i = 0.2 - 0.3$, $T_i/T_e \geq 1$, $Z_{eff} \leq 2$, and P_{aux} on the order of hundreds of kW.

Auxiliary heating from reconnection is required to avoid a predicted radiative collapse in these plasmas. This is illustrated in Figure 6.18 which shows 0-D model projections of the nominal baseline scenario (#7145). These calculations assume: $\ell_i = 0.3$, $T_i/T_e = 1$, $Z_{eff} = 1$, and neo-Alcator τ_E scaling. The only difference between these calculations is that one does not include any P_{aux} (dotted line) and one assumes $P_{aux} = 0.6$ MW (dash-dotted line). In the calculation without P_{aux}, the radiated power exceeds the total heating power ($P_{in} = I_p^2 R_p$) which leads to radiative collapse of the plasma ($I_p, \langle T_e \rangle \rightarrow 0$). For these assumed inputs, approximately $P_{aux} = 0.6$ MW is required to avoid this collapse and generally match the experimentally measured $I_p(t)$. This assumed P_{aux} is roughly 30% of the total injector power ($P_{inj} = I_{inj} V_{inj} \approx 2$ MW). Additionally,

it is comparable to the amount of P_{aux} that was needed in previous work to achieve consistency with experimental data albeit with significant uncertainty [30,92].

There is significant uncertainty in the amount of P_{aux} required to recreate the measured $I_p(t)$. A major source of this uncertainty arises from the assumed confinement scaling. If the energy confinement in LHI discharges is worse/better than what is assumed in the model, then the amount of P_{aux} required to avoid radiative collapse would increase/decrease. This is illustrated in Figure 6.19 which provides a nominally identical set of calculations as Figure 6.18 except for an assumed global stochastic confinement scaling model. Here, the same behavior is illustrated in that some

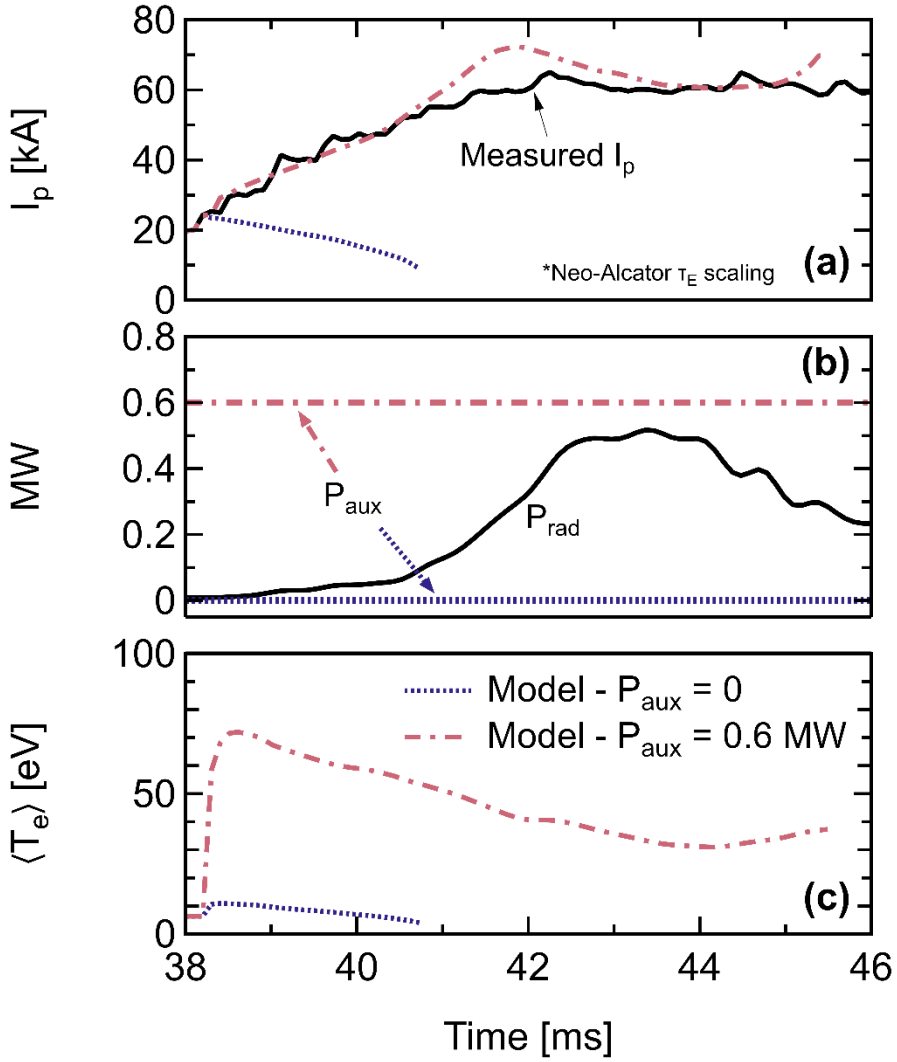

Figure 6.18: Interpretative 0-D power balance model analysis of Pegasus-III discharge #7145 with (dash-dotted line) and without (dotted line) P_{aux} assuming neo-Alcator confinement scaling: (a) I_p, (b) P_{aux} and P_{rad}, (c) and volume-averaged T_e.

amount of P_{aux} needs to be provided to avoid radiative collapse. However, the globally stochastic model requires 1.2 MW of auxiliary heating to recover the measured I_p trajectory. It is important to note that this factor of 2 difference in P_{aux} does not necessarily reflect the true difference in the underlying energy confinement between the two models. This is because the stochastic model (described in Section 2.8.3) only provides a relative variation of τ_E with Lundquist number and does not offer an absolute estimate. An arbitrary reference is required to normalize this stochastic scaling model within the 0-D model calculation. Here, τ_E is initialized to the value predicted by

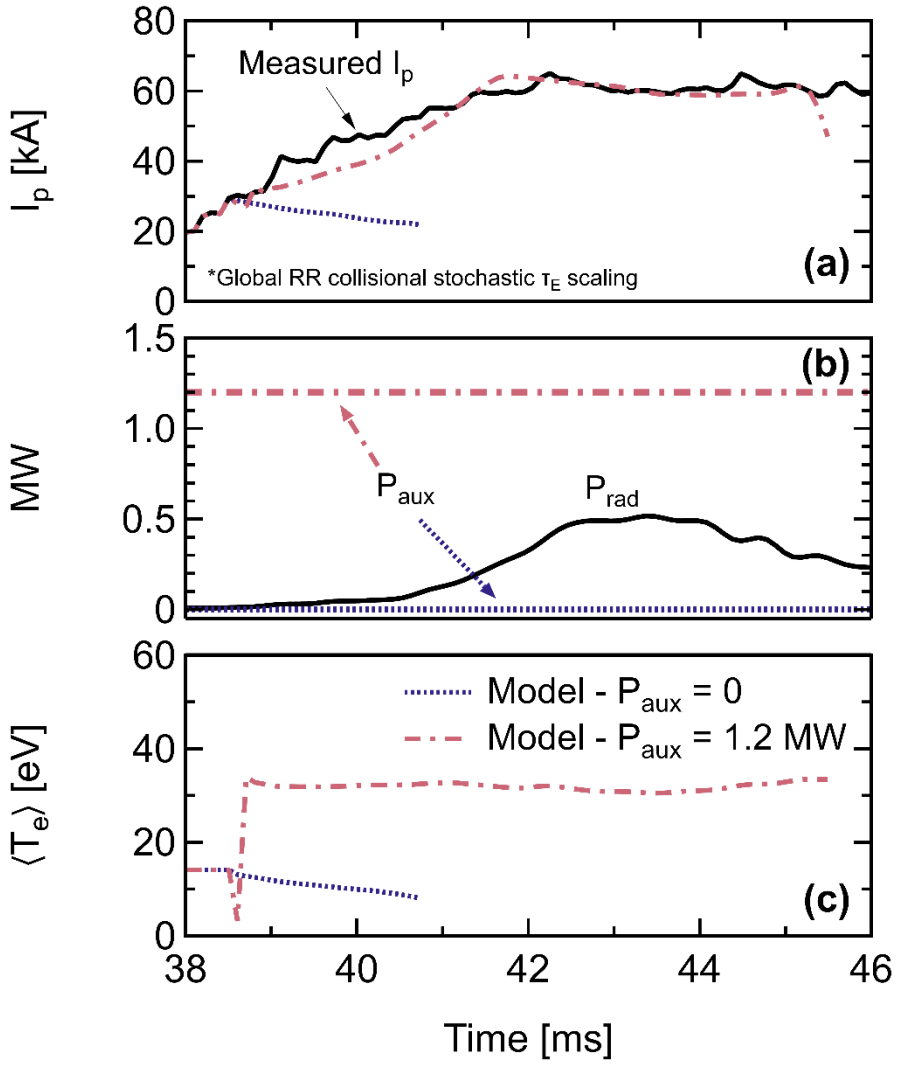

Figure 6.19: Interpretative 0-D power balance model analysis of Pegasus-III discharge #7145 with and without P_{aux} assuming a global Rechester-Rosenbluth collisional stochastic confinement scaling model: (a) I_p, (b) P_{aux} and P_{rad}, (c) and volume-averaged T_e.

the neo-Alcator empirical relation equation 2.26 when the power balance calculation begins ($t = 38.5$ ms). From this point, τ_E is scaled based on the expected $\tau_E \sim a^2/\chi_e$ scaling from the Rechester-Rosenbluth collisional stochastic thermal transport model given by equation 2.34. The relatively similar solutions between this stochastic model and the neo-Alcator scaling is a consequence of this normalization. Nonetheless, comparing the qualitative experimental trends with model predictions for this stochastic model are still meaningful even if the quantitative agreement is forced.

The $P_{aux} = 0.6$ and 1.2 MW calculations shown in Figure 6.18 and Figure 6.19 for the neo-Alcator and globally stochastic confinement models, respectively, are used as the baseline for a series of 0-D model calculations. These calculations vary the model input parameters to replicate the experimental parametric scans described earlier in this chapter. In these scans, the P_{rad} input is varied to be consistent with the experimental measurements. The inputs without direct measurements (i.e. ℓ_i, T_i/T_e, Z_{eff}, and P_{aux}) are assumed to be fixed across the various scenarios. This is done to prevent these free parameters from influencing the observed trends without a clear indication of how they varied during the experiments.

The qualitative trends predicted by the 0-D model when assuming the globally stochastic scaling model are identical to the expectations from the steady-state model that were previously shown in Table 5. The model calculations designed to replicate the B_T scan discussed in Section 6.2 are shown in Figure 6.20. The power balance calculations begin at $t = 38.5$ ms and are initialized with the experimentally measured I_p at that time. The total P_{rad} shown in Figure 6.20(b) is similar in both cases with the higher B_T case having somewhat higher radiated power early in the flattop. The predicted I_p and $\langle T_e \rangle$ evolutions in Figure 6.20(a) and (c), respectively, are essentially identical at both B_T levels. The unchanging $\langle T_e \rangle$ during the flattop is consistent with the limited MPTS profiles which did not vary significantly with B_T or throughout the flattop. However, the measured flattop I_p did modestly increase with B_T which is not predicted in these calculations.

The stochastic scaling model calculations for the n_e scan discussed in Section 6.3 are shown in Figure 6.21. Here, the same baseline discharge (red dash-dotted line) is again used. The assumed $n_e(t)$ for the high-density calculation has the same temporal shape as the baseline scenario but scaled up by the ratio of the measured core n_e measured by MPTS during the I_p flattop. The total

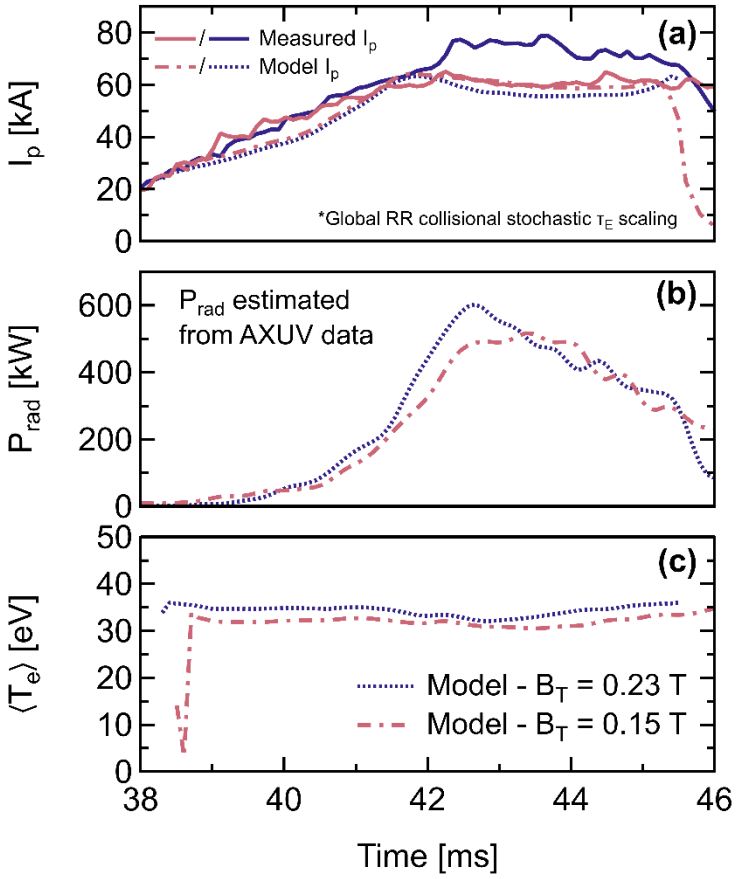

Figure 6.20: 0-D power balance model calculations to represent Pegasus-III B_T scan assuming global Rechester-Rosenbluth collisional stochastic confinement scaling model: (a) I_p, (b) P_{rad}, (c) and volume-averaged T_e for discharges at $B_T = 0.15$ T (dot-dashed line) and $B_T = 0.23$ T (dotted line). Solid lines in (a) represent experimental $I_p(t)$ for each scenario.

P_{rad} is similar in the baseline and higher density case. The other inputs are identical between the two calculations. The I_p and T_e trends predicted in these calculations are consistent with the experimental observations. The predicted I_p and $\langle T_e \rangle$ evolutions shown in Figure 6.21(a) and (c), respectively, do not exhibit any significant variation between the two density levels. This same behavior was also observed experimentally and discussed in Section 6.3. Additionally, the predicted $\langle T_e \rangle$ does not change significantly throughout the I_p flattop portion of the evolution which is consistent with the limited time-resolved MPTS measurements during this same period (Figure 6.9).

Figure 6.22 shows the 0-D model calculations meant to replicate the experimental B_T scan for an assumed neo-Alcator τ_E scaling. The predicted I_p evolutions in Figure 6.22(a) are comparable

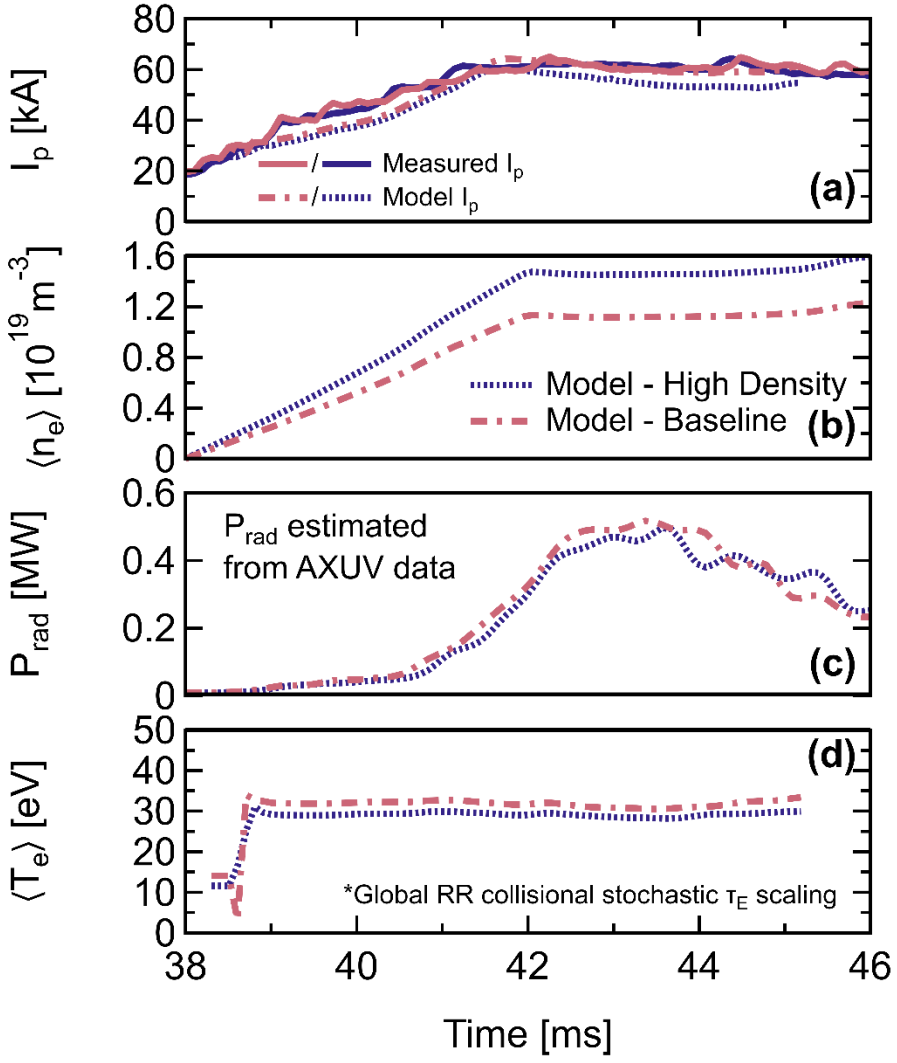

Figure 6.21: 0-D power balance model calculations to represent Pegasus-III n_e scan assuming global Rechester-Rosenbluth collisional stochastic confinement scaling model: (a) I_p, (b) volume-averaged n_e (c) P_{rad}, (d) and volume-averaged T_e. Solid lines in (a) represent experimental $I_p(t)$ for each scenario.

at both levels with the higher B_T evolutions being marginally higher during the flattop portion of the discharge. This qualitative behavior is consistent with the measured $I_p(t)$ which is also shown in Figure 6.22(a). The variation in $\langle T_e \rangle$ during the flattop is also consistent with the MPTS profiles which were also relatively unaffected by B_T. In these calculations, the predicted $\langle T_e \rangle(t)$ is relatively constant after ~42 ms and the variation between the different B_T levels during this period is ~5 eV. This level of variation is comparable to the MPTS measurement error and thus the experimental measurements could not realistically distinguish such a variation. There is a

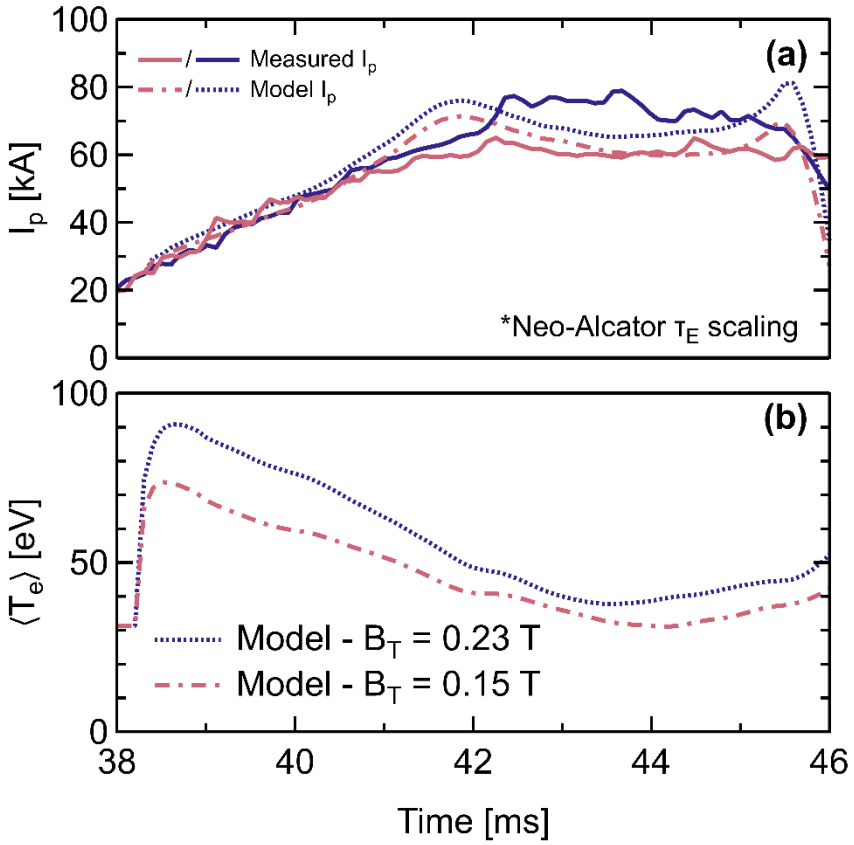

Figure 6.22: 0-D power balance model calculations to represent Pegasus-III B_T scan assuming neo-Alcator τ_E scaling: (a) I_p and (b) and volume-averaged T_e for discharges at $B_T = 0.15$ T (dot-dashed line) and $B_T = 0.23$ T (dotted line). Solid lines in (a) represent experimental $I_p(t)$ for each scenario.

larger predicted difference in $\langle T_e \rangle$ during the I_p ramp but MPTS measurements were not taken during this period to compare with these predictions.

Despite the encouraging qualitative agreement between model and experiment, there are noticeable quantitative discrepancies. For instance, there is a larger difference in the experimental flattop I_p than what is predicted by the model at the different B_T levels. Additionally, the model predicts $\langle T_e \rangle \sim 40$ eV during the flattop which is roughly twice the $T_e(R)$ measured by the MPTS diagnostic (Figure 6.6). These quantitative discrepancies are not surprising given the rough assumptions used for a variety of input parameters. However, these differences could equally be a result of the neo-Alcator empirical estimates being an inadequate benchmark for scaling LHI. This highlights the importance of expanding the diagnostic capabilities in future work to provide better constraints on these model inputs. This will allow a more definitive assessment of the ability to estimate the scaling of LHI plasmas with simple global confinement models.

Figure 6.23 shows the 0-D model calculations meant to replicate the experimental n_e scan for an assumed neo-Alcator τ_E scaling. The I_p and T_e trends predicted by the model are consistent with the experimental observations. The predicted I_p and $\langle T_e \rangle$ evolutions shown in Figure 6.23(a) and (c), respectively, do not exhibit any significant variation between the two density levels. This same behavior was also observed experimentally and discussed in Section 6.3. Additionally, the

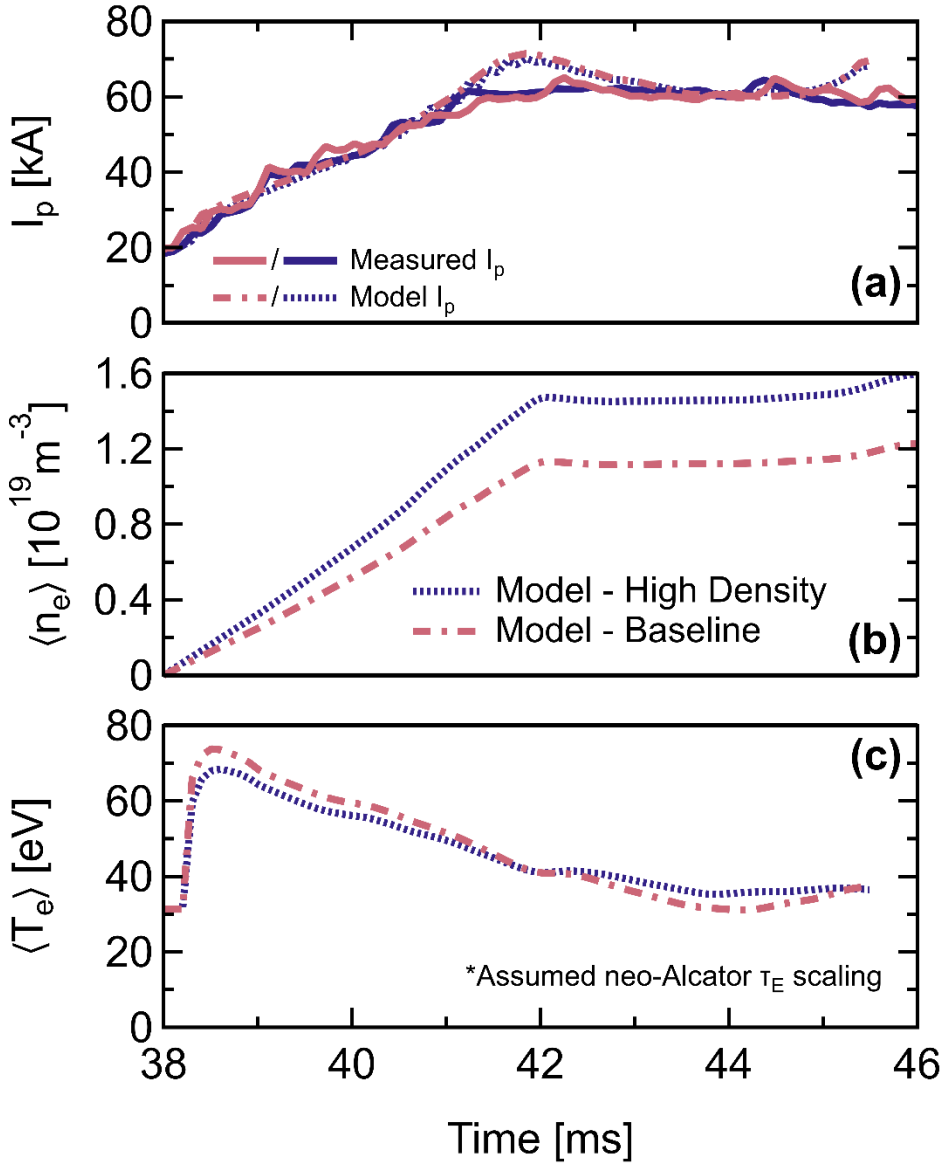

Figure 6.23: 0-D power balance model calculations to represent Pegasus-III n_e scan assuming neo-Alcator τ_E scaling: (a) I_p, volume-averaged (b) n_e, and (c) T_e. Solid lines in (a) represent experimental $I_p(t)$ for each scenario.

predicted $\langle T_e \rangle$ does not change significantly throughout the I_p flattop portion of the evolution which is consistent with the time-resolved MPTS measurements during this same period.

To summarize these calculations, the globally stochastic confinement scaling model reproduces most, but not all, of the qualitative trends observed in the B_T and n_e scans described in Sections 6.2 and 6.3, respectively. Notably, the calculations do not predict the variation in I_p with B_T. In contrast, the model calculations for an assumed empirical neo-Alcator scaling qualitatively reproduce all the experimental I_p and $\langle T_e \rangle$ trends. These trends are slightly different than what was predicted by the steady-state model which are summarized in Table 5. Most notably, the expectations from the steady-state confinement model expected both I_p and $\langle T_e \rangle$ to increase with B_T. Whereas only I_p significantly increased in the experiment. This may be a result of the significant amount of P_{rad} measured in these scenarios. In the 0-D model calculations, the T_e did increase with B_T but only slightly and of comparable magnitude to the experimental measurement uncertainty. This is largely a result of the radiated power dissipating a large fraction of the available heating power in these scenarios and preventing a significant increase in T_e.

This hypothesis is supported by the pair of discharges discussed in Section 6.4 which had varying amounts of P_{rad} and observed a bifurcation in I_p at otherwise similar parameters. This same behavior is also predicted by representative 0-D power balance model calculations which are shown in Figure 6.24. The calculations use identical inputs other than the different total P_{rad} estimated from the AXUV measurements which are shown in Figure 6.24(b). This difference in P_{rad} results in the I_p bifurcation that was observed in experiment. The reduced P_{rad} case (red dot-dashed line) ramps up to a higher I_p flattop which agrees well with the experimental $I_p(t)$ that is sustained until the calculation is terminated. Additionally, the predicted $\langle T_e \rangle$ is also $\sim 50\%$ higher in the reduced P_{rad} calculation throughout the flattop portion of the evolution. This is consistent with the observed increase in the $T_e(R)$ measured by MPTS at $t = 45$ ms (Figure 6.14).

As discussed in the preceding section, the radiated power in these scenarios appears to be correlated to excessive PMI on local injector limiter structures. A redesign of these structures is underway to mitigate this PMI and hopefully reduce the total P_{rad}. These experiments should be revisited when a lower P_{rad} operating scenario is identified. In particular, the B_T scan should be prioritized as it can distinguish between the competing neo-Alcator and collisional stochastic scaling models. This is illustrated by another set of 0-D model calculations shown in Figure 6.25.

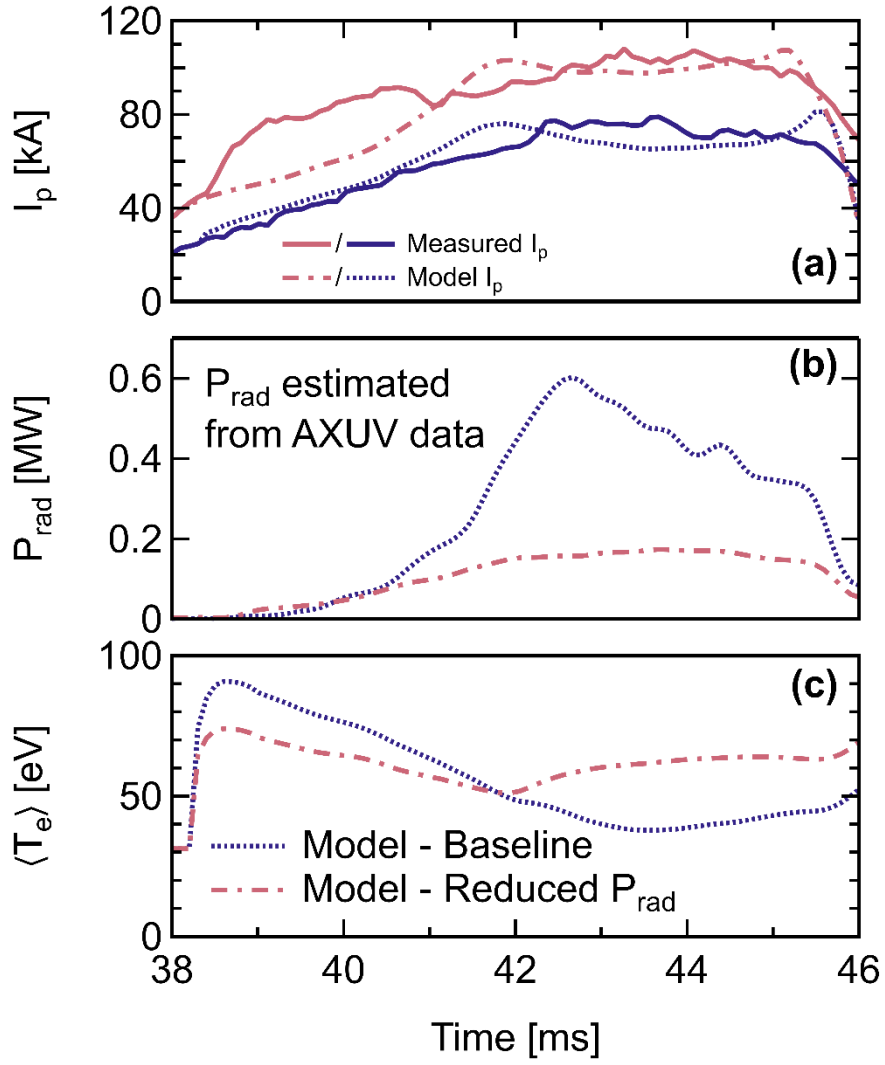

Figure 6.24: 0-D power balance calculations to represent Pegasus-III discharges with different P_{rad} assuming neo-Alcator τ_E scaling: (a) I_p, (b) P_{rad}, (c) and volume-averaged T_e Solid lines in (a) represent experimental $I_p(t)$ for each scenario.

These calculations use the same inputs as the "Reduced P_{rad}" scenario discussed in Figure 6.24 but at two different B_T levels. At this lower level of radiated power, these discharges are not in a radiation-limited regime for the given amount of heating power. This allows for the assumed neo-Alcator confinement scaling to dictate the performance resulting in an increase in I_p and $\langle T_e \rangle$. Therefore, repeating this experiment in an operating space with a reduced amount of radiated power may provide a more definitive test of the applicability of the neo-Alcator scaling for describing the scaling of LHI performance.

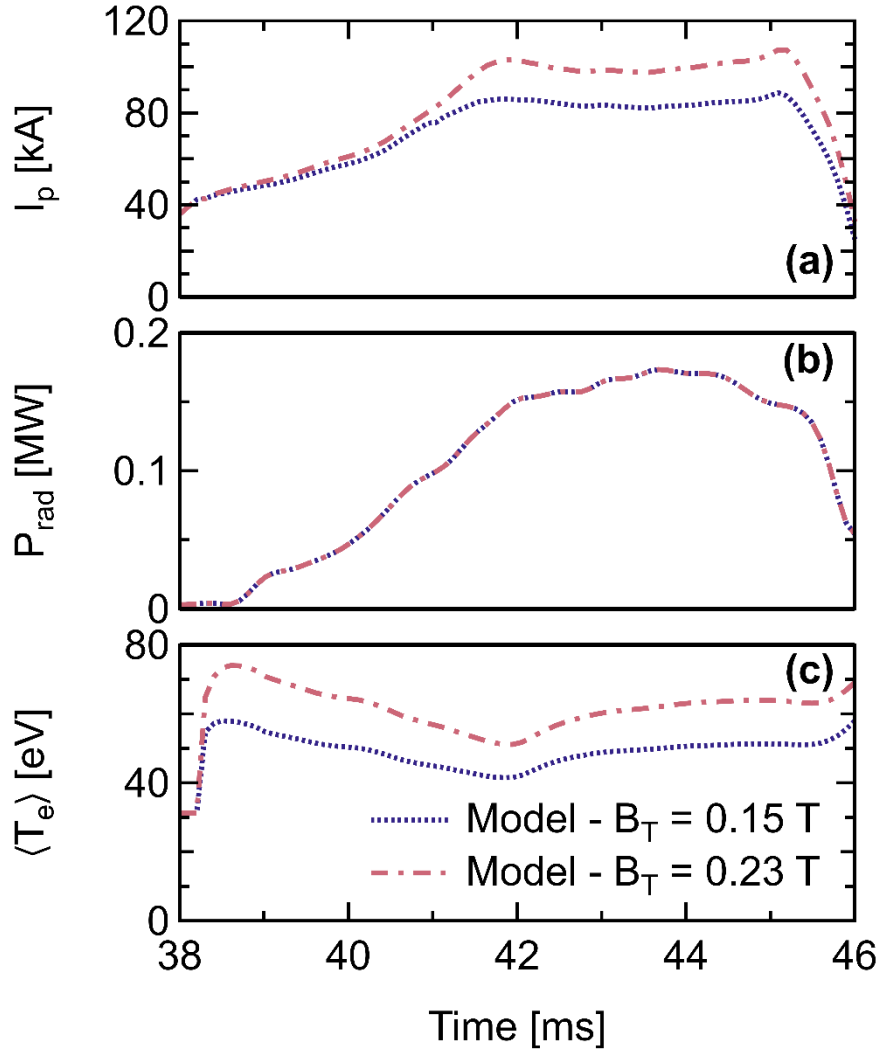

Figure 6.25: 0-D power balance calculations to represent a hypothetical Pegasus-III B_T scan with lower P_{rad} assuming neo-Alcator τ_E scaling: (a) I_p, (b) P_{rad}, (c) and volume-averaged T_e.

Realistically, these experiments and analysis do not provide a definitive assessment of the various candidate global confinement models for describing LHI plasmas. The 0-D modeling does suggest that experimental observations are qualitatively consistent with an ohmic-like scaling when considering the significant amount of radiated power. However, there are numerous under-constrained parameters in the model which could not be inferred from the experiment. It remains uncertain how those parameters varied in the experiment and what impact they may have on the interpretation of the observations. Therefore, qualitative agreement between model and experiment is merely a suggestive result at this point that requires further exploration. This necessitates

deploying diagnostic capabilities that can directly or indirectly quantify a variety of inputs, including Z_{eff}, T_i, and P_{aux}.

These experiments also highlight the importance of proper impurity control and radiation losses. In addition to complicating the interpretation of the qualitative trends in these studies, excessive radiation losses appear to be limiting the performance throughout the initial LHI campaigns on Pegasus-III. Impurity control has been a long-standing issue that has been identified throughout the development of CHI [22,106,178]. Previous ohmic-handoff studies on Pegasus demonstrate that the LHI technique can generate plasmas with sufficiently low impurity content to robustly couple to traditional ohmic-induction sustainment [48]. This suggests that LHI is not fundamentally inhibited by an impurity or radiation problem. However, this does not exclude such issues arising if there are non-optimal aspects of the injector design or installation. This appears to be the cause of the excessive radiation throughout these studies.

In addition to the global confinement models, the observed T_e in these experiments may also be described by open field line models. A relatively simple model for the T_e that can be sustained on open magnetic field lines was proposed by Hooper et al. [116]. This model predicts the following estimate for the maximum electron temperature that can be sustained along the injected current path

$$T_{e,max}[\mathrm{eV}] = 0.25\left(J_{inj}[\mathrm{A/cm^2}]L_{inj}[\mathrm{cm}]Z_{eff}\right)^{2/5}. \tag{6.1}$$

In this work, the maximum J_{inj} was typically $\leq 750\ \mathrm{A/cm^2}$ at the injector aperture. Assuming this current density is constant along the injected current path, $T_{e,max}$ can be computed as a function of the injected field line length. This calculation is presented in Figure 6.26 for $Z_{eff} = [1,2]$ which is represented by the black shaded region. For comparison, the horizontal red shaded region represents the typical range of T_e measured by the MPTS diagnostic throughout this work. This simple calculation suggests that field-line lengths $< 5\ \mathrm{m}$ could reasonably describe the measured T_e. Additionally, this model does not consider additional radiative losses or the possibility that J_{inj} may be reduced along the injected current path which would lead to reduced $T_{e,max}$ for a given L_{inj}. Despite the relative simplicity of this estimate, this range of L_{inj} to achieve the types of T_e measured in these experiments are comparable to field line lengths predicted by

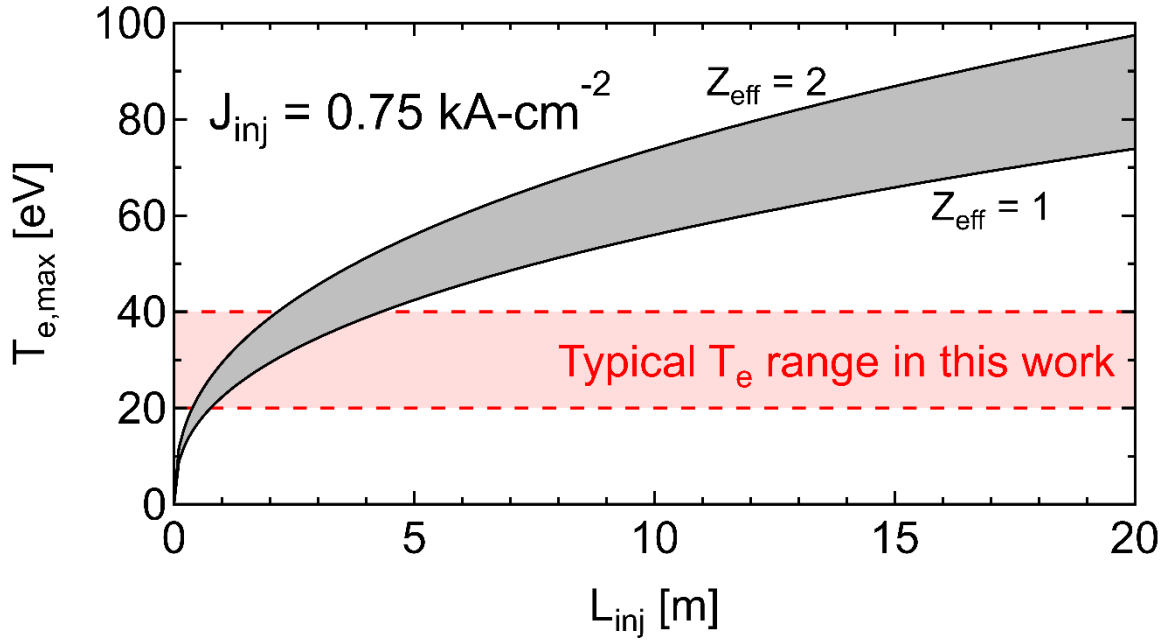

Figure 6.26: Estimated maximum T_e sustained along open field lines as a function of the field line length using equaiton 6.1 for a range of assumed Z_{eff} and uniform current density $J_{inj} = 0.75$ kA/cm^2. Horizontal dotted lines indicate approximate bounds of typical T_e measured by MPTS diagnostic in this work.

previous NIMROD simulations of LHI discharges [50]. This suggests that such open field line models merit continued consideration for describing the T_e that can be sustained during LHI.

Another open field line model proposed by Moses et al. relates the maximum T_e that can be sustained during DC helicity injection to the applied bias voltage, $T_{e,max} \leq V_{inj}/4$ [108]. This limit provides a theoretical absolute maximum T_e with additional radiative losses leading to even lower T_e. To date, this model for LHI confinement is also plausible as experiments have not exceeded this predicted limit.

Chapter 7
Conclusions

The development of predictive models for LHI performance is needed to design and reliably project high-current startup scenarios on Pegasus-III and other facilities. To this end, this thesis work has been focused on advancing this predictive understanding by characterizing the scaling of global I_p limits in a significantly expanded operating space. This chapter summarizes the key findings from this experimental work and highlights the technical accomplishments in support of this effort. Finally, several possible avenues to extend this work in future research are described.

7.1 Technical Accomplishments

The technical achievements of this work largely builds on the initial development of the 0-D power balance model and the ShapeFIT fast boundary reconstruction code by Barr [87]. As described in Chapter 4, these codes were significantly expanded in this work.

Accurate projections of LHI performance by the 0-D power balance model require a validated, self-consistent estimate of the dissipation within the model. The code development throughout this work provides a practical step towards this goal by extending the model to incorporate a self-consistent $\langle T_e \rangle$ evolution for an assumed energy confinement scaling model. Further, this extended model was able to successfully recreate the measured I_p and $\langle T_e \rangle$ for a well-documented ohmic discharge developed on Pegasus. Such agreement provides validation for the model output accuracy when a suitable global confinement scaling is known. With the aid of this extended

model, ongoing work will continue to focus on identifying a global confinement scaling suitable for describing LHI performance.

LFS LHI discharges are characterized by a dynamic shape evolution which dictates the $I_p(t)$. Further, the plasma shape is a critical input for interpretative analysis of LHI discharges with the 0-D power balance model. As such, continued development and refinement of the ShapeFIT fast boundary reconstruction code is critical for analysis and scenario development on Pegasus-III. To this end, significant improvements to the ShapeFIT code were made throughout this work. These include: incorporating data loading and post-processing of the new Pegasus-III magnetic diagnostic suite; implementation of new kernels for representing the plasma current distribution; overhaul of the graphical user interface for improved workflow and data visualization; and characterization of the output uncertainty for analysis of LHI discharges.

In addition to these code development efforts, this thesis work relied on the construction and commissioning of the new Pegasus-III facility. A wide variety of technical work was completed in support of this extensive facility upgrade. This included the development of a database of model equilibria to inform the design of the Pegasus-III magnetic diagnostic suite [149] and divertor coil assemblies [148]. Additionally, contributions were made to numerous sub-systems, including: routing of power transmission cables; construction of capacitor banks and H-bridge switch assemblies; design and deployment of LHI circuit assemblies; deployment of capacitor charge and dump systems; deployment of 100 psi deuterium fueling lines; construction and installation of toroidal field magnet components; installation and metrology of magnetic flux loops.

7.2 LHI Taylor Limit Scaling Validated in Expanded Pegasus-III Operating Space

The properties of the relaxed plasma state impose a global limit on the amount of current that can be driven by LHI, referred to as the Taylor limit. Increasing this limit provides a path toward more effective utilization of the helicity input provided by LHI and ultimately higher I_p startup plasmas. This limit can be increased through injector (I_{inj}, w_{inj}) or facility (B_T) design. Pegasus-III and its LHI system are designed to increase this Taylor limit and expand the LHI physics basis.

Initial Pegasus-III LHI experiments described in this work demonstrate that increasing the Taylor limit continues to be a viable path toward higher I_p in the expanded operating space. The

expected $I_{TL} \propto \sqrt{B_T I_{inj}}$ scalings have been validated for B_T and I_{inj} up to 0.3 T and 12 kA, respectively. Between Pegasus and Pegasus-III, this scaling has proven to be robust over an eight-fold and 12-fold variation in B_T and I_{inj}, respectively.

These initial experiments also demonstrate that injector design can be leveraged to optimize the Taylor limit in future LHI systems. Comparison of data from different injector installations with varying aperture widths have different inferred effective w_{inj}. Further, the variation in the effective w_{inj} is consistent with $w_{inj} \sim d_{inj}$. This motivates designing and testing injectors with narrower apertures to further optimize the Taylor limit ($I_{TL} \propto w_{inj}^{-1/2}$).

The discharges developed in this work provide a large parameter space to test the accuracy of the Taylor limit estimate developed for LHI. Generally, the predicted $I_{TL}(t)$ and measured $I_p(t)$ agreed within $\pm 20\%$ for discharges that were sustained at $I_p = I_{TL}$. This level of agreement is comparable to the uncertainty in I_{TL} predictions due to the uncertainty in the plasma shaping moments inferred from ShapeFIT. The inferred plasma boundary needs to be better constrained to further refine and validate the accuracy of the Taylor limit estimates generated by the model.

Throughout these scaling studies, discharges were sustained at $I_p = I_{TL}$ with excess helicity input. The magnetic fluctuations in these discharges increased as the system was increasingly over-driven at the Taylor Limit. Specifically, intermittent bursts of $n = 1$ magnetic activity occurred more often as the system was increasingly over-driven. The increased magnetic activity coincides with an observed flattening of the λ profile indicative of a plasma with a higher degree of magnetic relaxation. These observations are consistent with an increased amount of large-scale reconnection events predicted by NIMROD. These events appear to be driving relaxation in these discharges by more effectively transporting current from the plasma edge into the core.

7.3 Scaling of Helicity Dissipation during LHI Assessed in Pegasus-III

Future LHI systems on larger, higher B_T devices expect to operate in a regime in which the Taylor limit is sufficiently high such that the $I_p(t)$ is dictated by the balance of helicity input and dissipation. To reliably project the performance of these systems a more refined understanding of how the helicity dissipation scales to other operating regimes is needed. Previous LHI studies on

Pegasus identified a robust linear I_p scaling with V_{LHI} which was consistent with both ohmic-like and globally stochastic-like confinement estimates [30] but these studies were unable to distinguish between these competing models. This work sought to extend those studies with B_T and n_e scans in LHI discharges to differentiate between these competing scaling models.

Overall, these studies demonstrated that I_p increased with B_T while T_e was relatively unaffected. Further, the performance was relatively unaffected by variations in n_e. These qualitative trends were not entirely consistent with either the empirical neo-Alcator or globally collisional stochastic scaling expectations from a simple steady-state confinement model. However, the LHI discharges developed in this work observed persistent PMI on local injector limiter structures leading to a significant amount of radiated power. This radiated power appears to have a significant impact on the performance of these discharges and could potentially mask variations in the underlying transport processes and energy confinement. This hypothesis is supported by a pair of bifurcated discharges which were nominally identical other than a significant difference in the PMI behavior and consequently different measured P_{rad}. The discharge with lower P_{rad} was accompanied with an increase in both I_p and T_e for a fixed amount of helicity input.

The extended 0-D power balance model was used to assess if the observed experimental trends were consistent with either ohmic or globally stochastic confinement scalings when incorporating the time-varying P_{rad}. This analysis found that the qualitative trends observed in experiment were generally consistent with neo-Alcator confinement scaling. However, there are numerous input parameters that were not well-constrained in this analysis, such as ℓ_i, T_i/T_e, Z_{eff}, and P_{aux}, and assumed to be constant. If these parameters varied significantly throughout these discharges, then the interpretation of these qualitative trends may be impacted. Therefore, future work should focus on providing more constraints on these quantities to provide a more definitive assessment.

7.4 Future Work

This thesis work has characterized the scaling of the Taylor limit and helicity dissipation over an expanded operating space provided by the new Pegasus-III facility. This experimental characterization along with model development advances the predictive capabilities for projecting LHI performance. However, reliable predictive tools still require ongoing development and

advances in understanding. This work directly informs several potential avenues of future research focus.

Upcoming Pegasus-III experimental campaigns are planned to expand on the characterization of the Taylor limit described in this work. The Pegasus-III facility has recently been commissioned to its full $B_T = 0.6$ T capability [179]. This will enable the robust Taylor limit scaling relation to be tested at increasing B_T. Additionally, experiments are planned to test a novel, non-circular injector design. This injector features a narrow aperture width to optimize the Taylor limit and further assess how the injector design impacts the effective w_{inj}. These planned campaigns are expected to have an increased Taylor limit and enable access to even higher I_p LHI plasmas on Pegasus-III. Further, these increases in the Taylor limit may lead to an operating space in which $I_p(t)$ is predominantly set by helicity dissipation rather than the Taylor limit. Therefore, an improved understanding of the scaling of helicity dissipation is needed to further push LHI performance.

The extended 0-D model developed in this work may prove to be a powerful tool in interpreting LHI discharges for this purpose. However, the model requires stronger experimental constraints on numerous inputs to more definitively assess which, if any, global confinement scaling models are descriptive of LHI discharges. This necessitates deploying diagnostic capabilities that can directly or indirectly be used to quantify a variety of inputs, including Z_{eff}, T_i, and P_{aux}. Additionally, recharacterizing the scaling of helicity dissipation in an operating space with reduced PMI and radiated power could provide better insight into the underlying energy confinement properties of LHI discharges. To this end, the injector limiting structures have been redesigned and installed on Pegasus-III. If this redesign is successful in mitigating the PMI and excessive radiated power, the B_T and n_e scans described in Chapter 6 should be revisited.

To this point, LHI has been predominantly assessed in the context of global confinement scalings. While such models have demonstrated some success in describing the scaling of LHI performance, the measured T_e is also consistent with various open-field line models. As such, experiments should be designed to assess the viability of these models for describing LHI plasmas. Specifically, experiments should be designed at low V_{inj} to test the limit predicted by Moses et al. [108], $T_{e,max} \leq V_{inj}/4$. Additionally, simple analytic models which balance ohmic heating with parallel heat losses conducted to the wall along open field lines predict $T_{e,max} \propto J_{inj}^{2/5}$.

Therefore, future experiments should characterize how T_e scales with J_{inj} to compare with this prediction as the other global scaling models do not directly depend on J_{inj}. However, it is important to consider the anomalous reconnection ion heating in such experiments which scales $\propto I_{inj}$ and needs to be included in the global power balance [53].

Finally, LHI discharges over-driven at $I_p = I_{TL}$ in this work experienced increased bursts of $n = 1$ magnetic activity consistent with large-scale reconnection events predicted by NIMROD. These intermittent bursts appeared to drive magnetic relaxation in these discharges as indicated by a flattening of the λ profile. This may provide a means for some level of current profile control in LHI plasmas which should be explored further. Additionally, these bursts were not prevalent in all discharges throughout this work and have been absent in previous LHI operating regimes [12,46]. It is possible that this behavior is being driven by the amount of excess helicity input in these discharges. However, this cannot be accurately assessed at this time given the present understanding of helicity dissipation mechanisms during LHI. Therefore, future work should also focus on characterizing the necessary conditions for driving this bursty behavior as well as the relaxation processes that are active in their absence.

Appendix A

Utility of the Steady-state Confinement Model

In the absence of a more sophisticated confinement model for LHI plasmas, a simple steady-state confinement model was introduced in Section 2.9. It can be used to predict the variation of achievable I_p for different assumed global confinement scalings. This appendix benchmarks calculations from the model against data from a variety of tokamaks to provide some credibility to the empirical tokamak confinement scalings used in this work. Overall, the simple model showed good agreement with data across a variety of machines.

An example of this agreement is shown in Figure A.1. Figure A.1(a) shows data from Alcator C-MOD illustrating the transition from the LOC to the SOC regime [123]. At low densities, the confinement time increases linearly with density as described by neo-Alcator scaling (2.26). Then at around $n_e \sim 10^{20}$ m^{-3}, the confinement saturates with increasing density and is well described by the ITER89-P [180] scaling. Figure A.1(b) shows the steady-state confinement model estimates using input parameters consistent with the Alcator C-MOD experiment. The calculations

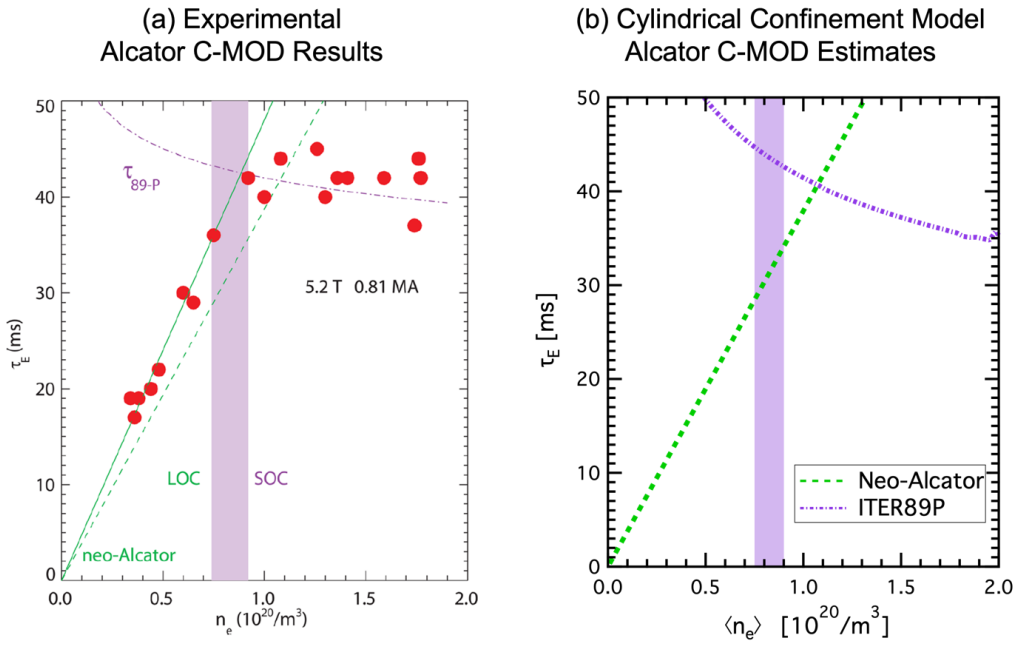

Figure A.1: Comparison of Alcator C-MOD (a) experimental data [123] to (b) estimates from the steady-state confinement model.

reproduce the experimentally observed confinement times in both regimes as well as the critical density at which the transition occurs. There is a small discrepancy between the ITER89-P curves plotted in Figure A.1(a) and (b). However, this is not surprising because the model assumes various parameters to be fixed across the density scan which varied during the experiment, such as Z_{eff}, P_{rad}, T_e/T_i, etc. [123].

The steady-state confinement model also reproduced numerous operating points from a variety of spherical tokamaks. Table A.1 compares calculations to data from START [132], MAST [181], NSTX [182,183], and Globus-M [184]. The inputs to the model were consistent with the available published data. However, not every paper provided information on all the required inputs for the model. This was most often the case for information regarding impurity concentrations. When this was the case, reasonable estimates were used, such as assuming $Z_{eff} \leq 3$ or radiated power fraction $\leq 30\%$.

Even with the uncertainty in some of the inputs, the calculations from the simple model show good agreement across all devices and operating regimes. The model takes I_p as an input, so the exact agreement with experiment is expected. On the other hand, the estimated $T_{e,0}$ and V_{loop} are determined from a self-consistent solution for the assumed confinement scaling. Despite the

simplistic nature of the estimates, the model agrees within 20% of the experimental $T_{e,0}$ and V_{loop} for most of the operating points. This is especially relevant when considering the purpose of using these estimates is to provide insight into the scaling of helicity dissipation in LHI, via T_e, on Pegasus-III. This provides confidence in the ability of the steady-state confinement model to produce reasonable predictions for standard tokamak confinement scaling estimates.

Device	**Parameter**	**Experiment**	**Steady-state confinement Model Estimates**
START [132]	Confinement scaling	LOC	neo-Alcator [125]
	$\boldsymbol{I_p}$ **[MA]**	$\mathbf{0.1}$	$\mathbf{0.1}$
	$\boldsymbol{V_{loop}}$ **[V]**	$\mathbf{1.5}$	$\mathbf{1.5}$
	$\boldsymbol{\bar{n}_e}$ $\boldsymbol{[/10^{20}\ m^{-3}]}$	$\mathbf{0.72}$	$\mathbf{0.72}$
	$\boldsymbol{T_{e,0}}$ **[keV]**	$\mathbf{0.2}$	$\mathbf{0.18}$
	$\boldsymbol{\tau_E}$ **[ms]**	$\mathbf{2.8 \pm 0.5}$	$\mathbf{2.5}$
NSTX [182,183]	Confinement scaling	NBI H-mode (H_{89P}=2.7)	ITER89-P (H_{89P}=2.7)[92]
	$\boldsymbol{I_p}$ **[MA]**	0.8	0.8
	$\boldsymbol{V_{loop}}$ **[V]**	$\mathbf{\sim 0.1}$	0.1
	$\boldsymbol{\bar{n}_e}$ $\boldsymbol{[/10^{20} m^{-3}]}$	0.5	0.5
	$\boldsymbol{T_{e,0}}$ **[keV]**	1.1	1.3
	$\boldsymbol{\tau_E}$ **[ms]**	54	64
MAST [181]	Confinement scaling	NBI H-mode	Low-$\boldsymbol{A}$ H-Mode [185]
	$\boldsymbol{I_p}$ **[MA]**	0.9	0.9
	$\boldsymbol{V_{loop}}$ **[V]**	1.3	1.1
	$\boldsymbol{\bar{n}_e}$ $\boldsymbol{[/10^{20} m^{-3}]}$	0.6	0.6
	$\boldsymbol{T_{e,0}}$ **[keV]**	$\mathbf{\sim 1.4}$	1.0
	$\boldsymbol{\tau_E}$ **[ms]**	50	60
Globus-M [184]	Confinement scaling	LOC/SOC	neo-Alcator / ITER97Lth [125]
	$\boldsymbol{I_p}$ **[MA]**	0.2	0.2 / 0.2
	$\boldsymbol{V_{loop}}$ **[V]**	1.28	1.38 / 1.45
	$\boldsymbol{\bar{n}_e}$ $\boldsymbol{[/10^{20} m^{-3}]}$	0.3	0.3 / 0.3
	$\boldsymbol{T_{e,0}}$ **[keV]**	0.69	0.69 / 0.66
	$\boldsymbol{\tau_E}$ **[ms]**	5.8	6.1 / 5.6

Table A.1: Comparison of ST data to steady-state confinement model estimates

Appendix B

New ShapeFIT Kernel Implementation

In this work, the ShapeFIT code was expanded to enable use of a FCF model for the plasma current kernel. In this model, the plasma is represented by a collection of current nodes to represent the plasma. Each node is a rectangular cross-section toroidally symmetric ring of current with the following user-defined parameters: geometric center of coil ($R_{c,i}$, $Z_{c,i}$), radial thickness $t_{c,i}$, vertical height $h_{c,i}$, and angular tilt in the $R-Z$ plane $\theta_{c,i}$. The only free parameter for each node is the amount of current $I_{c,i}$. The sum of the current in all N nodes is the total measured toroidal plasma current, $I_p = \sum_i^N I_{c,i}$. In this work, each node was constrained to have current flowing in the same direction.

There are several potential benefits to using this new FCF model as opposed to the previously implemented VCF model described in Section 4.2.1. The fixed geometry enables the Greens' functions to be precomputed for computational efficiency to map the toroidal current distribution from the current nodes defined in the $R-Z$ plane to the magnetic diagnostics and $\Psi(R,Z)$. This enables the use of a finite, rectangular geometry for each current source used to represent the plasma current distribution. Specifically, these calculations compute the magnetic field and flux from the discrete current sources by using an adaptive algorithm which subdivides the finite,

rectangular current source into filaments. The adaptive algorithm ensures that this subdivision respects the assumptions that are built into well-known Greens' functions [168] which use a Chebyshev approximation of the elliptic integrals [186]. These calculations are more accurate than the filament representation previously used in ShapeFIT but are sufficiently computationally prohibitive for use when they cannot be precomputed in the fitting process (i.e. when plasma filaments have variable geometry).

The fixed kernel geometry also may have greater flexibility in describing the current distribution that exists in LHI plasmas. By construction, the previously implemented VCF kernel was designed to represent a typical "D-shaped" tokamak plasma and constrained to move rigidly. LHI discharges have characteristic hollow current profiles and significant open-field line currents which may not be well-represented by this choice of kernel. In the new FCF model, the kernel can be defined by an arbitrary distribution of current elements which may be designed to better represent the current distribution that exists during LHI discharges. Additionally, it may inform the design of new VCF kernels that better represent LHI plasmas.

The fitting process for the FCF method is very similar to what was described in Section 4.2.1 with several notable differences. The Greens' functions for the magnetic field and flux due to the current in each of the nodes are precomputed to enable more efficient calculation of the diagnostic responses during the fit and $\Psi(R,Z)$ following fitting. To mitigate point-source like features arising in the $\Psi(R,Z)$ computation, the coarse grid of current nodes which are treated as free parameters are used to interpolate a finer resolution current density grid. This is visually represented in Figure B.1 where the red outlined cells indicate the "coarse" grid points, and the rest of the cells are interpolated on a denser grid (20×20 shown here). The color scale represents current density in each grid cell with darker shades corresponding to more current. This interpolation utilizes a Delaunay triangulation algorithm provided in the Igor Pro software package from WaveMetrics, Inc. The new, finer resolution current density grid is then re-normalized such that the total current on the finer grid matches the original coarse grid. Finally, fitting at each time point uses a 2-pass fitting algorithm. On the first pass, the minimal χ^2 solution is identified using all the current nodes as free parameters. For the 2nd pass, current nodes carrying a sufficiently small fraction of the total current (typically $< 0.1\%$) are nulled out and not used as free parameters. This is done to eliminate inconsequential free parameters and allow the Levenberg-Marquardt minimization algorithm to find a minimal χ^2 solution in a potentially easier free parameter space

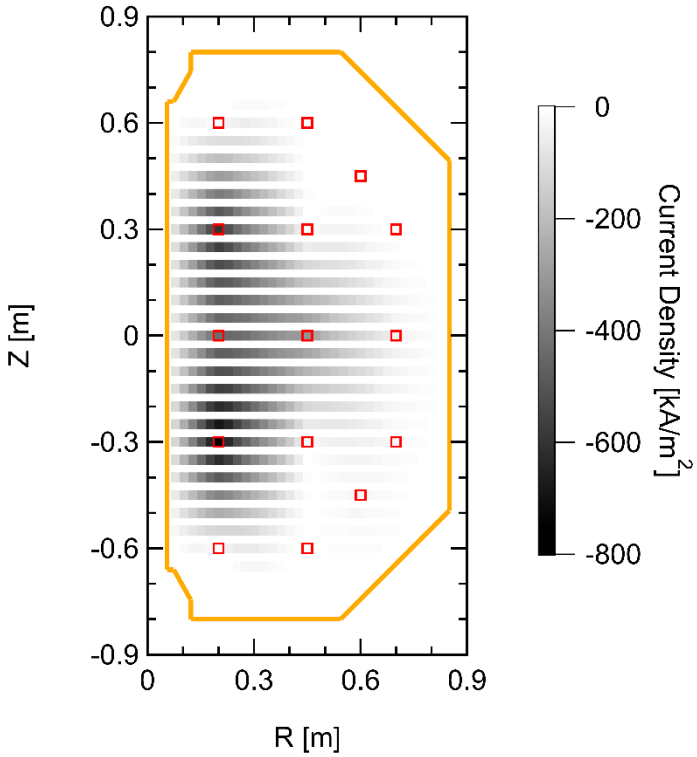

Figure B.1: Representative $N = 15$ FCF kernel node distribution (red squares) and interpolated toroidal current density grid (shaded cells).

to navigate. Other than these specific differences, the rest of the algorithm is identical to what was outlined in Section 4.2.1.

Despite the development of this new flexible filament FCF method, comparisons to the available equilibrium reconstructions and optical diagnostics indicate that the VCF method still provides a more realistic prediction of the plasma boundary during LHI discharges. As such, the standard four filament VCF kernel was used exclusively for the analysis in this work. However, continued development of the FCF method and incorporation of additional fitting constraints may be an interesting avenue for future work. Especially considering the potentially greater flexibility in capturing some of the effects of the injected current streams and separating their current distribution from the bulk plasma.

Bibliography

[1] *International Energy Outlook 2023 (IEO2023)* (2023).
[2] IPCC, *Global Warming of 1.5°C* (Cambridge University Press, 2022).
[3] U. N. E. Programme, *Emissions Gap Report 2024: No More Hot Air … Please! With a Massive Gap between Rhetoric and Reality, Countries Draft New Climate Commitments* (United Nations Environment Programme, n.d.).
[4] J. D. Lawson, Proc. Phys. Soc. Sect. B **70**, 6 (1957).
[5] J. Wesson, *Tokamaks*, 3rd ed. (Oxford University Press Inc., Oxford, 2004).
[6] S. Li *et al.*, Abstr. Appl. Anal. **2014**, (2014).
[7] F. Troyon *et al.*, Plasma Phys. Control. Fusion **26**, 209 (1984).
[8] E. J. Strait, Physics of Plasmas **1**, 1415 (1994).
[9] Y.-K. M. Peng and D. J. Strickler, Nucl. Fusion **26**, (1986).
[10] Y.-K. M. Peng, Phys. Plasmas **7**, 1681 (2000).
[11] D. J. Schlossberg *et al.*, Phys. Rev. Lett. **119**, 035001 (2017).
[12] J. A. Reusch *et al.*, Phys. Plasmas **25**, 056101 (2018).
[13] M. Ono and R. Kaita, Phys. Plasmas **22**, (2015).
[14] J. E. Menard *et al.*, Nucl. Fusion **62**, 036026 (2022).
[15] M. R. Wade and J. A. Leuer, Fusion Sci. Technol. **77**, 119 (2021).
[16] J. Menard *et al.*, Nucl. Fusion **37**, 595 (1997).
[17] V. A. Chuyanov and M. P. Gryaznevich, Fusion Eng. Des. **122**, 238 (2017).
[18] A. E. Costley and S. A. M. McNamara, Plasma Phys. Control. Fusion **63**, (2021).
[19] J. E. Menard *et al.*, Nucl. Fusion **56**, (2016).
[20] A. E. Costley, Philos. Trans. R. Soc. A Math. Phys. Eng. Sci. **377**, 20170439 (2019).
[21] D. Mueller, Phys. Plasmas **20**, (2013).
[22] R. Raman and V. F. Shevchenko, Plasma Phys. Control. Fusion **56**, (2014).
[23] M. W. Bongard *et al.*, Nucl. Fusion **59**, (2019).
[24] J. A. Leuer *et al.*, Nucl. Fusion **51**, (2011).
[25] M. Ushigome *et al.*, Nucl. Fusion **46**, 207 (2006).
[26] A. Sykes *et al.*, *First Results from MAST* (n.d.).
[27] R. Imazawa *et al.*, Electr. Eng. Japan **179**, (2012).
[28] J. B. Taylor and M. F. Turner, Nucl. Fusion **29**, (1989).
[29] J. L. Barr *et al.*, Nucl. Fusion **58**, (2018).
[30] G. M. Bodner *et al.*, Phys. Plasmas **28**, 102504 (2021).
[31] A. C. Sontag *et al.*, IEEE Trans. Plasma Sci. **50**, 4009 (2022).
[32] J. M. Finn and T. M. Atonsen, Comments Plasma Phys. Control. Fusion **9**, (1985).
[33] M. A. Berger, Plasma Phys. Control. Fusion **41**, (1999).
[34] T. H. Jensen and M. S. Chu, Phys. Fluids **27**, 2881 (1984).
[35] J. B. Taylor, Rev. Mod. Phys. **58**, (1986).

[36] J. B. Taylor, Phys. Rev. Lett. **33**, (1974).
[37] A. H. Boozer, Phys. Fluids **29**, 4123 (1986).
[38] R. Raman *et al.*, Nucl. Fusion **41**, (2001).
[39] A. J. Redd *et al.*, Phys. Plasmas **15**, (2008).
[40] R. Raman *et al.*, Phys. Plasmas **18**, (2011).
[41] F. Ebrahimi and R. Raman, Nucl. Fusion **56**, (2016).
[42] F. Ebrahimi *et al.*, Phys. Plasmas **20**, (2013).
[43] K. C. Hammond, R. Raman, and S. C. Jardin, Phys. Plasmas **26**, (2019).
[44] M. Ono *et al.*, Phys. Rev. Lett. **59**, 2165 (1987).
[45] D. S. Darrow *et al.*, Phys. Fluids B **2**, 1415 (1990).
[46] J. M. Perry *et al.*, Nucl. Fusion **58**, (2018).
[47] K. E. Thome *et al.*, Nucl. Fusion **57**, (2017).
[48] C. M. B. Pierren, An Assessment of the Startup Target Quality of Local Helicity Injection Initiated Plasmas via Ohmic Current Drive Sustainment on the Pegasus Spherical Tokamak, University of Wisconsin-Madison, 2024.
[49] J. B. O'Bryan, C. R. Sovinec, and T. M. Bird, Phys. Plasmas **19**, (2012).
[50] J. B. O'Bryan and C. R. Sovinec, Plasma Phys. Control. Fusion **56**, (2014).
[51] J. O'Bryan, Numerical Simulation of Non-Inductive Startup of the Pegasus Toroidal Experiment, University of Wisconsin-Madison, 2014.
[52] D. J. Battaglia *et al.*, Phys. Rev. Lett. **102**, (2009).
[53] M. G. Burke *et al.*, Nucl. Fusion **57**, (2017).
[54] C. W. Barnes *et al.*, Phys. Fluids **29**, 3415 (1986).
[55] H. Ji, S. C. Prager, and J. S. Sarff, Phys. Rev. Lett. **74**, 2945 (1995).
[56] S. C. Prager, Plasma Phys. Control. Fusion **41**, A129 (1999).
[57] L. Marrelli *et al.*, Nucl. Fusion **61**, 023001 (2021).
[58] J. B. Taylor, Phys. Plasmas **7**, 1623 (2000).
[59] T. R. Jarboe, Phys. Plasmas **12**, (2005).
[60] S. Cappello *et al.*, in *AIP Conf. Proc.* (AIP, 2008), pp. 27–39.
[61] H. Qin *et al.*, Phys. Rev. Lett. **109**, 235001 (2012).
[62] E. Hameiri and A. Bhattacharjee, Phys. Rev. A **35**, 768 (1987).
[63] D. Montgomery and L. Phillips, Phys. Rev. A **38**, 2953 (1988).
[64] M. K. Bevir, A. Caloutsis, and C. G. Gimblett, Plasma Phys. Control. Fusion **35**, 133 (1993).
[65] B. Dasgupta *et al.*, Phys. Rev. Lett. **81**, 3144 (1998).
[66] R. Bhattacharyya, M. S. Janaki, and B. Dasgupta, Phys. Plasmas **7**, 4801 (2000).
[67] R. Bhattacharyya, M. S. Janaki, and B. Dasgupta, Phys. Lett. A **291**, 291 (2001).
[68] B. Dasgupta *et al.*, Phys. Rev. E **65**, 046405 (2002).
[69] R. Farengo and J. R. Sobehart, Plasma Phys. Control. Fusion **36**, 1691 (1994).
[70] C. Zhang, S. Zhu, and L. Shen, Phys. Plasmas **5**, 178 (1998).
[71] A. DiVita and M. Brusati, Plasma Phys. Control. Fusion **37**, 1075 (1995).
[72] M. Y. Kucinski, Plasma Phys. Control. Fusion **40**, 111 (1998).
[73] A. DiVita and M. Brusati, Plasma Phys. Control. Fusion **37**, 1075 (1995).
[74] D. J. Den Hartog *et al.*, Phys. Plasmas **6**, 1813 (1999).
[75] H. Ji, S. C. Prager, and J. S. Sarff, Phys. Rev. Lett. **74**, 2945 (1995).
[76] J. P. Sauppe and C. R. Sovinec, Phys. Plasmas **24**, (2017).
[77] B. Hudson *et al.*, Phys. Plasmas **15**, (2008).

[78] E. B. Hooper *et al.*, Plasma Phys. Control. Fusion **54**, 113001 (2012).
[79] S. C. Hsu and P. M. Bellan, Phys. Rev. Lett. **90**, 215002 (2003).
[80] P. L. García-Martínez and R. Farengo, Phys. Plasmas **16**, (2009).
[81] B. I. Cohen *et al.*, Phys. Plasmas **16**, (2009).
[82] C. R. Sovinec, J. M. Finn, and D. Del-Castillo-Negrete, Phys. Plasmas **8**, 475 (2001).
[83] K. J. McCollam and T. R. Jarboe, Plasma Phys. Control. Fusion **44**, 493 (2002).
[84] B. A. Nelson *et al.*, Phys. Rev. Lett. **72**, 3666 (1994).
[85] E. B. Hooper and C. R. Sovinec, Phys. Plasmas **23**, (2016).
[86] N. J. Richner *et al.*, Phys. Rev. Lett. **128**, 105001 (2022).
[87] J. L. Barr, Inductive Evolution and MHD in Local Helicity Injection Discharges on Pegasus, University of Wisconsin-Madison, 2016.
[88] D. J. Battaglia *et al.*, Nucl. Fusion **51**, (2011).
[89] W. C. Turner *et al.*, Phys. Fluids **26**, 1965 (1983).
[90] C. T. Holcomb *et al.*, Phys. Plasmas **13**, (2006).
[91] O. Sauter, C. Angioni, and Y. R. Lin-Liu, Phys. Plasmas **6**, 2834 (1999).
[92] G. M. Bodner, Electron Heating During Local Helicity Injection in the Pegasus Toroidal Experiment, University of Wisconsin-Madison, 2020.
[93] C. Rodriguez Sanchez *et al.*, in *Am. Phys. Soc. Div. Plasma Phys.* (2024).
[94] K. Nagaoka *et al.*, J. Korean Phys. Soc. **49**, 92 (2006).
[95] F. M. Poli *et al.*, Nucl. Fusion **55**, 123011 (2015).
[96] T. R. Jarboe, Plasma Phys. Control. Fusion **36**, (1994).
[97] R. D. Wood *et al.*, Nucl. Fusion **49**, (2009).
[98] C. R. Sovinec *et al.*, Phys. Rev. Lett. **94**, 035003 (2005).
[99] B. I. Cohen *et al.*, Phys. Plasmas **12**, (2005).
[100] H. S. McLean *et al.*, in *Phys. Plasmas* (2006).
[101] M. V. Umansky *et al.*, Plasma Phys. Control. Fusion **48**, 235 (2006).
[102] A. B. Rechester and M. N. Rosenbluth, Phys. Rev. Lett. **40**, 38 (1978).
[103] R. Raman *et al.*, Nucl. Fusion **53**, (2013).
[104] B. A. Nelson *et al.*, Phys. Plasmas **2**, (1995).
[105] W. T. Hamp *et al.*, Phys. Plasmas **15**, (2008).
[106] R. Raman *et al.*, Phys. Rev. Lett. **104**, 095003 (2010).
[107] A. H. Boozer, Phys. Fluids B **5**, 2271 (1993).
[108] R. W. Moses, R. A. Gerwin, and K. F. Schoenberg, Phys. Plasmas **8**, 4839 (2001).
[109] R. Raman *et al.*, Nucl. Fusion **45**, (2005).
[110] B. A. Nelson *et al.*, Nucl. Fusion **51**, (2011).
[111] D. J. Schlossberg, Electron Temperature and Density in Local Helicity Injection and High Bt Plasmas, University of Wisconsin-Madison, 2017.
[112] N. Richner, Characterization of Magnetic Activity During Local Helicity Injection, University of Wisconsin-Madison, 2021.
[113] E. J. Doyle *et al.*, Nucl. Fusion **47**, S18 (2007).
[114] M. R. Stoneking *et al.*, Phys. Plasmas **5**, 1004 (1998).
[115] J. S. Sarff *et al.*, Nucl. Fusion **43**, 1684 (2003).
[116] E. B. Hooper, R. H. Cohen, and D. D. Ryutov, J. Nucl. Mater. **278**, 104 (2000).
[117] F. L. Hinton and R. D. Hazeltine, Rev. Mod. Phys. **48**, 239 (1976).
[118] M. Yoshida *et al.*, Nucl. Fusion **65**, 033001 (2025).
[119] J. Abbate *et al.*, Phys. Plasmas **31**, (2024).

[120] B. C. Lyons *et al.*, Phys. Plasmas **30**, (2023).
[121] G. M. Staebler *et al.*, Nucl. Fusion **64**, 085002 (2024).
[122] A. Y. Pankin *et al.*, Comput. Phys. Commun. **312**, 109611 (2025).
[123] J. E. Rice *et al.*, Phys. Plasmas **19**, (2012).
[124] J. E. Rice *et al.*, Nucl. Fusion **60**, (2020).
[125] I. P. E. G. on C. Transport, I. P. E. G. on C. Database, and I. P. B. Editors, Nucl. Fusion **39**, 2175 (1999).
[126] S. M. Kaye *et al.*, Nucl. Fusion **37**, 1303 (1997).
[127] F. Wagner, Eur. Phys. J. H **43**, 523 (2018).
[128] A. Sykes *et al.*, Nucl. Fusion **39**, (1999).
[129] G. S. Kurskiev *et al.*, Plasma Phys. Control. Fusion **59**, (2017).
[130] M. Ono *et al.*, Nucl. Fusion **41**, (2001).
[131] S. M. Kaye *et al.*, Phys. Plasmas **8**, 1977 (2001).
[132] A. Sykes *et al.*, Plasma Phys. Control. Fusion **35**, 1051 (1993).
[133] M. Valovič *et al.*, Nucl. Fusion **45**, 942 (2005).
[134] S. M. Kaye *et al.*, in *Nucl. Fusion* (2006), pp. 848–857.
[135] A. Y. Dnestrovskij, J. W. Connor, and M. P. Gryaznevich, Plasma Phys. Control. Fusion **61**, (2019).
[136] N. N. Bakharev *et al.*, Nucl. Fusion **58**, (2018).
[137] M. Valovič *et al.*, Nucl. Fusion **49**, (2009).
[138] G. S. Kurskiev *et al.*, Nucl. Fusion **62**, 016011 (2022).
[139] S. M. Kaye *et al.*, Nucl. Fusion **53**, (2013).
[140] W. Guttenfelder *et al.*, Phys. Plasmas **19**, (2012).
[141] R. J. Bickerton, Plasma Phys. Control. Fusion **39**, 339 (1997).
[142] J. W. Connor and J. B. Taylor, Phys. Fluids **27**, (1984).
[143] G. Miller, Plasma Phys. Control. Fusion **26**, 1119 (1984).
[144] S. C. McCool, A. J. Wootton, and R. V. Bravenec, *Optimization of a Mega-Ampere Spherical Tokamak for Beta-Limit and Confinement Studies* (Oakland, CA, 1994).
[145] J. M. Perry, Experiments Using Local Helicity Injectors in the Lower Divertor Region as the Majority Current Drive in a Tokamak Plasma, University of Wisconsin-Madison, 2018.
[146] G. D. Garstka *et al.*, Nucl. Fusion **46**, (2006).
[147] M. W. Bongard *et al.*, IEEE Trans. Plasma Sci. **50**, 4021 (2022).
[148] J. A. Reusch *et al.*, IEEE Trans. Plasma Sci. **50**, 4015 (2022).
[149] J. A. Reusch *et al.*, Rev. Sci. Instrum. **95**, (2024).
[150] C. Rodriguez Sanchez *et al.*, Rev. Sci. Instrum. **95**, (2024).
[151] E. T. Hinson, Physics of the Current Injection Process during Localized Helicity Injection, University of Wisconsin-Madison, 2015.
[152] G. M. Bodner *et al.*, Rev. Sci. Instrum. **87**, (2016).
[153] D. J. Schlossberg *et al.*, Rev. Sci. Instrum. **87**, (2016).
[154] L. Porte *et al.*, Rev. Sci. Instrum. **70**, (1999).
[155] J. M. Perry, Experiments Using Local Helicity Injectors in the Lower Divertor Region as the Majority Current Drive in a Tokamak Plasma, University of Wisconsin-Madison, 2018.
[156] A. C. Sontag *et al.*, Nucl. Fusion **48**, 095006 (2008).
[157] M. W. Bongard, Edge Magnetohydrodynamic Instability Studies in the Pegasus Toroidal

Experiment,University of Wisconsin-Madison, 2011.
[158] M. W. Bongard *et al.*, Nucl. Fusion **54**, 114008 (2014).
[159] J. S. Bendat and A. G. Piersol, *Engineering Applications of Correlation and Spectral Analysis* (John Wiley & Sons, Inc., 1980).
[160] O. Reynolds, *Papers on Mechanical and Physical Subjects* (Cambridge University Press, 1903).
[161] L. G. Leal, *Advanced Transport Phenomena* (Cambridge University Press, 2007).
[162] R. L. Miller *et al.*, Phys. Plasmas **5**, 973 (1998).
[163] F. Wagner and U. Stroth, Plasma Phys. Control. Fusion **35**, 1321 (1993).
[164] L. Lao *et al.*, Nucl. Fusion **25**, 1421 (1985).
[165] D. W. Swain and G. H. Neilson, Nucl. Fusion **22**, 1015 (1982).
[166] V. M. Amoskov *et al.*, Plasma Phys. Reports **29**, 997 (2003).
[167] F. Hofmann and G. Tonetti, Nucl. Fusion **28**, 519 (1988).
[168] R. A. Schill, IEEE Trans. Magn. **39**, 961 (2003).
[169] T. C. Luce, Plasma Physics and Controlled Fusion **57**, (2015).
[170] J. D. Weberski *et al.*, J. Fusion Energy **43**, 72 (2024).
[171] E. T. Hinson *et al.*, Phys. Plasmas **23**, (2016).
[172] J. L. Pachicano, Characterization of High Field Side MHD Activity During Local Helicity Injection, University of Wisconsin-Madison, 2018.
[173] D. J. Battaglia, Non-Solenoidal Tokamak Startup Using Localized Current Sources near the Outboard Midplane, University of Wisconsin-Madison, 2009.
[174] J. L. Luxon and B. B. Brown, Nucl. Fusion **22**, 813 (1982).
[175] B. Dasgupta *et al.*, J. Plasma Phys. **75**, 273 (2009).
[176] H. P. Summers and R. W. P. McWhirter, J. Phys. B At. Mol. Phys. **12**, 2387 (1979).
[177] C. Rodriguez Sanchez *et al.*, Rev. Sci. Instrum. **95**, (2024).
[178] R. Raman *et al.*, Phys. Plasmas **14**, (2007).
[179] M. D. Nornberg *et al.*, Fusion Sci. Technol. 1 (2025).
[180] P. N. Yushmanov *et al.*, Nucl. Fusion **30**, 1999 (1990).
[181] A. R. Field *et al.*, Plasma Phys. Control. Fusion **44**, (2002).
[182] D. A. Gates, Phys. Plasmas **10**, 1659 (2003).
[183] M. Ono *et al.*, Plasma Phys. Control. Fusion **45**, (2003).
[184] G. S. Kurskiev *et al.*, Phys. At. Nucl. **80**, 1313 (2017).
[185] J. G. Cordey *et al.*, Nucl. Fusion **45**, 1078 (2005).
[186] W. J. Cody, Math. Comput. **19**, 105 (1965).